HEALTH MONITORING OF TREES AND INVESTIGATION OF TREE ROOT SYSTEMS USING GROUND PENETRATING RADAR (GPR)

LIVIA LANTINI

A Thesis submitted in partial fulfilment of the

requirements of The University of West London

for the degree of Doctor of Philosophy

Supervisory team:

Professor Amir M. Alani

Executive Dean of the School of Computing and Engineering, University of West London

Professor Fabio Tosti

Professor of Civil Engineering, School of Computing and Engineering, University of West London

May 2021

‘da la meta mai

Non torcer gli occhi’

Alessandro Manzoni, “In morte di Carlo Imbonati”, 1805

Abstract

Evidence suggests that trees and forests around the world are constantly being threatened by disease and environmental pressures. Over the last decade, new pathogens spread rapidly in European forests, and quarantine measures have mostly been unable to contain outbreaks. As a result, millions of trees were infected, and many of these have already died. It is therefore vital to identify infected trees in order to track, control and prevent disease spread.

In addressing these challenges, the available methods often include cutting of branches and trees or incremental coring of trees. However, not only do the tree itself and its surrounding environment suffer from these methods, but they also are costly, laborious and time-consuming.

In recent years the application of non-invasive testing techniques has been accepted and valued in this particular area. Given its flexibility, rapidity of data collection and cost-efficiency, Ground Penetrating Radar (GPR) has been increasingly used in this specific area of research. Consequently, this PhD Thesis aims at addressing a major challenge within the context of early identification of tree decay and tree disease control using GPR. In more detail, two main topics are addressed, namely the characterisation of the internal structure of tree trunks, and the assessment of tree root systems' architecture. As a result, a comprehensive methodology for the assessment of both tree trunks and roots using GPR is presented, which includes the implementation of novel algorithms and GPR signal processing approaches for the characterisation of tree trunks' internal structure and the three-dimensional mapping of tree root systems. Results of this research project were promising and will contribute towards the establishment of novel tree evaluation approaches.

About the Author

Livia Lantini received the BSc (Hons.) degree in Civil Engineering and the MSc degree in Infrastructure and Transportation Engineering with the Department of Engineering, Rome Tre University, Rome, Italy. Since 2018 she is pursuing the PhD degree with the School of Computing and Engineering, University of West London, London, UK. Her research focuses on the assessment of civil engineering infrastructures using GPR and other non-destructive techniques, and in health monitoring and assessment of trees using GPR. Miss Lantini was a recipient of the Best Paper Award at the 2020 43rd International Conference on Telecommunications and Signal Processing.

Metrics (from 2018 to 15/05/2021)

Scopus

- Papers: **16**
- Citations: **55**
- H-index: **5**

Google Scholar

- Papers: **25**
- Citations: **104**
- H-index: **6**
- i10-index: **6**

International Peer Reviewed Journal Papers

- Tosti, F., Gennarelli, G., **Lantini, L.**, Catapano, I., Soldovieri, F., Giannakis, I., and Alani, A. M. (2020). The Use of GPR and Microwave Tomography for the Assessment of the Internal Structure of Hollow Trees. *IEEE Transactions on Geoscience and Remote Sensing* (under review).
- **Lantini, L.**, Tosti, F., Giannakis, I., Zou, L., Benedetto, A., and Alani, A. M. (2020). An Enhanced Data Processing Framework for Mapping Tree Root Systems using Ground Penetrating Radar. *Remote Sensing,* 12(20), 3417*.* DOI: 10.3390/rs12203417
- Alani, A. M., Giannakis, I., Zou, L., **Lantini, L.**, and Tosti, F. (2020). Reverse-Time Migration for Evaluating the Internal Structure of Tree-Trunks Using Ground-Penetrating Radar. *NDT&E International*. DOI: 10.1016/j.ndteint.2020.102294
- **Lantini, L.**, Alani, A. M., Giannakis, I., Benedetto, A., and Tosti, F. (2019). Application of Ground Penetrating Radar for Mapping Tree Root System Architecture and Mass Density of Street Trees. *Advances in Transportation Studies*.
- Giannakis, I., Tosti, F., **Lantini, L.**, and Alani, A. M. (2019). Diagnosing Emerging Infectious Diseases of Trees using Ground Penetrating Radar. *IEEE Transactions on Geoscience and Remote Sensing,* 1-10*.* DOI: 10.1109/TGRS.2019.2944070
- Alani, A. M., Soldovieri, F., Catapano, I., Giannakis, I., Gennarelli, G., **Lantini, L.**, Ludeno, G., and Tosti, F. (2019). The use of ground penetrating radar and microwave tomography for the detection of decay and cavities in tree trunks. *Remote Sensing*, 11(18), 1-19. DOI: 10.3390/rs11182073

- Alani, A. M., and **Lantini, L.** (2019). Recent advances in tree root mapping and assessment using non-destructive testing methods: a focus on ground penetrating radar. *Surveys in Geophysics*, 1-42. DOI: 10.1007/s10712-019-09548-6
- Giannakis, I., **Lantini, L.**, Tosti, F., and Alani, A. M. (2019). Health monitoring of tree-trunks using ground penetrating radar. *IEEE Transactions on Geoscience and Remote Sensing,* 57(10), 8317-8326*.* DOI: 10.1109/TGRS.2019.2920224

Conference Papers

- **Lantini, L.**, Tosti, F., Bianchini Ciampoli, L., and Alani, Amir M. (2020). A frequency spectrum-based processing framework for the assessment of tree root systems. In: *Proc. SPIE 11525, SPIE Future Sensing Technologies, 115251J*, Online event, November 09-13, 2020. DOI: 10.1117/12.2580583v
- **Lantini, L.**, Tosti, F., Giannakis, I., Zou, L., Egyir, D., Mortimer, D., and Alani, A. M. (2020). Health assessment of trees using GPR-derived root density maps. In: *2020 IEEE Radar Conference (RadarConf20)*, Online event, September 21-25, 2020.
- **Lantini, L.**, Giannakis, I., Tosti, F., Mortimer, D., and Alani, A. M. (2020). A Reflectivity-Based GPR Signal Processing Methodology for Mapping Tree Root Systems of Street Trees. In: *2020 43rd International Conference on Telecommunications and Signal Processing (TSP 2020),* Online event, July 07-09, 2020. DOI: 10.1109/TSP49548.2020.9163517
- Tosti, F., Gennarelli, G., **Lantini, L.**, Catapano, I., Zou, L., Soldovieri, F., and Alani, A. M. (2020). Assessing the Internal Structure of Hollow Trees Using

GPR and Microwave Tomography. In: *2020 43rd International Conference on Telecommunications and Signal Processing (TSP 2020),* Online event, July 07-09, 2020. DOI: 10.1109/TSP49548.2020.9163459

- **Lantini, L.**, Tosti, F., Giannakis, I., Egyir, D., Benedetto, A., and Alani, A. M. (2019). A Novel Processing Framework for Tree Root Mapping and Density Estimation using Ground Penetrating Radar. In: *10th International Workshop on Advanced Ground Penetrating Radar (IWAGPR 2019).* The Hague, The Netherlands, September 8-12, 2019. DOI: 10.3997/2214-4609.201902564
- Giannakis, I., Tosti, F., **Lantini, L.**, Egyir, D., and Alani, A. M. (2019). Signal Processing For Tree-Trunk Investigation Using Ground Penetrating Radar. In: *10th International Workshop on Advanced Ground Penetrating Radar (IWAGPR 2019).* The Hague, The Netherlands, September 8-12, 2019. DOI: 10.3997/2214-4609.201902601
- Alani, A. M., Soldovieri, F., Gennarelli, G., Giannakis, I., Catapano, I., **Lantini, L.**, Ludeno, G., and Tosti, F. (2019). A Tomographic Inversion Approach for the Detection of Decay and Cavities in Tree Trunks using Ground Penetrating Radar. In: *10th International Workshop on Advanced Ground Penetrating Radar (IWAGPR 2019).* The Hague, The Netherlands, September 8-12, 2019. DOI: 10.3997/2214-4609.201902567
- **Lantini, L.**, Holleworth, R., Egyir, D., Giannakis, I., Tosti, F., and Alani, A. M. (2018). Use of ground penetrating radar for assessing interconnections between root systems of different matured tree species. In: *2018 IEEE International Conference on Metrology for Archaeology and Cultural Heritage.* Cassino, Italy, October 22-24, 2018. DOI: 10.1109/MetroArchaeo43810.2018.13682

- Alani, A. M., Bianchini Ciampoli, L., **Lantini, L.**, Tosti, F., and Benedetto, A. (2018). Mapping the root system of matured trees using ground penetrating radar. In: *2018 17th International Conference on Ground Penetrating Radar.* Rapperswil, Switzerland, June 18-21,2018. DOI: 10.1109/ICGPR.2018.8441535

Conference Abstracts

- **Lantini, L.**, Tosti, F., Bianchini Ciampoli, L., and Alani, A. M. (2021). On the Use of Short-Time Fourier Transform for the Analysis of Tree Root Systems using Ground Penetrating Radar. European Geosciences Union (EGU) General Assembly 2021, Online event, April 19–30, 2021. DOI: 10.5194/egusphere-egu21-13463
- **Lantini, L.**, Tosti, F., Giannakis, I., Munisami, K. J., Mortimer, D., and Alani, A. M. (2020). Advanced GPR Signal Processing Techniques for Root Detection in Urban Environments. European Geosciences Union (EGU) General Assembly 2020, Online event, May 04-08, 2020. DOI: 10.5194/egusphere-egu2020-11954
- Giannakis, I., Tosti, F., Zou, L., **Lantini, L.**, and Alani, A. M. (2020). Tree Monitoring Using Ground Penetrating Radar: Two Case Studies Using Reverse-Time Migration. European Geosciences Union (EGU) General Assembly 2020, Online event, May 04-08, 2020. DOI: 10.5194/egusphere-egu2020-19697
- Tosti, F., Soldovieri, F., Catapano, I., Giannakis, I., Gennarelli, G., **Lantini, L.**, Ludeno, G., and Alani, A. M. (2020). GPR and Microwave Tomography for the Assessment of Hollowed Tree Trunks. European Geosciences Union (EGU)

General Assembly 2020, Online event, May 04-08, 2020. DOI: 10.5194/egusphere-egu2020-20841

- Alani, A. M., Chambers, J., Melarange, P., **Lantini, L.**, and Tosti, F. (2020). The Use of Ultrasonic Tomography for the Non-destructive Assessment of Tree Trunks. European Geosciences Union (EGU) General Assembly 2020, Online event, May 04-08, 2020. DOI: 10.5194/egusphere-egu2020-20872
- **Lantini, L.**, Tosti, F., Giannakis, I., Egyir, D., Benedetto, A., and Alani, A. M. (2019). The Use of Ground Penetrating Radar for Mapping Tree Root Systems in Urban Environments. In: *2019 COTA International Symposium on Emerging Trends in Transportation (ISETT)*. Rome, Italy, October 3-5, 2019.
- Giannakis, I., Alani, A., **Lantini, L.**, Mortimer, D., and Tosti, F. (2019). Diagnosing acute oak decline using ground penetrating radar. *TERRAenVISION abstracts, Vol. 2, TNV2019-TOOLS-2054, 2019*. TERRAenVISION 2019, Barcelona, Spain, September 2-7, 2019. DOI: 10.3390/proceedings2019030024
- **Lantini, L.**, Giannakis, I., Tosti, F., Benedetto, A., and Alani, A. M. (2019). Advances in Ground Penetrating Radar Signal Processing for Mapping Tree Root Systems. *Geophysical Research Abstracts Vol. 21, EGU2019-11467-3, 2019*. European Geosciences Union (EGU) General Assembly 2019, Vienna, Austria, April 7-12, 2019.
- Giannakis, I., Tosti, F., **Lantini, L.**, and Alani, A. M. (2019). Evaluating the Internal Structure of Tree Trunks Using Ground Penetrating Radar. *Geophysical Research Abstracts Vol. 21, EGU2019-11532-1, 2019*. European Geosciences Union (EGU) General Assembly 2019, Vienna, Austria, April 7-12, 2019.

Table of Contents

List of Figures

List of Tables

List of Abbreviations

AGC	*Automatic Gain Control*
AOD	*Acute Oak Decline*
BA	*Born Approximation*
CRIM	*Complex Refractive Index Model*
CT	*Computed Tomography*
EID	*Emerging Infectious Diseases*
EM	*Electromagnetic*
ERT	*Electrical Resistivity Tomography*
FDTD	*Finite-Difference Time-Domain*
F-K	*Frequency-Wavenumber*
GPR	*Ground Penetrating Radar*
PEC	*Perfect Electric Conductor*
PML	*Perfectly Matched Layer*
PSO	*Particle Swarm Optimisation*
RT	*Reverse-Time*
SEC	*Spherical and Exponential*
SFCW	*Stepped Frequency Continuous-Wave*
STFT	*Short-Time Fourier Transform*
SVD	*Singular Value Decomposition*
TM-FDTD	*Transverse Magnetic Finite-Difference Time-Domain*
TSVD	*Truncated Singular Value Decomposition*

1. Introduction

Trees and plants have always been part of life on planet Earth. The earliest identified fossil tree, from over 386 million years ago, was recently found in the New York State, USA (Stein, et al., 2020). The impact of trees and their value to human life and the environment have been widely discussed in the literature for decades. In more detail, the value of trees within the context of modern life could be considered under the following areas:

- Ecological and environmental
- Community and social
- Aesthetics
- Commercial and economic

Trees and forests are every society's asset and must be looked after and cherished. The contribution of trees and their importance to environmental sustainability are so vast that they can only be compared to the existence of icebergs and our oceans. Prevention from the destruction of trees and plants by cutting them at an alarming rate for materialistic reasons (i.e. creating wealth in different shapes and forms) is vital to the preservation of life, both for humans and animals, on the planet Earth.

Likewise, safeguarding and having planned health monitoring and assessment of the existing trees and plants are equally important. Within this context, the understanding of the health of tree roots and plants (i.e. growth, architecture and interaction with the soil and other tree roots) are of paramount importance.

Appropriately managing and caring for natural heritage is more critical than ever today (Innes, 1993), and there is a growing awareness of the need to protect the

environment. In particular, the preservation of veteran or ancient trees presents a series of conservation challenges that differ from standard arboricultural practices.

Various methods have been used to study the trunks and root systems of plants. Such investigations are usually carried out using destructive methods, such as core drilling, excavation or uprooting. Although these techniques can provide direct measurements, they are onerous, time-consuming and above all, destructive. The damage that these techniques inflict on trees leads to a reduction in the number of measurements which can be carried out in the future, making it impossible to assess the status of the roots during a given period. Also, the damage suffered by the trees using these inspection methods makes them susceptible to infections and diseases, which can lead to the death of the tree.

The use of non-destructive techniques for tree inspection and analysis has gained popularity in recent years, as this method can provide information about both the internal structure of the tree and the tree root architecture without harming the plant. It also enables long-term monitoring, as no disturbance is caused by the application of these techniques.

In this framework, ground penetrating radar (GPR) is widely acknowledged to be a powerful geophysical non-destructive tool, useful in locating buried objects such as bedrocks, artefacts, utilities infrastructure and objects, voids and sub-surface water levels. Recently, several studies have been carried out about the use of GPR for the characterisation of the internal structure of trees, as well as for root detection, mapping and estimation of root biomass and diameter. This technique has shown great potential due to the reliability of the results and its ease of use. However, research has led to contradictory results, due probably to difficulties in surveying non-homogeneous

media. To this extent, the primary aim of this research is to investigate the potential of GPR in the assessment and health monitoring of trees, and in the investigation of tree root systems and their interaction with the soil.

This Thesis is organised as follows:

Chapter 1 provides an overview of this study. A background is provided, the problem stated, and a summary of the current state of the research is presented.

Chapter 2 provides a theoretical background on the subject. A brief explanation of the tree structure is given, followed by a review on both the health issues that could affect the trees and the damages that the trees could cause to the built environment. An extensive review of the main destructive and non-destructive testing methods for the assessment of tree trunks and the detection of tree roots is therefore given. Subsequently, a detailed description of the GPR is given, ranging from the theory of electromagnetic (EM) waves to the main GPR systems and antenna configurations, arriving to a review of the applications of GPR in this research area.

Chapter 3 identifies the scope of the present research, outlining aims and objectives of the project, and defining research questions and paradigms.

Chapter 4 describes the research carried out on the characterisation of the internal structure of tree trunks. Three main research lines are described:

- Interpretation of complex reflection patterns
- Detection of early decays using a Modified Kirchhoff Migration and Reverse-Time Migration
- Application of microwave tomography for detection of decays and cavities.

For all the above topics, a theoretical framework is provided, followed by an explanation of the research methodology and the description of the numerical experiments and the case studies carried out. Results are then discussed, and conclusions are given.

Chapter 5 describes the research performed on the use of GPR for the reconstruction of tree root systems architecture. A comprehensive explanation of the data processing framework is given, and three research lines are described through case studies:

- Assessment of tree root systems
- Evaluation of tree root system interconnections
- Assessment of tree root systems for street trees

Once again, the theoretical basis for the method is given, accompanied by an overview of the research methodology itself and a review of the field case studies carried out. Results are therefore discussed and conclusions are drawn.

Chapter 6 contains the conclusions of the work and general recommendations that emerged from the analysis of the results obtained.

2. Research Background and Theoretical Framework

This Chapter deals with the existing literature on the use of GPR in the health monitoring and assessment of trees. To this extent, an overview of the tree structure and main organs is given, followed by a review on the major tree health, structural and environmental-related issues. Following, a review of the most important destructive and non-destructive testing methods for tree assessment is presented, where the advantages and limitations of every technique are examined and compared. Finally, an in-depth study on GPR is presented, including theoretical and practical aspects of this survey method. A review of the GPR applications in the assessment of tree trunks and tree roots is also given.

2.1. Tree Structure

As vascular plants, trees are organised into three principal organs: the roots, the bole (commonly known as trunk or stem), and the crown (Figure 1). The crown consists primarily in branches and foliage, which are the principal photosynthetic organs of the tree. This structure is supported by the trunk, which is responsible for conduction of minerals and water, storage of nutrients and structural support. The roots are connected to the trunk and are commonly located below the soil surface. The role of the root system is to anchor the tree to the soil while absorbing water and minerals and storing nutrients.

The paragraphs of this Chapter have been published as part of a journal paper in Surveys in Geophysics (Alani & Lantini, 2019). Note that minor changes have been introduced to make the text consistent with the other Chapters of this Thesis.

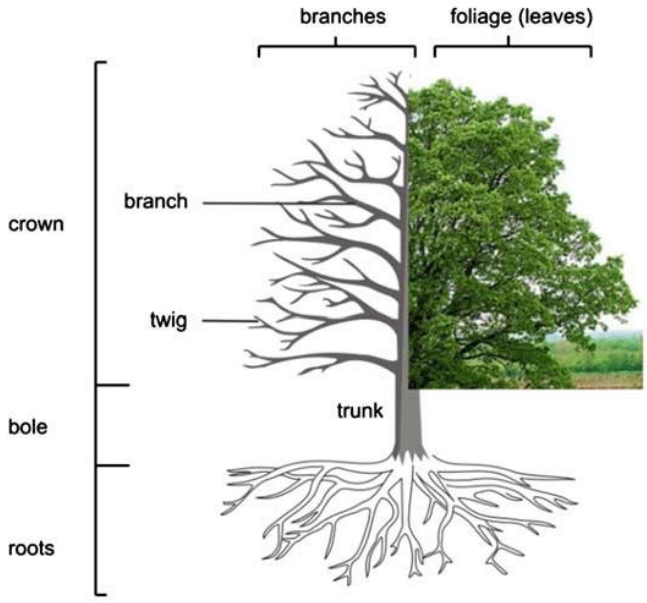

Figure 1: The structure of a tree (Ningal, et al., 2010)

For the purposes of this Thesis, the study will focus on the analysis of the trunk and the root system. Please refer to specialised literature for further details on the crown (Pallardy, 2008).

2.1.1. The Trunk

The trunk is the main axis of a tree, connecting roots with the crown and providing shape and strength to the tree.

According to Côté (1968), the structure of a tree trunk can be mainly divided into three parts. Nonetheless, a more comprehensive classification, as mentioned by Pallardy (2008), describes the layers of the tree trunk as follows (Figure 2):

- the outer bark: a layer made of dead tissue, whose function is to protect the tree from external agents like diseases, insects or fungi, weather conditions or fire.
- the inner bark (or phloem): a thin layer of living cells, responsible for the transport of nutrients from the roots to the leaves and vice versa.

- the cambium: the plant's principal growth tissue. It generates secondary xylem inwardly, towards the pith, while producing secondary phloem outwardly to the bark.
- the sapwood (or xylem): this layer includes the living wood. Its cells are responsible for the transportation of water through the tree, as well as the storage of nutrition.
- the heartwood: central part of the trunk, made of sapwood cells that have become inactive due to the tree growth. Heartwood can be distinguished from the sapwood as it is darker in colour, being filled with resins, oils and minerals. The primary function of this layer is to provide structural strength, as it is no longer involved in nutrition transport processes.

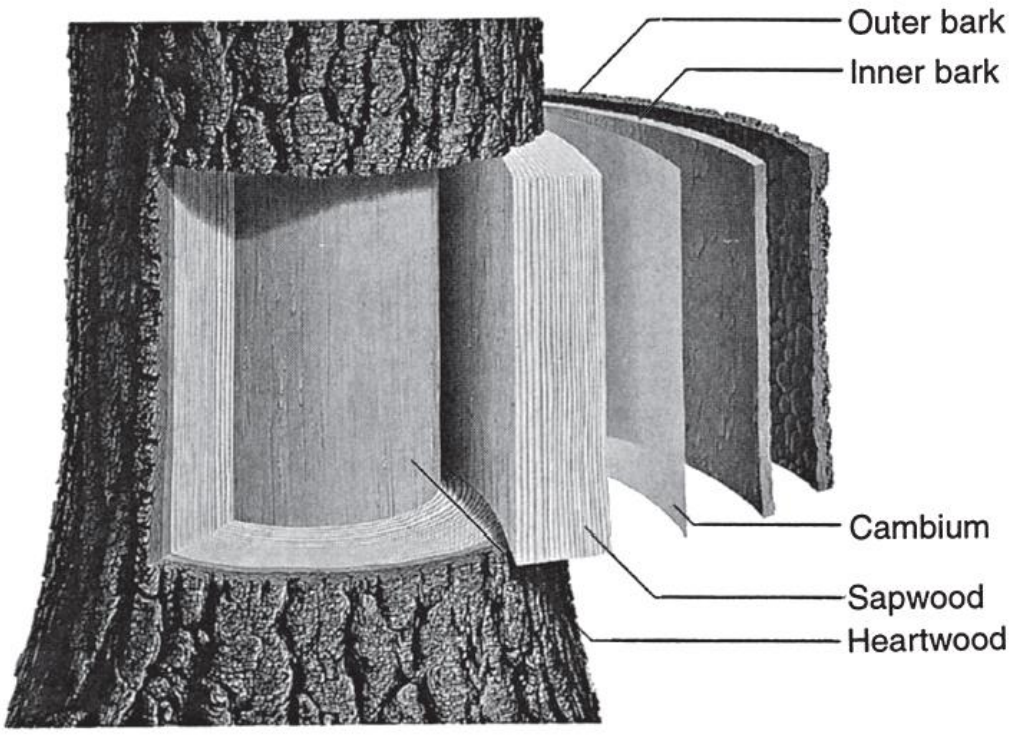

Figure 2: Generalised structure of a tree trunk (Pallardy, 2008)

Tree trunks narrow from the base to the top depending on tree species, age, height, and the number of trees per unit of land area (Pallardy, 2008).

2.1.2. The Root System

Tree roots are responsible for water and mineral uptake, carbohydrate storage and hormonal signalling (Pallardy, 2008), as well as for providing support and anchorage in the ground (Coutts, 1983). Thus, the health of the root system, and as a consequence the health of the tree, is closely linked to the soil conditions (Gregory, 2006).

Tree roots are usually composed of complex structures, and they can be divided into two main groups:

- Woody roots: roots that have gone through secondary growth, resulting in a more rigid structure. Such roots have a structural role, as they are essentially responsible for anchoring the tree in the ground, and their lifespan is perennial (Pallardy, 2008). Wilson (1964) observed that woody roots that are located within one or two meters of the stem, the so-called zone of rapid taper, have different features from the roots that are located beyond this area, as the former often exhibit considerable secondary thickening. If the thickening is along the vertical plane, they are called buttress roots, the presence of which has been associated with soils that offer poor anchorage (Henwood, 1973). Beyond the zone of rapid taper emanates a framework of woody structural roots that gather water and nutrients from long distances to the trunk: their size is often influenced by mechanical stresses such as the wind load (Stoke, 1994).
- Non-woody roots: also known as fine or absorbing roots, they are responsible for the absorption of water and nutrients (Pallardy, 2008), the synthesis of rooting hormone, root exudation, and symbiosis with soil microorganisms. As the name suggests, they do not undergo secondary thickening, are generally

small in diameter (< 2 mm) and their lifespan ranges from days to weeks, depending on soil conditions and temperature (Pallardy, 2008).

Root architecture is quite complex and varies between and within plant species (Gregory, 2006). As far as rooting depth is concerned, it is influenced not only by the tree species but also by the type and conditions of the soil (Stone & Kalisz, 1991). In fact, the downward penetration of roots can be impeded by soils that are poorly aerated or too dense, and by the presence of rock layers or by low soil temperatures. Stone and Kalisz (1991) carried out an extensive study on tree roots, reviewing the existing literature and performing on-site surveys on a wide variety of tree species, demonstrating that root extent is strictly related to site conditions. Indeed, evidence has been found that many species can reach considerable depths if not limited by soil characteristics. According to Jackson et al. (1996), there can be significant differences in rooting depths, depending on the features of the surrounding environment: rooting profiles are shallowest in boreal forests, temperate grasslands, and tundra, due not only to the convenient characteristics of soil moisture and aeration but also the presence of physical barriers to root vertical growth, such as permafrost in tundras and some boreal forests (Bonan, 1992). On the other hand, root distribution is deeper in deserts and xeric shrublands, as the lack of water and nutrients in the shallow subsurface, together with extreme soil surface temperatures, inhibits root development in the upper soil layers (Nobel, 2003) and forces them to grow deeper. Regardless, there is undoubtedly a tendency for tree roots to be concentrated in the surface soil (Wilson, 1964; Wang, et al., 2006), as it is usually better aerated and moist, it contains a higher concentration of minerals than the deeper layers. Pallardy (2008) states that root density is often higher in the first 0.30 m below the soil surface.

On the other hand, root spread seems to be less closely related to soil temperature and characteristics (Strong & La Roi, 1983). The extent of root development seems to rely upon the tree species, but also upon the stand density (Stone & Kalisz, 1991) and the presence of competing species (Shainsky & Radosevich, 1992). Many rules of thumb have been presented for estimating root spread, the most common of which is a relation between root extent and canopy diameter (Tubbs, 1977); however, Stone and Kalisz (1991) reported many examples of a maximum lateral root extent of more than 30 m from the trunk, and in some cases more than 50 m. This seems to demonstrate that roots tend to explore the largest possible soil area, in order to exploit its resources and provide anchorage and stability. These estimates commonly assume that there are few significant physical impediments to root extent; moreover, not much is known about how different trees compete for water and mineral uptake when root systems come in contact with one another.

2.2. Tree Health, Structural and Environmental-Related Issues

2.2.1. Tree Health and Stability

Tree diseases are an integral part of natural ecosystems, as they regulate the development of forests (Hansen & Goheen, 2000). The coexistence of plants and pathogens is therefore necessary for the survival of both. However, human activities have often altered the natural balance, breaking down the geographical barriers that had preserved the ecosystems and allowing the movement of wild species (Richardson, et al., 2001).

Mechanisation and air pollution have led to an increase in tree disease and attacks from wood-boring insects both in commercial forestry and in amenity trees in the landscape and along roadsides (Habermehl, 1982). One of the factors of tree decay

is the presence of pathogens carried along by the wind, which can grow to epidemic phenomena and often to a quick death of entire forests (Robinson, 1976). In this regard, significant changes to woodlands and forests in the last century are due to invasive Emerging Infectious Diseases (EIDs) caused by pathogens, pests and fungi (Broome, et al., 2018; Santini, et al., 2012). Recent examples include the European beech decline (Jung, 2009), the chestnut blight that almost brought the chestnut trees of North America to an extinction (Ellison, et al., 2005; Anagnostakis, 1987) and the Dutch elm disease that caused significant damage to the elm forests in central Europe (Brunet, et al., 2014). Clear evidence suggests that modern socioeconomic factors such as accelerating human population (Guo, et al., 2012), international travelling (Santini, et al., 2012), global timber trade (Broome, et al., 2018) and artificial erosion of geographic barriers (Santini, et al., 2012), have largely increased the spreading rate of invasive pathogens (Guo, et al., 2012). In addition, climate change has raised the global temperature, which has further contributed to the spreading of EIDs (Santini, et al., 2012; Jung, 2009). Such diseases not only have severe ecological consequences, but they can also have economic repercussions (Aukema, et al., 2011).

The reasons above led to an exponential increase of EIDs (Broome, et al., 2018). It is indicative that from 1995-2010, EIDs have shown a 13-fold increase (Fisher, et al., 2012). The most prominent of them are the ash dieback, the acute oak decline (AOD) and the Xylella Fastidiosa. Ash dieback (Figure 3) is a significant threat to European ash forests (Stocks, et al., 2017) with high susceptibility (Kjær, et al., 2012) and mortality rates (Stocks, et al., 2017). It was confirmed in the UK in 2012 (Broome, et al., 2018) and it has rapidly spread since then mostly in Wales and southeast England (Stocks, et al., 2017).

Figure 3: Cross-section of a tree trunk showing the symptoms of the ash dieback. ©Fera-Crown

Apart from ash dieback, AOD is another recently introduced EID that poses a major threat to European oak populations (Denman, et al., 2014). AOD is a multi-agent EID that has spread rapidly in the UK in the last decade (Denman, et al., 2014). The progression of the disease is exceptionally fast and can lead to tree mortality within 3-5 years (Denman, et al., 2014). Ash dieback and AOD have already infected thousands of trees in the UK. Nonetheless, their impact is dwarfed in comparison to the millions of trees affected by Xylella Fastidiosa in Italy (Bosso, et al., 2016). Xylella Fastidiosa is a vector-transmitted, slow-progressing bacterium (Janse & Obradovic, 2010; Cella, et al., 2018) that has spread in Italy with devastating effects to the overall population of olive trees (Bosso, et al., 2016). Italy has declared a state of emergency since 2015 and is now under European quarantine control (Abbott, 2018). The international scientific community and the media (Zarco-Tejada, et al., 2018) have underlined that under the current framework, eradication of EIDs is a laborious task and new forestry approaches should be developed for monitoring and diagnosing EIDs (Santini, et al., 2012).

Nevertheless, tree diseases do not necessarily represent a threat to tree endurance. Some pathologies, like the heart rot disease (Basham, et al., 1968; Lee & Yahya,

1999), causes wood decay at the centre of trunks or branches and can escalate into heartwood decomposition. As a consequence, the latter softens and rots, eventually forming a tree hollow (Cockle, et al., 2012; Clark & Clark, 2000) (Figure 4).

Figure 4: A tree hollow

As already stated, the heartwood is composed of dead tissues, which are not involved in the tree's biological and physiological processes (Pallardy, 2008), and as such, its decay does not jeopardise tree survival (Zheng, et al., 2016). A hollow tree can, in fact, keep increasing in size (Edworthy & Martin, 2014), as transportation and storage of nutrients take place in living wood, that is the sapwood (Pallardy, 2008). Furthermore, tree hollows are an essential resource for a wide variety of animal species (Bennett, et al., 1994), including bats, birds, snakes, insects and also fungi (Gibbons & Lindenmayer, 2002; Ranius & Hedin, 2001; Antonsson, et al., 2005). They are used for diurnal and nocturnal shelters and as breeding grounds, and the scarcity of hollows can be a limiting factor for certain species (Bennett, et al., 1994). Nevertheless, the

decomposition of the heartwood, the primary purpose of which is to provide structural support (Pallardy, 2008), and the possible development of the hollows, may have a considerable effect on the tree's stability. Strength of the stem is diminished by the development of cavities and hollows, with the result that trees are structurally unstable and more likely to fall under the effect of external forces, such as wind load (Mattheck, et al., 1994). This occurrence does have significant importance in forests and woodlands, as a dead hollow tree continues to provide food and protection for wildlife. However, in urban environments, a hollow tree can represent a hazard for people, structures and infrastructures (Mattheck, et al., 1994).

Regarding the tree root system, fungal infections are one of the main causes of root disease, as fungi are natural components of forests (Hansen & Goheen, 2000). These typically contaminate trees which have already been weakened by other factors, such as other pests or climatic changes (Williams, et al., 1986), and they usually spread from the roots of dead or uprooted trees (Rishbeth, 1972). Fungi penetrate the bark and initiate decay in roots, inducing root rot and infecting coarse roots and the lower stems of trees (Figure 5).

Figure 5: Roots and lower stem of a tree infected by *Armillaria root rot* fungi (Canadian Forest Service, 2015)

Plants can live for a long time even if sick, as they continue to collect water and nutrients from healthy roots. Within this time, the infection can spread to other trees through root contact (Hansen & Goheen, 2000). Eventually, rotten roots will not be able to provide anchorage and sustenance, and the contaminated tree will die either by wind-throw or disease, if the infection spreads from the roots to the rest of the plant (Rishbeth, 1972).

The recognition of root diseases is difficult, as fungal infections do not show visible symptoms. Manifestations of diseases can include the production of mushrooms around the tree base, foliage discolouration and reduced growth (Williams, et al., 1986). However, these symptoms can take several years to materialise if the tree is large or old, and by the time the disease is recognised, it is often too late for any interventions.

2.2.2. Built Environment

2.2.2.1. Buildings

Despite being an essential presence in urban and archaeological sites, trees can also cause damage to structures and buildings. Damage can occur through direct contact with tree roots (Satriani, et al., 2010), as their growth can cause structures to uplift. This is more likely to take place near the tree trunk, as the pressure exerted by roots decreases rapidly with distance (MacLeod & Cram, 1996). This usually occurs when trees are allocated an inadequate space: as the tree grows up, the roots start spreading and making their way underneath buildings (Day, 1991). The pressure that roots are capable of exerting is relatively weak and is further diminished by urban soil compaction (Roberts, et al., 2006). Moreover, modern building foundations are designed to withstand root-inducted movement.

Indirect damage is a more common cause of disturbance to structures, especially the shrinkage of expansive soils (Driscoll, 1983). Roots belonging to trees growing close to buildings tend to develop under the foundations, as the moisture content there tends to be higher than in the surrounding soil (Figure 6). The extraction of water by roots creates a reduction in soil volume, resulting in subsidence and cracks in the structures (Day, 1991).

Figure 6: Tree roots growing under foundations (CNT Foundations, 2020)

Cutler and Richardson (1981) and Biddle (2001) have reviewed several cases of damage to buildings, producing an extensive analysis of how tree root interaction with the surrounding environment can damage buildings. Regarding damage to ancient structures, Caneva, Ceschin and De Marco (2006) have carried out a risk evaluation of root-induced damage which archaeological sites are exposed to, while Caneva et al. (2009) have surveyed the archaeological site of Villa Torlonia in Italy, investigating the root expansion and evaluating the tendency of various species to harm ancient monuments.

2.2.2.2. Utilities

Underground services, especially sewers, are frequently obstructed or damaged by the growth of roots. This damage usually occurs in old systems (Randrup, et al., 2001), as these were built with materials which could deteriorate with time, such as bricks or concrete. Moreover, roots are attracted by the presence of moisture around pipes,

which are commonly cooler than the surrounding soil (Brennan, et al., 1997) and tend to grow around the pipe (Figure 7).

Figure 7: Roots growing around a pipe (911HVAC, 2019)

Modern sewers are made of plastic, iron or reinforced concrete, which are unlikely to be damaged by root growth pressure. Potential leakages due, for example, to a broken joint (Schrock, 1994) or poor construction (Sullivan, et al., 1977; Brennan, et al., 1997) can lead to roots penetrating the pipe, and eventually blocking it.

2.2.2.3. Roads and Pavements

Urban trees provide several environmental, social and economic benefits, but they can also cause extensive damage to road infrastructures. Root development can cause disruptions to road surfaces, such as cracking or uplifting (Francis, et al., 1996) (Figure 8). This damage can have serious consequences (Tosti, et al., 2018), leading to additional pavement maintenance or repair and interventions on the tree (Mullaney, et al., 2015).

Figure 8: Damages to road pavement due to tree roots (Alani & Lantini, 2019)

One of the principal causes of conflict between roots and infrastructures seems to be the limited space provided for the development of trees (Barker, 1983; Francis, et al., 1996). Tree size at maturity should be considered when choosing tree species to plant, as it will influence the necessary volume of soil (Trowbridge & Bassuk, 2004). Such amounts of soil are not typical of urban environments, and trees are usually confined to tree lawns, which restrict not only the roots but also the branch and canopy development (Pokorny, et al., 2003). Also, trunk flare and root buttresses are associated with road infrastructure damages (Wagar & Barker, 1983), and the tendency of species to develop them should be considered when choosing which tree to plant (Costello & Jones, 2003). Finally, when large trees are planted in cities, there is a significant danger of wind-throw, as tree roots are often cut during pavement repairs and therefore cannot offer sufficient resistance to wind load (Pokorny, et al., 2003). Therefore, a selection of species adequately matched to the site conditions is advisable (Costello & Jones, 2003), as this can lead to a significant reduction of

hazards; however, McPherson and Peper (2000) state that this resolution would reduce the benefits gained from larger trees.

Another factor which limits root development is soil compaction, as it decreases soil aeration, restricts air and water movement, limits water-holding capacity, and impedes root penetration (Boyer, 1995). This is a significant issue in urban areas, as it conflicts with road engineering specifications, which require a load-bearing base to support pavement loading (Grabosky, et al., 1998). The essential requirement is to increase soil compaction in order to reduce cavities and increase contact between the grains, thus giving the lithic structure a high frictional resistance. Moreover, this minimises deferred subsidence, providing greater functionality and security to the infrastructure. The resulting level of compaction produces unbearable conditions for root growing (Blunt, 2008; Grabosky, et al., 2009) as it limits access to oxygen, water and nutrients (Loh, et al., 2003; Lucke, et al., 2011; Tracy, et al., 2011). Table 1 compares the prescriptions for bulk densities of soils based on the Proctor Compaction Test (ASTM D698/AASHTO T99) with the maximum level of compaction, which inhibits root penetration.

Table 1: Critical bulk densities for differing textures' soils (ASTM D698/AASHTO T99). Critical bulk density is defined as the compaction level at which the roots are no longer able to penetrate the soil. Units are given as dry bulk density in grams per cubic centimetre (gm/cc). WG is with gravel; MG is minus gravel (Lindsey & Barlow, 1994)

Bulk density of soils at 70 - 95% relative compaction						
		Landscape		Paving		Critical bulk density
		70%	85%	90%	95%	
Soil type	Loamy sand (WG)	1.52	1.85	1.96	2.07	1.75
	Sandy loam (WG)	1.43	1.74	1.85	1.95	1.70
	Sandy loam (MG)	1.35	1.64	1.74	1.83	1.70
	Sandy silty clay	1.29	1.56	1.66	1.75	1.50
	Silt	1.19	1.45	1.53	1.62	1.40
	Silty clay	1.22	1.49	1.58	1.66	1.40
	Clay	1.15	1.40	1.49	1.57	1.40

Such levels of compaction cause roots to develop at the interface between the pavement and soil, where nutrients and moisture are available (Kopinga, 1994; Wagar & Franklin, 1994; Randrup, et al., 2001). The favourable conditions that roots find at the interface between the surface layer and the sub-base make them grow faster, resulting in accelerated secondary thickening that can cause damage to the road surface (Nicoll & Armstrong, 1998).

Other issues that can interfere with root growth in urban environments and lead to road infrastructure damage are waterlogging (Boyer, 1995; Pokorny, et al., 2003) and severe water deficiency (Boyer, 1995; Mullaney, et al., 2015). In the former case, soil saturation displaces air, making soil aeration more restrictive as depth increases and therefore forcing roots to grow within the soil surface; these conditions encourage the development of root pathogens. In the latter case, water deficit causes trees to slow down their leaf growth, resulting in a surplus of carbohydrates, which then become

available for root growth. The immediate consequence, therefore, is that the root dimensions of water-stressed plants are higher than average.

2.3. Tree Assessment Methods

The detection of the early symptoms of tree decay represents a major challenge for the identification of tree diseases or tree hollows. Similarly, locating tree roots and estimating their depth and spread is a significant challenge, and a necessary condition for several practices, ranging from tree health preservation to safety assessment in urban areas. At present, several assessment methods for tree assessment are available, which can be divided into destructive or non-destructive techniques.

This Section aims at providing a comprehensive review of the most used assessment techniques for the assessment of tree trunks and tree root systems. Some of the presented techniques can be implemented in both scenarios. To this extent, Table 2 provides an overview of the tree assessment methods and their area of application.

Table 2: Tree assessment methods and their area of application

		TRUNK	ROOTS
DESTRUCTIVE TESTING METHODS	INGROWTH CORE		✓
	AUGER METHOD	✓	✓
	MONOLITH METHOD		✓
NON-DESTRUCTIVE TESTING METHODS	(MINI)RHIZOTHRONES		✓
	PULLING TEST	✓	✓
	ELECTRICAL RESISTIVITY TOMOGRAPHY (ERT)	✓	✓
	ACOUSTIC DETECTION	✓	✓
	X-RAY COMPUTED TOMOGRAPHY	✓	✓
	GROUND PENETRATING RADAR (GPR)	✓	✓

2.3.1. Destructive Testing Methods

Destructive testing methods allow for the investigation of tree trunks and root systems only at the time of sampling and, therefore, they are of limited value for investigating developmental processes. Moreover, these techniques are not only destructive to the tree itself and its immediate environment (Taylor, et al., 1991), but are also expensive, time-consuming and laborious (Krainyukov & Lyaksa, 2016). As far as tree roots are concerned, given the variability of a root system architecture, several replicated samples are needed to assess root parameters precisely. This is also true for the investigation of tree trunks, as the assessment of a tree health status may require many samples to be taken at different heights (Grissino-Mayer, 2003). However, this practice destroys the tree and exposes it to diseases and infections that can lead to its death (Smit, et al., 2013). Nevertheless, these techniques are still widely used, as they provide reliable quantitative results.

The main destructive techniques are:

- Ingrowth core method
- Auger method
- Monolith method

2.3.1.1. Ingrowth Core Method

Ingrowth cores are commonly used to quantify fine root production and to estimate the rate of growth during a given period (Smit, et al., 2013). They are also adopted to examine the effect of experimental manipulation on root growth (Majdi, et al., 2005). The operating principle of this technique is to replace a volume of soil (as it is) with the same volume of root-free soil, enclosed in a mesh bag, which is resampled after a determined period (Figure 9). This method is widely acknowledged to be

straightforward and inexpensive, and it illustrates how long it takes for roots to develop in a particular soil. However, it can lead to misinterpretation, as the soil structure is altered when the mesh bags are introduced into the cores (Smit, et al., 2013), and this can affect root growth rates. Moreover, since the initial coring damages roots, their development into the root-free samples can be unnatural (Majdi, et al., 2005).

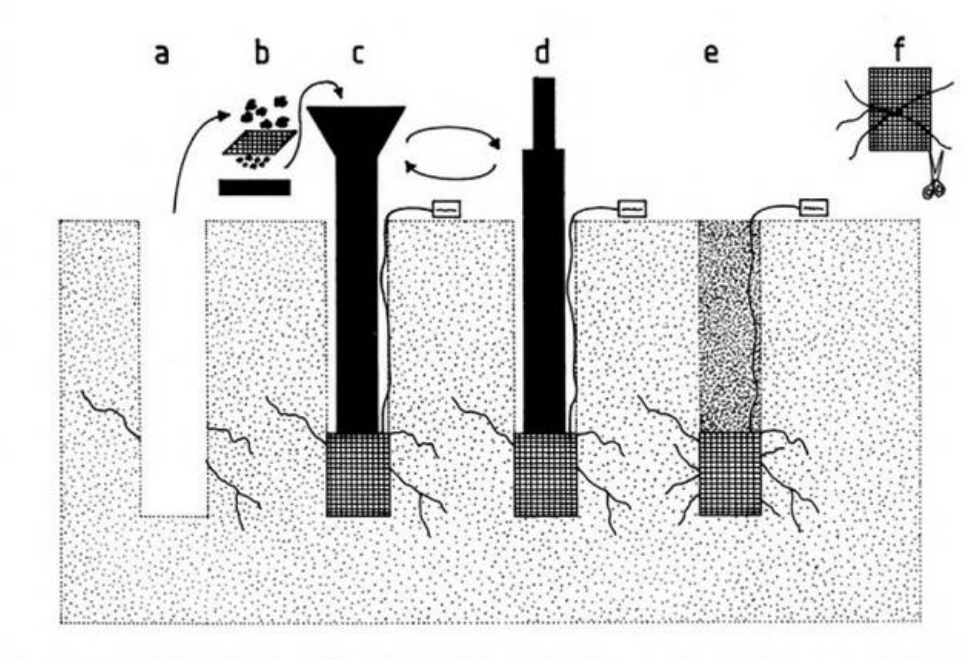

Figure 9: Procedure for installing the mesh bags for the root ingrowth core technique (Smit, et al., 2013). a) a core of soil is removed and b) the soil is sieved to remove the roots; c) a mesh bag is placed in the hole, which is filled with the sieved soil; d) the soil is packed to the initial bulk density using a pestle; e) the mesh bag is left in place for a determined time, after which it is recovered and f) non-woody roots are trimmed.

2.3.1.2. Auger Method

The auger method is the most convenient for investigating root density. It involves taking soil samples from the field, which are then washed to separate roots from the soil (Bohm, 2012; Smit, et al., 2013). The soil core extraction can be made using either a hand-operated or a mechanical sampler, depending on the hardness of the investigated soil. The former is faster to use, being a cylindrical tube 0.15 m long with an inside diameter of 0.07 m, equipped with a T–handle at the top that simplifies the penetration into the soil by rotation. However, if core samples need to be taken from

hard soil or considerable depths, the auger is driven into the soil by a motorised dropping hammer, and then pulled back using a screw-jack (Smit, et al., 2013).

When related to the investigation of tree trunks, this method is often called core drilling or increment coring, and it is a typical tree age and growth measurement system (van Mantgem & Stephenson, 2004). This technique is also widely used to determine wood density (Chave, 2005).

There exists uncertainty about the frequency of samples required in order to obtain reliable results (Bohm, 2012). However, increasing the number of samples will lower the uncertainty and improve the variability of data collected (Smit, et al., 2013). Consequently, this technique is time-consuming (Majdi, 1996) and the large number of replicates required harms a considerable part of the investigated trunk or root system (Smit, et al., 2013). Moreover, when used for root investigations, the type of soil can prevent the sampler from being inserted, such as in stony or dry clay soils (Smit, et al., 2013).

2.3.1.3. Monolith Method

The monolith method requires large blocks of soil to be removed and washed out in order to separate the roots from the soil (Boyer, 1995; Bohm, 2012). Contrary to the auger method, which requires just the root volume to be quantified, in this technique, roots are washed without displacing them from their original position (Weaver & Voigt, 1950). This is possible thanks to the use of special boards covered with spikes, called pinboards, which are driven into the soil to preserve the root architecture while the soil is washed away (Boyer, 1995) (Figure 10).

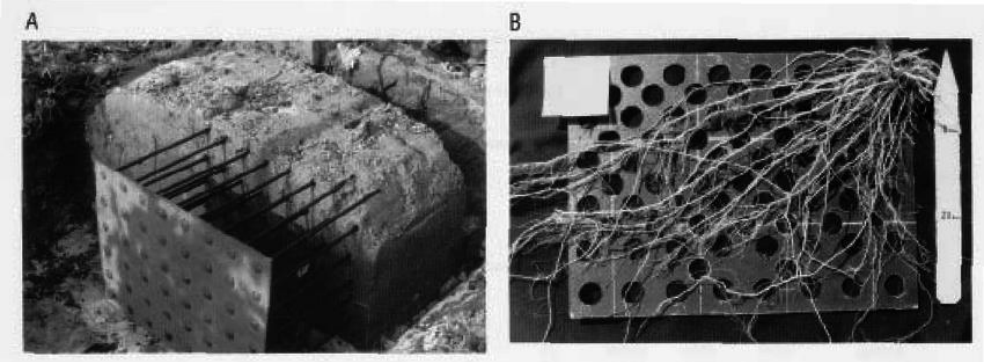

Figure 10: Metallic monolith pinboard used for excavating the soil-root samples (left) and roots after extraction and washing from the soil (right) (Leskovar, et al., 1994)

This technique provides useful information, as it is possible to have a general view of the root system architecture (Smit, et al., 2013). On the other hand, the collection of the samples requires great skill in order not to displace the roots, so the pinboards are usually of limited dimensions; additionally, the washing process can introduce biases, as significant losses of fine roots can occur (Smit, et al., 2013). Finally, this method is often non-repeatable, as the hole will be filled up with new soil that could lead the roots to develop differently, affecting the results of a second inspection (Schuurman & Goedewaagen, 1965).

2.3.2. Non-destructive Testing Methods

Non-destructive evaluations are acknowledged as being effective in investigating different materials, without harming or damaging them (Buza & Divos, 2016). Furthermore, these techniques are easily repeatable, which means that long-term investigation and monitoring of trees can be achieved (Buza & Divos, 2016).

The main non-destructive techniques applied in tree assessment are:

- Rhizotrons and minirhizotrons
- Pulling test
- Electrical resistivity tomography (ERT)

- Acoustic detection
- X-ray computed tomography (CP)
- Ground penetrating radar (GPR)

2.3.2.1. Rhizotrons and Minirhizotrons

One of the first NDT methods for tree root system observations was to put glass plates into the soil, so that it was possible to observe root development and growth against them. This method has evolved into the modern rhizotron, namely an underground chamber equipped with glass walls (Boyer, 1995).

This technique provides repeated and non-destructive access to soil and roots, allowing for a better understanding of underground processes as they are in nature. Nevertheless, since such an instalment is impossible to set up for assessment of urban trees, minirhizotrons have become increasingly popular. These instruments consist of small plastic tubes (about 0.05 m in diameter and 2 to 3 m long), which can be driven into the ground at different angles (Majdi, 1996). A fibre optic light and a camera are then lowered down the tube, in order to observe the roots' developmental process over time (Boyer, 1995), sometimes in combination with dedicated image processing software (Majdi, 1996) (Figure 11).

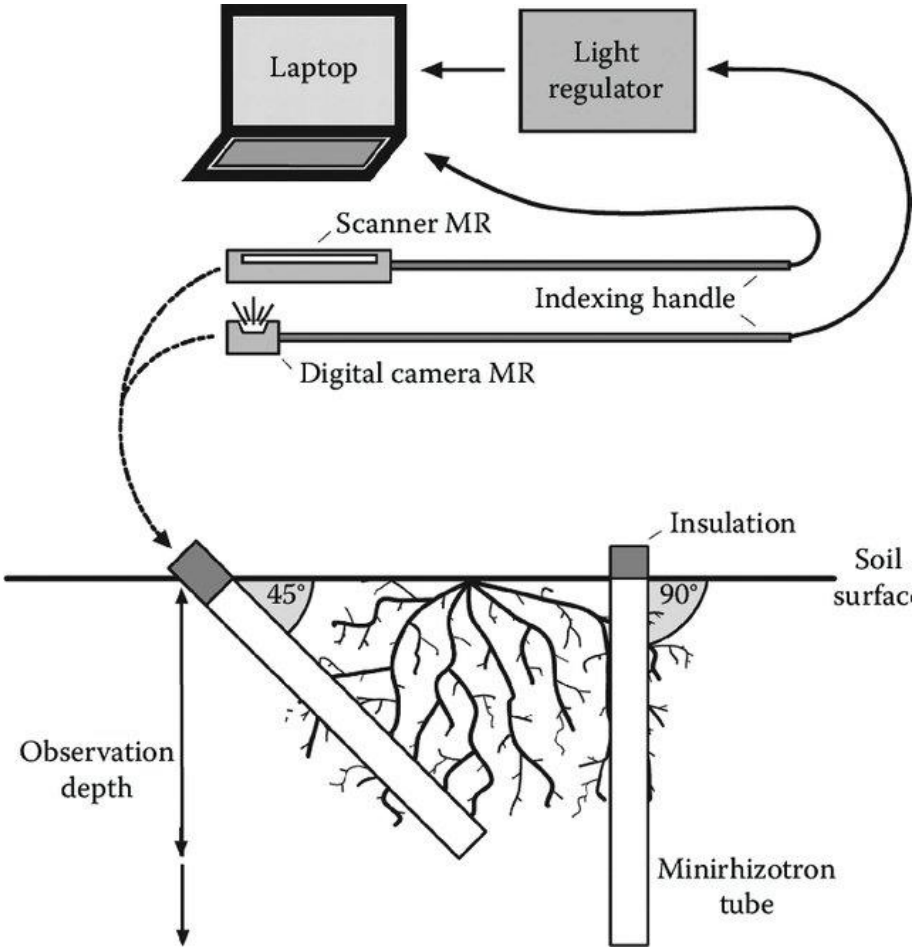

Figure 11: Minirhizotron typical setups (diagonal and vertical installation) (Eshel & Beeckman, 2013)

This method is commonly used for quantitative investigations on root length production, root length mortality, longevity, rooting density and root diameter, as well as to achieve qualitative information about root colour, branching and decomposition (Majdi, 1996).

The main limitations of this technique are linked to its installation in hard or stony soils (Majdi, 1996). Moreover, the viewing window is static, providing only a limited, 2D visualisation that is unrepresentative of the architecture of a tree root system (Mooney, et al., 2012). Another limitation arises from the fact that rhizotrons are not entirely non-invasive, as they may create an altered soil-root interface that could affect root growth (Amato, et al., 2009; Neumann, et al., 2009). Finally, the effectiveness of

minirhizotrons as opposed to other techniques, especially when used in the shallow subsurface, is still an object of discussion (Heeraman & Juma, 1993).

2.3.2.2. Pulling Test

The pulling test is principally applied to test the root system anchorage to the soil. Its primary application is the assessment of the reaction of the tree to a determined load, especially the one caused by the wind (Buza & Divos, 2016), in terms of the resulting bending of the stem and the inclination of the root plate (Fay, 2014).

During a pulling test, a load is applied to the subject tree by securing a cable to the tree trunk. The pulling force applied using a load cell or force meter is measured, and factors such as the inclination, elongation and dislocation of the ground are monitored (Buza & Divos, 2016; Marchi, et al., 2018). In order to evaluate the risk of tree uprooting, an inclinometer is applied to the trunk close to the ground. Depending on the tree species and conditions, limits are placed on the possible inclination of the tree, in order to prevent damage to tree roots. Destructive pulling tests were conducted in several studies (Coutts, 1983; Brudi & Wassenaer, 2002; Lundström, et al., 2007), which report root failure models and maximum inclination values for different tree species.

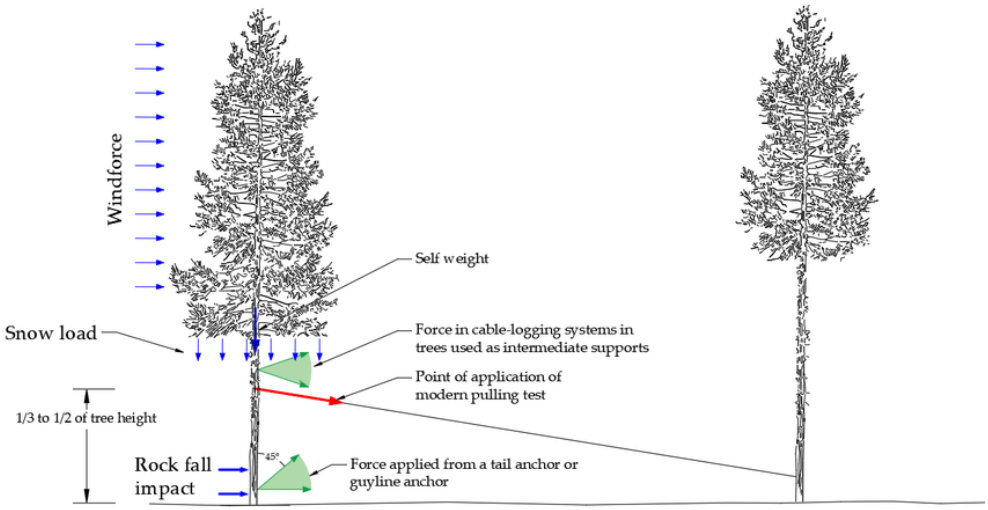

Figure 12: Schematic representation of a pulling test (Marchi, et al., 2018)

The primary output of a pulling test is a safety factor, which is given by the ratio between the tree capacity and the calculated load (Buza & Divos, 2016). According to field studies (Fay, 2014), a tree is considered stable when its safety factor is greater than 1.5.

The pulling test provides useful information on the stability of trees, evaluating their resistance to external loads. It can be performed not only to assess the tree root plate conditions, but also the status of the trunk in terms of maximum bending moment (Fay, 2014). However, the main limitation of this method is that it is not entirely non-invasive, as both the trunk and the roots can be damaged when the pulling force is applied (Marchi, et al., 2018).

Other limitations to this methodology arise from the fact that the applied load cannot represent the complex action of the wind, but can only cause a reaction in the tree which can be compared to the one produced by the wind load (Fay, 2014). Moreover, the test could be affected by factors such as the temperature conditions of both the soil and the tree (Buza & Divos, 2016). Finally, the pulling test cannot predict the

moment or the conditions under which the tree will fail (Fay, 2014), but can only assess the conditions of the tree at the time of testing.

2.3.2.3. Electrical Resistivity Tomography

Electrical resistivity tomography (ERT) is a geophysical technique used for the calculation of the subsurface distribution of soil electrical resistivity (Zenone, et al., 2008). Electrical resistivity (ρ) is defined as the electrical resistance through a uniform body of unit length and unit cross-sectional area and represents a measure of the ability of materials to limit the transfer of electrical current. This method has been extensively used for the characterisation of soil heterogeneity.

Soil resistivity is measured by applying electric currents through at least two conductors (current electrodes) and measuring the resulting differences in electric potential (voltage) on at least two separate conductors (potential electrodes). There are different possible geometric configurations for electrodes. The potential electrodes could be placed between the current electrodes (Wenner array, Figure 13) or next to them (dipole-dipole configuration). The investigation depth relies on the configuration choice and increases with the spacing between electrodes (Amato, et al., 2009).

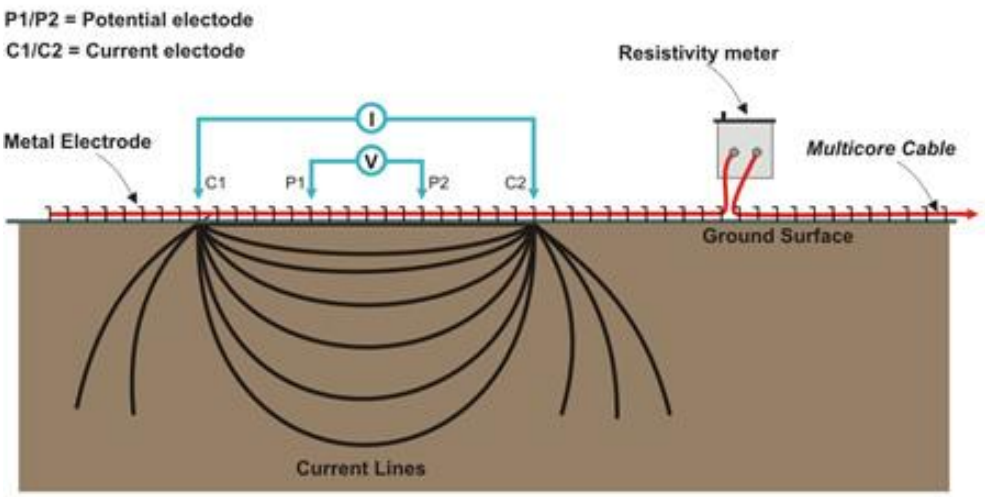

Figure 13: General ERT operating principles for a Wenner array configuration

The voltage distribution in space is a function of the different resistivity of soil volumes (Kearey, et al., 2013).

Geophysical surveys performed using electrical exploration have qualitative purposes, and are based on the contrast between the resistivity of different soil layers or the heterogeneous materials within each layer. In heterogeneous media, the current flow lines are deformed and tend to be concentrated in conductive volumes. Resistivities are first calculated according to the theoretical flow-line distribution in isotropic media and are called apparent resistivity values (Paglis, 2013). These are attributed to soil coordinates corresponding to the hypothesis of homogeneous current distribution and arranged in a pseudosection. In order to obtain real resistivity values, correctly positioned in space (true section), a procedure called inversion is applied. The investigated soil domain is divided into elementary cells, and resistivity data are imaged by assigning values corresponding to each elementary soil volume to a point which corresponds to the intersection of two lines conducted through the centres of the quadrupoles (Figure 14) (Amato, et al., 2009).

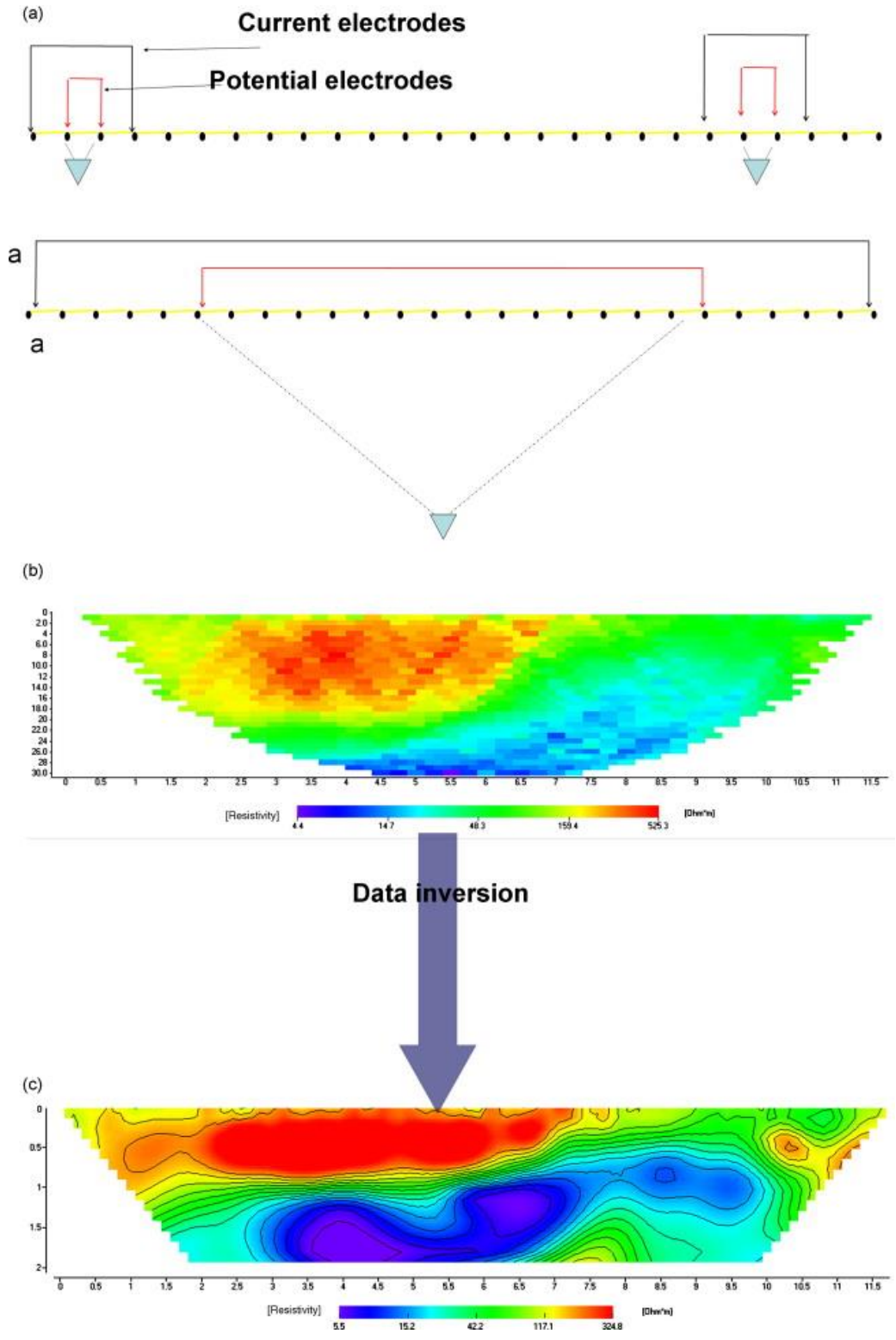

Figure 14: Data acquisition and processing in ERT; (a) a linear array of electrodes with two quadrupoles at minimum spacing (top) and one quadrupole at maximum spacing (bottom). Dots represent electrodes, and full triangles represent the centre of soil volumes measured by the corresponding quadrupole; (b) soil apparent resistivity 2D pseudosection obtained after data acquisition; (c) soil resistivity 2D section obtained after data inversion with numerical modelling (Amato, et al., 2009)

ERT has been widely applied for detecting soil compaction (Besson, et al., 2004), water content and flow in soil and plants (Loperte, et al., 2006), soil cracks (Samouelian, et al., 2005) and tillage effects (Basso, et al., 2010). The plant root zone shows variations in soil electrical resistivity (Panissod, et al., 2001), and resistive soil volumes have been correlated to large tree root structures (Amato, et al., 2008; Zenone, et al., 2008).

Amato, et al. (2008) conducted research in which the root biomass of alder trees was accurately mapped in 2D. This study demonstrated that the use of ERT for the non-destructive characterisation of root systems' spatial structure could reduce the coefficient of variability of root measurements, which is more significant than that of above-ground plant parts (Amato & Ritchie, 2002).

A quantitative relationship between the electrical resistivity of the soil and the biomass of the roots has been widely demonstrated (Loperte, et al., 2006; Amato, et al., 2008). However, in the case of low root biomass densities, the electrical response of the roots is indistinguishable from the background noise. In fact, it is assumed that it is of the same order of magnitude as the response coming from the other characteristics of the soil, and consequently too weak to be detected (Amato, et al., 2009).

The use of ERT was also investigated for imaging the trunks' internal electrical structures in living standing trees (Al Hagrey, 2006). Wu, et al. (2009) showed the potential use of ERT to map changes in tree trunks' moisture content over time. Also, Guyot, et al. (2013) used ERT to identify the boundary between sapwood and heartwood, based on its correlation with wood moisture content and electrolyte concentration.

The main advantage of this technique is that it is totally non-destructive, as it does not disturb the structure nor the functioning of the soil. Subsurface heterogeneities can be determined, in one, two or three dimensions, both non-invasively and dynamically (Samouelian, et al., 2005). Variations in time of root systems can be obtained, and different and more detailed information can be obtained by varying the operating configurations or the distance between the electrodes, depending on soil properties. Furthermore, this methodology has a low application cost, and can be applied on a large scale.

However, this investigation technique can be influenced by several factors, which could potentially act at the same time, making interpretation of the results difficult. Systematic errors can result from poor electrode contact or noise averaging, although these can be avoided by carrying out replicated and reciprocal measurements (positive and negative current and potential electrodes reversed) (Samouelian, et al., 2005). Moreover, ERT field investigations should be coupled with laboratory studies, to calibrate the resistivity against different soil conditions. (Samouelian, et al., 2005).

2.3.2.4. Acoustic Detection

The acoustic detection of wood is widely used for tree investigations, ranging from the detection of decay, cracks, hollows or holes (Buza & Goncz, 2015; Grabianowski, et al., 2006; Wang, et al., 2007) to material characterisation for wood evaluation and quality assessment (Bucur, 2006). Also, the acoustic detection of roots has been tested, based on the difference of velocity in wood and soil. In fact, the velocity of the acoustic signal in the soil is between 250 – 400 m/s, depending on soil type and moisture content, while the velocity in wood is between 2000 and 4000 m/s (Bucur, 2006; Buza & Goncz, 2015).

The device for acoustic measurements consists of a transmitter, a receiver, and a time-measuring component. The transmitter is needle-like and must be placed onto the trunk at ground level, while the receiver is a long metal spike (0.30 m or longer), which has a suitable coupling for the soil (Figure 15) (Buza & Goncz, 2015). During an investigation, the transmitter sends a very short signal, which is then reflected and read by the receiver. The presence of roots decreases the travel time significantly, making it possible to locate them.

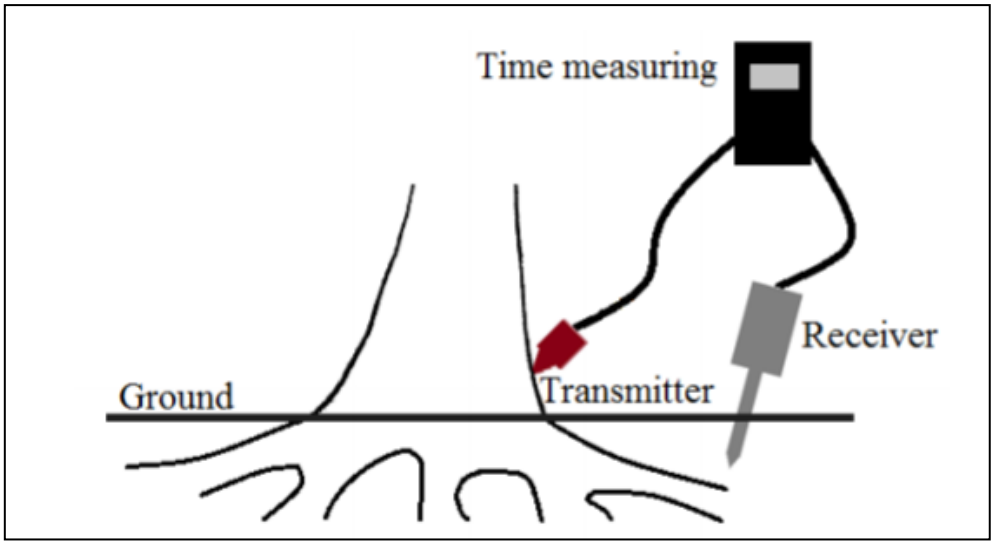

Figure 15: Device for acoustic detection of roots (Buza & Goncz, 2015)

Using this technique, it is possible to identify roots with a diameter of 0.04 m upwards, with a maximum depth of investigation of 0.50 m. Furthermore, it is possible to separate two roots from each other if they are at least 0.20 m apart (Buza & Divos, 2016). These achievements are limitations as well, as the detection of small or deep roots is not possible. Furthermore, research carried out by Iwase, et al. (2015) demonstrated that the signal is highly sensitive to water content. Finally, other buried objects, such as rocks, can disguise the signal, making it challenging to recognise root system architecture correctly (Divos, et al., 2009). Given that this methodology,

despite the promising results, is still in its infancy, it is often coupled with other NDT methods, in order to investigate further its potential (Buza & Goncz, 2015).

2.3.2.5. X-ray Computed Tomography

X-ray computed tomography (CT) is a non-destructive, non-invasive technique that can be used to visualise the interior of objects in 2D and 3D based on the principle of attenuation of an EM wave. X-ray CT has been repeatedly demonstrated to be an efficient methodology for imaging and studying soil systems. CT uses X-rays to obtain cross-sectional images of an object, which contain information regarding the attenuation of the X-rays, a function of the density of the sample material (Mahesh, 2002). These slices are then reconstructed to provide a 3D visualisation of the sample volume.

During CT acquisition, X-rays are produced in a highly evacuated tube, which contains an anode, usually platinum or tungsten, and a cathode (Wildenschild, et al., 2002). When a high voltage is applied across these electrodes, accelerated electrons produce X-rays as they strike the anode. As the X-ray beams pass through a sample, the object itself becomes a secondary source of X-rays and electrons. A portion of the primary incident beam is therefore absorbed or scattered. This reduction in the intensity of the X-ray as it passes through the investigated object is called attenuation. The beam is projected onto the detector, which measures the change in energy intensity (Mooney, et al., 2012).

X-ray CT offers great potential for examining undisturbed root systems architecture in soils, and its potential has been widely investigated within the last decades (Heeraman, et al., 1997; Gregory, et al., 2003). The imaging of plant roots in soil using X-ray CT relies on sufficient contrast in X-ray attenuation between growth medium

solids, air-filled pores, soil water, plant material and organic matter. The attenuation of these materials varies with several factors including soil type, soil moisture content, the proximity of roots to organic matter or air-filled pores and root water status (Kaestner, et al., 2006).

As per the investigation of tree trunks, X-ray CT has been employed in the evaluation of wood density (Fromm, et al., 2001), in wood moisture content monitoring (Fromm, et al., 2001; Wang, et al., 2019), and in locating internal features (Stängle, et al., 2015) and decays (Hervé, et al., 2014).

The limitations of this technique are the overestimation of root diameter during image analysis due to the proximity of water and air within the soil (Perret, et al., 2007), and the underestimation of root length and the number of lateral roots, since root material cannot be easily distinguished from other soil components. To minimise the effects of similar attenuation between the soil and plant fractions, researchers have focused on plants with coarse roots (Hargreaves, et al., 2009), artificial soil systems (Perret, et al., 2007), manipulating the water content of the sample and undertaken convoluted image processing to enhance contrast. Still, it is difficult to distinguish the boundaries between adjacent structures (Mooney, et al., 2012).

Advancements in CT technology include a reduction in scan and reconstruction times by at least an order of magnitude, automated algorithms to remove artefacts and more sophisticated detectors that have significantly increased the raw scan image quality (Mooney, et al., 2012). Research is now focused on investigating this technique's future potential in terms of the interaction between roots and their soil environment (Tracy, et al., 2010).

2.3.3. Conclusions

In conclusion, all the NDT mentioned above methods have proven viability in the health assessment of trees. However, the knowledge of the application of some of these techniques in tree assessment is still in its infancy. Moreover, their employment can be troublesome, as the required equipment is often difficult to operate. Besides, the application of these methods can often be costly. The advantages and limitations of the ND techniques mentioned above in the assessment of tree trunks and root systems are summarised in Table 3.

On the other hand, GPR is gaining attention because of its high versatility, the rapidity of its data collection and the provision of reliable results at relatively limited costs. It has also proven to be a reliable instrument for the assessment of tree root systems, as it will be explained in the following Section.

Table 3: Non-destructive testing methods for the assessment of tree trunks and root systems.

Working principle	Method	Characteristics	Applications	Advantages	Limitations
Imaging	**(Mini)Rhizotrons**	Non-destructive Slightly invasive	Quantification of fine root growth	• High-resolution imaging • Frequent inspections	• Modification of soil hydrology and physics • Only small portions of the root system can be observed • Disparity in results obtained from different image processing methods • Cost of installation • Expensive equipment • Impossible to install in specific environments (i.e. urban trees)
Mechanical	**Pulling test**	Non-destructive Invasive	Assessment of tree root plate stability Assessment of the trunk in terms of maximum bending moment	• Provides a safety factor for tree stability • Test of the elastic response of the tree trunk	• Invasive • Not completely realistic (i.e. cannot simulate wind effects) • Affected by temperature conditions • Not useful for understanding the causes of tree instability
Electrical	**ERT**	Non-destructive Non-invasive	Detection of root distribution Quantification of root biomass Imaging of the trunks' internal structures	• Easiness of data collection • Suitable for measurements repeated over time • Various scales application • Possibility of 1D, 2D and 3D surveys • Depth of detection	• Systematic errors due to poor electrode contact • Long measurement times • Laboratory calibration phase needed • Non-uniqueness of the solution in the inversion scheme • Difficult to discern the effect of roots from the background noise for low root biomass
Acoustic	**Acoustic detection**	Non-destructive Slightly invasive	Detection of decay, cracks, hollows or holes in trunks Detection of roots	• Successful detection of coarse roots	• Small roots (diameter < 0.04 m) are not detected • Superficial depth of detection (< 0.50 m) • High sensitivity to water content • Difficult to discern roots from other buried objects
Electromagnetic	**X-ray CT**	Non-destructive Non-invasive	3D mapping of roots Quantification of root length and diameter Evaluation of wood density and wood moisture content Detection of decay, cracks, hollows or holes in trunks	• High-resolution imaging • Suitable for measurements repeated over time • Detection of fine roots	• Difficulty in distinguishing the boundary between roots and other materials • High dependence on soil-related factors (i.e. soil type, soil moisture content, presence of organic matter or air-filled pores, root water status) • Overestimation of root diameter • Underestimation of root length • Complex image processing

2.4. Ground Penetrating Radar

GPR is a non-destructive testing method used to detect changes in physical properties within the shallow subsurface (Daniels, 1996). It has been successfully employed for many applications and in several disciplines, such as archaeological investigations (Goodman, 1994), bridge deck (Alani, et al., 2013) and tunnel analyses (Alani & Tosti, 2018), the detection of landmines (Potin, et al., 2006), civil and environmental engineering applications (Tosti, et al., 2018; Benedetto, et al., 2017; Benedetto, et al., 2015; Loizos & Plati, 2007), and planetary explorations (Tosti & Pajewski, 2015), for about forty years.

As previously introduced, GPR operates by transmitting EM waves towards the investigated medium, and by receiving the transmitted or back-reflected signal. The operating principles of a GPR system are based on the theory of EM fields, which is described by Maxwell's equations (Jol, 2009). Also, GPR effectiveness relies on the response of the investigated materials to the EM fields, which is ruled by the constitutive equations (Jol, 2009). Therefore, the combination of the EM theory with the physical properties of the material is essential for a quantitative description of the GPR signal.

2.4.1. GPR Operating Principles

During a GPR investigation, as it was previously stated, the transmitting antenna generates EM energy, which is launched into the investigated medium where it propagates in the form of EM waves (Daniels, 1996). When these waves hit a target with different electrical or magnetic properties, reflections are generated, which are then diffracted back towards the surface and recorded by the receiving antenna. The

remaining energy, conversely, continues to travel into the medium until it is completely attenuated (Daniels, 1996).

A standard GPR system consists of three essential components: a control unit (including a pulse generator, computer, and associated software), antennas (including paired transmitting and receiving antennas), and a display unit (Guo, et al., 2013) (Figure 16).

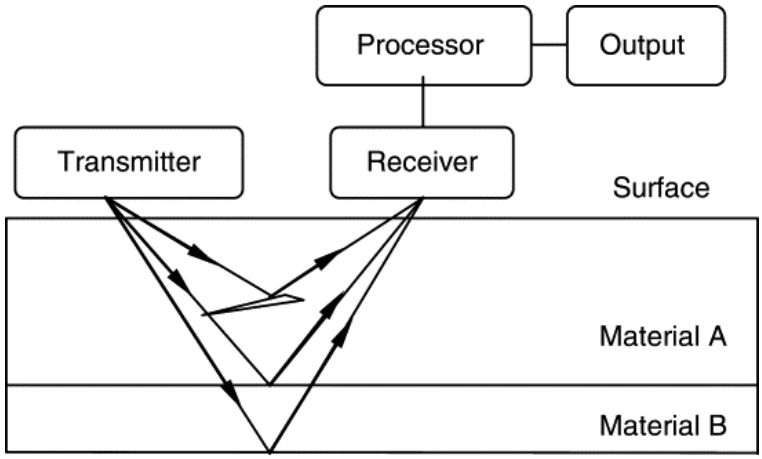

Figure 16: GPR operating principles

Once the control unit has sampled and filtered the collected information, this can be displayed in different ways, as it is explained below.

2.4.1.1. Signal Imaging Modes

GPR data can be considered to be of the form (Daniels, 2004):

$$f(x, y, z) = A(x_i, y_j, z_k) \tag{2.1}$$

Where i, j and k range from 1 to N, M and P, respectively.

A single reflection trace, or waveform, is named A-scan and it is defined as follows:

$$f(z) = A(x_i, y_j, z_k) \tag{2.2}$$

An A-scan records the time between the emission of the reflected signal and its reflection on the vertical axis and the amplitudes of the received signals on the horizontal axis (Daniels, 2004). The depth of a target can then be derived from the propagation velocity v (Equation (2.27)), as follows (Daniels, 1996):

$$d = \frac{v \times t}{2} \tag{2.3}$$

where

- d is the depth
- t is the two-way travel time

Being an individual trace, the A-scan provides punctual information about the subsurface configuration (Benedetto, et al., 2017). It is important to note that the z axis can represent both time and depth, which are correlated through the propagation speed, as explained above.

During a survey, GPR is moved along a detection transect, and EM pulses are generated at a specified interval of time or distance. Several reflected signals are therefore recorded and integrated. A set of consecutive A-scans along a particular direction is called B-scan or radargram, and it is represented as follows:

$$f(x, z) = A(x_i, y_j, z_k) \tag{2.4}$$

where i ranges from 1 to N, z ranges from 1 to P and j is constant, or

$$f(y, z) = A(x_i, y_j, z_k) \tag{2.5}$$

where j ranges from 1 to M, z ranges from 1 to P and i is constant.

B-scans allow for a 2D representation of the subsurface (Figure 17). The B-scan mode is a widely used imaging methodology, as it permits to visualise the presence of buried objects (Bianchini Ciampoli, et al., 2019).

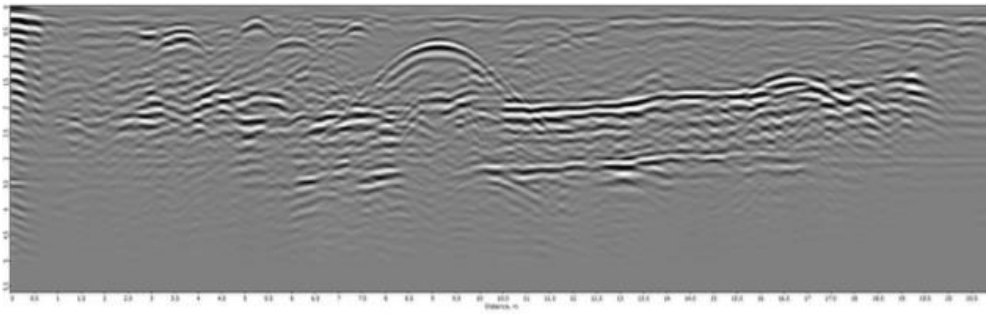

Figure 17: A typical radargram or B-scan

The GPR transmitting antenna produces energy in the form of a beam that penetrates the ground in the form of an elliptical cone. As the propagation depth increases, the cone radius also expands, resulting in a larger footprint scanned beneath the antenna (Figure 18a). The footprint area can be approximated by the formula (Conyers, 2002):

$$A = \frac{\lambda}{4} + \frac{d}{\sqrt{\varepsilon_r + 1}} \tag{2.6}$$

where

- A is the long dimension radius of footprint
- λ is the centre frequency wavelength of radar energy
- d is the depth from the ground surface to the reflection surface
- ε_r is the average relative dielectric permittivity of scanned material from the ground surface to the depth of reflector (D)

Based on this feature of propagating waves, radar energy will therefore be reflected before and after the antenna is positioned above a buried object. As the antenna

moves closer to the object, the recorded two-way travel time decreases, while when the antenna moves away from it, the same phenomenon is repeated conversely, generating a reflection hyperbola, the apex of which indicates the exact location of the buried object (Guo, et al., 2013) (Figure 18b)

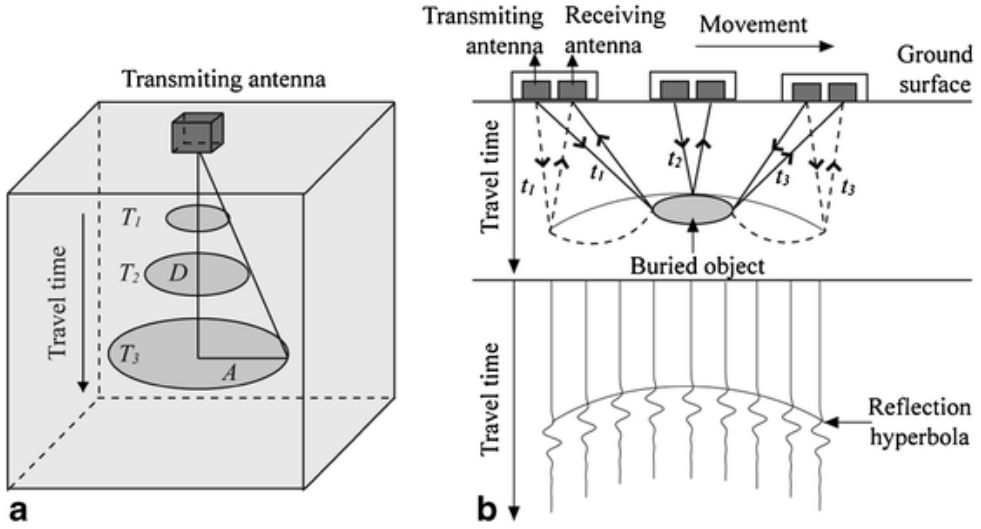

Figure 18: Schematic illustration of the conical radiating pattern of GPR waves and generation of a reflection hyperbola (Guo, et al., 2013): a) development of a footprint with increasing travelling time; b) detection of a buried object with the creation of a reflection hyperbola

The GPR resolution, and therefore its capability to discriminate between two closely spaced targets as well as the minimum size detectable, correlates negatively with the footprint area. GPR detection resolution depends on the antenna frequency, the EM properties of the medium, and the penetrating depth (Hruska, et al., 1999). Therefore in a survey, the selection of the appropriate GPR features, including frequency operations, the type of antenna or its polarization relies on several factors, such as the size and shape of the target and the transmission properties of the investigated medium, as well as the characteristics of the surface (Daniels, 2004).

Advances in GPR data processing and visualisation software have allowed for the creation of 3D pseudo-images of the subsurface, obtained by interpolating multiple 2D radargrams. This is achieved collecting a set of B-scans and fixing a constant value

along the z axis. The resulting visualization of the x, y domain is named C-scan, and it is defined as follows:

$$f(x, y, z) = A(x_i, y_j, z_k) \tag{2.7}$$

Where i and j range from 1 to N and M, respectively, for a selected value of z ($k = cost$). A C-scan provides an amplitude map at a specific time (or depth) of collection (Benedetto, et al., 2017), and is therefore helpful in visualising a trend of the amplitude values all over the investigated domain.

2.4.2. Maxwell's Equations and Dielectric Properties of Materials

This paragraph introduces an overview of the laws ruling the propagation of EM waves, emphasising on the physical interpretation of the dielectric properties of materials.

2.4.2.1. Maxwell's Equations

The foundation of electromagnetism is described by the Lorentz force law and a set of partial differential equations named Maxwell's equations. The combination of the latter with the charge conservation, the force law, the law of motion and the gravitation law describes the fundamentals of classical physics (Feynman, et al., 1963). Maxwell's equations can be formulated both in integral and differential equations, and are determined by the Faraday's law, the Ampere's law, the Gauss's law and the Gauss's law for magnetism (Jol, 2009).

2.4.2.1.1. The Faraday's Law

Faraday's law quantitatively describes the relationship between a changing magnetic field and the associated electric field created by the change (Feynman, et al., 1963):

$$\oint_{\Gamma} E \cdot ds = -\int_{S} \frac{\partial B}{\partial t} \cdot nda \tag{2.8}$$

Where

- Γ is any closed curve
- S is any surface bounded by Γ
- E is the magnetic field $[V/m]$
- ds is an infinitesimal vector element of the curve Γ
- B is the magnetic flux density $[T]$
- n is the unit vector perpendicular to da

Using the Stoke's theorem (Kreyszig, 2006), the differential form of Equation (2.8) can be deduced, as Maxwell first wrote it as one of his equations (Feynman, et al., 1963):

$$\nabla \times E = -\frac{\partial B}{\partial t} \tag{2.9}$$

2.4.2.1.2. The Ampere's Law

Ampere's law states that the line integral of the magnetic field around a closed curve segment is equal to the electric current passing through the surface which is surrounded by the closed-loop (Balanis, 1989):

$$\oint_{\Gamma} H \cdot ds = I_{enc} \tag{2.10}$$

Where

- H is the magnetic field $[A/m]$
- I_{enc} is the electric current intensity passing through Γ $[A]$

Replacing the current intensity with the surface integral of the current density in a closed curve:

$$\oint_{\Gamma} H \cdot ds = \int_{S} J \cdot n \, da \tag{2.11}$$

Where

- J is the electric current density $[A/m^2]$

The differential form of Equation (2.11) can be derived using Stoke's theorem (Kreyszig, 2006):

$$\nabla \times H = J \tag{2.12}$$

Equation (2.12) was modified by Maxwell by adding the contribution of the displacement current density $J_d = \frac{\partial D}{\partial t}$, where $\vec{D}$ is the electric flux density $[C/m^2]$.

Therefore,

$$\nabla \times H = J + J_d \tag{2.13}$$

And consequently

$$\nabla \times H = J + \frac{\partial D}{\partial t} \tag{2.14}$$

2.4.2.1.3. The Gauss's Law

Gauss's law, also known as Gauss's flux theorem, relates the distribution of electric charge to the resulting electric field. Gauss law states that the surface integral of the electric flux on a closed surface is equal to the total charge surrounded by that surface:

$$\int_S D \cdot da = \int_V q \cdot dv \tag{2.15}$$

Where

- V is the volume enclosed by S
- q is the electric charge density $[C/m^3]$

The differential form of Equation (2.15) is obtained by applying the Gauss vector theorem (Kreyszig, 2006):

$$\nabla \cdot D = q \tag{2.16}$$

2.4.2.1.4. The Gauss's Law for Magnetism

The Gauss law for magnetics results from the statement that magnetic monopoles do not exist (Jackson, 1999). This is expressed mathematically as:

$$\int_S B \cdot n \, da = 0 \tag{2.17}$$

Applying the Gauss vector theorem results in the differential form of Equation (2.17):

$$\nabla \cdot B = 0 \tag{2.18}$$

2.4.2.2. ***Properties of Materials***

The matter is characterised by specific physical properties, different for each material, which constitute the response of that material to external stimuli, such as the application of a force. In electromagnetism, the behaviour of materials influenced by electric and magnetic fields is described by their dielectric properties, namely the electric conductivity, the dielectric permittivity and the magnetic permeability. The relation between dielectric properties and the applied EM field is described by the constitutive equations, which provide a macroscopic description of how electrons atoms and molecules respond to the application of an EM field (Jol, 2009):

$$\boldsymbol{J} = \sigma \boldsymbol{E} \tag{2.19}$$

$$\boldsymbol{D} = \varepsilon\, \boldsymbol{E} \tag{2.20}$$

$$\boldsymbol{B} = \mu \boldsymbol{H} \tag{2.21}$$

Where

- σ is the electrical conductivity $[S/m]$
- ε is the dielectric permittivity $[F/m]$
- μ is the magnetic permeability $[H/m]$.

Electrical conductivity σ is a measure of the ability of a material to conduct an electric current under the influence of an external electrical field. When an external electric field is applied to a material, the charges start moving apart. Before the external field is balanced and an equilibrium is reached, energy is dissipated proportionally to the amount of charge and the distance (Olhoeft, 1998; Jol, 2009). Electrical conductivity is, therefore, a dissipation process from charge movement (Olhoeft, 1998).

Dielectric permittivity ε characterises displacement of charge constrained in a material structure in response to the application of an electric field (Jol, 2009). When a material is subjected to an external electric field, the charges separate until an internal electric field is created that balances the external field. This process of molecular orientation is called polarization (Powers, 1997), and it results in net energy storage (Jol, 2009). Permittivity is, therefore, the ability of a material to support polarization (Olhoeft, 1998).

Magnetic permeability μ is characterised similarly to the dielectric permittivity. In fact, it measures the ability of a material to support the formation of a resulting magnetic field when influenced by an external magnetic field. This involves a correlated spin response of the electrons (Olhoeft, 1998), distorting intrinsic magnetic moments and storing energy in the material (Jol, 2009).

Dielectric permittivity and magnetic permeability can also be expressed in relation to their absolute values, the permittivity of free space or electric constant ε_0 and the magnetic permeability of free space or magnetic constant μ_0 (Olhoeft, 1998):

$$\varepsilon_r = \frac{\varepsilon}{\varepsilon_0} \tag{2.22}$$

$$\mu_r = \frac{\mu}{\mu_0} \tag{2.23}$$

Where

- ε_r is the relative dielectric permittivity (commonly known as dielectric constant)
- μ_r is the relative magnetic permeability

2.4.3. Types of GPR Systems

The two most common categories of GPR are the pulsed and the continuous-wave (CW) GPR systems. These radar systems differ from one another in the data acquisition method, as the pulsed GPR operates in the time domain while the CW GPR operates in the frequency domain (Jol, 2009). In this paragraph, a basic description of pulsed radars and stepped-frequency CW radars is given. Descriptions of advanced techniques and variations of GPR, such as ultra-wideband (UWB) or synthetic-aperture radar (SAR), can be found in the literature (Ali, et al., 2017; Chan & Koo, 2008).

2.4.3.1. Pulsed GPR Systems

Pulsed GPR systems are the most common in the commercial market, due to the relative easiness of data interpretation, the low-cost parts and their applicability in a broad range of disciplines (Jol, 2009).

GPR systems incorporating the impulse technique send a short pulse to an antenna, which produces an EM wave, whose central frequency and associated bandwidth are dependent on the characteristics of the antenna (Jol, 2009). The pulse is transmitted to the investigated medium through the antenna, and the reflected energy from the subsurface objects is then recorded. The two-way travel time to the targets can therefore be measured in the time domain between the reflected pulses.

Pulsed GPR systems are commercialised since the 1970s (Morey, 1974), and they have been successfully employed in several different applications (Annan & Davis, 1976; Brunzell, 1999; Colla, et al., 1997; Yarovoy, et al., 2002).

Within the drawbacks of this GPR system, undesirable ringing, inefficient use of transmit power and the resolution limited by pulse width can be acknowledged (Jol, 2009).

2.4.3.2. Stepped-Frequency Continuous-Wave GPR Systems

Stepped frequency continuous-wave (SFCW) radar systems operate in the frequency domain and, as the name implies, transmit EM waves continuously.

The system produces linear increments of a frequency sweep over a chosen bandwidth, performed between two specific initial and final frequencies. The amplitude and phase of energy scattered from subsurface objects are indicated by the reflected energy, which is received as a function of frequency. The received-to-emitted signal is sampled during the sweep and recorded at each discrete frequency step. The digitised waveform is then transformed into the time domain to create the synthesised pulse.

SFCW radar systems are known since the 1970s (Robinson, et al., 1974), and technological advancements have been carried out in the following years (Iizuka, et al., 1984). SFCW applications include landmines detection (van Genderen & Nicolaescu, 2003; Fang & Sato, 2005; Soldovieri, et al., 2010), through-wall imaging (Gaikwad, et al., 2011; Fioranelli, et al., 2014), motion detection (Hunt, 2009), characterisation of the dielectric properties of the subsurface (Lambot, et al., 2003), and pavement engineering applications (Ihamouten, et al., 2018).

SFCW radar systems have several advantages, such as the controlled transmission frequencies, an efficient use of power and sampling of ultra-wideband signals (Jol, 2009). Also, SFCW radars have some advantages over the time domain GPRs: larger frequency bandwidth (Daniels, 1996), higher mean power, lower noise figure, and the

possibility of shaping the power spectral density (Nicolaescu & van Genderen, 2012). However, the main drawbacks of this GPR system are the high costs and the complexity of use.

2.4.4. Types of GPR Antennas

The functioning of a GPR system is based on the use of transmitting and receiving antennas, to produce and receive EM waves. Depending on the number of antennas used, a GPR system can be mono-static (i.e., the same antenna is used as a transmitter and a receiver), bi-static (i.e., one transmitting antenna and one receiving antenna), or multi-static (different combinations of transmitters and receivers).

Depending on the deployment of antennas, GPR systems are classified as ground-coupled or air-coupled systems.

2.4.4.1. Ground-Coupled GPR Systems

In ground-coupled GPR systems, the antenna operates in contact with (or very close to) the ground. Pulsed GPRs usually operate as ground-coupled systems, and these are usually arranged so that the polarisation of the transmitted and received signals are parallel (Daniels, 1996). Ground-coupled systems can operate with a wide range of central frequencies, varying from 80 MHz to 1500 MHz, the choice of which depends on the objective of the survey.

Comparing to the air-coupled system, this configuration allows for a higher signal depth of penetration, when the same frequency is considered. Another strength of this configuration is the greater vertical resolution, which allows the identification of very small targets, such as reinforcement bars (Alani, et al., 2013) or thin cracks (Benedetto, 2013).

On the other hand, this system also has some limitations, which arise precisely from the configuration and contact with the ground. In fact, the information obtained during data acquisition may not be representative if not correctly processed. Moreover, this type of GPR is strongly conditioned by the speed of data acquisition, which ranges from 5 km/h to 30 km/h. This affects the productivity of the system and makes it unsuitable for applications where long-distance investigations are required.

2.4.4.2. Air-Coupled GPR Systems

Air-coupled (or air-launched) GPR systems operate being elevated above the surface of the ground, usually at a height of between 0.30 m and 0.50 m. This configuration allows radar surveys to be performed at higher speeds than the ground-coupled system. The possibility of being mounted on a moving vehicle makes an air-launched radar particularly suitable for carrying out road investigations at traffic speed (Loizos & Plati, 2007), significantly increasing the productivity and avoiding the closure of the infrastructure.

These systems produce a relatively clean radar signal, and the penetration depth usually ranges from 0.50 m up to 0.90 m (Lahouar, et al., 2002). Traditionally, air-coupled antenna systems are pulsed radar systems generally operating in the range 500 – 2500 MHz, with the most common central frequency being 1000 MHz.

Another advantage of air-coupled GPR systems, together with the aforementioned full speed analysis and the consequent high productivity, is the independence between antenna coupling and changes in the investigated medium properties. On the other hand, the main limitation of this configuration is the impedance mismatch, since part of the EM energy, sent by the antenna, is reflected back by the pavement surface.

2.4.5. GPR Signal Processing

Regarding GPR data processing and analysis, appropriate signal processing techniques are needed to provide easily interpretable images to operators and decision-makers (Daniels, 2004). Most of the techniques that are applied today originate from seismic theory (Benedetto, et al., 2017), as both disciplines involve the collection of pulsed signals in the time domain. It is not possible to establish a unique methodology, as it depends on the purpose of the survey, the features of the used radar and the conditions of the investigated medium. Furthermore, the analysis of GPR data is a challenging issue, as the interpretation of GPR data is generally non-intuitive and considerable expertise is therefore needed.

In the following paragraphs, a brief outline is given of a representative set of processing methods applied to GPR, which are going to be extensively used in the following chapters. Figure 19 shows a typical GPR signal processing framework which includes the aforementioned techniques.

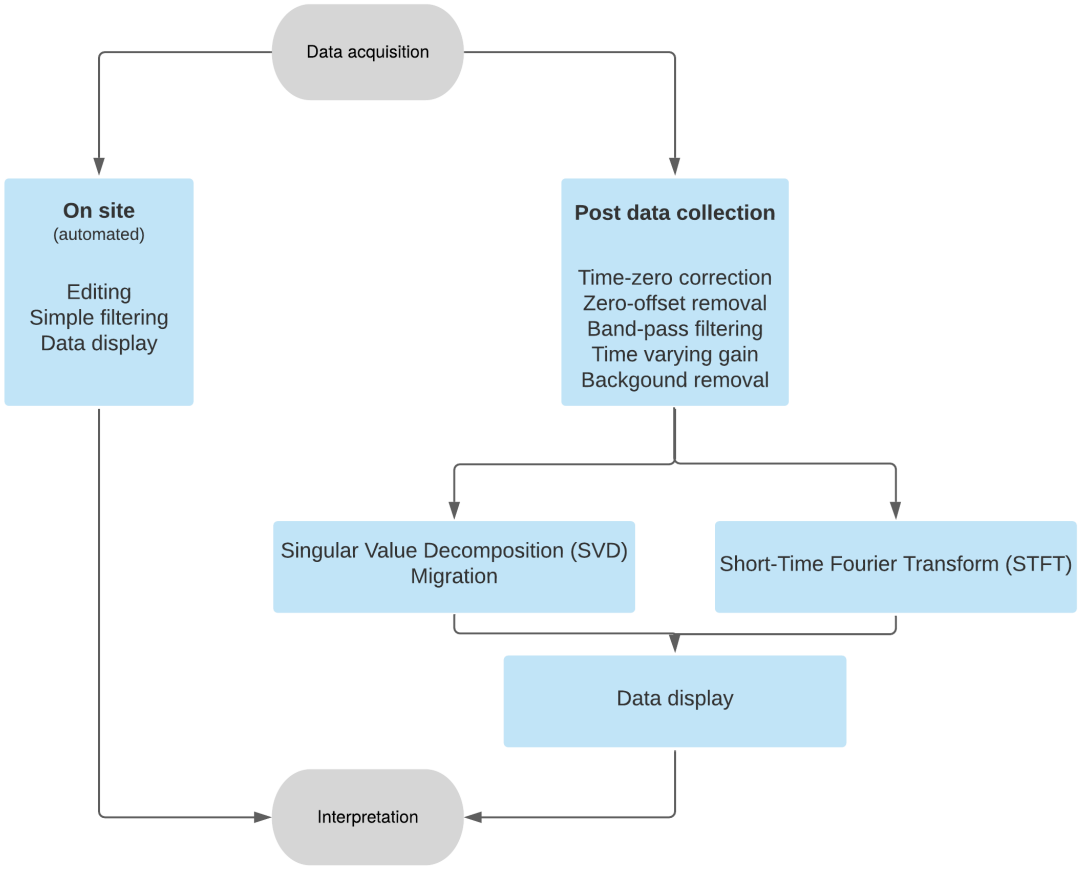

Figure 19: Typical GPR processing framework

2.4.5.1. Time-zero correction

In order to compare the reflection time and, consequently, the depth of the buried targets, it is necessary to set a unique time-zero point for the GPR data. However, due to factors such as the air gap between the transmitting antenna and the soil surface or the ground level inhomogeneities, the position of the air-ground surface reflection could vary across the different A-scans. To this extent, the air layer between the signal source point and the ground has to be eliminated across the whole sequence of A-scans. Depending on both the type of antenna and the central frequency of the investigation, the correct location of this threshold along the A-scan is expressed in the accuracy of the findings (Benedetto, et al., 2017).

2.4.5.2. Zero-offset removal

A unique aspect of GPR data arises from the proximity of the receiver to the transmitting antenna. The fields near the transmitter contain low-frequency energy associated with electrostatic and inductive fields, which rapidly decay with distance. This energy often adds a component that slowly changes over time to the data measured in the field, and causes a rise or fall of the received signal, distorting the average towards amplitude values other than zero. This effect is known as wow, and can inhibit further processing. The problem can be effectively solved by applying a simple algorithm for subtracting the average, such as the following:

$$y'(n) = y(n) - \frac{1}{N}\sum_{k=1}^{N} y(k) \tag{2.24}$$

Where

- $y'(n)$ is the amplitude of the n^{th}signal of the processed trace
- $y(n)$ is the amplitude of the n^{th}signal of the raw trace

and with n and k ranging from 1 to N. The result of the application of this technique is an A-scan with mean equal to zero, that is with a symmetric probability distribution of amplitude along the scan.

2.4.5.3. Band-pass filtering

The application of a filter in the frequency domain represents a crucial step for a correct visualisation and interpretation of GPR data. This technique aims at increasing the signal-to-noise ratio, filtering the data by eliminating the signal components that are outside the main frequency range of the GPR system.

A band-pass filter can be considered as the combination of two frequency filters, namely, the high-pass and the low-pass filters (Benedetto, et al., 2017). The high-pass

filter operates removing the low-frequency components from the frequency spectrum of each A-scan. This allows filtering the clutter caused by antenna-ground interactions. On the other hand, the low-pass filter works by cutting off the high-frequency components from the spectrum.

Operatively, a band-pass filter operates as follows:

$$Y'(\omega) = Y(\omega) \cdot H(\omega) \tag{2.25}$$

Where

- $Y'(\omega)$ is the spectral representation of the processed signal trace in the frequency domain
- $Y(\omega)$ is the spectral representation of the raw signal trace in the frequency domain
- $H(\omega)$ is the band-pass filter.

Among the existing types of band-pass filters, one of the most common is the Butterworth filter, which is expressed as:

$$H(\omega) = \frac{B^n\left(\frac{\omega}{\omega_c}\right)}{B^m\left(\frac{\omega}{\omega_c}\right)} \tag{2.26}$$

Where

- $B^n(\omega)$ is a k-order Butterworth polynomial
- ω_c is the cutting-off frequency

The limits for the width of the passband are not defined by a rule, as the risk is to exclude frequency regions which could contain relevant information. Therefore, the limits are usually set after an observation of the signal spectrum. A common and valid

practice is to set a pass bandwidth of 1.5 times the central frequency of the GPR system (Jol, 2009).

2.4.5.4. Time-varying gain

Radar signal attenuates rapidly when it propagates through the investigated media. This is due to the dispersive nature of EM waves, which relates to the electrical properties of the medium, as explained before. For this reason, the response from targets which are located deep can be hardly detected, especially when dealing with lossy materials (Benedetto, et al., 2017).

The application of a time-varying gain to each A-scan compensates for the rapid fall of GPR signal, equalising amplitudes and making the response from deeper targets more visible (Jol, 2009). It is worth noting, though, that this alters the radar signal, resulting in artefacts and misinterpretations if applied to noisy data. Therefore, the application of the time-varying gain processing technique is effective if performed after an appropriate decluttering.

A time-varying gain function can be presented as follows:

$$y'(n) = y(n) \cdot k \cdot n \tag{2.27}$$

Where

- $y'(n)$ is the amplitude of the n^{th}signal of the processed trace;
- $y(n)$ is the amplitude of the n^{th}signal of the raw trace;
- k is the weighting function of the sample n.

Several possible gain functions are commonly applied to GPR data, depending on the purpose of the investigation. Among the most popular, there is the spherical and

exponential (SEC) function, which compensates the loss of energy applying a linearly increasing time gain combined with an exponential increase. Also, the automatic gain control (AGC) function equalises the amplitudes all the way down each trace (Bristow & Jol, 2003). In this case, the compensation is a function of the difference between the average amplitude within a chosen time window and the maximum amplitude of the whole trace (Benedetto, et al., 2017).

2.4.5.5. Background removal

An effective way to reduce clutter in GPR data is to apply signal processing techniques on the total of acquired A-scans. In particular, the background removal technique removes clutter by subtracting from each A-scan the average value of the amplitude related to a singular sample, assessed over the whole set of A-scans (Benedetto, et al., 2017). The technique operates as follows:

$$y'(n) = y(n) - \frac{1}{K}\sum_{k=1}^{K} y_k(n) \tag{2.28}$$

Where

- $y'(n)$ is the processed trace
- $y(n)$ is the raw trace
- n is the number of the sample
- k is the number of the trace within the selected set of A-scans

Background removal is effective at enhancing reflections from the subsurface, especially if the number of targets is limited and these are distant from each other (Daniels, 2004). However, as it is defined, this technique has the disadvantage of eliminating most of the reflections deriving from planar interfaces. To this extent, this

technique may be ineffective, if not even counterproductive, when the objective of the radar investigation is the characterization of the subsoil layers.

2.4.5.6. Singular Value Decomposition

The aim of the Singular Value Decomposition (SVD) technique is to reduce the ringing noise and to subtract the ground reflection from the raw data. If GPR data are severely contaminated by ringing noise, this can be considered as a consistent component of the raw radar data, and therefore highly correlated to it. On the other hand, reflections due to potential targets are more random and scattered, and therefore less correlated (Kim, et al., 2007). The SVD filter operates decomposing an image into different sub-images, each of which contains features with gradually increasing correlation. With this approach, ringing noise can be separated from the real response of the targets.

Operationally, a B-scan can be expressed as a 2D matrix:

$$D = USV^T \tag{2.29}$$

Where

- $U = [u_1, u_2, \dots, u_n]$ and $V = [v_1, v_2, \dots, v_n]$ are orthogonal matrices of $m \times m$ and $n \times n$, respectively
- S is an $m \times n$ diagonal matrix

D is called eigenimage, U and V are called eigenvectors, while the diagonal elements of the matrix S, namely $s_i = \lambda_i$ (with $\lambda_i > \lambda_{i+1}$), are called eigenvalues.

Equation (2.29) can be rewritten as:

$$D = \sum_{i=1}^{n} s_i u_i v_i \tag{2.30}$$

Equation (2.30) implies that a B-scan can be divided into n different images, and can be considered as the linear combination of these (Kim, et al., 2007).

Considering that the eigenvalues are ordered in decreasing magnitude, therefore the first eigenimage will contain the most common feature of the original image, the ringing noise, as explained above. On the other hand, for values of i very close to n, the features contained in the eigenimage will be extremely uncorrelated to the original image. The removal of these contributions can be expressed as:

$$D_{filt} = \sum_{i=j}^{k} s_i u_i v_i \tag{2.31}$$

Where $1 < j \leq k < n$.

2.4.5.7. Migration

Migration is commonly used to enhance section resolution and to create more spatially realistic subsurface images and is perhaps the most controversial of GPR processing techniques. Migration techniques were initially designed for the seismic industry, where they are considered vital for even basic interpretations. Unfortunately, these appear to be less efficient with GPR, and while these can be used in relatively uniform settings, they are not as good with complex heterogeneous sites. That said, traditional techniques have been successfully applied to a variety of different applications (Cassidy, 2009). Examples include reverse-time (RT) migration (Fisher, et al., 1992), frequency-wavenumber (F-K) (Pipan, et al., 1996) migration and Kirchhoff migration (Moran, et al., 1998).

More specifically, unique GPR-based methods have been developed to address some of the limits of seismic routines. These new methodologies have yet to be implemented

into standard GPR processing packages, although most of them include some reasonably advanced migration algorithm. The most popular are diffraction stack migration, F-K migration (or Stolt migration), Kirchhoff migration and finite-difference wave equation, which can be implemented on 2D parts or through 3D data volumes (Cassidy, 2009).

Although each of these methods operates differently, they all aim at recreating the GPR section in a spatially correct form using a subsurface velocity model. Diffraction hyperbolas are therefore collapsed to a point source and the reflections repositioned to their correct location (Cassidy, 2009). Essentially, the problem of data focusing can be considered from the point of view of a source of radiation (i.e. a point reflector and the measured wavefront). If the velocity in the material is known and constant, a relatively straightforward geometric approach can be employed in a 2D case (Daniels, 2004). If the measured time to the point reflector is t, then the distance to the point reflector is given by $z = vt/2$. At any position along the x axis the distance z is also given by (Daniels, 2004)

$$z_i = \sqrt{(x_i - x_0)^2 + z_0^2} \tag{2.32}$$

Equation 2.32 shows that the measured wavefront appears as a hyperbolic image or a curve of maximum convexity. The geometric migration technique simply moves or migrates a segment of an A-scan time sample to the apex of a curve of maximum convexity. The hyperbolic curve needs to be well separated from other features, and a good signal to noise ratio is needed (Daniels, 2004).

2.4.5.8. Short-Time Fourier Transform

Short-Time Fourier Transform (STFT) is a series of Fourier transforms of a windowed signal. STFT produces time-located frequency information for cases where the frequency components of the signal change over time, while the regular Fourier transform provides the frequency information distributed over the entire time interval of the signal (Kehtarnavaz, 2008). The STFT equation is as follows (Al-Qadi, et al., 2008):

$$STFT(t,\omega) = \int_t [x(t) \cdot w(\tau - t)] \cdot e^{-j\omega t} dt \quad (2.33)$$

where

- STFT is the frequency energy at time *t* and frequency *ω*
- *x* is the reflected amplitude
- *w* is the window function

2.4.6. GPR applications in the assessment of tree trunks

The use of GPR for the evaluation of tree trunks is still in its infancy. Ježová, et al. (2016) report that the assessment of living tree trunks using GPR is difficult because of their shape, inner structure, anisotropy, water content, density, temperature and frequency of the applied field.

Rodríguez-Abad, et al. (2011) analysed anisotropy of wood using GPR, describing the strong dependence of its dielectric properties on the grain orientation (i.e. the longitudinal arrangement of wood fibres). Perez-Gracia, et al. (2014) used GPR to study the internal structure of wooden beams. Butnor, et al. (2009), Lorenzo, et al. (2010), and Fu, et al. (2014) have attempted to investigate the internal structure of living trees, using different antenna systems and configurations. Nevertheless, all the authors reported strong reflections caused by the EM contrast between external and internal zones of the trunk (Ježová, et al., 2016). The main drawback to this technique is, therefore, the poor contact between the antenna and the bark, as air gaps between the antenna and the bark lead to degradation of the radar image (Ježová, et al., 2016). To this extent, it is evident that novel survey techniques, together with the development of dedicated antenna systems, will help towards the success of GPR for tree trunk investigation. Moreover, dedicated signal processing techniques, assisted by numerical simulations and modelling techniques, will improve the results of the investigations.

2.4.7. GPR applications in the assessment of tree root systems

Although GPR has commonly been used to characterise soil profiles (Lambot, et al., 2002; Huisman, et al., 2003), roots have often been considered an unwanted source of noise that usually complicates radar interpretation (Zenone, et al., 2008). However, over the past decade, GPR has been increasingly used for tree root assessment and

mapping, as it is completely non-invasive and does not disturb the soils or bring harm to the examined trees or the surrounding environment. For these reasons, repeated measurements of root systems are possible, allowing for the study of the roots' developmental processes.

The first application of GPR that relates to the mapping of tree root systems dates back to 1999 (Hruska, et al., 1999). In this study, a GPR system with a central frequency of 450 MHz was employed to map the coarse roots of 50-year-old oak trees, and measurements were made in two directions within a 6 m by 6 m square, with a 0.25 m x 0.25 m profile grid, at 0.05 m intervals. After data processing, the root system of the large oak tree was analysed in detail by applying depth correlations of GPR indications from single profiles to develop a 3D picture. Additionally, the root system was excavated and photographed, and root lengths and diameters were measured to verify the radar data. The researchers confirmed that the resolution of the GPR system was sufficient to distinguish the roots that were 0.03 m to 0.04 m in diameter. Diameters of roots detected by the GPR system corresponded to measured diameters of excavated roots with an error of between 0.01 and 0.02 m. The GPR system determined the length of individual roots, from the stem to the smallest detectable width, with an error margin of about 0.02 m to 0.03 m. The researchers also claimed that higher frequencies, together with smaller measurement intervals, were applied, and this method improved the resolution and accuracy to less than 0.01 m (although these results have not been published and are considered controversial). In conclusion, the researchers claimed to have successfully tested GPR in a forest and woodland environment, where the soil is relatively homogenous. The output of this study was criticised several years later (Guo, et al., 2013), because the 3D views of the coarse root system were redrawn manually based on the GPR radargram, but no

specific information was provided regarding how it had been done (Figure 20). Assuming that the maps were redrawn arbitrarily according to the operator's personal experience, bias may therefore have been introduced.

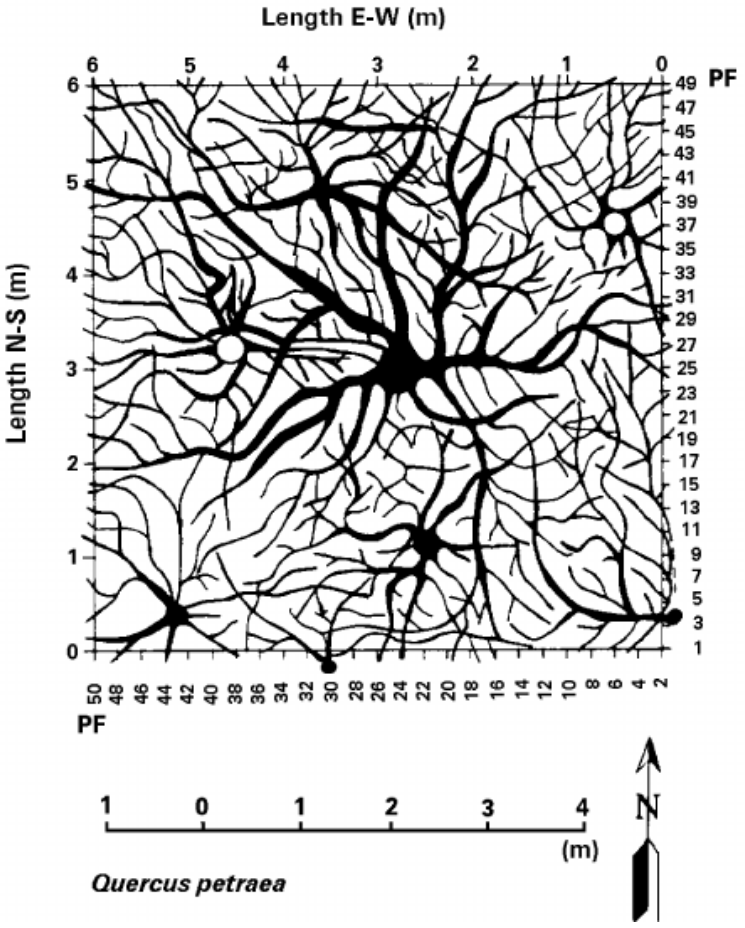

Figure 20: Hand-drawn reconstructed ground plain view of a tree root system based on the analysis of GPR data (Hruska, et al., 1999)

Attempts to map tree root systems have continued throughout the years (Sustek, et al., 1999) (Cermak, et al., 2000) (Wielopolski, et al., 2000), with variable and controversial results. The most significant barrier to mapping complete root systems with GPR is the inability to distinguish individual roots when tight clusters of roots are encountered, as they give one only large parabolic reflection (Butnor, et al., 2001). Furthermore, many pieces of research were carried out under controlled conditions (Barton & Montagu, 2004), therefore limiting the significance of the results for in situ

tree root mapping. Moreover, the minimum detectable size for tree roots is still a subject of discussion. In fact, tests conducted under controlled conditions confirmed that it was possible to detect fine roots (0.005 m in diameter or less) (Butnor, et al., 2001), while tests carried out in the field demonstrated that only coarse roots with diameters greater than 0.05 m could be identified (Ow & Sim, 2012).

Furthermore, research has concentrated on the use of GPR as an appropriate tool for use on valuable trees, or trees in situations where excavation is not possible, such as growing near pavements, roads, buildings or on unstable slopes (Stokes, et al., 2002). GPR data were able to locate roots under pavements reliably and provided a reasonably accurate root count in the compacted soil under concrete (Bassuk, et al., 2011) and asphalt (Cermak, et al., 2000). This is possible thanks to the difference in water content between roots and soil, which can provide the necessary permittivity contrast and therefore allow root detection by GPR (Wielopolski, et al., 2000). Also, it facilitates the distinction between roots and buried utilities (i.e. cables and pipes), which could otherwise generate signal interference, affecting the GPR survey (Ow & Sim, 2012).

Another testing issue that has been investigated is the survey methodology. Two experimental sites situated in Italy, subject to different climates and hydrological conditions, were investigated for this purpose (Zenone, et al., 2008). In this study, GPR measurements were taken using antennas of 900 and 1500 MHz applied in square and circular grids (Figure 21): even though square grids are preferable for GPR lines, results obtainable with circular transects (created by rotating the GPR around the tree, keeping a constant radial distance) were tested to ensure a quasi-perpendicular scanning of root systems. The primary difficulty in this setup, however, arose from soil

unevenness, as it was challenging to push a radar system in circles over roots and stones.

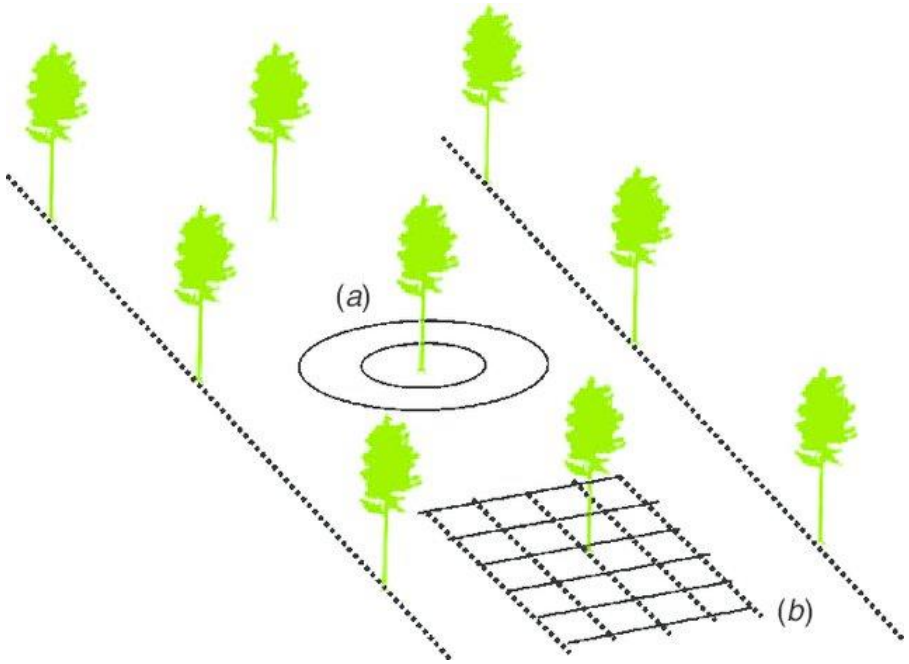

Figure 21: GPR setups for tree root system survey using a) circular transects and b) square grids (Zenone, et al., 2008)

Most of the methodologies mentioned above tested the reliability of their results by digging or uprooting the investigated trees. Zenone, et al. (2008) excavated the root system with an air-spade and pulled it out using a digger; a laser measurement system was then applied in order to create a scan, and the 3D root system architecture was reconstructed.

A comparison between the laser scan point cloud and the sections of GPR scans (Figure 22) returned a limited agreement (Guo, et al., 2013). The authors of the study stated that this might be due to an alteration of the root system architecture that occurred during the excavation. Nevertheless, the use of GPR for 3D coarse root system architecture reconstruction was further criticised (Guo, et al., 2013).

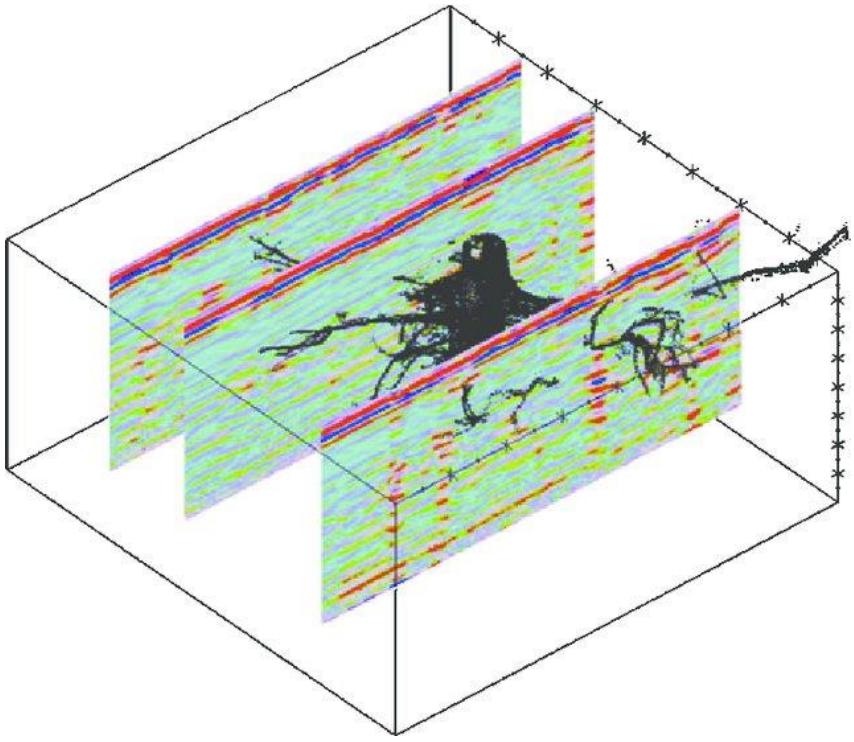

Figure 22: Comparison between 3D rendering from a laser scanner and GPR B-scans (Zenone, et al., 2008)

Set aside the recognition and mapping of tree roots, a challenge that is still object of discussion is the quantification of the biomass of tree roots. As it is widely acknowledged, the estimate of tree root mass density is crucial for the evaluation of the health status of the tree, for the stability of the tree itself and the stability of the soil, as tree roots are used for the reinforcement of slopes. Not least, root mass evaluation is essential for understanding the storage of carbon in the ecosystem (Stover, et al., 2007).

Traditional methods for estimating root biomass are usually destructive, time-consuming and expensive, as well as often inaccurate (Birouste, et al., 2014). The application of NDT methods in this research area is still at the early stage, and the achieved results are still not accurate enough (Aulen & Shipley, 2012).

GPR has proven to be efficient in the estimation of coarse root biomass (Guo, et al., 2013). Several studies have been conducted so far in field conditions (Butnor, et al.,

2001; Butnor, et al., 2003; Stover, et al., 2007; Butnor, et al., 2008; Samuelson, et al., 2008; Borden, et al., 2014) and in a laboratory environment (Cui, et al., 2011). GPR has shown potential for root quantification, as coarse root biomass has been assessed with reasonably good accuracy (Guo, et al., 2013). However, uncertainty still affects the precision of the existing methodologies. Currently, a limiting factor for a correct root density estimation is the root water content which, if too low, can lead to an underestimation of root biomass (Guo, et al., 2013).

2.5. Summary

In order to properly assess the health of trees, it is crucial to acquire knowledge on the main structure and biochemical processes. Non-destructive testing methods have already proven particular viability in the assessment of trunk decays and defects as well as the investigation of tree root systems. Within these techniques, GPR is acknowledged to be reliable, cost-effective and relatively easy to use. However, bibliographic research has identified the existence of some gaps in knowledge. These gaps will form major open issues to address in the future within the research subject area. Within the context of tree trunk investigations, the following open issues have been identified:

- to improve the GPR potential for detection of early decays. Butnor et al. (2009) have identified two significant issues to limit GPR capacity in the quantification of wood decays, i.e. i) whether there is sufficient EM contrast to distinguish rotten from healthy wood, and ii) whether the standard conditions of moisture content, density, resin pockets and heartwood formation interfere with the defects detection.
- to identify GPR characteristics suitable for the evaluation of tree trunks. With regards to tree investigations, the complexity of tree trunks (e.g. circular shape, anisotropy, moisture content, density etc.) limits the efficacy of microwave sensing (Ježová, et al., 2016). The identification of specific investigation frequencies, as well as the choice of the appropriate radar system (i.e. ground-coupled or air-coupled), related to the characteristics of the tree (e.g. tree species or diameter), is therefore essential for effective GPR investigations.
- to outline primary decays within the full range of detectable defects. Mapping the full range of possible diseases may be challenging, as a large variety of tree

species have to be taken into account. The challenge is to prioritise defects across the sets of potential decays occurring in tree trunks. Studies (Alani, et al., 2017) have tested the viability of numerical simulation to address this problem with promising results, paving the way to further research.

Regarding the tree root systems architecture, it has been found that factors like root diameter, root water content and distance between roots are crucial when investigating roots with GPR, and their misinterpretation could lead to an underestimation of root mass (Hirano, et al., 2009). The following advances need to be addressed:

- to recreate a 3-D map of the tree root system. The reconstruction of the root system in a three-dimensional space is a testing issue, which up to now has been achieved with controversial results (Hruska, et al., 1999; Guo, et al., 2013; Zenone, et al., 2008).
- to estimate the root diameter from GPR data analysis. The investigation of root diameter, as well as of other small cylindrical-shaped objects is a challenging task (Cui, et al., 2011) still under investigation. However, recent research (Yeung, et al., 2016) explored the correlation between root diameter and signal characteristics, represented by several waveform parameters. The outcomes of this study are promising, and require further research to be explored and validated.
- To gain knowledge about the interaction between roots and the surrounding environment. There is no detailed information about the interaction between root systems and the soil they are buried into. Moreover, not much is known about how root systems belonging to different trees are interconnected, and how this affects the fight for resources acquisition.

3. Scope of the research

3.1. Aims and objectives

The present research focuses on early identification of tree decay and detection of tree disease using mainly GPR. A better understanding of the internal configuration of tree trunks and the interaction between the root system and the surrounding environment will be pursued by the implementation of new survey methodologies, health monitoring and assessment methods and numerical developments.

The above aims will be achieved through the following main research objectives:

- to develop novel survey methodologies for tree trunk assessment and three-dimensional root mapping
- to develop enhanced data processing algorithms and interpretation techniques for tree assessment
- to develop numerical simulations and modelling of root systems and trunk decays
- to assess mutual interaction between root systems of different tree species
- to estimate tree roots' mass density

3.2. Research questions

To address the objectives mentioned above, the following research questions will be addressed:

- How do the EM properties of living wood (depending on moisture content, wood density and the frequency of the applied EM field), along with the contribution given by the irregular shape of trunks and the variety of possible decays, affect

the results of a GPR investigation (in terms of identification and localisation of internal decays)?

- How do parameters such as the root system architecture (i.e., root orientation) and site-specific conditions (e.g., soil unevenness) affect methodologies of surveying in GPR investigations as well as data processing and interpretation?
- How can we improve current limitations in the geometric and physical characterisation of tree root systems (e.g., mass density of roots) using GPR and other complementary non-destructive testing methods?
- How can we appreciate side effects on the built environment related to growth and functioning of tree roots in the soil?

3.3. Research paradigm

In order to provide the research questions with a strong theoretical and practical background, the proposed research adopts a positivist approach, which relies on quantifiable observations and statistical analyses of collected data. According to the characterisation of the research paradigms through their ontology, epistemology and methodology made by Guba (1990), positivism research philosophy assumes that there is one actual reality, external and independent, which can be observed and measured. The positivist paradigm involves a process of experimentation used to explore observations and answer questions (Kivunja & Kuyini, 2017). For this reason, this paradigm is widely used in scientific research, attempting to investigate reality in terms of facts and measurable entities (Kaboub, 2001).

The method that will be used to carry out this research follows a quantitative approach, providing explanations and making predictions by collecting and analysing measurable outcomes. The use of test parameters will help to identify similarities or

variations between different scenarios, laying the groundwork for further discussion and the production of original knowledge.

4. Use of GPR for the Characterization of the Internal Structure of Tree Trunks

4.1. Interpreting Complex Reflection Patterns using Common Offset Configuration

GPR is traditionally applied to smooth surfaces, in which the assumption of half-space is an adequate approximation that does not deviate much from reality. Nonetheless, using GPR for internal structure characterisation of tree trunks requires measurements on an irregularly shaped closed curve. Typical hyperbola-fitting has no physical meaning in this context since the reflection patterns are strongly associated with the shape of the tree trunk. Instead of a perfect hyperbola, the reflections give rise to complex-shaped patterns that are difficult to be analysed, even in the absence of clutter. In this section, a novel processing scheme is described that can interpret complex reflection patterns assuming a circular target subject to any arbitrarily shaped surface. The proposed methodology can be applied using commercial hand-held antennas in real-time avoiding computationally costly tomographic approaches that require the usage of custom-made bespoke antenna arrays. The validity of the current approach is illustrated both with numerical and real experiments.

4.1.1. Methodology

4.1.1.1. Arc-length Parameterisation

Typical GPR surveys take place in flat surfaces along a straight line. Each A-scan is associated with a given position on that line based on the distance measured from a

The paragraphs of this Chapter have been published as part of journal papers in IEEE Trans. Geos. Rem. Sens. (Giannakis, et al., 2019; Giannakis, et al., 2019; Tosti, et al., 2020), Remote Sensing (Alani, et al., 2019) and NDT&E International (Alani, et al., 2020). Note that minor changes have been introduced to make the text consistent with the other Chapters of this Thesis.

reference point. This distance is measured using a wheel-measuring device which is often incorporated in commercial GPR transducers. It is apparent that when the survey takes place in a straight line, distance can be trivially associated with a unique ordinate. This is not the case when the measurements are taken on irregular surfaces such as tree trunks. This problem is known as arc-length parameterisation and has a wide range of applications to computer graphics (Sharpe & Thorne, 1982; Guenter & Parent, 1990).

4.1.1.1.1. Transforming Distance to Coordinates

In this section, an inclusive scheme based on Guenter & Parent (1990) is described that can be applied in any arbitrarily shaped host medium. Initially, the shape of interest is defined in x, y coordinates $\{x, y \in \mathbb{R} | x, y > 0\}$ discretised with an arbitrary non-uniform discretisation step. The coordinates x, y are stored into the vectors $\boldsymbol{x} \in \mathbb{R}^n$ and $\boldsymbol{y} \in \mathbb{R}^n$ respectively, where n is the number of points used to discretise the shape of the host medium. The vector $\boldsymbol{t} = \langle t_1, t_2, \dots, t_n \rangle$ $\{\boldsymbol{t} \in \mathbb{R}^n | 0 \leq t_i \leq 1\}$ is then defined which is going to be used as the arbitrary variable for the parametric representation of the shape of the host medium. The components of $\boldsymbol{t}$ increase linearly from 0 to 1 with a constant step $1/n$, i.e. $\boldsymbol{t} = \langle 0, \frac{1}{n}, \frac{2}{n}, \dots, 1 \rangle$. Using spline interpolation for the vectors $(\boldsymbol{y}, \boldsymbol{t})$, a set of polynomial functions are obtained. The latter map y to t in a continuous manner:

$$P_i : [t_i, t_{i+1}] \rightarrow \mathbb{R} \tag{4.1}$$

Similarly, spline interpolation is used to map x with respect to t:

$$Q_i : [t_i, t_{i+1}] \rightarrow \mathbb{R} \tag{4.2}$$

Each of the functions P_i, Q_i are polynomials of the third order:

$$P_i(t) = A_{p,i}t^3 + B_{p,i}t^2 + C_{p,i}t + D_{p,i}, \qquad \forall t \in [t_i, t_{i+1}] \tag{4.3}$$

$$Q_i(t) = A_{p,i}t^3 + B_{p,i}t^2 + C_{p,i}t + D_{p,i}, \qquad \forall t \in [t_i, t_{i+1}] \tag{4.4}$$

Therefore, an arbitrary complex shape defined through discretised measurements can now be expressed in a vector form as $\boldsymbol{F} = \langle P(t), Q(t) \rangle$. The shape can now be mapped with an arbitrary step, since both x and y are expressed continuously.

The arc length of a planar curve in $\mathbb{R}^2$ written in a vector form $\boldsymbol{F}$ $\{\boldsymbol{F} \in \mathbb{R}^2\}$ is evaluated by Kreyszig (2006):

$$s(\tau) = \int_0^\tau \left\| \frac{dF}{dt} \right\| dt = \int_0^\tau \sqrt{\left(\frac{dP(t)}{dt}\right)^2 + \left(\frac{dQ(t)}{dt}\right)^2}\, dt \tag{4.5}$$

Where

$$\frac{dP_i(t)}{dt} = 3A_{p,i}t^2 + 2B_{p,i}t + C_{p,i}, \qquad \forall t \in [t_i, t_{i+1}] \tag{4.6}$$

$$\frac{dQ_i(t)}{dt} = 3A_{p,i}t^2 + 2B_{p,i}t + C_{p,i}, \qquad \forall t \in [t_i, t_{i+1}] \tag{4.7}$$

Arc-length (Equation (4.5)) has analytical solutions for a limited number of curves (circle, catenary function etc.). For complicated shapes such as tree trunks, the integral in Equation (4.5) can be approximated numerically by:

$$s(N\Delta t) \approx \sum_{k=0}^{N} \left\| \frac{d\langle P(k\Delta t), Q(k\Delta t) \rangle}{dt} \right\| \Delta t \tag{4.8}$$

Where $\Delta t = \tau / N$. From Equation (4.8), it is evident that:

$$s(N\Delta t) \approx s\big((N-1)\Delta t\big) + \left\| \frac{d\langle P(N\Delta t), Q(N\Delta t)\rangle}{dt} \right\| \Delta t \tag{4.9}$$

Equation (4.9) is an efficient way to compute $s(\tau)$ from its previous values without having to evaluate the summation in Equation (4.8) for every time step. Using a spline interpolation, the values of τ can be mapped with respect to s in a continuous manner:

$$T_i : [s_i, s_{i+1}] \rightarrow \mathbb{R} \tag{4.10}$$

The function $T(s)$ approximates the value of the parameter τ with respect to the length s. Thus, for a given distance s the parametric variable τ associated with this distance can be estimated. Consequently, the positional vector $\boldsymbol{F} = \langle P(T(s)), Q(T(s))\rangle$ can now be connected to a given distance s. In that way, the distance measured by the wheel-measuring devices in commercial GPR antennas can be transformed to x, y coordinates using a limited amount of points to discretise the curve of interest.

4.1.1.1.2. Reflection-Arrival Travel-Time

The reflection-arrival travel-time is related to the distance (relative to a reference point) of each measurement via a hyperbolic equation (Mertens, et al., 2015). The interpretation of the resulting hyperbola gives us an insight into the burial-depth of the target, the velocity of the host medium and the size of the target (Mertens, et al., 2015). The above holds when the assumptions are met, i.e. when the host medium has a flat surface, when the target is circular and when the host medium is homogeneous. When the investigated surface is not flat, the resulting reflection patterns can no longer be approximated with a hyperbola (Ježová, et al., 2018; Bonomo, et al., 2015). In Jezova, et al. (2018) and Bonomo, et al. (2015), the reflection patterns that occur when the host medium is a cylinder are investigated and analysed in detail. The scheme

presented by Jezova, et al. (2018) and Bonomo, et al. (2015) can be expanded to any arbitrary shape via:

$$t(s) = \left(\left\|\boldsymbol{F}(s) - \langle x_g, y_g \rangle\right\| - R\right)\frac{\sqrt{\varepsilon}}{c_0} \tag{4.11}$$

Where

- t is the time $[s]$
- $\boldsymbol{F}(s) = \langle x_s, y_s \rangle$ is the positional vector along the surface of the tree with respect to the distance from a reference point $[m]$
- $\langle x_g, y_g \rangle$ are the coordinates of the centre of the target $[m]$
- R is the radius of the cylindrical target $[m]$
- ε is the relative permittivity of the host medium
- c_0 is the speed of light $[m/s]$

As it is shown in Figure 23, the relationship between s and t (Equation (4.11)) for realistic tree trunks is complicated and highly related to the shape of the tree.

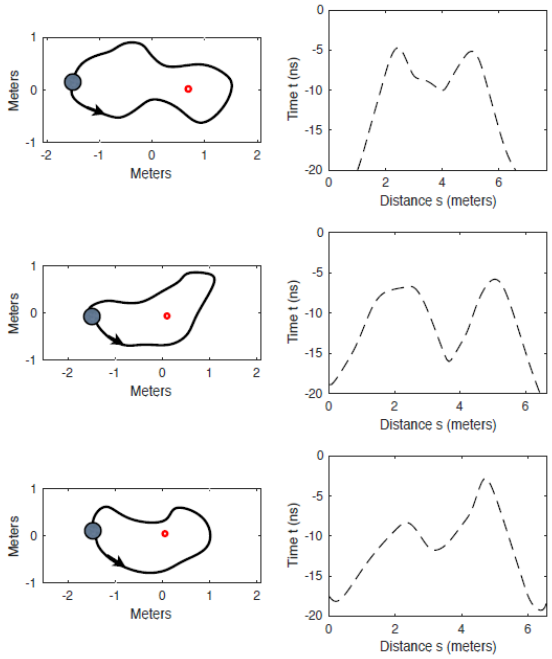

Figure 23: Left: With black line is the shape of the host medium. The grey circles indicate the starting points of the measurements. The direction of the measurements is counter-clockwise. Red circles indicate the targets of interest. Right: The arrival travel-time from the target is plotted with respect to the distance relative to the starting point (Equation (4.11)).

4.1.1.2. Ringing Noise Removal

A generic tree trunk consists of five distinct layers, as mentioned in Section 2.1.1. The layers mentioned above differ with respect to water content as well as chemical composition and texture (Russell & Cutler, 2004). This results in dielectric contrasts that give rise to repetitive reflections, contributing to the overall ringing noise. Due to that, two different methodologies are employed to reduce ringing noise and increase the overall signal to clutter ratio. The data are collected along a given curve and each A-scan $\boldsymbol{A}_s \in \mathbb{R}^w$ is a vector with size w, which is measured at distance s from the starting point. The B-scan $\boldsymbol{B} \in \mathbb{R}^{w \times S}$ is a 2D matrix with $w \times S$ dimensions where S is the number of measurements and $\boldsymbol{B} = \langle \boldsymbol{A}_{s1}^T, \boldsymbol{A}_{s2}^T, \dots, \boldsymbol{A}_{sw}^T \rangle$ (T denotes the transpose sign). Ringing noise shows similar behaviour between A-scans (Brunzell, 1999; Wu, et al., 2001). This is the reason why a simple average removal (Daniels, 2004) can often efficiently decrease ringing noise. Nonetheless, as it is stated in (Kim, et al.,

2007), other approaches like SVD provide a more accurate and systematic way to reduce ringing noise in challenging scenarios with low signal to clutter ratio.

SVD is a powerful tool for removing ringing noise, nonetheless, as it is stated in Giannakis, et al. (2016), the performance of processing frameworks are case dependent, and there is no conclusive approach that over-performs the rest. To that extent, a linear approximation of the signal is also considered as an alternative to SVD (Giannakis, 2016; Giannakis, et al., 2015). The linear approximation uses a matrix $\boldsymbol{J} \in \mathbb{R}^{w \times q}$ that contains q number of randomly selected traces without the presence of any target. Subsequently, it is assumed that any A-scan consists of the target's response $\boldsymbol{E}_s$ plus clutter $\boldsymbol{E}_c$:

$$\boldsymbol{A}_i = \boldsymbol{E}_{i,c} + \boldsymbol{E}_{i,s} \tag{4.12}$$

The term clutter here is used to describe ringing noise, noise and the cross-coupling between the transmitter and the receiver. Approximating $\boldsymbol{A}_i$ as a linear combination of the traces in $\boldsymbol{J}$ will result in a sufficient approximation of $\boldsymbol{E}_c$ and a poor approximation of $\boldsymbol{E}_s$. This is because the clutter is correlated between the traces, and it is easier to be modelled based on previous A-scans. Using least squares, the linear coefficients of the matrix $\boldsymbol{J}$ are evaluated, and subsequently the predicted clutter is subtracted from each A-scan:

$$\overline{\boldsymbol{A}_i^T} = \boldsymbol{A}_i^T - \boldsymbol{J}(\boldsymbol{J}^T\boldsymbol{J})^{-1}\boldsymbol{J}^T\boldsymbol{A}_s^T \tag{4.13}$$

4.1.1.3. Model Fitting

The current subsection presents the equivalent of “hyperbola fitting” (Olhoeft, 2000) to the more inclusive and generic reflection patterns that are expected in tree trunks.

Through a manual threshold, the anomaly of interest can be gathered in a set of points $M = \{(s_i, t_i) \in \mathbb{R} | i = 1,2, \dots, z\}$, where z is the number of observations. Based on M and Equation (4.11), the centre $\langle x_g, y_g \rangle$ of the target, its radius R and the relative permittivity of the host medium ε are finely tuned in order to minimise:

$$\underset{x_g, y_g, \varepsilon, R}{\operatorname{argmin}} \sum_{i=1}^{z} \left(t_i - \left(\left\| \boldsymbol{F}(s_i) - \langle x_g, y_g \rangle \right\| - R \right) \frac{\sqrt{\varepsilon}}{c_0} \right) \tag{4.14}$$

It is easy to show that Equation (4.14) can be re-written as

$$\underset{x_g, y_g, \varepsilon, R}{\operatorname{argmin}} \sum_{i=1}^{z} \left(t_i - \left\| \boldsymbol{F}(s_i) - \langle x_g, y_g \rangle \right\| \frac{\sqrt{\varepsilon}}{c_0} + R \frac{\sqrt{\varepsilon}}{c_0} \right) \tag{4.15}$$

From Equation (4.15), it is apparent that the radius R and the relative permittivity ε form a non-unique product. That means that different sets of (R, ε) might result in similar outputs. Thus, in the presence of noise, the minimisation in Equation (4.15) is sensitive due to non-uniqueness. This phenomenon was derived experimentally in (Mertens, et al., 2015) for flat surface surveys.

To overcome this, the bulk relative permittivity of the tree trunk can be approximated using the two-way travel-time from the reflection of the opposite side of the tree. Knowing the time needed for the EM wave to travel a known distance, the mean relative permittivity can be evaluated straightforwardly. If the relative permittivity is not readily available, then the minimisation in Equation (4.15) can be executed subject to an idealised point target, i.e. for $R = 0$.

The function to be minimised in Equation (4.15) is subject to multiple local minimal due to the nature of the problem as well as the inherited noise in the measured M. To avoid initialisation and overcome local minimal, a global optimiser is used for executing

Equation (4.15). Particle swarm optimisation (PSO) (Eberhart & Kennedy, 1995) is chosen due to its popularity in electromagnetics (Robinson & Rahmat-Samii, 2004; Kelley, et al., 2007) and geophysics (Martínez, et al., 2010). Using a different global optimiser (i.e. genetic algorithms, ant colony optimisation etc.) will have minor differences on the overall performance and computational requirements of the detection scheme. PSO initially generates a number of particles u that are placed randomly in the optimisation space. For the case that permittivity is known, each particle k is a vector $\boldsymbol{q}_k = \langle x_k, y_k, R \rangle \{\boldsymbol{q}_k \in \mathbb{R}^3\}$. The cost function is then evaluated for every particle, and their positions are updated iteratively:

$$\boldsymbol{v}_k^{\tau} = b_0 \boldsymbol{v}_k^{\tau-1} + b_1 V_1 \left(\boldsymbol{q}_k^{\tau-1} - \boldsymbol{q}_{k,b}\right) + b_2 V_2 \left(\boldsymbol{q}_k^{\tau-1} - \boldsymbol{q}_g\right) \tag{4.16}$$

$$\boldsymbol{q}_k^{\tau} = \boldsymbol{q}_k^{\tau-1} + \boldsymbol{v}_k^{\tau} \tag{4.17}$$

Where b_0, b_1 and b_2 are constants associated with the convergence rate and the ability of PSO to converge to global solutions. In general, large values of b_0 and small values of b_2 decrease the convergence rate and the probability of the algorithm to be trapped in local minimum. The parameters $V_1, V_2 \in [0,1]$ are random numbers with a uniform distribution, and $\tau \in \mathbb{Z}$ is the integer iteration number. The vector $\boldsymbol{v}_k \in \mathbb{R}^3$ is the velocity in the three dimensions of $\boldsymbol{q}_k$. The vector $\boldsymbol{q}_{k,b}$ is the position $\langle x_k, y_k, R \rangle$ of the particle k in which the cost function got its minimum value until the iteration τ. Lastly, the vector $\boldsymbol{q}_g$ is the position $\langle x, y, R \rangle$ in which the cost function from all the particles got its minimum value until the iteration τ. For the current case, through a trial and error procedure, it is derived that $u = 50$ and $b_0 = b_1 = b_2 = 1$ balances between efficiency and accuracy.

4.1.2. Numerical Experiments

In the current section, the proposed methodology is tested on synthetic data. A second-order in both space and time finite-difference time-domain (FDTD) (Taflove & Hagness, 2005) method is used in order to evaluate Maxwell's equations for a given dielectric distribution numerically. To accelerate the computations, gprMax (Warren, et al., 2016), an open-source CUDA-based GPU engine (Warren, et al., 2019) is employed. The spatial discretisation step is assumed to be uniform throughout the grid and equal with $\Delta x = \Delta y = \Delta z = 0.001\, m$. The time step Δt follows the Courant limit (Taflove & Hagness, 2005).

The dielectric properties of wood vary seasonally as well as concerning the type of the tree (Tomasanis, 1990). In general, softwoods contain more water content compared to hardwoods. Consequently, the permittivity of softwoods is substantially higher than the one of hardwoods (Tomasanis, 1990). The permittivity is also related to the orientation of measurement, i.e. the tree trunk is an anisotropic material, with the lowest permittivity values observed perpendicular to the layering of the tree (Tomasanis, 1990). In addition to the standard tree trunk layers, thinner rings of dense material occur periodically and almost parallel to each other (Russell & Cutler, 2004). The water content of the structures mentioned above greatly varies between different types of trees. For example, hardwoods consist of a dry heartwood and saturated sapwood in contrast to softwoods, for which both sapwood and hardwood are equally saturated (Tomasanis, 1990). Numerous attempts have been made to generate semi-empirical models for the dielectric properties of trees similar to the semi-empirical models that exist for soils (Peplinski, et al., 1995). Nonetheless, a conclusive formula is not yet to be derived due to the complexity of the tree structure and its multi-phase composition.

Experimental evidence supports the premise that the permittivity of trees increases linearly with the increase of water content (Broadhurst, 1970). Electrolytes and cellulose seem to have a secondary effect (Tomasanis, 1990). Due to its water content and the bipolar nature of the latter, the relative permittivity of the tree trunk can be expressed as an extended Debye model (Tomasanis, 1990; Brown & Curry, 1982; James, 1975):

$$\varepsilon(\omega) = \varepsilon_{\infty} + \frac{\Delta\varepsilon}{1 + j\omega t_0} - \frac{\sigma}{j\omega\varepsilon_0} \tag{4.18}$$

Where

- ε is the relative permittivity of the material with respect to ω
- ω is the angular frequency
- ε_{∞} is the relative permittivity at infinity frequency
- $\Delta\varepsilon$ is the difference between the static relative permittivity and the relative permittivity at infinity frequency
- $j = \sqrt{-1}$
- t_0 is the relaxation time
- σ is the conductive term

In order to map the underlying relationship between the dielectric parameters in Equation (4.18) and the water content of the trunk, the complex refractive index model (CRIM) (Birchak, et al., 1974) is used. The latter assumes that the tree trunk is a two-phase material and its relative bulk permittivity equals with:

$$\sqrt{\varepsilon} = f_t\sqrt{\varepsilon_t} + f_w\sqrt{\varepsilon_w} \tag{4.19}$$

Where

- ε is the relative bulk permittivity of the material
- $\varepsilon_t = 5$ is the relative permittivity of the solid phase of the tree
- $\varepsilon_w = 4.9 + \frac{78}{(1+j\omega(9.23e-12))}$ is the dispersive relative permittivity of the water (Peplinski, et al., 1995)
- f_t is the volumetric fraction for the solid phase
- f_w is the volumetric fraction for the water phase

with $f_t + f_w = 1$.

The CRIM model provides a simple and elegant way to express the bulk permittivity of a multi-phase medium with respect to its phases. Nonetheless, CRIM cannot be implemented directly to FDTD. To overcome this, Equation (4.19) should be replaced with a function compatible with FDTD (Giannakis & Giannopoulos, 2014). Given a specified volumetric water fraction, Equation (4.19) can be approximated for a given frequency range $[\omega_l, \omega_u]$ by a multi-Debye pole:

$$f_t\sqrt{\varepsilon_t} + f_w\sqrt{\varepsilon_w} \approx \varepsilon_\infty + \sum_{h=1}^{H} \frac{\Delta\varepsilon_h}{1 + j\omega t_{0,h}} \quad \forall\omega \in [\omega_l, \omega_u] \tag{4.20}$$

The approximation above can be seen as a minimisation problem:

$$\underset{\Delta\varepsilon_h, t_{0,h}, \varepsilon_\infty}{\operatorname{argmin}} \sum_{i=l}^{u} \left(f_t\sqrt{\varepsilon_t} + f_w\sqrt{\varepsilon_w} - \varepsilon_\infty - \sum_{h=1}^{H} \frac{\Delta\varepsilon_h}{1 + j\omega_i t_{0,h}} \right) \tag{4.21}$$

The minimisation in Equation (4.21) is executed using the hybrid scheme proposed in Kelley, et al. (2007) for approximating Havriliak-Negami media with multi-Debye expansions. From Figure 24, it is clear that one Debye pole $(H = 1)$ is sufficient for

approximating Equation (4.20) for the frequency range of $0.01 - 10\ GHz$. In the current numerical study, the water content of the tree layers is chosen, such as to simulate saturated hardwoods like oaks or relatively dry softwoods like cedars. The Debye properties of the tree layers derived from Equation (4.21) and used in this numerical study are shown in Table 4. The conductivities are chosen based on typical values measured using electrical resistivity tomography (Brazee, et al., 2010; Guyot, et al., 2013).

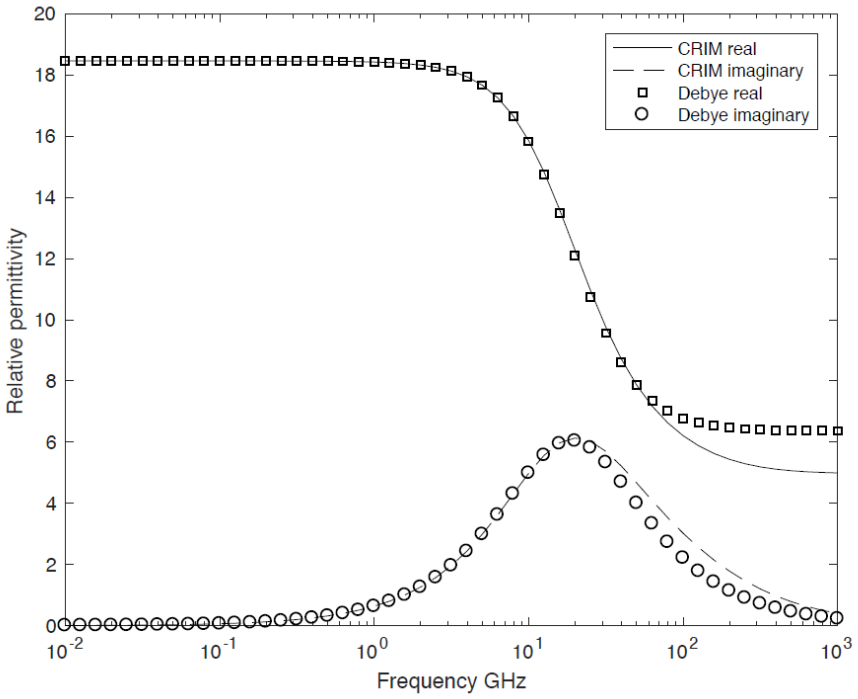

Figure 24: Dielectric properties for the outer sapwood using CRIM model and its Debye equivalent. It is apparent that up to 10 GHz, one Debye pole is adequate for the approximation in Equation (4.20)

Table 4: The extended Debye properties of the tree layers.

Name	$\boldsymbol{WC}$ [%]	$\boldsymbol{\varepsilon_\infty}$	$\Delta\boldsymbol{\varepsilon}$	$\boldsymbol{\sigma}$ $[\boldsymbol{\Omega^{-1}m^{-1}}]$	$\boldsymbol{t_0}$ $[\boldsymbol{s}]$
Cambium Layer	40	6	18	1	9.23e-12
Outer Sapwood	30	6.1	12.36	0.033	9.23e-12
Inner Sapwood	25	5.9	9.66	0.02	9.23e-12
Rings	10	5.4	3.1	0.0083	9.23e-12
Heartwood	5	5.22	1.43	0.005	9.23e-12
Bark	0	5	0	0	9.23e-12

4.1.2.1. Numerical Case Study

Hollow cavities throughout the tree trunk are a typical sign of tree decay and a robust indicator of the health status of the tree (Shortle & Dudzik, 2012; Larsson, et al., 2004). Detecting cavities in a non-destructive manner is of high importance since extended cavities can compromise the stability and the structural integrity of the trunk leading to tree falls (Shortle & Dudzik, 2012). In the current numerical study, the ability of the current scheme on detecting hollow cavities is investigated in two different numerical experiments. The first case study is shown in Figure 25. One saturated hardwood and one semi-saturated softwood are investigated. For the saturated hardwood, the trunk consists of bark, cambium layer, outer sapwood and heartwood. In the second case, the trunk consists of bark, cambium layer and outer sapwood. For the excitation of the FDTD, a numerical equivalent of the commercial antenna GSSI 1500 MHz is used (Giannakis, et al., 2018; Warren & Giannopoulos, 2011). The excitation of the antenna is constrained to be parallel to one of the Cartesian axes, due to the arrangement of the fields in FDTD. Therefore, the models described in Giannakis, et al. (2018) and Warren & Giannopoulos (2011) do not support tilted measurements. To overcome this, instead of rotating the antenna around the trunk, the trunk is rotated while the position of the antenna remains fixed. The resulting B-scan is processed using an SVD filter removing the six dominant eigenvalues. From Figure 25, it is evident that the proposed scheme can accurately recover both the size as well as the location of the decay when the permittivity is known. For the current example, a mean relative permittivity $\varepsilon = 18$ is assumed. If the permittivity is treated as an unknown in Equation (4.15), the centre of the target can be accurately estimated. Nonetheless, its radius must be constrained to be zero in order to avoid non-uniqueness (Mertens, et al., 2015).

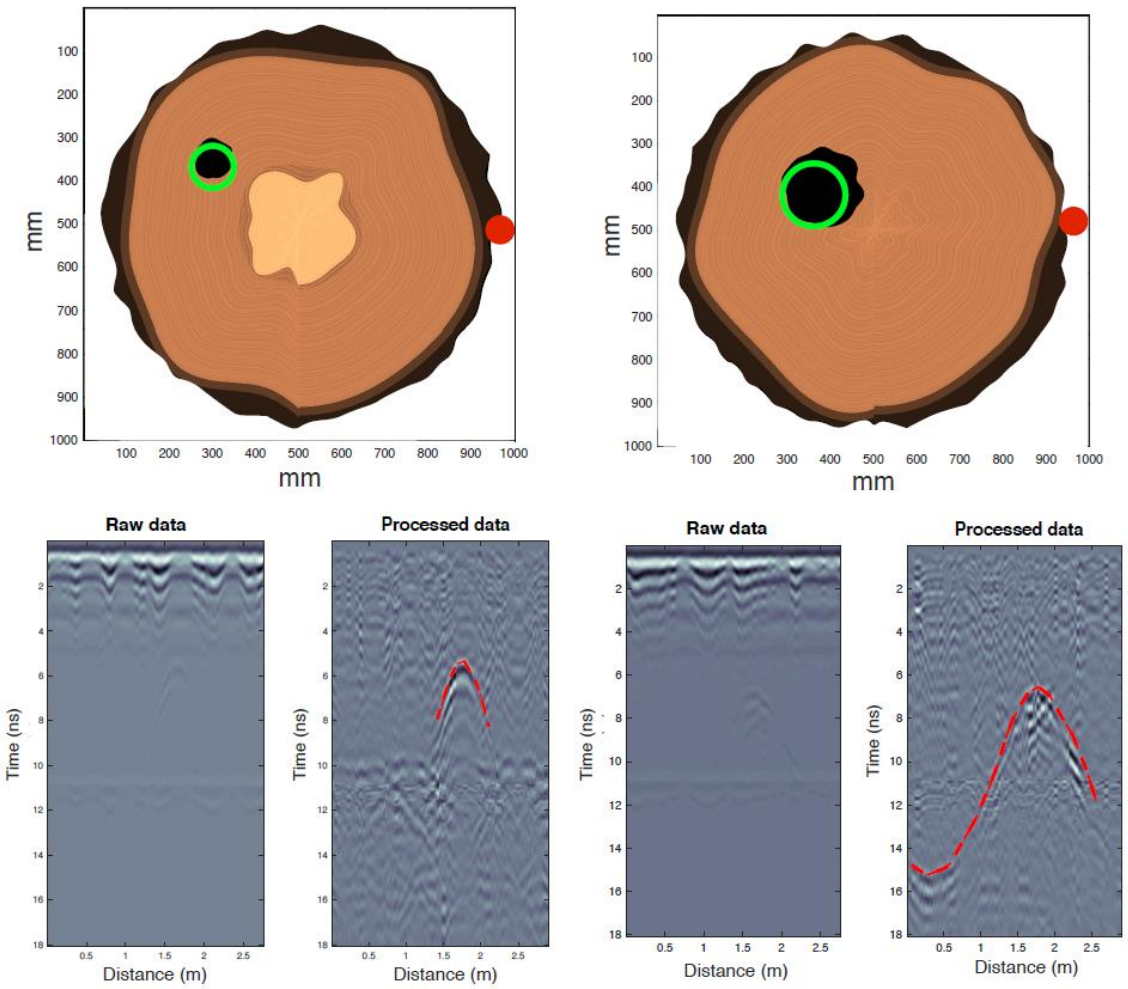

Figure 25: One saturated hardwood (left) and one semi-saturated softwood (right) are numerically simulated. The green lines indicate the recovered tree decays using the suggested scheme. Red circles indicate the starting point. The measurements are taken clockwise.

The second case study examines how the proposed scheme performs in complex-shaped tree trunks like the one shown in Figure 26. A complex-shaped hardwood is examined with bark, cambium layer, outer sapwood, inner sapwood and heartwood. Notice that the complex shape of the trunk does not allow the tree to be rotated subject to a fixed antenna position. Due to that, the excitation source chosen for this case study is an ideal Hertzian dipole using a modulated Gaussian pulse with 1500 MHz central frequency. Similar to the previous example, an SVD filter is applied to remove the ringing noise. The bulk relative permittivity is constrained to be equal to $\varepsilon = 14$. The reflection patterns in the post-processed B-scan are highly complicated and

deviate from the typical hyperbolic features expected in GPR surveys. Patterns like these are difficult to be interpreted and can give the false impression of apparent layers or complex-shaped targets. The proposed methodology manages to accurate recover both the position and the size of the decay, by fitting the anomaly subject to the shape of the tree trunk.

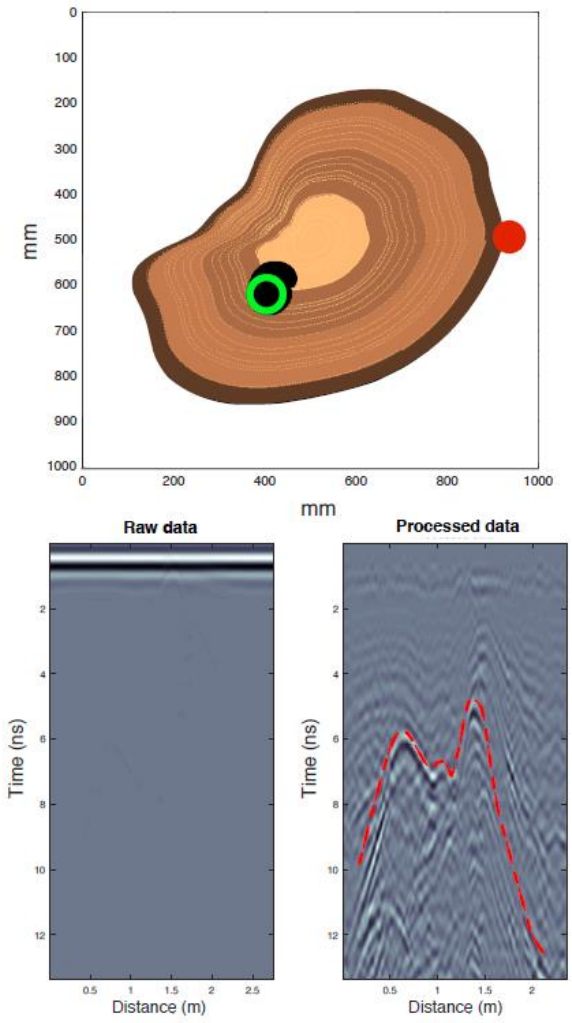

Figure 26: A complex-shaped hardwood is numerically simulated. Green colour illustrates the recovered position and radius of the tree decay. The starting measuring point is highlighted with a red circle. The measurements are taken clockwise.

4.1.3. Laboratory Case Study

The suggested scheme is now applied to real data collected at The Lord Faringdon Centre at the University of West London (UWL). In the current case study, the ability of the proposed scheme to detect AOD is tested under laboratory conditions. The host material is a dead oak with three drilled holes with different sizes. One hole with 0.02 m radius and two holes with 0.04 m radius. The gaps were subsequently filled with sawdust mixed with water in an effort to simulate the liquid-filled cavities that occur in AOD infected oaks (see Figure 27). The antenna system used is the Aladdin 2000 MHz hand-held antenna from IDS Georadar (Part of Hexagon). Aladdin has been successfully applied in many high-frequency GPR applications (Ahmad, et al., 2012; Lameri, et al., 2017), and its size is suitable for measuring curved surfaces such as tree trunks. The measurements are taken counter-clockwise every 0.01 m using a measuring wheel. Using the approach described in Section 4.1.1.1.1, the distance is transformed to coordinates. Zero-time removal, time-varying gain and DC-removal are initially applied to the raw data. Subsequently, an SVD and linear filter are used in an effort to reduce the ringing noise present in the B-scan. In particular, two dominant eigenvalues are filtered out before linear filtering. The latter uses three randomly selected A-scans to form the J matrix in Equation (4.13).

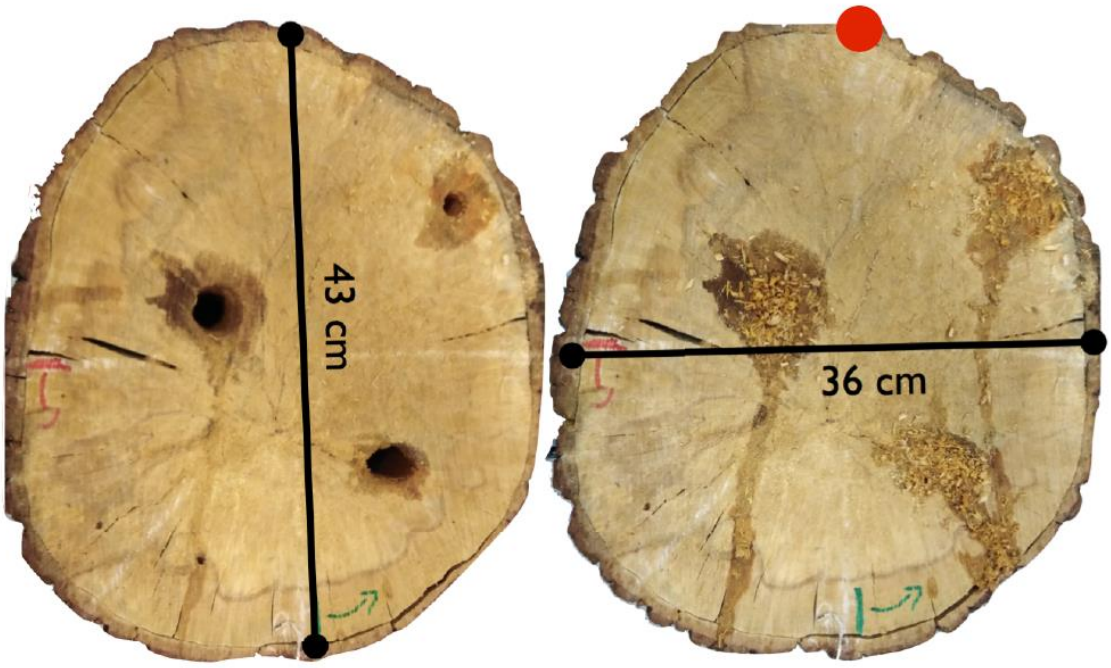

Figure 27: Left: The tree sample used in the current case study. Right: Sawdust mixed with water used to fill the holes in order to simulate the liquid-filled chambers in the early stages of AOD. Red circle illustrates the starting point of the measurements. The measurements are taken counter-clockwise

Figure 28 shows both the raw and the processed B-scans using a perpendicular polarisation. Three hyperbolic-features are clearly visible from the post-processed B-scans. In order to estimate the position and size of the decay that best fits these features, the relative permittivity of the host material should be evaluated first. The bulk relative permittivity of the tree trunk was estimated $\varepsilon \approx 3$ at 2000 MHz frequency, by measuring the two-way travel time from the opposite side of the trunk. A perfect electric conductor (PEC) sheet was used in order to enhance the reflection further.

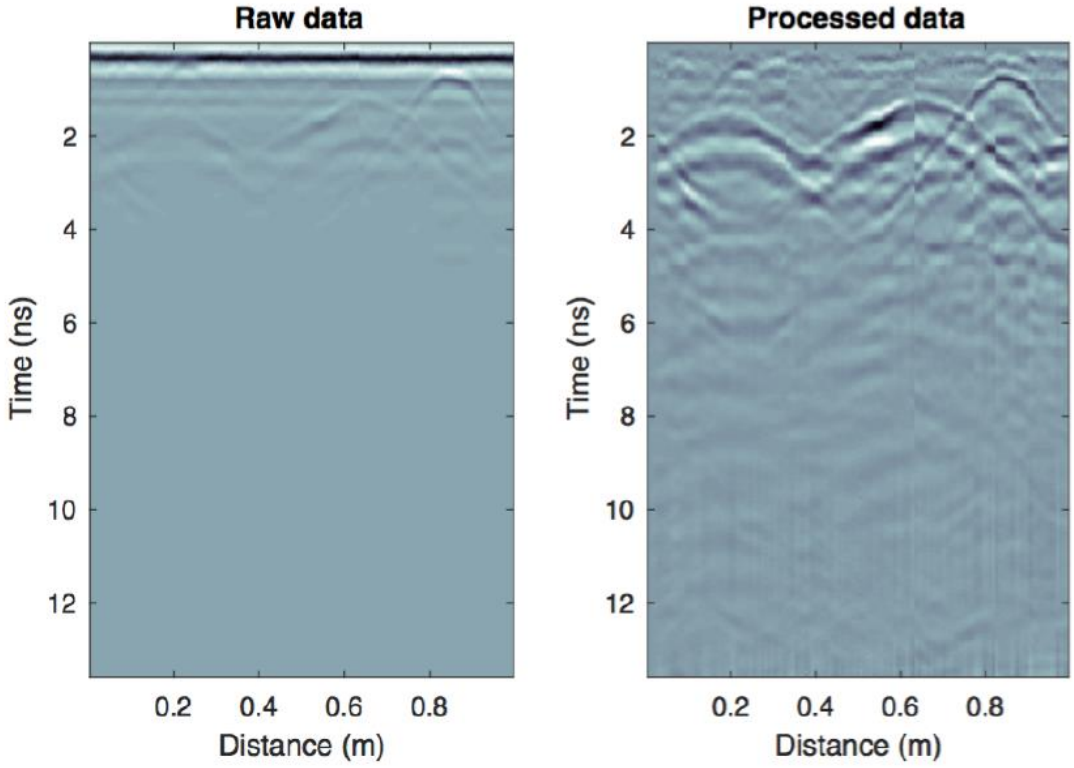

Figure 28: Left: The raw data collected using Aladdin with perpendicular polarisation on the tree sample shown in Figure 27. Right: The post-processed B-scan.

Figure 29 shows the recovered coordinates and radii using the proposed fitting scheme. Three distinct and clearly visible patterns in the B-scans were manually picked. Based on the shape of the tree and its mean relative permittivity, the minimization in Equation (4.15) converged to three targets that best fit the data (see Figure 30). It is evident from Figure 29 that, using the suggested methodology, the positions, and the radii of the decays can be successfully and efficiently recovered.

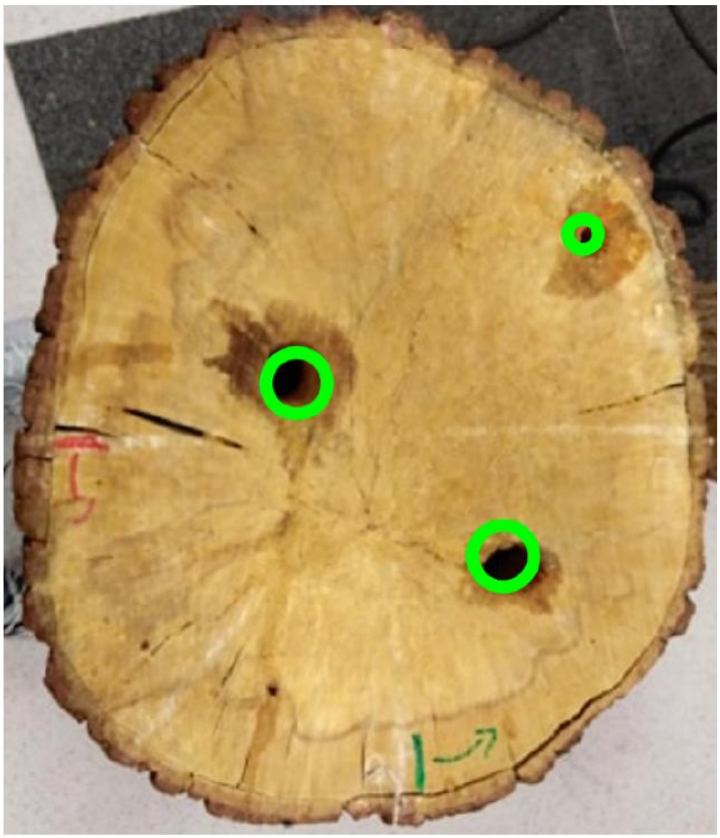

Figure 29: The estimated coordinates and radii of the decays using the proposed detection scheme are illustrated with green circles. The holes in the tree were filled with saturated sawdust during the measurements (see Figure 27). The holes are plotted empty in the current figure for comparison purposes.

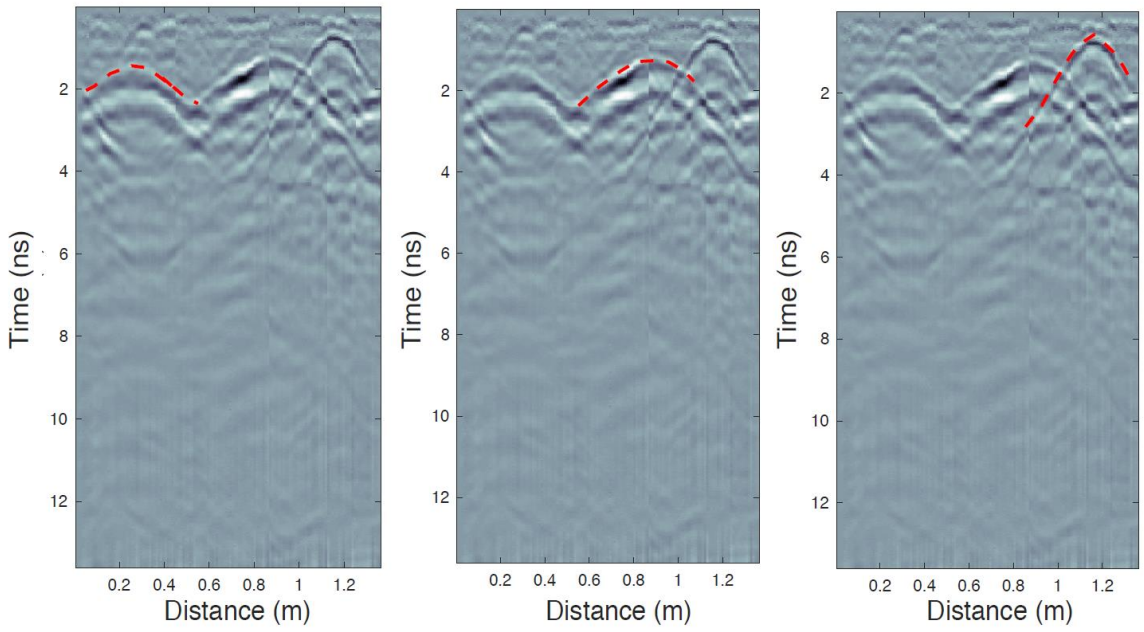

Figure 30: Three different anomalies used to recover the coordinates and radii of the decays shown in Figure 29.

4.1.4. Conclusions

This research describes a novel processing framework that, based on GPR surveys, can interpret the internal structure of irregularly shaped tree trunks. The proposed method can be coupled with commercial antennas with minimum computational and operational requirements. Numerical examples are provided to support the premise that tree decays can be successfully located using typical GPR surveys and thus avoiding tomographic approaches that require custom-made bespoke systems to be deployed on the site of interest. Also, an experimental case study is presented in which the current scheme is successfully used to locate liquid-filled chambers associated with AOD. The accuracy and the efficiency of the current methodology on detecting early signs of AOD, make it commercially appealing for applications such as assessing the health status of trees on forestry applications.

This research line addresses the following objectives of the present Thesis (see Section 3.1):

- *to develop novel survey methodologies for tree trunk assessment:* in this research, the effectiveness of examining tree trunks using circular scans is investigated. Results have shown the viability of the proposed technique. The objective is therefore achieved.
- *to develop numerical simulations and modelling of trunk decays:* the proposed methodology was tested using numerical simulations for different scenarios. Results have helped to refine the proposed technique, showing that the method is capable of recovering both the position and the size of the decay accurately. This objective is therefore achieved.

4.2. Detection of Early Decays in Tree Trunks using a Modified Kirchhoff Migration and Reverse-Time Migration

The central core of the proposed methodology is the qualitative reconstruction of the internal structure of trees using Kirchhoff and RT migration (see Section 2.4.5.7). These methods complement each other, and they provide robust and efficient interpretation tools for tree surveys. The measurement configuration applied in this study consists of parallel scans orthogonal to the main axis of the trunk.

4.2.1. Methodology

Before migration, every A-scan should be assigned with a specific set of coordinates $(x, y) \in \mathbb{R}$. Commercial GPR systems use a wheel-measuring device to position each A-Scan. This approach is suitable for line measurements in half-spaces but is not applicable when measurements are taken on irregular surfaces (Giannakis, et al., 2019). To this end, an arc-length parameterisation (see Section 4.1.1.1) is used to transform the wheel-based measured distance to 2D coordinates. Subsequently, a pre-processing step is executed that includes a zero-offset removal, a time-zero correction, a linear time-varying gain and an SVD filter (see Section 2.4.5).

The filtered B-scans are then in a suitable format for the modified Kirchhoff and the RT migration. Although special care is taken in the pre-processing step to remove unwanted signal, nonetheless, the reconstructed internal structure of the trunk is still corrupted with migration artefacts and remaining clutter. In an effort to further increase the overall signal to clutter ratio and facilitate interpretation, the post-migrated images are squared and subsequently smoothed using a Gaussian blur filter (Nixon & Aguado, 2008). The above processing methodology consists of sequential steps with minimum computational requirements. Pre-processing, migration and post-processing can be

executed in mainstream computers within a reasonable time, which makes the suggested framework commercially appealing for large scale forestry applications.

4.2.1.1. Modified Kirchhoff Migration

The Kirchhoff integral for $t = 0$ and subject to an arbitrary closed surface is given by

$$Q(\boldsymbol{r}_m) = \frac{1}{2\pi} \oiint_{S_0} \frac{\partial R}{\partial n} \left(\frac{1}{R^2} W\left(\boldsymbol{r}, \frac{R}{v}\right) - \frac{W'\left(\boldsymbol{r}, \frac{R}{v}\right)}{vR} \right) dS \tag{4.22}$$

where

- $W(\boldsymbol{r}, t)$ is the filtered B-Scan measured at the position $\boldsymbol{r} = \langle x, y, z \rangle$
- $W'(\boldsymbol{r}, t) = \frac{\partial W(\boldsymbol{r}, t)}{\partial t}$ is the derivative of the filtered B-Scan with respect to time t
- $\boldsymbol{r} \in S_0$ is a vector where S_0 is a closed surface in the 3D space

The reconstructed image is denoted as $Q(\boldsymbol{r}_m)$ where $\boldsymbol{r_m} = \langle x_m, y_m, z_m \rangle$ are the cartesian coordinates of the investigated point. The distance between the investigated point $\boldsymbol{r}_m$ and a point at the surface S_0 is given by $R = \|\boldsymbol{r} - \boldsymbol{r}_m\|$. The velocity in the medium v is assumed to be homogeneous and is given in m/s. Notice that the velocity v used in Equation (4.22) is half the actual velocity in order to compensate for the two-way travel time present in GPR measurements. Lastly, the derivative $\frac{\partial R}{\partial n}$ is the derivative of the distance R on the direction normal to the surface S_0.

In the current study, the measurements are taken along the surface of the tree on equidistant and parallel scans with respect to the ground. Consequently, the measurement grid is dense along the circumference and sparse along the main axis of the trunk. Due to that, 3D migration will have negligible advantages compared to pseudo-3D migration, consisting of 2D migrated slices on the x, y plane (parallel to the

ground) (Giannakis, et al., 2016). In that context, and in order to reduce the complexity and keep the algorithm computationally efficient, a 2D migration is performed for each circular scan, and the results are combined to a pseudo-3D image. The generalised Kirchhoff integral for 2D is now evaluated over the closed curve T_0, a continuous and differentiable function that lies on the x, y plane. The vectors $\boldsymbol{r}_m$ and $\boldsymbol{r}$ are now fixed at the z axis. Using the arc parameterisation of the trunk (Giannakis, et al., 2019) (Section 4.1.1.1), T_0 is approximated using the vector $\boldsymbol{F} = \langle P(s), L(s) \rangle$. Notice that r denotes a 3D set of points that lie along the curve $\boldsymbol{F}$. Therefore, the Kirchhoff integral for a 2D curve T_0 along a constant depth z can be re-written as

$$Q(\boldsymbol{r}_m) = \frac{1}{2\pi} \int_0^M \frac{\partial R}{\partial n} \left(\frac{1}{R^2} W\left(\boldsymbol{F}, \frac{R}{v}\right) - \frac{W'\left(\boldsymbol{F}, \frac{R}{v}\right)}{vR} \right) ds \tag{4.23}$$

where

- $R(s, m) = \|\boldsymbol{r}_m - \boldsymbol{F}\|$
- M is the circumference of the tree (i.e. the maximum distance s from the reference point)

Via interpolation, the variable $W\left(\boldsymbol{F}, \frac{R}{v}\right)$ in Equation (4.23) can be easily evaluated continuously since each A-Scan is correctly positioned with respect to the distance s using the arc parameterisation approach described in Section 4.1.1.1. The derivative $W'\left(\boldsymbol{F}, \frac{R}{v}\right)$ is evaluated numerically using a second-order finite-difference scheme. The directional derivative $\frac{\partial R}{\partial n}$ denotes the derivative of the distance R on the direction normal to the curve F. Therefore, $\frac{\partial R}{\partial n}$ can be written as $\frac{\partial R}{\partial n} = \nabla R$ (Kreyszig, 2006), where

$\boldsymbol{n} = \frac{\boldsymbol{A}}{\|\boldsymbol{A}\|}$ is the unit vector orthogonal to F (i.e. $A = \langle \frac{\partial L(s)}{\partial s}, \frac{-\partial P(s)}{\partial s} \rangle$) (Kreyszig, 2006). Lastly, the velocity v is estimated using the focal criterion described in Section 4.2.1.3.

The integral in Equation (4.23) can be evaluated numerically in a straightforward manner with minimum computational requirements. The numerical evaluation of Equation (4.23) can be seen as a diffraction summation scaled with respect to the distance R and to the directional derivative $\frac{\partial R}{\partial n}$. The latter increases the contribution from the segments in $\boldsymbol{F}$ that are aligned with the orthogonal lines to $\boldsymbol{F}$ that pass from the investigated point $\boldsymbol{r}_m$. Through this, directivity aspects are incorporated in the migration making the process more robust and accurate. Scaling the diffraction summation with respect to R increases the contribution of early reflections and masks deeper structures. In order to overcome this, a modified Kirchhoff migration is suggested:

$$Q(\boldsymbol{r}_m) = \frac{R_m}{2\pi} \int_0^M \frac{\partial R}{\partial n} \left(\frac{1}{R^2} W\left(\boldsymbol{F}, \frac{R}{v}\right) - \frac{W'}{vR}\left(\boldsymbol{F}, \frac{R}{v}\right) \right) ds \tag{4.24}$$

where $R_m = \min_{s \in [0,M]} R(s,m)$. This implies that every diffraction summation is scaled with respect to a normalised distance. The distance is normalized subject to the minimum distance $R(s,m)$ between the investigated point $\boldsymbol{r}_m$ and the closed curve $\boldsymbol{F}$. Using this approach, each diffraction curve is independently scaled based on its minimum distance from $\boldsymbol{F}$. In the original Kirchhoff migration (Equation (4.23)), late reflections are repressed in general regardless of the diffraction curve. In the modified scheme (Equation (4.24)), late reflections with respect to the diffraction apex are repressed. Thus, scaling still occurs, but it is no more biased to shallow targets.

4.2.1.2. Reverse-Time Migration

Maxwell's equations for linear, non-dispersive and nonmagnetic media are given by (see Section 2.4.2.1):

$$\nabla \times \boldsymbol{H} = \varepsilon \frac{\partial \boldsymbol{E}}{\partial t} + \sigma \boldsymbol{E} + \boldsymbol{J} \tag{4.25}$$

$$\nabla \times \boldsymbol{E} = -\mu_0 \frac{\partial \boldsymbol{H}}{\partial t} \tag{4.26}$$

$$\nabla \cdot (\varepsilon \boldsymbol{E}) = q \tag{4.27}$$

$$\nabla \cdot (\mu_0 \boldsymbol{H}) = 0 \tag{4.28}$$

where

- $\boldsymbol{E} = \langle E_x, E_y, E_x \rangle$ is the electric field $[V/m]$
- $\boldsymbol{H} = \langle H_x, H_y, H_x \rangle$ is the magnetic field $[A/m]$
- $\boldsymbol{J} = \langle J_x, J_y, J_x \rangle$ is the electric current density $[A/m^2]$
- σ is the electrical conductivity $[S/m]$
- ε is the dielectric permittivity $[F/m]$
- μ_0 is the magnetic permeability of free space $[H/m]$
- q is the electric charge density $[C/m^3]$

In RT migration for GPR, the filtered B-scan $W(\boldsymbol{F}, t)$ for the interval $\{[0, t_{max}] \in \mathbb{R} | t_{max} > 0\}$ is initially reversed with respect to time $W(\boldsymbol{F}, t_{max} - t)$. Subsequently, the reversed measurements are used as inputs for the impressed current sources $J_u(\boldsymbol{F}, t) = W(\boldsymbol{F}, t_{max} - t)$, where $u \in \{x, y, z\}$ is the polarisation of the receiver. Notice that the forward model must be evaluated only one time since the impressed sources J_u are excited simultaneously and not in a sequential manner like a typical B-scan.

This greatly reduces the computational time necessary for the backpropagation of the received signals. Similar to Kirchhoff migration, the velocity used in the RT migration is half the actual velocity in order to simulate the two-way travel time effectively. Using the revised velocity structure and the reversed current sources, the electric and the magnetic fields are back-propagated until the diffractions collapse to their origin at $\boldsymbol{E}(\boldsymbol{r}_m, t = 0)$ (Leuschen & Plumb, 2001).

In the proposed scheme, the fields are back-propagated using a second-order transverse magnetic finite-difference time-domain (TM-FDTD) (Yee, 1966; Taflove & Hagness, 2005). A 2D configuration is chosen in order to reduce the computational requirements further. A TM-FDTD consists of $\langle E_z, H_x, H_y \rangle$. Thus, the polarisation of the antenna is assumed to be parallel to the main axis of the tree and perpendicular to the curve of measurements T_0. Consequently, the revised impressed sources are implemented as z-polarized soft line-sources $J_z(\boldsymbol{F}, t) = W(\boldsymbol{F}, t_{max} - t)$ and the resulting migrated image equals with $Q(\boldsymbol{r}_m) = E_z(\boldsymbol{r}_m, 0)$.

RT migration using FDTD is subjected to large numerical errors due to the low velocities needed to be implemented (half the estimated velocity) (Taflove & Hagness, 2005). Numerical dispersion is proportional to the implemented permittivity (Taflove & Hagness, 2005) and can be reduced either through increasing the order of accuracy or decreasing the discretisation step (Kantartzis & Tsiboukis, 2005). To that extent, for all the case studies examined, a small discretisation step is chosen $\Delta x = \Delta y = 1\ mm$. and the time step Δt is calculated subject to the Courant stability conditions (Taflove & Hagness, 2005). Consequently, each A-Scan of $W(\boldsymbol{F}, t_{max} - t)$ is interpolated in time in order to be synchronised with the employed Δt. To repress boundary effects,

FDTD is effectively truncated using the time-synchronised convolutional perfectly matched layer (PML) (Giannakis & Giannopoulos, 2014) with ten-layer thickness.

4.2.1.3. Auto-focusing

Applying migration to dense measurements subject to an accurate estimation of the bulk permittivity should result in a sharp and focused image (Wei & Zhang, 2014). Therefore, there is an underlying relationship between the sharpness of the migrated image and the estimated velocity of the medium (Wei & Zhang, 2014). This rational is exploited in auto-focusing methods in which the migration is executed for a range of ε and the sharpness for each migrated image is then calculated. The permittivity that results in the most focused-sharp image is used to approximate the bulk permittivity of the host medium (Wei & Zhang, 2014).

Estimating the sharpness of an image is not a trivial task, and different focal criteria have been reported in the literature (Wei & Zhang, 2014). For the presented case studies, a scaled entropy coupled with Kirchhoff migration is proven an accurate and reliable criterion for estimating the bulk permittivity of the host medium. The scaled entropy is proportional to the sharpness of the image and is calculated via

$$F = \frac{maxQ(\boldsymbol{r}_m)}{\sum_{i=1}^{n} p_i log_2(p_i)} \tag{4.29}$$

where

- $\{p_i \in \mathbb{R} | p_i > 0 \; \forall i\}$ is the histogram values of the investigated image $Q(\boldsymbol{r}_m)$
- n is the total number of histograms $\boldsymbol{r}_m$

Before auto-focusing, the pre-processing step should be applied in order to remove unwanted clutter and ringing noise. The latter can give rise to artefacts that can compromise the accuracy and reliability of Equation (4.29).

Figure 31 illustrates how the estimated permittivity affects F in Equation (4.29). Two numerical studies are examined in which three low-dielectric targets with $\varepsilon = 2$ are incorporated in a homogeneous medium. In the first case, the permittivity of the medium is $\varepsilon = 7$ and in the second case $\varepsilon = 14$. A 2D-FDTD is used for the simulations with $\Delta x = \Delta y = 1\,mm$ and Δt follows the Courant stability condition (Taflove & Hagness, 2005). Circular measurements are taken every four degrees using a mono-static configuration with central frequency equals to 1500 MHz. The proposed detection scheme is applied to the raw data (pre-processing, migration, post-processing). The modified Kirchhoff migration is employed using different permittivity values varying in the range $\varepsilon \in [1,18]$ and the scaled entropy F is then calculated for each ε. From Figure 31 it is evident that the scaled entropy is maximized in the proximity of the actual permittivity supporting the validity of the proposed focal criterion (Equation (4.29)). The permittivity in the second example (Figure 31B) is slightly overestimated ($\varepsilon = 15$ instead of $\varepsilon = 14$) due to the numerical dispersion inherited in the FDTD-based synthetic data (Taflove & Hagness, 2005). Numerical dispersion is more dominant in low-velocity media, and thus it does not affect the first example (Figure 31A). From Figure 31 it is also apparent that apart from the main peak at $\varepsilon \approx 7$, there is a smaller one at $\varepsilon \approx 17$. The local maximum are model-dependent fluctuations resulting from the interpretation of multiple hyperbolas under a specific velocity background as part of one hyperbola in a different velocity medium. The suggested auto-focusing criterion is based on the global maximum and model-dependent fluctuations and local maximal should be ignored.

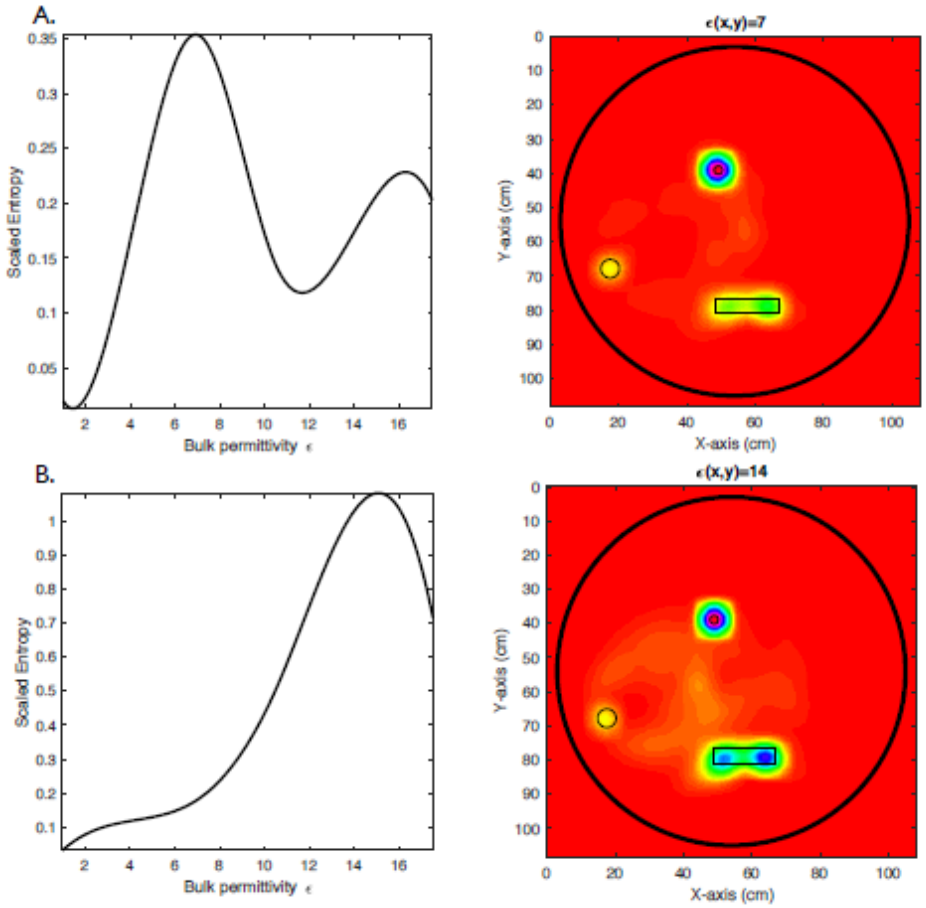

Figure 31: Two case studies used to illustrate the capabilities of the scaled entropy on estimating the bulk permittivity of the host medium. Three low dielectric targets ($\varepsilon = 2$) are buried in a homogeneous medium with A) $\varepsilon = 7$ and B) $\varepsilon = 14$. The targets are illustrated with solid black lines. The right images illustrate the migrated data using the velocities estimated based on the scaled entropy (Equation (4.29)). The left images show the scaled entropy (Equation (4.29)) calculated for different $\varepsilon \in [1, 18]$

4.2.2. Numerical Experiments

Trees are complex media with different shapes and sizes, as explained in Section 2.1.1. Regarding their dielectric properties, tree layers can be seen as two-phased materials consisted of water and foliage matter (Giannakis, et al., 2019; Broadhurst, 1970). Consequently, both bipolar relaxation mechanisms (from water) and dispersionless components (from dry foliage) are expected to be present within the trunk (Brown & Curry, 1982). In that context, a CRIM is suggested (Giannakis, et al., 2019), that estimates the complex bulk permittivity of the layers based on their volumetric water fraction. In order for the CRIM model to be compatible with FDTD,

the bulk permittivity is approximated with a single Debye pole (Giannakis, et al., 2019) using the hybrid optimization scheme proposed in Kelley, et al. (2007). The extended Debye media that are used to fit the resulting complex permittivity for each layer are shown in Table 4 (Section 4.1.2). Similar to Giannakis, et al. (2019), the water fraction and the resistivity for each layer are chosen such as to resemblance a saturated hardwood or a semi-dry softwood (Guyot, et al., 2013; Brazee, et al., 2010).

Two numerical case studies are examined in this section in order to assess the capabilities of the proposed approach (Figure 32). In both examples, two complex-shaped decay with different shapes and sizes are incorporated in the outer layers of the trunk. Circular measurements are taken every two degrees using a monostatic ideal Hertzian dipole with 1500 MHz central frequency. The simulations are executed using a TM-FDTD with $\Delta x = \Delta y = 1\ mm$ and $\Delta t = 2.357\ \mathrm{ps}$ (Courant limit (Taflove & Hagness, 2005)). The Debye poles are implemented using the polarization density method (Giannakis & Giannopoulos, 2014), and the boundaries of the grid are truncated using the semi-implicit PML (Giannakis & Giannopoulos, 2014).

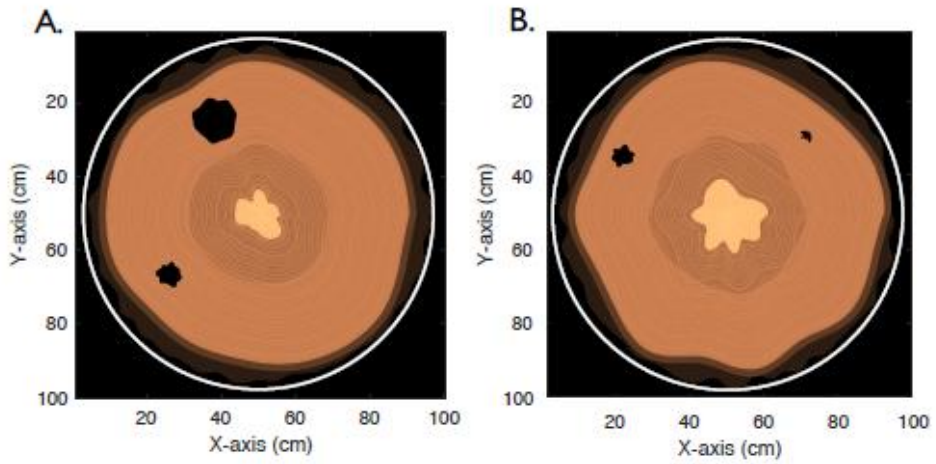

Figure 32: The simulated trees (A, B) represent generic semi-saturated hardwoods with both inner/outer sapwood and a dry heartwood at the centre. The decays are hollow complex-shaped voids with varying sizes placed within the outer sapwood. The shape of the bark does not deviate much from a circle, and therefore the measurements for the current case studies follow a circular configuration (white lines).

The first case study (Figure 32A) examines the capabilities of the proposed methodology on detecting prominent decay present on the outer sapwood. Before migration, a linear gain and an SVD filter are applied to the raw data (pre-processing step). The SVD filter is set to four eigenvalues. Using the proposed auto-focusing criterion (Equation (4.29)) for the permittivity range $\varepsilon = 1 - 26$, the bulk permittivity of the trunk has been estimated at the proximity of $\varepsilon \approx 17$ (Figure 33A). Based on that, the Kirchhoff migration has been applied assuming a homogeneous medium with $\varepsilon = 17$. The RT migration has the ability to incorporate any arbitrary permittivity distribution. Thus, the shape of the trunk is implemented in the model while keeping its interior homogeneous with $\varepsilon = 17$. Figure 34A illustrates the reconstructed internal structure of the trunk after migration and post-processing (squared and smoothed using Gaussian blur filter). It is evident that both the decay and the heartwood are accurately detected using the modified Kirchhoff migration. RT migration detects the investigated decay and sufficiently maps the heartwood and the inner sapwood. Nonetheless, the reconstructed image using RT migration is corrupted with clutter distributed in the outer layers of the trunk. The clutter is due to the unfiltered ringing noise and cross-coupling phenomena which do not seem to considerably affect the performance of the modified Kirchhoff migration (Figure 34A).

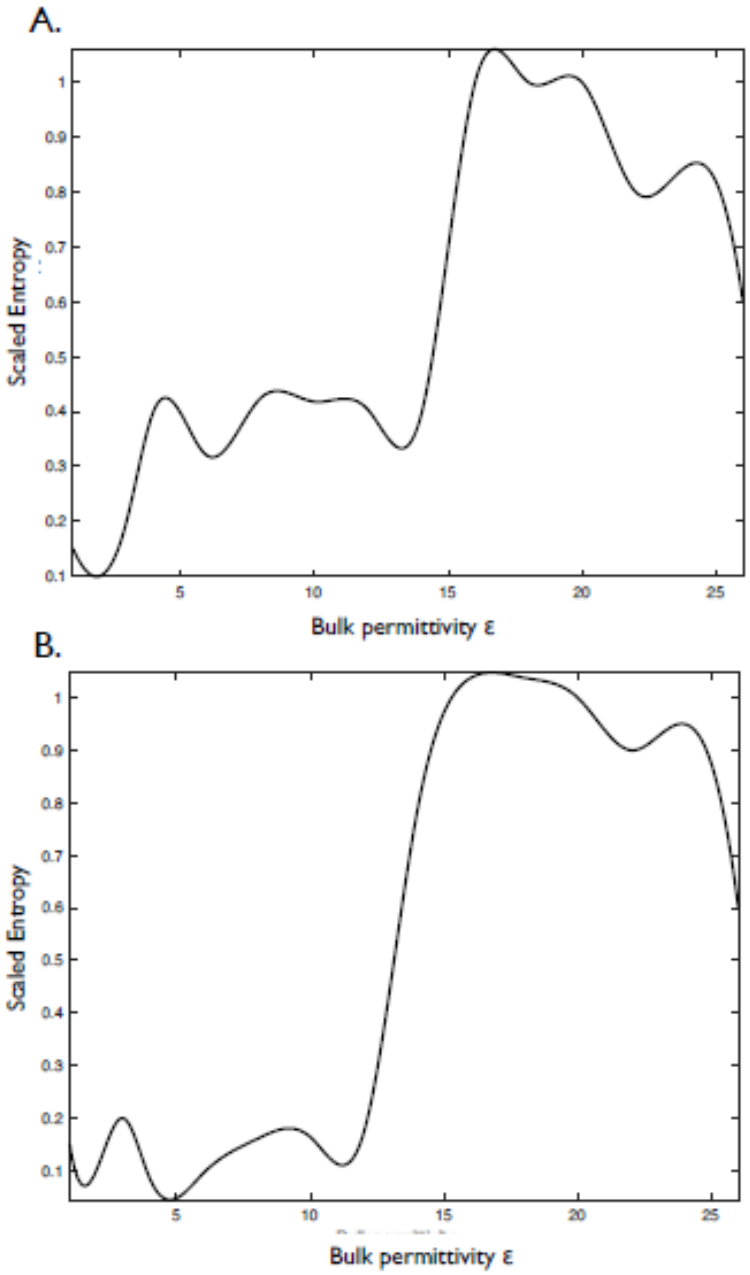

Figure 33: The scaled entropy for the two synthetic case studies illustrated in Figure 32. The global maximum for both of the tree samples occurs at $\varepsilon \approx 17$.

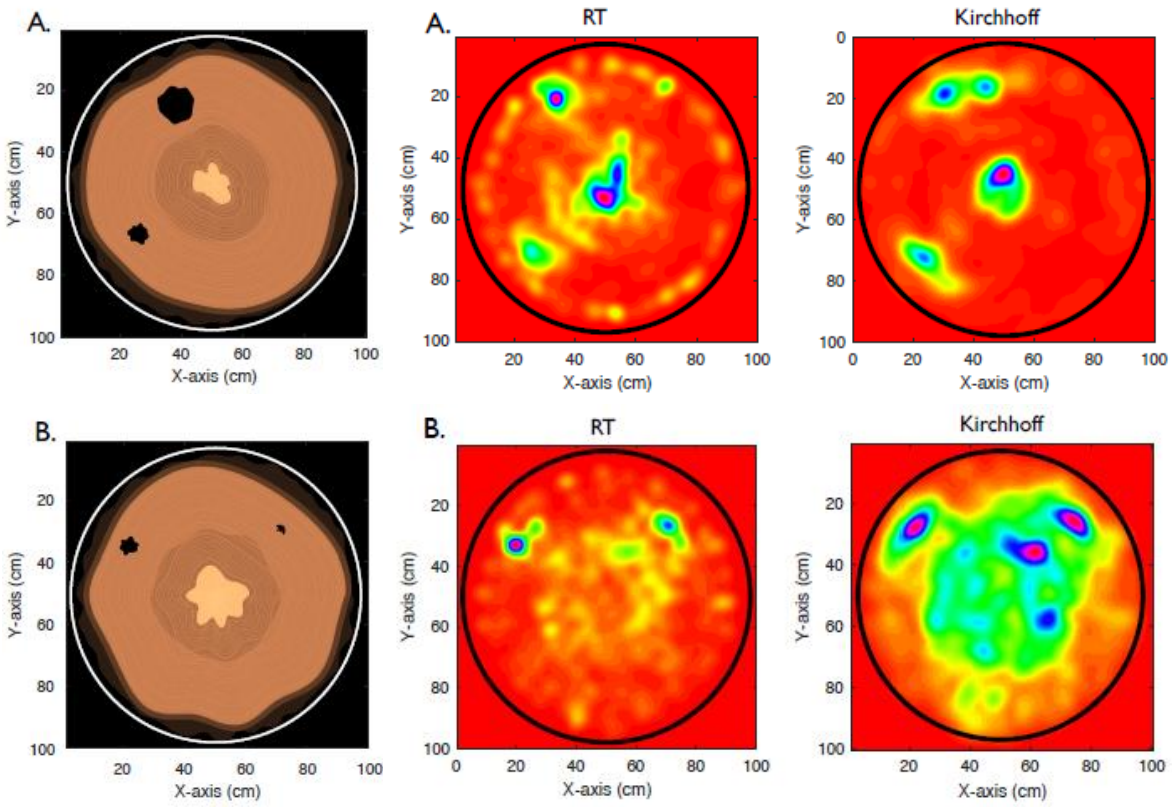

Figure 34: The reconstructed images using both the modified Kirchhoff and the RT migration for the case study A) and B) illustrated in Figure 32. The processing is based on circular measurements along the solid black lines.

The second case study (Figure 32B) investigates the ability of the current framework on detecting small decay as a manifestation of early stages of EIDs. Detecting early decay is particularly challenging due to the low signal-to-clutter ratio, making interpretation of Q_{r_m} problematic. In order to tackle this, an SVD filter is applied before migration removing the twelve most dominant eigenvalues. This exhaustive SVD approach should be applied with caution since it filters out large targets and spatially correlated reflections resulting from targets close to the centre of the trunk. Nonetheless, it is necessary for the investigated case study in order to further reduce ringing noise, enhance the weak reflections from early decay and increase the overall signal to clutter ratio. Similar to the first example, using the proposed autofocusing

criterion for the permittivity range $\varepsilon = 1 - 26$, the bulk permittivity of the tree is estimated at approximately $\varepsilon \approx 17$ (Figure 33B). Figure 34B illustrates the results using both the modified Kirchhoff and RT migration. Indications for the presence of two targets are given using both approaches. Nonetheless, it is evident that RT outperforms the modified Kirchhoff migration providing with a more detailed and precise reconstruction of the early decay.

4.2.3. Laboratory Case Study

The proposed methodology is now tested on real measurements collected at The Lord Faringdon Centre at the University of West London (UWL). The two investigated trees are shown in Figure 35.

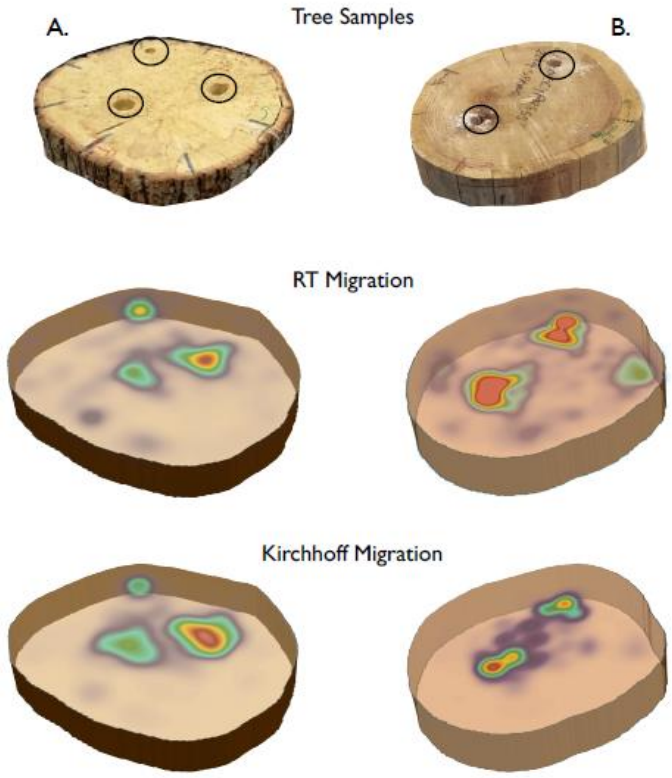

Figure 35: The investigated tree samples and their reconstructed internal structure using the modified Kirchhoff and RT migration. The circumference of both tree samples is approximately $\approx 0.35 - 0.45\ m$. Circles indicate the positions of the artificially drilled decay. The decays are filled with saturated sawdust to simulate the liquid-filled chambers present in AOD-infected trees (Giannakis, et al., 2019).

The tree samples have approximately the same size (diameter $\approx 0.35 - 0.45\,m$) and contain artificially created decays. These were filled with saturated sawdust in an effort to simulate liquid-filled chambers, a typical symptom of AOD (Giannakis, et al., 2019). All the artificially created decay extend parallel to the main axis of the trunks and orthogonal to the curve of acquisition (T_0). Circular measurements were taken using the Aladdin 2000 MHz hand-held antenna from IDS Georadar (Part of Hexagon). Aladdin is a commercial dual-polarised antenna that utilizes a wheel-based measuring device to position each A-scan. Therefore, an arc parameterisation was used for positioning each A-scan on the irregular T_0. The resulting scattering field from a cylindrical target is maximised when the main axis of the cylinder is aligned with the polarisation of the antenna (Radzevicius & Daniels, 2000). Therefore, in an effort to maximise the overall signal, the antenna polarisation chosen for the investigated case studies was perpendicular to T_0 and parallel to the artificial decay. The raw data were subjected to time-zero correction, zero-offset removal, linear-gain and an SVD filter (pre-processing step). The SVD filter was set to two dominant eigenvalues. Figure 36 illustrates the raw and processed data for the investigated case studies. In order to further enhance the post-migrated signal and facilitate interpretation, the reconstructed $Q_{\boldsymbol{r}_m}$ is squared and smoothed using a Gaussian blur filter (postprocessing step).

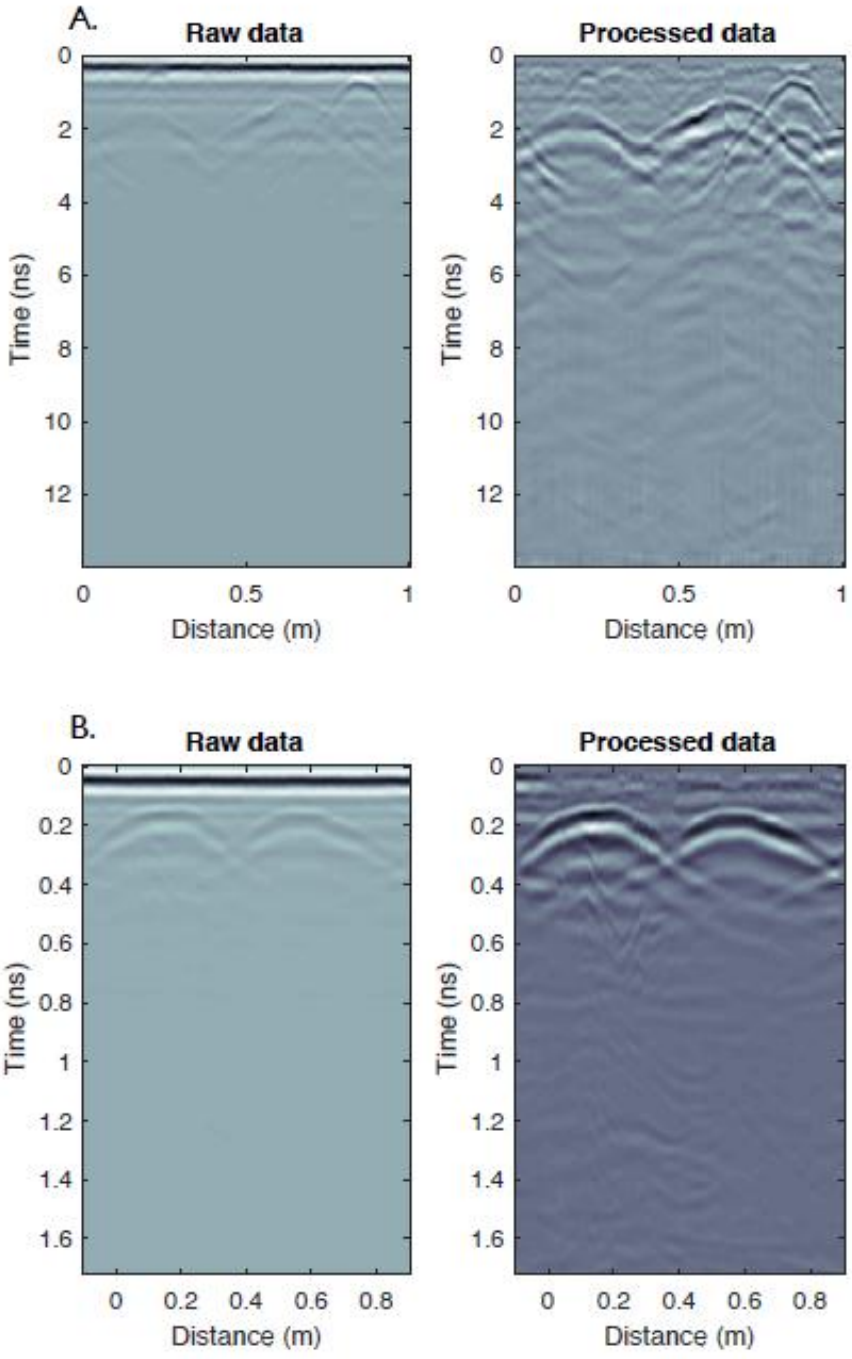

Figure 36: The raw and processed data for the tree samples (A, B) illustrated in Figure 5. The processing method consists of zero-time removal, zero-offset removal, linear gain and SVD filter removing the two dominant eigenvalues.

The tree sample used for the first case study is shown in Figure 35A. A decay with 0.02 m diameter and two decay with 0.04 m diameter were drilled. For the second case study (Figure 35B), two cylindrical holes were drilled with a diameter of 0.03 m. The tree samples were relatively dry, and the bulk permittivities (estimated using the

suggested auto-focussing criterion for the range $\varepsilon = 1 - 10$) are $\varepsilon = 3.5$ and $\varepsilon = 4$ for the first (A) and the second (B) sample respectively (Figure 37).

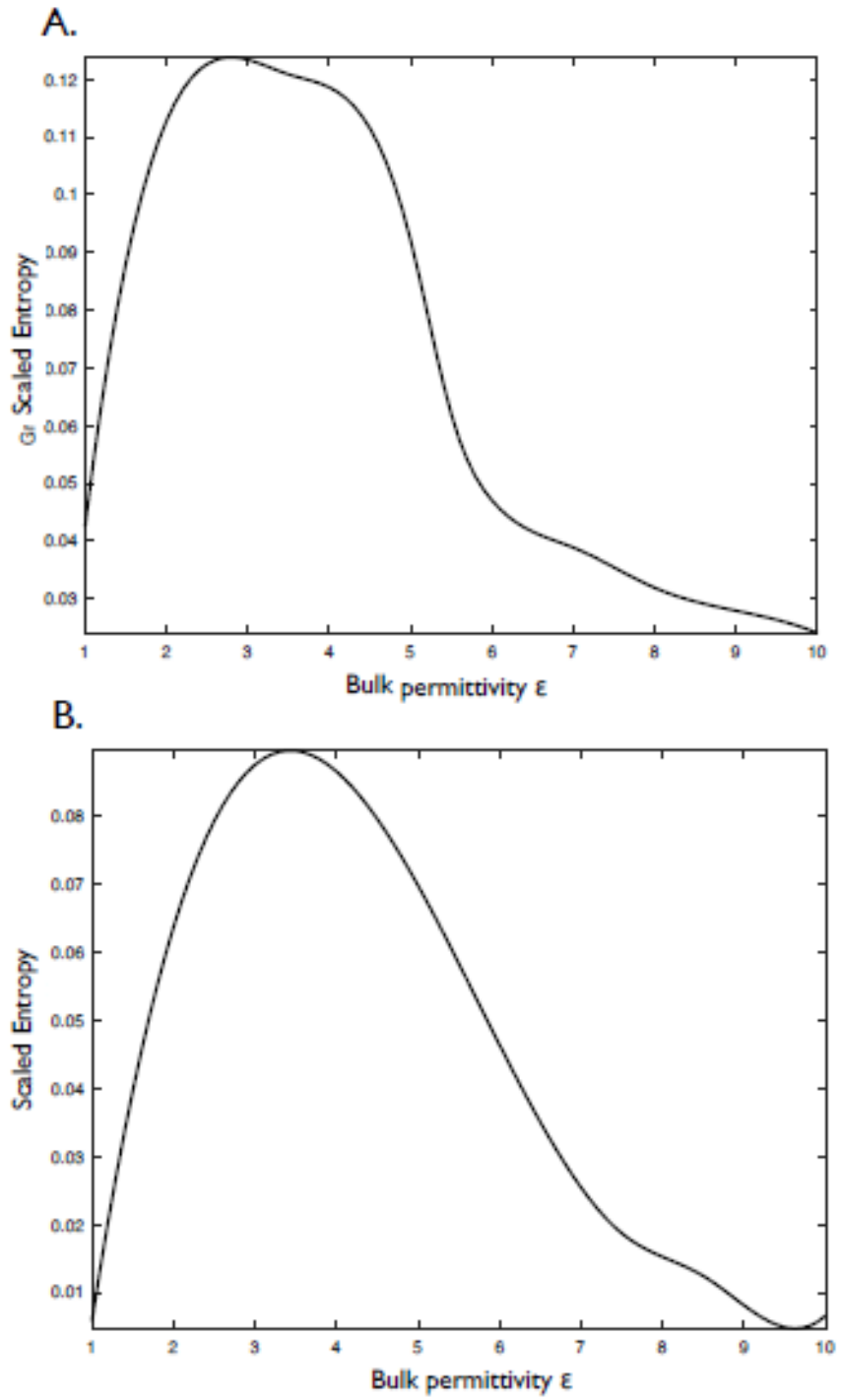

Figure 37: The scaled entropy for the two tree samples illustrated in Figure 35. The global maximum occurs at $\varepsilon \approx 3$ and $\varepsilon \approx 3.5$ for the A and B sample respectively.

Figure 35 shows the reconstructed decay using both RT and the modified Kirchhoff migration. It is evident that the suggested detection scheme manages to adequately reconstruct the artificial decay in a clear, efficient and semi-automatic manner. Clutter is sufficiently repressed, and both large and early decays are clearly detectable. Similar to the numerical experiments discussed in the previous section, the modified Kirchhoff migration is not affected by the remaining ringing noise while RT migration produces minor artefacts near the surface of the trunk.

4.2.4. Field Case Study

The proposed detection scheme is now tested in a real-field case study from a diseased tree located at Gunnersbury Park, London, UK (Figure 38). The employed antenna for this experiment was the dual-polarised hand-held antenna Aladdin from IDS GeoRadar (Part of Hexagon). The central frequency of Aladdin is 2000 MHz, the time-step equals to $dt = 6.25e - 11\ s$ and the spatial step of the measuring wheel is $\Delta = 0.01\ m$. Circular scans were collected every 0.05 m along the main axis of the tree and parallel to the ground. The overall scanned area is 1.35 m long and consists of 27 parallel circular scans. The inspected area has a semi-cylindrical shape with a varying circumference. The circumference of each section was accurately estimated and subsequently incorporated into the detection scheme by means of the measuring-wheel device attached to the antenna.

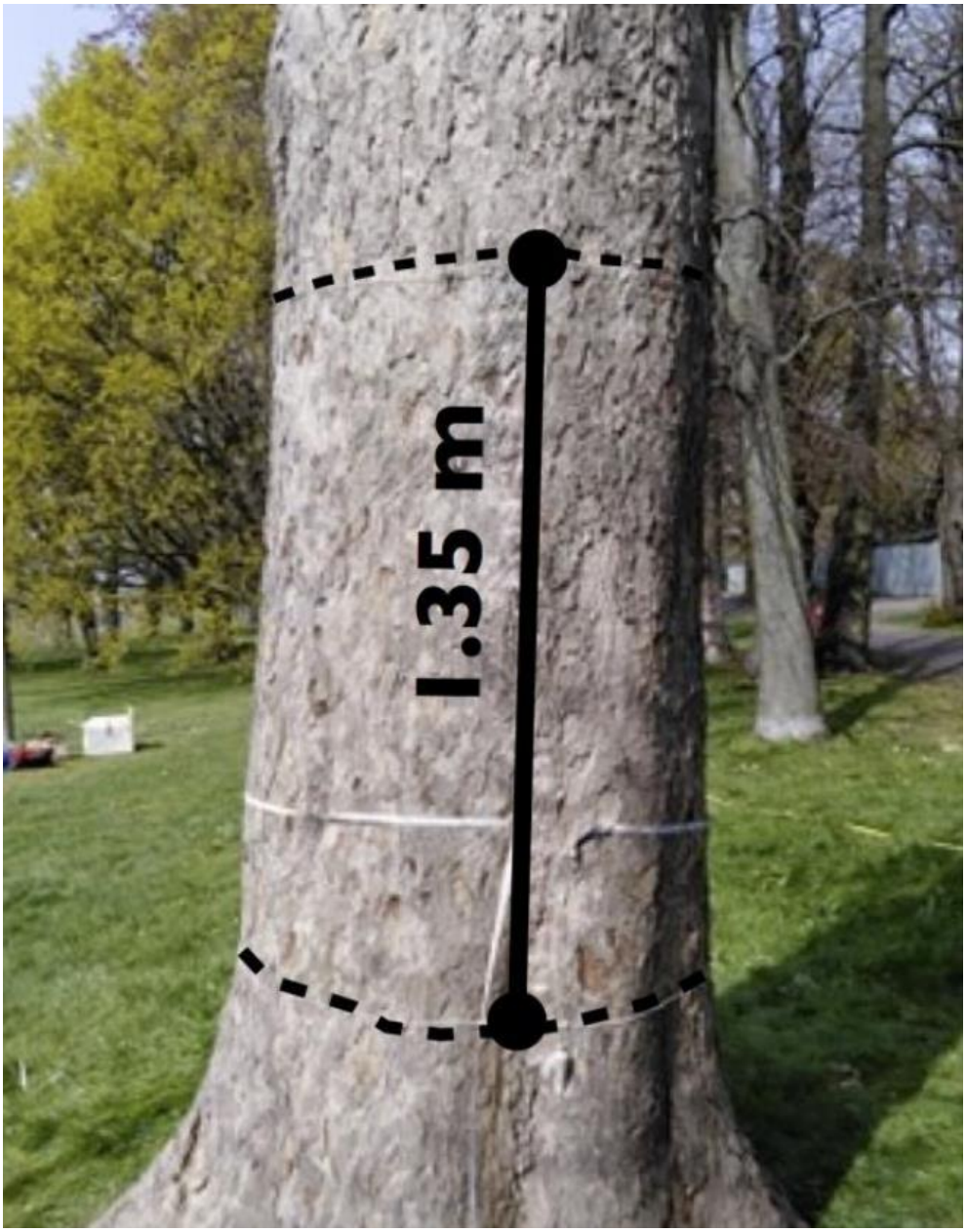

Figure 38: The investigated tree at Gunnersbury Park, London, UK. The scanned area is highlighted between the dotted lines.

Prior to the measurements, the bulk permittivity of the trunk was estimated at $\varepsilon \approx 30$. The permittivity was calculated based on the two-way travel time needed for the wave to travel from one side of the trunk to the other. The permittivity measurements were conducted using the 1000 MHz horn antenna system from IDS GeoRadar (Part of Hexagon). The high-directivity of the horn antenna made it possible to get a clear

reflection from the back of the trunk. To further enhance the signal, a PEC sheet was attached to the tree.

After the completion of the measurements, the tree was torn down (Figure 39) and cut into several slices in an effort to get an insight into its internal structure. From Figure 40, a dominant decay extending along the main axis of the trunk is clearly visible. The decay has an irregular shape and a sharp transition from the healthy sapwood. The diameter of the decay is approximately ~ 0.60 m and does not show any dominant increasing or decreasing trend along the trunk.

Figure 39: The investigated tree was torn down after the completion of the measurements in order to get an insight on its internal structure.

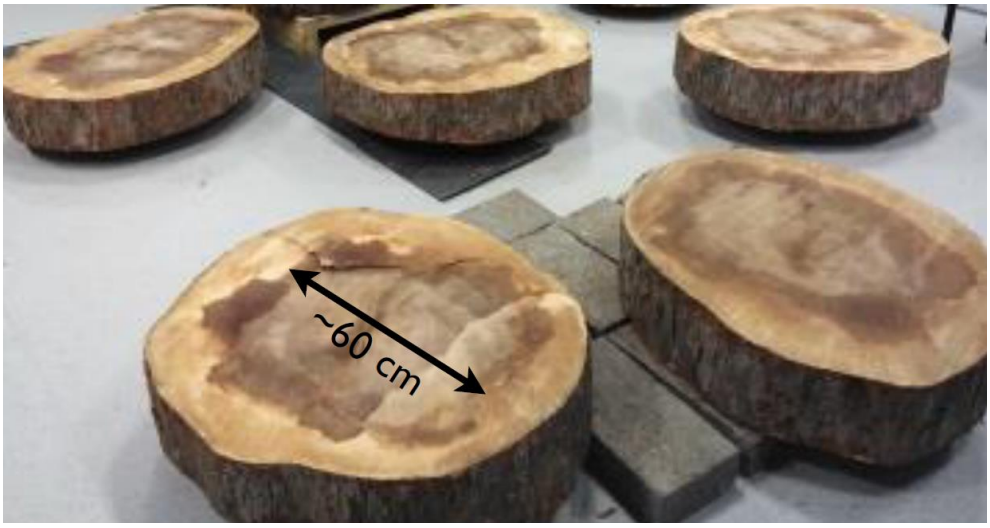

Figure 40: Slices collected from the investigated tree shown in Figure 38. A dominant decay (with a diameter of approximately ~60 cm) extending along the main axis of the trunk is clearly visible.

Figure 41 illustrates the reconstructed image using the methodology described in Section 4.2.1. Every B-scan is initially processed using a time-zero correction, a zero-offset removal, a linear gain and an SVD filter (five dominant eigenvalues are filtered out). Subsequently, an RT migration (Section 4.2.1.2) is applied to each processed B-scan subject to a homogenous medium with $\varepsilon = 30$. The migrated images are furthermore squared and smoothed using a Gaussian blur filter (kernel size equals to 30 and $\sigma = 15$). The resulting 2D images are then combined to create a pseudo-3D model of the trunk. From Figure 41, it is apparent that there is clear evidence of a major feature at the centre of the trunk extending along its main axis. This is in good agreement with the actual structure of the tree, shown in Figure 40. A reconstructed slice of the tree and its corresponding processed B-scan are shown in Figure 42. The shape and size of the decay are adequately recovered. Discrepancies between the actual and the predicted shape are due to local variations of permittivity within the trunk that deviate from the assumption of a homogenous medium with $\varepsilon = 30$.

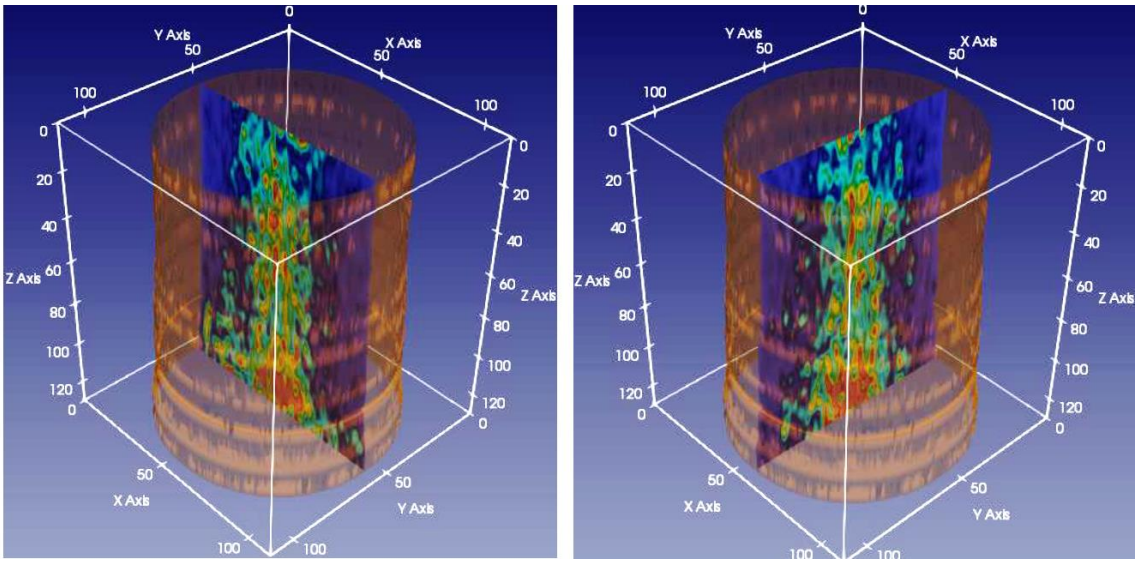

Figure 41: The reconstructed internal structure of the scanned area shown in Figure 38 using the processing scheme discussed in Section 4.2.1. The axes are in cm.

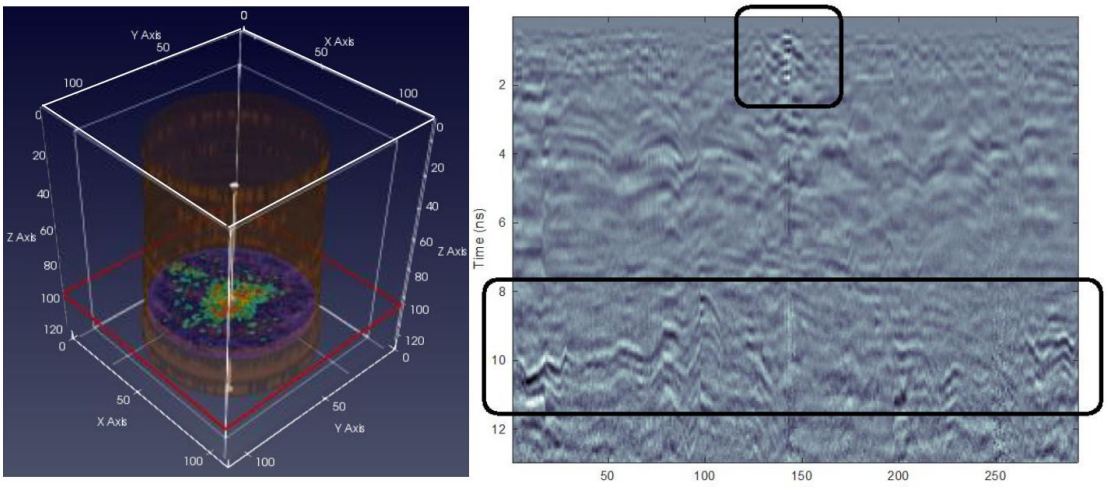

Figure 42: reconstructed slice (left) and its corresponding processed B-Scan (right). Two main decays are apparent, one shallow with small size and one bigger one at the centre of the trunk. The reflections of the two decays are highlighted within the black boxes.

4.2.5. Conclusions

Through numerical and laboratory experiments, the premise that GPR has the potential to become a coherent tool for early detection of tree decay as a manifestation of EIDs has been supported. A novel processing scheme is described that uses a scaled Kirchhoff and a RT migration in order to effectively evaluate the internal structure of the tree subject to a homogeneous velocity. The latter is estimated using a modified focal criterion that calculates the bulk permittivity based on the sharpness of the migrated image. The proposed framework can be applied in a straightforward manner using any commercial GPR system with minimum computational and operational requirements in the field. This makes it particularly appealing for large-scale forestry applications and is a step forward to the commercialisation of GPR as a diagnostic tool against EIDs.

This research line addresses the following objectives of the present Thesis (see Section 3.1):

- *to develop novel survey methodologies for tree trunk assessment:* in this research, the effectiveness of examining tree trunks using circular scans is

investigated. Results have shown the viability of the proposed technique. The objective is, therefore, achieved.

- *to develop numerical simulations and modelling of trunk decays:* the proposed methodology was tested using numerical simulations for different scenarios. Results have helped to refine the proposed technique, showing that the method is capable of recovering both the position and the size of the decay accurately. This objective is, therefore, achieved.

4.3. Application of microwave tomography for detection of decays and cavities in tree trunks

The studies described in the previous paragraphs have shown that GPR is an effective non-invasive tool, capable of generating information about the inner structure of tree trunks in terms of existence, location, and geometry of defects. Nevertheless, it has been shown how the cylinder-like shape of tree trunks creates challenges with the use of traditional GPR data processing techniques.

In an attempt to overcome these difficulties, a microwave tomographic approach is presented, for improved GPR data processing to detect and characterise the geometry of decay and cavities in trees. Microwave imaging of cylindrical objects has been widely employed for biomedical applications (Pastorino, 2010), using inversion schemes primarily based on linear approximations of the scattering phenomenon (Miao & Kosmas, 2017; Leucci, et al., 2011). Further application examples of these methods are found in other cylinder-like objects, such as columns (Leucci, et al., 2011) and tunnel imaging (Monte, et al., 2009).

The microwave tomographic approach is able to pinpoint the position of the measurement points on the tree surface explicitly and thus to consider the actual geometry of the sections beyond the circular ones. The robustness of the microwave tomographic approach with respect to noise and data uncertainty is tackled by exploiting a regularised scheme in the inversion process based on the Truncated Singular Value Decomposition (TSVD). A demonstration of the potential of the microwave tomography approach is provided for both simulated data and measurements collected in controlled conditions.

4.3.1. Methodology

4.3.1.1. Data Pre-Processing

In relation to the results presented in this Chapter, the raw data were collected in the time domain, whereas the input data to the inverse scattering approach were given in the frequency domain. In view of this, a pre-processing stage was necessary in order to achieve the appropriate input data such that the inverse scattering approach could be applied. The pre-processing consists of the following operations:

- *Zero timing*: This step consisted of cutting the first part of the signal, up to the flat-like reflection of the air–tree interface. Specifically, the zero time of the radargram was fixed in correspondence of the first peak of the radar signal, which was assumed as coincident with the location of the air–tree interface.
- *Time-gating*: This procedure consisted of selecting the observation time window wherein the useful portion of the signal was expected to occur. Since the time of flight is related to the target depth, the time gating allowed analysis of only the portion of the radargram corresponding to the depth range of interest, which was fixed by the maximum radius of the tree cross-section. Note that the lower boundary of the time-gating window could be selected as larger than the time zero in order to perform a more severe filtering of the first strong reflections coming from the air–tree interface.
- *Background removal* (see Paragraph 2.4.5.5): This operation consisted of replacing every single A-scan of the radargram with the difference between the single A-scan value and the average value of all the A-scans in the radargram. The background removal eliminated all the flat interfaces in the data (including

the air–tree interface, only partially removed by the application of the zero timing) and usually allowed the provision of a clearer image of the scene.

- *Time-varying gain* (see Paragraph 2.4.5.4): Deeper targets scatter a signal lower than shallower targets. In order to compensate this effect, a gain variable versus the depth distance is applied to the raw data.
- *Fourier transform*: The time-domain filtered raw data are converted into the frequency domain in order to be processed according to the microwave tomography approach. No window functions have been applied to the time domain pre-processed data before conversion into frequency domain data.

4.3.1.2. Formulation of the Tomographic Inversion Approach

The microwave tomographic approach exploits a linearised model of the EM scattering based on the Born Approximation (BA) (Soldovieri & Solimene, 2010; Solimene, et al., 2014). It is known that BA allows achieving a quantitative reconstruction only in the case of anomalies that are weak scatterers compared to the host medium. On the other hand, when the assumption of weak scattering is removed, solving an inverse scattering problem based on BA still allows reliable information to be gained about the presence, location and shape of potential targets (Soldovieri & Solimene, 2010; Persico, 2014; Solimene, et al., 2014).

A 2D scenario showing the cross-section of a tree trunk at a fixed height is considered in Figure 43. The investigation domain D corresponds to the trunk section with a constant relative dielectric permittivity ε.

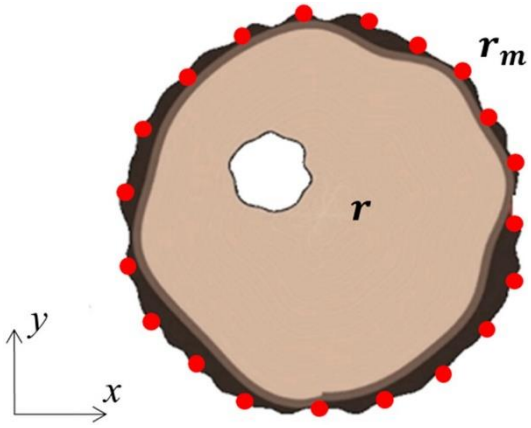

Figure 43: Geometry of a tree cross-section with an arbitrary shape. The red circles represent the Ground Penetrating Radar (GPR) measurement points along the outer surface of the bark; the white object is a randomly positioned target within the cross-section.

The scattering phenomenon is activated by a source modelled as a filamentary current polarised along the y axis (TM polarisation) and radiating an EM signal. The $exp(j\omega t)$ time dependence is assumed, with $\omega = 2\pi f$ being the angular frequency and f belonging to the frequency range $[f_{min}, f_{max}]$. The source and the measurement points $\boldsymbol{r}_m$, i.e., the location where the scattered field is collected, are located at the boundary of the probed area. Accordingly, the scattering model is defined under a multi-monostatic/multi-frequency measurement configuration. A generic point in D is denoted with r and $\chi = \frac{\varepsilon}{\varepsilon_b} - 1$ is the contrast function accounting for the presence of targets, which is modelled as a variation of the permittivity with respect to the known permittivity of the investigated medium.

For each measurement point $\boldsymbol{r}_m$ and angular frequency ω, the scattering phenomenon under the BA is described by the linear integral equation as follows:

$$E_s(\omega, \boldsymbol{r}_m) = k_b^2 \iint_D g_e(\boldsymbol{r}_m, \boldsymbol{r}, \omega) E_{inc}(\boldsymbol{r}, \boldsymbol{r}_m, \omega) \chi(\boldsymbol{r}) d\boldsymbol{r} = L(\chi) \qquad (4.22)$$

Where k_b is the wavenumber in D. Equation (4.22) expresses the field E_s scattered by the target (measured data) as radiated by the equivalent "source" defined by the

product between the unknown contrast function χ and the incident field E_{inc} in D, which is the field in the absence of targets. The quantity g_e is the "external" Green's function that accounts for the field generated at $\boldsymbol{r}_m$ by the elementary source located at $\boldsymbol{r}$. The scattering model underlying the inversion model considered in this work is based on the assumption that the radar signal propagation occurs in a homogenous medium. Such an assumption allows to simplify considerably the computation of the scattering operator L as the Green's function is available in closed form, i.e.:

$$g_e(\boldsymbol{r}_m, \boldsymbol{r}, \omega) = \frac{j}{4} H_0^{(2)}(k_b|\boldsymbol{r}_m - \boldsymbol{r}|) \tag{4.23}$$

Where $H_0^{(2)}$ is the Hankel function of the second kind and zero order.

It is noteworthy to emphasise that, as far as a qualitative image of the scene has to be achieved and the GPR data are collected at the air–tree interface, the homogenous medium assumption provides quite reliable results with a relatively low computation effort. On the other hand, more complicated layered models could be in principle adopted, although this would require the use of a priori information about the inner structure of the trunk, which is not available for the on-field surveys. The kernel of the linear radiation operator L is equal to the product between the external Green's function g_e and the incident field E_{inc}. The operator L directly relates the unknown contrast function to the scattered field. Therefore, the reconstruction of the contrast function is carried out through the inversion of Equation (4.22), that is an ill-posed linear inverse problem (Solimene, et al., 2014). Indeed, L is a compact operator, and this entails that a solution of the problem may not exist and does not depend continuously on the data, as deeply discussed in Bertero & Boccacci (1998). From a practical point of view, due to the inherent noise in the data, only a limited

representation accuracy of the scenario under investigation can be obtained. The lack of existence and stability of a solution can be remedied by introducing a regularisation scheme (Bertero & Boccacci, 1998; Persico, et al., 2005). However, the necessity to regularise the inverse problem introduces the use of a spatial filtering of the retrievable components of the unknown (Solimene, et al., 2014; Persico, et al., 2005). The regularisation of the inverse problem is herein carried out by resorting to the TSVD tool. Following the discretisation of Equation (4.22), the imaging task amounts to solving the matrix inverse problem:

$$\boldsymbol{E}_s = \boldsymbol{L}\boldsymbol{\chi} \tag{4.24}$$

where $\boldsymbol{E}_s$ is the $K = M \times F$ dimensional data vector, M being the number of spatial measurement points and F the number of frequencies, $\boldsymbol{\chi}$ is the N_p dimensional unknown vector, N_p being the number of pixels in D, and $\boldsymbol{L}$ is the $K \times N_p$ dimensional matrix obtained by discretising the integral operator in Equation (4.22). Since the matrix $\boldsymbol{L}$ stems from the discretisation of an ill-posed integral equation, the inversion of this matrix is an ill-conditioned problem, which means that the solution is very sensitive to measurement uncertainties and data noise. Hence, the TSVD scheme, as expressed in Equation (4.24), can be applied as a regularisation scheme in order to obtain a robust and physically meaningful solution:

$$\widetilde{\boldsymbol{\chi}} = \sum_{n=1}^{H} \frac{\langle \boldsymbol{E}_s, \boldsymbol{u}_n \rangle}{\sigma_n} \boldsymbol{v}_n \tag{4.25}$$

In Equation (4.25), $\langle , \rangle$ denotes the scalar product in the data space, H is a truncation index, $\{\sigma_n\}_{n=1}^{Q}$ is the set of singular values of the matrix $\boldsymbol{L}$ ordered in a decreasing way, $\{\boldsymbol{u}_n\}_{n=1}^{Q}$ and $\{\boldsymbol{v}_n\}_{n=1}^{Q}$are the sets of the singular vectors in the data and the unknown

spaces, respectively. The index $\{H \leq Q | Q = min(K, N_p)\}$ defines the "degree of regularisation" of the solution and is set in order to find a trade-off between the accuracy and the spatial resolution on one side (tending to increase H) and the solution stability on the other side (tending to reduce H).

The imaging result is a spatial map corresponding to the modulus of the retrieved contrast vector $\tilde{\chi}$ normalised to its maximum value in the scenario. Hence, the regions of *D* where the modulus of $\tilde{\chi}$ are significantly different from zero are representative of the position and geometry of the targets.

4.3.2. Numerical Experiments

Numerical simulations were carried out for three different scenarios:

- A circular softwood tree trunk (a homogeneous tree trunk without a dielectric discontinuity at the heartwood component)
- a circular hardwood tree trunk (where an inner core is present)
- a complex-shaped hardwood tree trunk

The gprMax numerical simulator package was used for this purpose (Warren, et al., 2016). Measurements data were generated every 0.15 m clockwise along the surface of the trunk in a 3D FDTD grid. The spatial discretisation step of the problem was fixed at $\Delta = 2\,mm$ and the time step at $\Delta t = 3.84\,ps$ (Courant limit). Regarding the excitation, a modelled equivalent of the GSSI 1500 MHz signal, was used (Giannakis, et al., 2018).

In regard to the softwood tree scenario, the target is a hollow segment with an approximately circular shape. The simulation layout and the starting point of measurements are shown in Figure 44. In the hardwood tree scenario (Figure 45), it

was considered that the section is usually drier than sapwood and provides overall non-homogeneous conditions for the propagation of the EM signal. The target is a hollow segment with an approximately circular shape and half of the dimensions of the previous target. The layout of the simulation and the starting point of the measurements relevant to the complex-shaped hardwood trunk scenario are shown in Figure 46.

It is worth mentioning that the numerical models of the trees above described are characterised by a spatially varying dielectric constant (see Table 4) to account for the layered structure of a tree section. Differently, for the purpose of the inversion process, the dielectric permittivity is assumed as spatially constant in the trunk section and its value is estimated considering the two-way travel time of the reflection from the opposite side of the trunk.

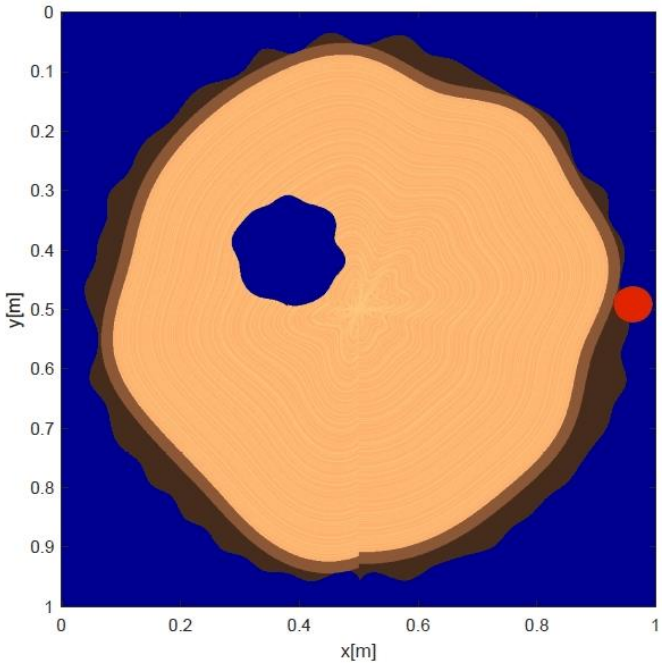

Figure 44: The circular softwood trunk scenario investigated using FDTD numerical modelling. The starting point of the measurements, taken clockwise, is represented by the red circle.

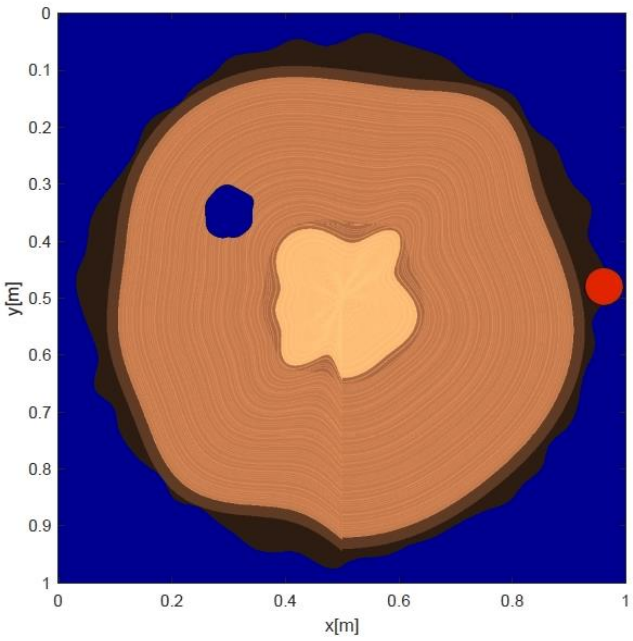

Figure 45: The circular hardwood trunk scenario investigated using FDTD numerical modelling. The starting point of the measurements, taken clockwise, is represented by the red circle.

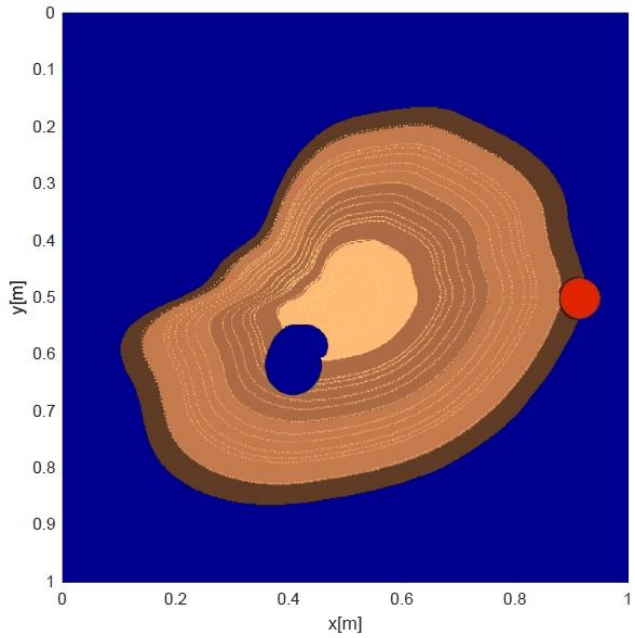

Figure 46: The complex-shaped hardwood trunk scenario investigated using FDTD numerical modelling. The starting point of the measurements, taken clockwise, is represented by the red circle.

4.3.3. Laboratory Case Study

The real data presented in this work were collected from a dead oak tree at The Faringdon Centre - Non-Destructive Testing Centre, University of West London (UWL). Three holes were drilled and subsequently filled with sawdust mixed with

water, in order to simulate rotting spots within the trunk cross-section. The 2000 MHz Aladdin hand-held antenna system, manufactured by IDS GeoRadar (Part of Hexagon), was used for testing purposes. Measurements were collected every 0.01 m counter-clockwise using the measuring wheel adapted to the antenna with a time-step $\Delta t = 7.8125\ ps$ along the trace. Figure 47 shows a picture of the investigated tree trunk. It is important to mention that the acquisition time required for a single 2D scan encircling the trunk (i.e., neglecting the time required for setting up the radar and the actual scanning line(s) along the trunk circumference) was approximately 30 seconds.

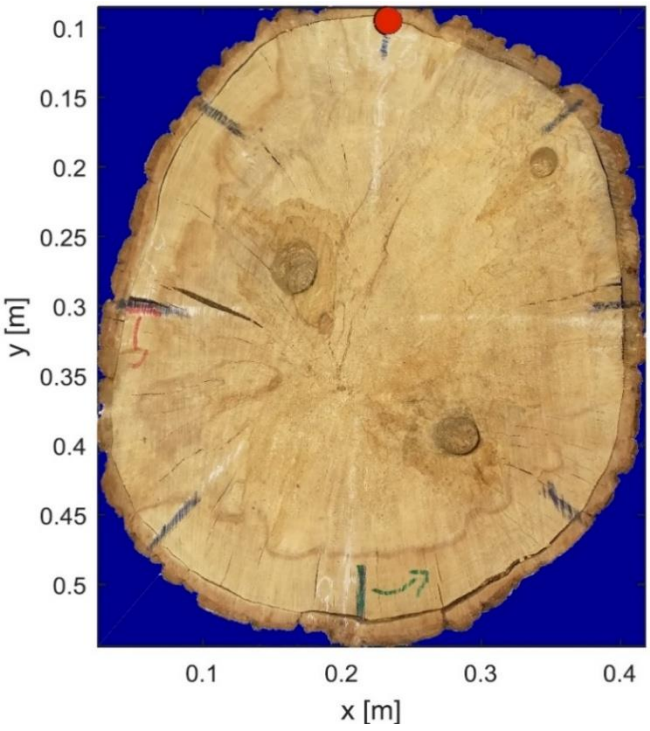

Figure 47: The oak tree trunk investigated at The Faringdon Centre – Non-Destructive Testing Centre, University of West London (UWL), UK. Measurements were taken counter-clockwise and the red circle denotes the starting point.

4.3.4. Field Case Study

The survey was performed at Gunnersbury Park, Ealing, London (United Kingdom) (Figure 48). The investigated sycamore (*Acer Pseudoplatanus*) tree was selected under the advice of the London Borough of Ealing's Tree Service. This tree was

located along a tree-lined avenue inside the park, approximately 10 m distant from the adjacent trees.

Figure 48: Test site location at Gunnesbury Park, London, UK. Overview of the area (a) and aerial view of the investigated tree (b).

As reported by the registered charity "Friends of Gunnersbury Park and Museum" (Friends of Gunnersbury Park and Museum, 2010), the investigated tree is monitored since 2010, when a large cavity was found in the stem. Over the last decade, the tree conditions have deteriorated, as increasing rotting and decay have been reported. This had created safety concerns to the public and, hence, it was decided to cut the tree. The GPR survey was planned before the scheduled tree felling in order to collect

reference information on the trunk internal structure, including the scale of the hollow and the thickness of the sapwood layer. In this way, the effectiveness of the GPR equipment and the viability of the proposed processing framework was assessed by comparing the reconstructed images with the evidence from the actual tree cross-sections.

The Aladdin 2000 MHz hand-held antenna system, manufactured by IDS GeoRadar (Part of Hexagon), was deployed for testing purposes. The radargrams were collected with a time-step equal to $\Delta t = 6.25 \cdot 10 - 11\ \mathrm{s}$ and a spatial step $\Delta s = 0.01\ \mathrm{m}$ between the traces. The survey methodology was based on pseudo-circular perimetric GPR acquisitions. Each measurement was accurately positioned based on the distance (calculated using the wheel encoder attached to the antenna) from a given reference starting point, using an arc-length parameterisation approach, as described in Giannakis, et al. (2019).

A number of 14 scans encircling the tree were performed parallel to the ground, spaced 0.10 m each to one another. Therefore, the investigated area was a “cylinder” of 1.30 m height (Figure 49). The first scan was taken at the bottom of the tree ($h = 0\ m$), whereas the final scan was collected at $h = 1.30\ m$. The average radius of the circle approximating the contour of the tree across the investigated section was estimated to be equal to 0.63 m.

Figure 49: GPR measurement layout around the investigated tree.

Following the GPR survey, the tree was cut and the investigated section was cut into ~0.20 m thick slices, which were subsequently used for the validation of the GPR reconstructed images.

4.3.5. Results

4.3.5.1. Numerical simulations

4.3.5.1.1. Circular Softwood tree

The raw data were pre-processed by setting the zero-time of the radar at 1 ns. Time-gating was applied up to 2 ns and was followed by a background removal operation. Figure 50 shows a comparison between raw (Figure 50a) and pre-processed (Figure 50b) data. The presence of the anomaly is identified in the processed data output as a hyperbolic feature located in the right part of the radargram, at a two-way travel time value of about 7 ns.

The microwave tomographic approach was applied on gated data by considering a working frequency band of 800–1800 MHz sampled with 21 frequencies spaced by 50 MHz. The relative permittivity of the trunk was assumed equal to 17. Note that such a value of permittivity can be regarded as equivalent to the permittivity of a real trunk in a relatively dry environment known to be an inhomogeneous medium consisting of several layers with different EM properties. The investigation domain was discretised into square pixels with 2.5 mm side. The choice of the TSVD is performed by the analysis of the curve of singular values. This was realised by neglecting the singular values below the knee of the curve, where the exponential decay takes place. Therefore, it was decided to truncate the singular values at a threshold of –25 dB with respect to the maximum singular value.

As shown in Figure 51a, a number of internal reflections are observed in correspondence of the real target location, whereas stronger reflections are present near the surface of the trunk. In order to assess the potentiality of the method in reconstructing the circle-like anomaly only, a more severe time-gating up to 6 ns was

applied. The reconstruction results displayed in Figure 51b demonstrate the capability of the tomographic approach for this purpose; in fact, the method is able to locate the defect with good accuracy and in a robust way.

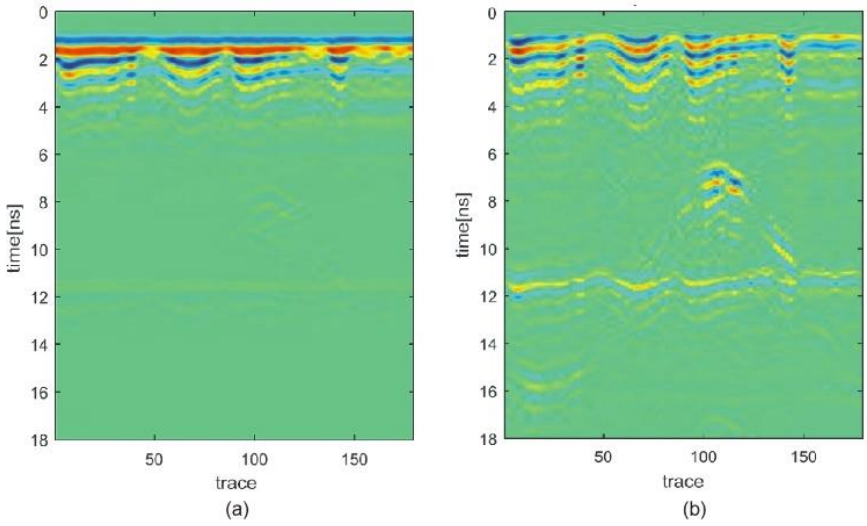

Figure 50: Radargrams of the simulations for the softwood tree scenario. (a) Raw radargram; (b) processed radargram after the application of the pre-processing stage.

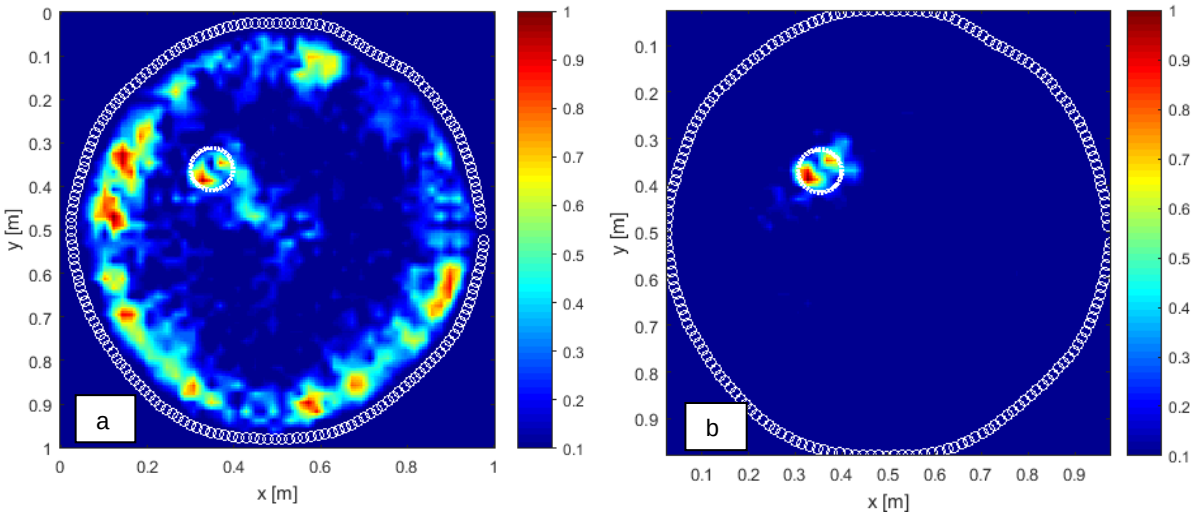

Figure 51: Tomographic reconstruction of the softwood scenario with time-gating a) up to 2 ns, and b) up to 6 ns. The dashed white circle indicates the actual position of the anomaly. The circles in solid white line along the trunk perimeter represent the positions of the measurement points. The colour scale represents the amplitude of the reconstructed contrast function normalised with respect to its maximum in the investigation domain.

4.3.5.1.2. Circular Hardwood Tree

The same preprocessing and reconstruction procedures were applied to the circular hardwood tree scenario shown in Figure 45. In this case, the TSVD threshold was set at −35 dB.

In regard to the pre-processing stage, Figure 52 shows a comparison between raw (Figure 52a) and pre-processed (Figure 52b) data. The use of the proposed preliminary processing stage contributed to clearly identify a hyperbolic feature located at a two-way travel time value of about 5 ns.

As shown in Figure 53a, the tomographic reconstruction carried out with a time-gating up to 2 ns proves the potentiality of this method to identify the shape of the hardwood. A weak reflection from the target as well as multiple surface reflections are observed as well. The application of higher time gating (up to 6 ns) in the pre-processing stage allows the identification of the anomaly and the central inner area of the trunk to be improved (see Figure 53b).

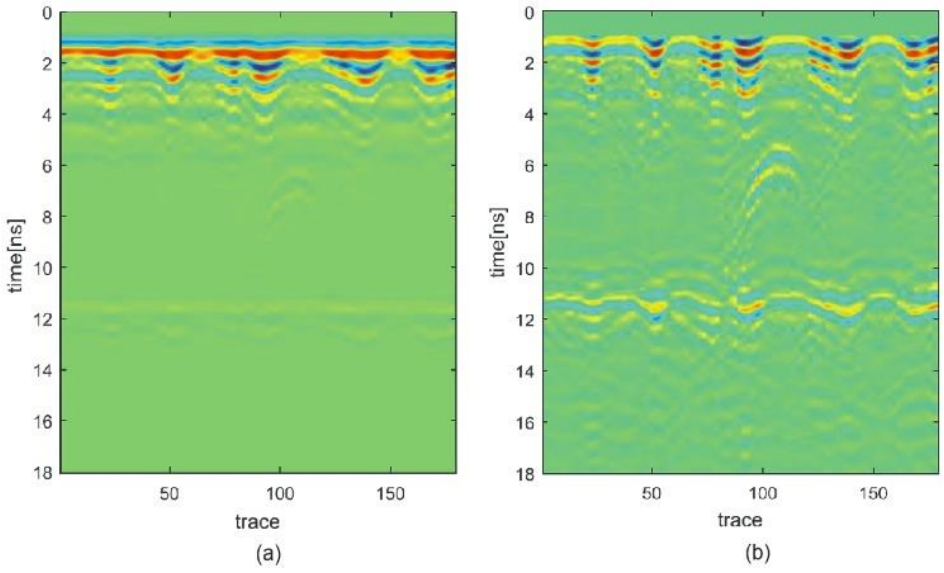

Figure 52: Radargrams of the simulations for the circular hardwood tree scenario. (a) Raw radargam; (b) processed radargram after the application of the pre-processing stage.

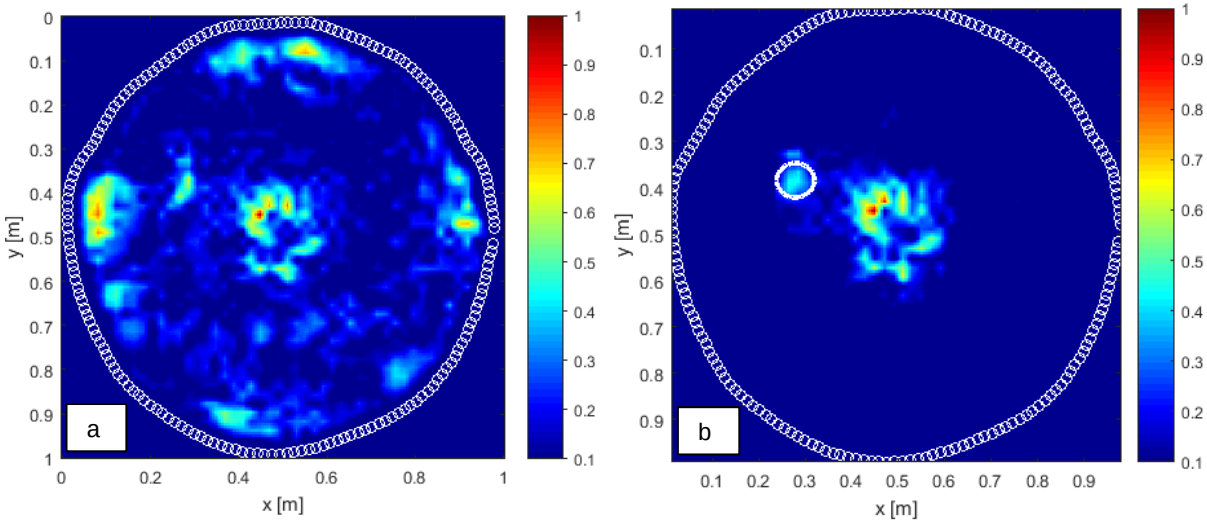

Figure 53: Tomographic reconstruction of the circular hardwood tree scenario with time-gating a) up to 2 ns, and b) up to 6 ns. The circles in solid white line along the trunk perimeter represent the positions of the measurement points. The colour scale represents the amplitude of the reconstructed contrast function normalised with respect to its maximum in the investigation domain.

4.3.5.1.3. Complex-Shaped Hardwood Tree

The same pre-processing and tomographic reconstruction schemes used for simulated data were applied to the complex-shaped hardwood tree scenario (Figure 46).

Figure 54 shows a comparison between raw (Figure 54a) and pre-processed (Figure 54b) data. The presence of the anomaly is identified in the processed data output by a hyperbolic feature located in the left-hand side of the radargram, at a two-way travel time value of about 6 ns. However, the presence of several reflections notably complicates the interpretation of the investigated scenario, so motivating the application of the microwave tomographic approach. Such an approach was applied by considering a working frequency band of 800–1800 MHz sampled with 27 frequencies spaced by 38 MHz. The relative dielectric permittivity of the trunk was assumed equal to 17. The TSVD threshold was fixed at −30 dB.

The tomographic reconstruction carried out with a time-gating up to 2 ns is reported in Figure 55a, proving the viability in identifying the target, the hardwood and the layer

surrounding the hardwood. Most notably, the highest reflection spots are located near the target. A further reconstruction was also performed without time gating, as reported in Figure 55b. As a result of this, it is observed that the output is very similar, excluding a new reflection pattern partially visible at the interface between the bark and the first internal layer.

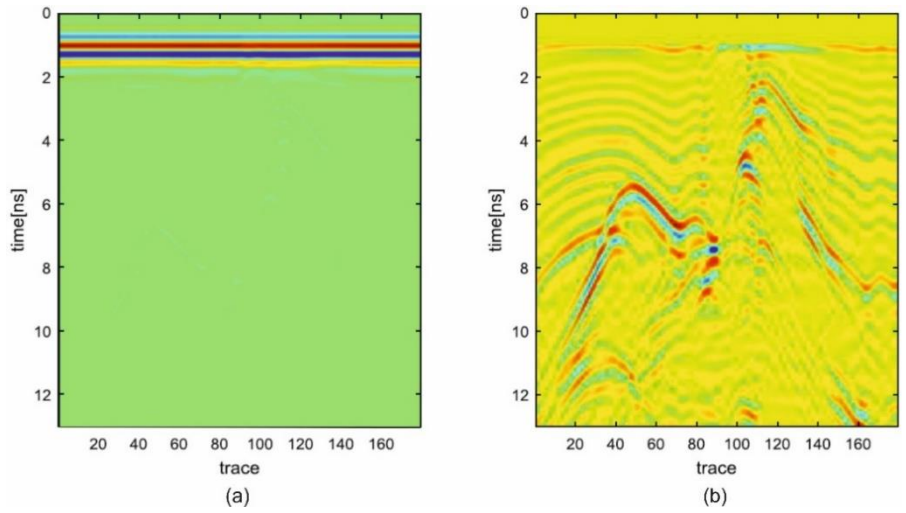

Figure 54: Radargrams of the simulations for the complex-shaped hardwood tree scenario. (a) Raw radargram; (b) processed radargram after the application of the pre-processing stage.

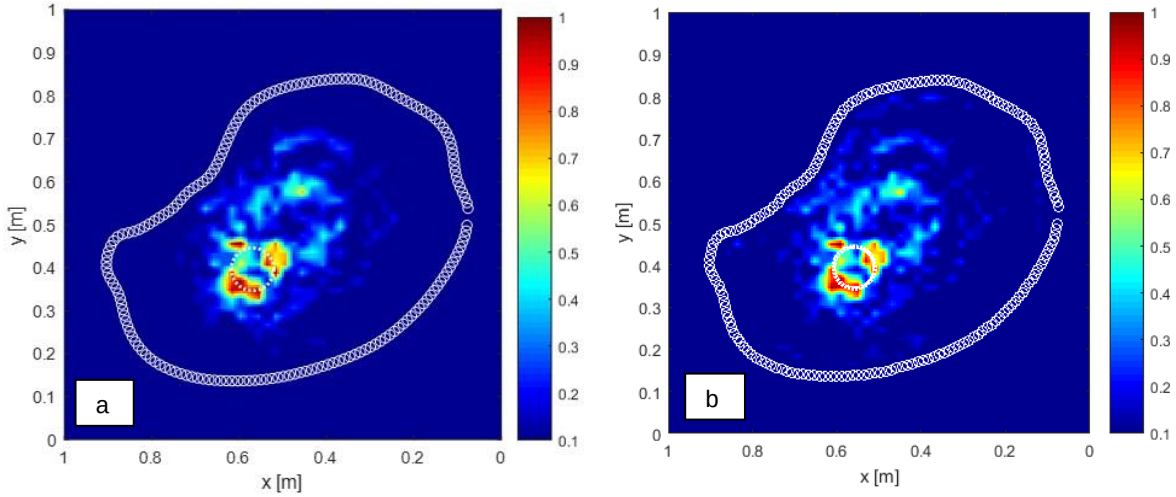

Figure 55: Tomographic reconstruction of the complex-shaped hardwood tree scenario a) with time-gating up to 2 ns, and b) without the application of time-gating. The dashed white circle indicates the actual position of the anomaly. The circles in solid white line along the trunk perimeter represent the positions of the measurement points. The colour scale represents the amplitude of the reconstructed contrast function normalised with respect to its maximum in the investigation domain.

4.3.5.2. Laboratory Case Study

The raw data were pre-processed by setting the zero-time at 1.9 ns. Afterwards, time-gating was applied up to 2.7 ns and followed by a background removal operation. Figure 56 shows a comparison between raw (Figure 56a) and pre-processed (Figure 56b) radargrams. The presence of the anomalies is identified in the processed data output by the three hyperbolic features whose apices are located approximately around trace 35, 90, and 120 in the radargram.

The tomographic approach was then applied considering a working frequency band of 1200–2300 MHz sampled with 23 frequencies spaced by 50 MHz. The relative dielectric permittivity of the trunk was estimated equal to 5 by measuring the two-way travel time associated with the reflection from the opposite side of the trunk. The TSVD threshold was fixed at −30 dB.

The tomographic reconstruction reported in Figure 57 turns out to be effective in identifying the three targets. It is worthy of note that the highest reflections are observed towards the bark, whereas the most internal reflection is more attenuated.

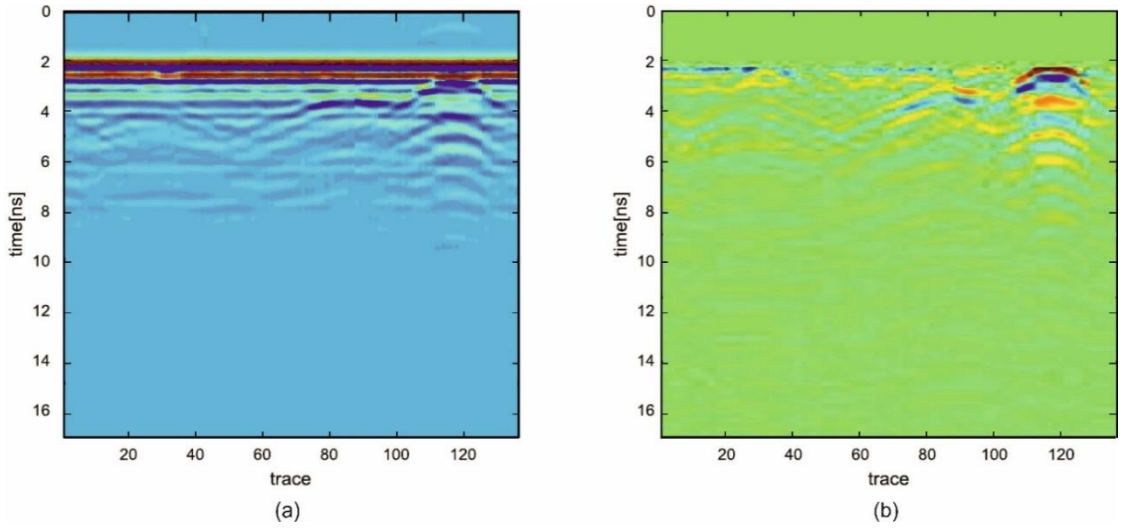

Figure 56: Radargrams of the real tree scenario. (a) Raw radargram; (b) processed radargram after the application of the pre-processing stage.

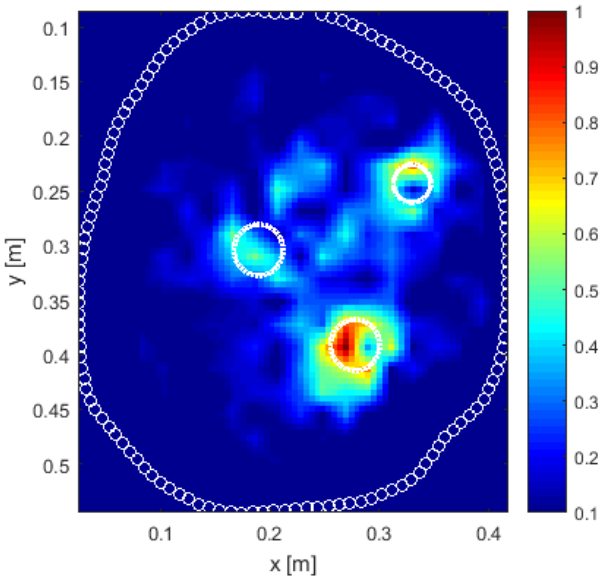

Figure 57: Tomographic reconstruction of the real tree scenario. The dashed white circles indicate the actual position of the anomalies. The circles in solid white line along the trunk perimeter represent the positions of the measurement points.

4.3.5.3. Field Case Study

4.3.5.3.1. Raw Data Analysis

In order to assess the effectiveness of GPR in detecting the presence of the cavity, geometrical models of the tree sections located at heights $h = 0\ m$ (P_1), $h = 0.6\ m$ (P_2) and $h = 1.3\ m$ (P_3), respectively, were built based on the visual information collected after the tree felling (Figure 58). The sections displayed in Figure 58 provide a comprehensive coverage of the overall inspected volume of the trunk from bottom to top.

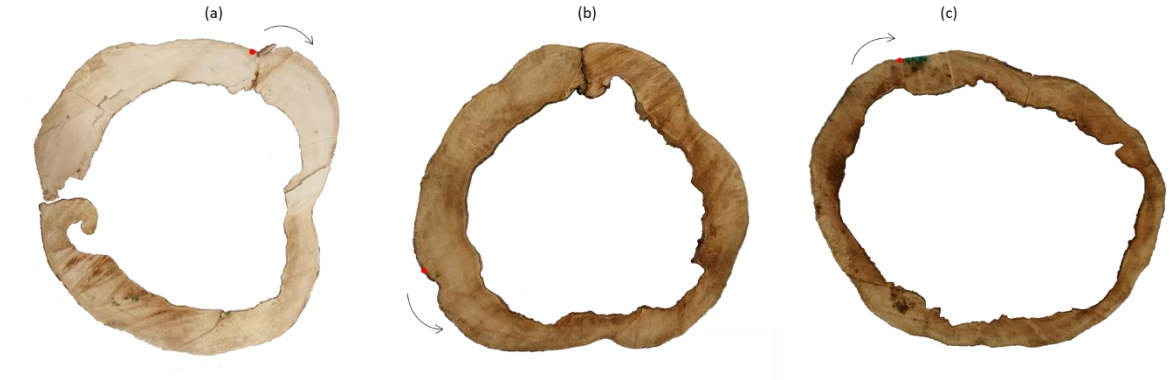

Figure 58: Plan view of the tree cross-sections at $h = 0\ m$ (a), $h = 0.6m$ (b) and $h = 1.3\ m$ (c). The red dot denotes the initial measurement point and the arrow indicates the movement direction of the GPR antenna along the bark.

Table 5 lists the main geometric characteristics of the above-mentioned sections. R_i and r_i denote the outer and inner radii of the cross-section at the i^{th} inspection height; $\bar{R}$ is the average radius of the trunk. $\bar{R} - \bar{r}$ is the average thickness of the sapwood; $\max|R_i - r_i|$ is the maximum i^{th} sapwood thickness; $\min|R_i - r_i|$ is the minimum i^{th} sapwood thickness. Moreover, ν is the percentage ratio expressing the sapwood area over the full cross-section area (i.e. the summation of the sapwood and the hollow areas); ρ is the percentage rate of sapwood thickness reduction considering the thickness at the base (i.e., section P_1) as the reference.

Table 5: Main geometric characteristics of the real cross-sections cut from the investigated tree trunk.

Section	$\bar{R}$ [cm]	$\bar{R} - \bar{r}$ [cm]	max $\lvert R_i - r_i \rvert$ [cm]	min $\lvert R_i - r_i \rvert$ [cm]	Hollow Area [cm^2]	Sapwood Area [cm^2]	ν [%]	ρ [%]
P1 ($h = 0\ m$)	69.31	20.17	26.84	11.19	7585.85	7505.22	49.73	0
P2 ($h = 0.6\ m$)	59.88	16.65	22.08	9.10	5871.00	5393.52	47.88	28.14
P3 ($h = 1.3\ m$)	62.33	11.63	16.48	6.69	8075.95	4129.68	33.83	44.98

From the data listed in Table 5, it is evident how the thickness of the sapwood drastically decreases from bottom to top, being $\rho = 28.14\%$ at the middle section, and $\rho = 44.98\%$ at the top section inspected. The average sapwood thickness $\bar{R} - \bar{r}$ is 20.17 cm (P_1), 16.65 cm (P_2) and 11.63 cm (P_3), with local maximum and minimum thickness values consistent with the upward-decreasing trend. It is also interesting to note that the area occupied by the sapwood is relatively similar to the hollow area at sections P_1 and P_2, whereas it decreases up to one third at section P_3 (i.e., $\nu = 33.83\%$). This behaviour is observed regardless of the fact that the full cross-section area decreases from the base to the middle section and increases from the middle to the top section.

The raw B-scans collected at the considered sections are depicted in Figure 59. The figures are displayed over a saturated colour scale and highlight a very similar behaviour despite the geometric differences observed for the tree cross-sections (see Figure 58). This claim is also supported by the curves plotted in Figure 60, where the average traces along the measurement direction for the three scans are compared.

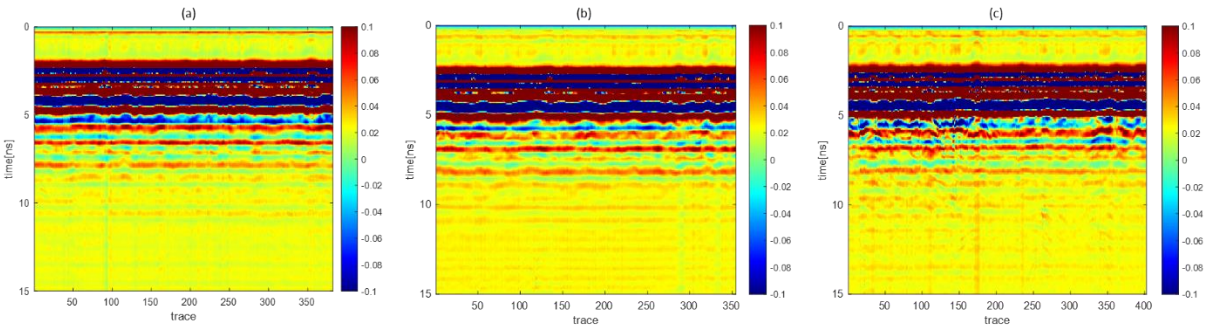

Figure 59: Raw radargrams collected at the considered tree sections. $h = 0\ m$ (a), $h = 0.6\ m$ (b) and $h = 1.3\ m$ (c).

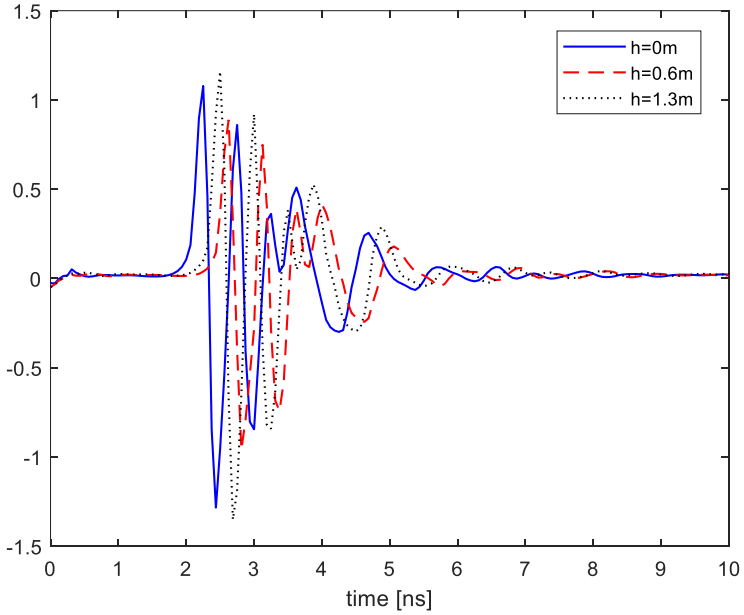

Figure 60: Average traces of the radargrams collected at the tree sections at $h = 0, 0.6, 1.3\ m$.

Except for a time shift less than 1 ns, the average traces show a similar trend, especially over the first 5 ns of the time window. A major trend observed across the radargrams is the presence of significant reflections occurring around the same travel time instants from the first radar echo. These reflections are likely related to the ringing effect caused by the antenna mismatch. According to Salas, et al. (1994), sapwood permittivity is the highest one compared to the permittivity of the bark and the heartwood tissues, matching the premise of a higher water content due to its main function of water nutrient transportation. Due to the high permittivity of the sapwood, which is in the range 15-30 (Koubaa, et al., 2008), a mismatching occurs between

GPR antenna impedance and the medium impedance. As a result, a significant ringing arises and overwhelms the response from buried targets. To cope with this problem, time-domain filtering operations (Catapano, et al., 1999; Solimene, et al., 2013) are required to mitigate the clutter and achieve reliable information.

4.3.5.3.2. Data Pre-Processing

The filtered radargrams are obtained for the tree sections by setting the zero-time at 2.3 ns, the gating-time at 5 ns and the application of the background removal (Figure 61).

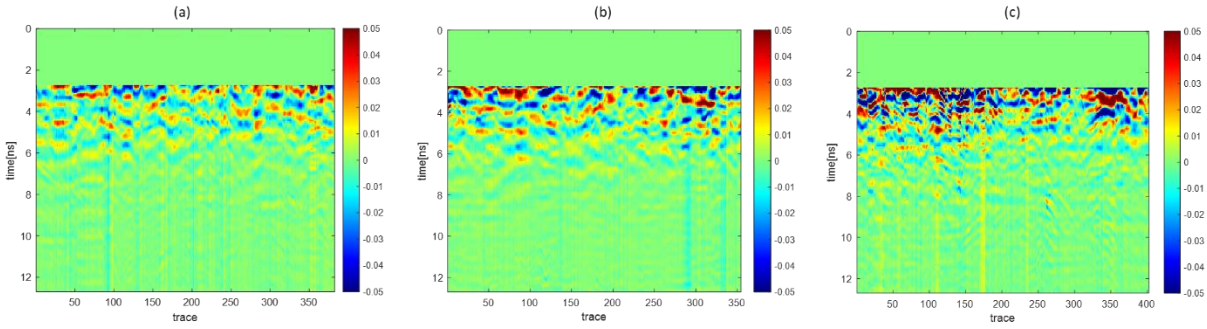

Figure 61: Radargrams achieved after the application of the zero-time setting, time-gating and background removal. $h = 0\ m$ (a), $h = 0.6\ m$ (b) and $h = 1.3\ m$ (c).

In order to demonstrate the effectiveness of the proposed time-domain processing, the radargrams processed by the application of the background removal only are reported in the upper panels of Figure 62a-c, whereas the radargrams achieved by the application of the time-gating only are reported in the bottom panels of Figure 62d-e. It can be seen that, differently from those in Figure 59, all sets of radargrams in Figure 62 are free from the horizontally constant clutter due to the antenna coupling, but they are still affected by a strong residual clutter. Specifically, the radargrams in the upper panels (Figure 62a-c) are affected by strong amplitude residual clutter in the early time response (up to about 3 ns), which is not fully removed by the background removal due to the surface irregularity of the bark. Conversely, those in the bottom panels

(Figure 62d-f) are affected by constant clutter occurring over the entire observation time window, with an amplitude comparable with that of the useful signals. Therefore, as confirmed by Figure 61, time-gating and background removal are both required to eliminate the residual clutter. Of course, since time gating enforces to zero the radargrams up to 5 ns, i.e. in the interval 0-2.7 ns once setting the zero time, it is not possible to achieve any information about the shallower part of the sapwood. On the other hand, the background removal attenuates the signals due to the sapwood-cavity interface occurring at the same travel time.

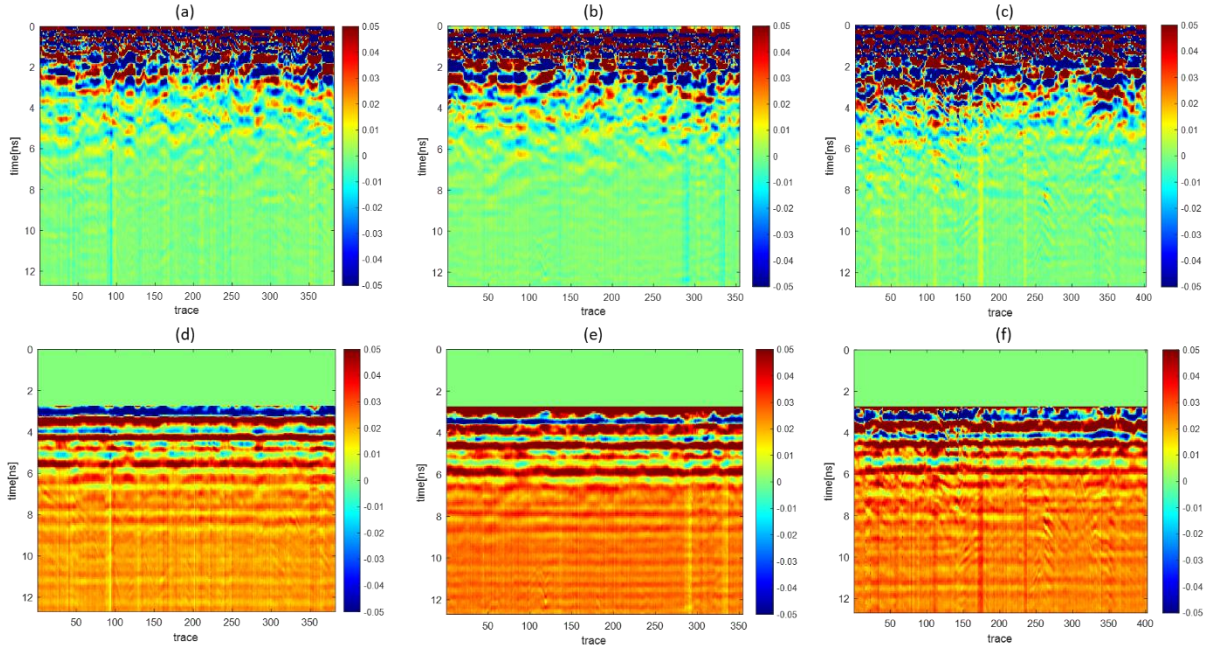

Figure 62: Radargrams achieved after the application of the zero-time setting with background removal only (upper panels) and with time-gating only (bottom panels). $h = 0\ m$ (a) (d), $h = 0.6\ m$ (b), (e), and $h = 1.3\ m$ (c), (f).

About the estimation of a reference average value of the tree dielectric permittivity, this is a very challenging task. In fact, the lack of clear diffraction hyperbolas in the radargrams as well as of any reflection from the opposite side of the trunk does not allow to estimate the velocity of the electromagnetic wave from the available data. Therefore, here we assume a relative permittivity of the hollow tree in the range 15-25, based on the available literature (Koubaa, et al., 2008; Salas, et al., 1994).

Accordingly, the “blind” zone in the sapwood due to time-gating operation extends from the bark up to a depth in the range 8-10 cm. In view of the above, the filtered radargrams in Figure 61 are the datasets used for the imaging in this case study.

4.3.5.3.3. Numerical Results

Before dealing with the processing of the experimental data, a numerical analysis of the capabilities of the microwave tomographic approach is performed, with the aim to provide useful insights for a reliable interpretation of the tomographic reconstructions in real-life scenarios. Specifically, the main goal in this study is to identify the presence of an inner cavity and the geometry of the sapwood (structural) layer. In this respect, it is worthy to recall the filtering properties of the linear inverse operator in Equation (4.22) under the reflection configuration here considered. In particular, a low-pass filtering along the direction of movement of the antenna and a band-pass filtering along the depth arise (Negishi, et al., 2020). Therefore, the tomographic images achieved by inverting Equation (4.22) will be able to reconstruct the fast variations of the contrast function along the depth. For the case at hand, significant and fast variations of the relative dielectric permittivity occur at the interface between the sapwood and the cavity (transition between the high permittivity of the sapwood and the free-space permittivity). Accordingly, the microwave tomography is able to detect and geometrically estimate the interface between the sapwood and the inner cavity.

The above considerations are clarified by the reconstruction performed on the simulated tree geometry represented in Figure 63. In this case scenario, the tree has a circular section with a radius of 0.8 m and contains a cavity with an irregular shape (dark brown area in Figure 63). The sapwood region (yellow area in Figure 63) is homogeneous with a relative permittivity ε_b=20 and an electric conductivity σ_b=0.05

S/m. The tree is probed by an electric line current operating in the band [500, 2000] MHz and moving along the tree perimeter with a spacing of 2.5 cm.

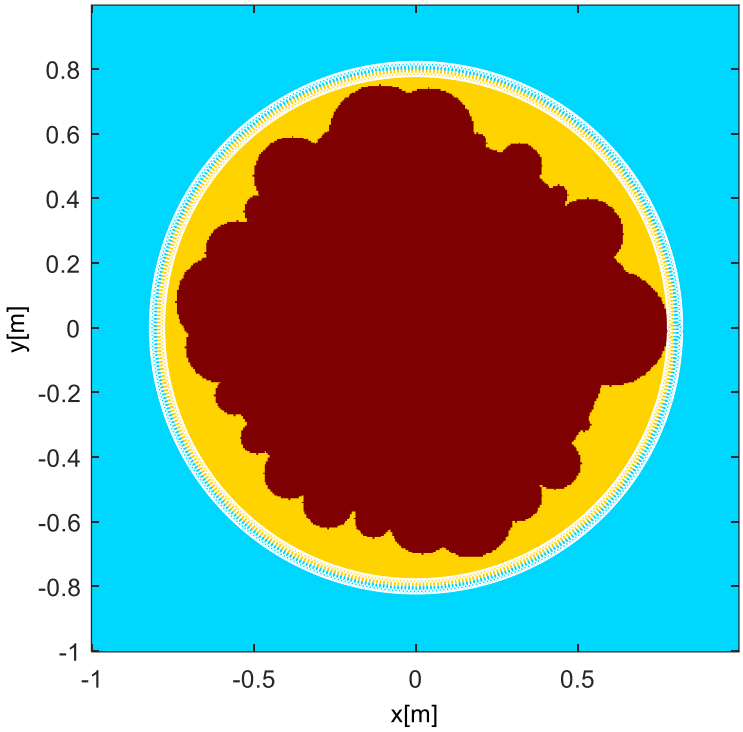

Figure 63: Simulated tree section with an inner cavity (dark brown region). The sapwood is the region in yellow.

A simulated radargram (Figure 64a) was generated by means of the numerical solver GPRmax2D (Warren, et al., 2016) and processed in the time-domain by setting the zero-time at 0.7 ns and applying a time-gating up to 1 ns followed by a background removal. The filtered radargram was transformed in the frequency domain over the operating band [500, 2000] MHz with steps of 25 MHz. A background scenario made of a homogeneous medium with relative dielectric permittivity equal to 20 has been considered for data inversion. The tomographic reconstruction is achieved via TSVD with a threshold level at -30 dB. The tomographic image is depicted in Figure 64b and shows a reliable reconstruction of the interface corresponding to the transition between the sapwood and the cavity. The resolution achievable at the interface sections is related to the bandwidth of the signal and the permittivity assumed in the

inverse model (Catapano, et al., 1999); in the case at hand, the resolution along the depth is about 2 cm.

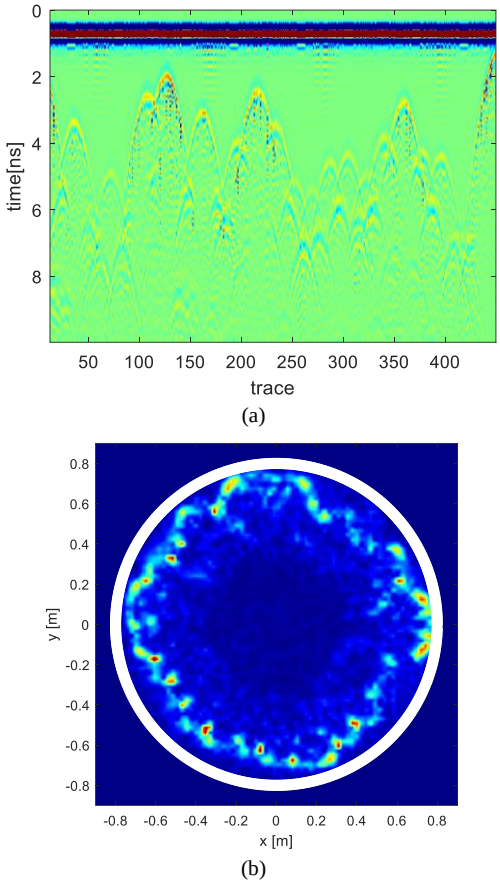

Figure 64: Simulated radargram (a) and tomographic reconstruction (b) for the scenario depicted in Figure 63.

4.3.5.3.4. Reconstruction Results

In this Section, the reconstruction results of the real tree sections in Figure 58 are shown, achieved by the application of the data processing framework described in Section 4.3.1.1. To this end, the filtered radargrams in Figure 61 are transformed into the frequency domain over the interval 500-2000 MHz with a step of 25 MHz.

For the data inversion, the measurement points are defined in such a way to account for the exact positions of the antenna along the tree trunk perimeter. The positions were determined using the arc-length parameterisation as described in Giannakis, et al. (2019).

The investigation domain matches the actual tree cross-section and it is discretised into square image pixels with size 0.01 m. The reconstruction results below presented are achieved by considering three different values of relative dielectric permittivity for the reference scenario. In particular, the values $\varepsilon_b = 15, 20, 25$ were considered. These values have been chosen in line with the outcomes obtained in Koubaa, et al. (2008).

The tomographic images reported in the top panels of Figure 65 refer to the lower cross-section at $h = 0\,m$ achieved with the three values of the background relative dielectric permittivity. Although it is not continuously mapped, the sapwood-cavity interface is clearly identified in all the three cases. This is in agreement with the tomographic reconstruction obtained in the simulated scenario. Moreover, higher reference permittivity values produce a resolution enhancement in the tomographic images and also the reconstruction of the interface is closer to the outer surface due to the smaller propagation velocity in the assumed model.

The bottom panels of Figure 65 show the tomographic images with the actual cross-sections superimposed. It can be noted that the use of $\varepsilon_b = 25$ allows to achieve the best reconstruction of the sapwood-cavity interface in terms of the accuracy of the localisation and the spatial resolution.

The tomographic images in Figure 66 refer to the cross-section at $h = 0.6\,m$. The interface between the sapwood and the cavity is again clearly identified and the permittivity value $\varepsilon_b = 25$ provides the best reconstruction in terms of localisation accuracy and the resolution of the sapwood-cavity interface.

Figure 67 displays the tomographic images relevant to the top section at $h = 1.3m$. In this case, the permittivity values $\varepsilon_b = 20$ and $\varepsilon_b = 25$ provide a similar reconstruction

of the interface in terms of the accuracy of the location, whereas an improved resolution is reached when $\varepsilon_b = 25$.

To conclude, a tomographic image of the tree cross-section at $h = 0.6\,m$ is shown, where only the background removal is applied to the raw data (reconstruction starting from the radargram depicted in Figure 62b). The reconstruction obtained with a medium permittivity $\varepsilon_b = 25$ is reported in Figure 68. Unlike the image in Figure 66c, it can be seen how the air cavity cannot be identified as the reconstruction is dominated by a strong residual clutter visible in the neighbourhood of the outer surface. Similar considerations apply to the rest of cross-sections and combinations of permittivity values, whose images are here omitted for sake of brevity.

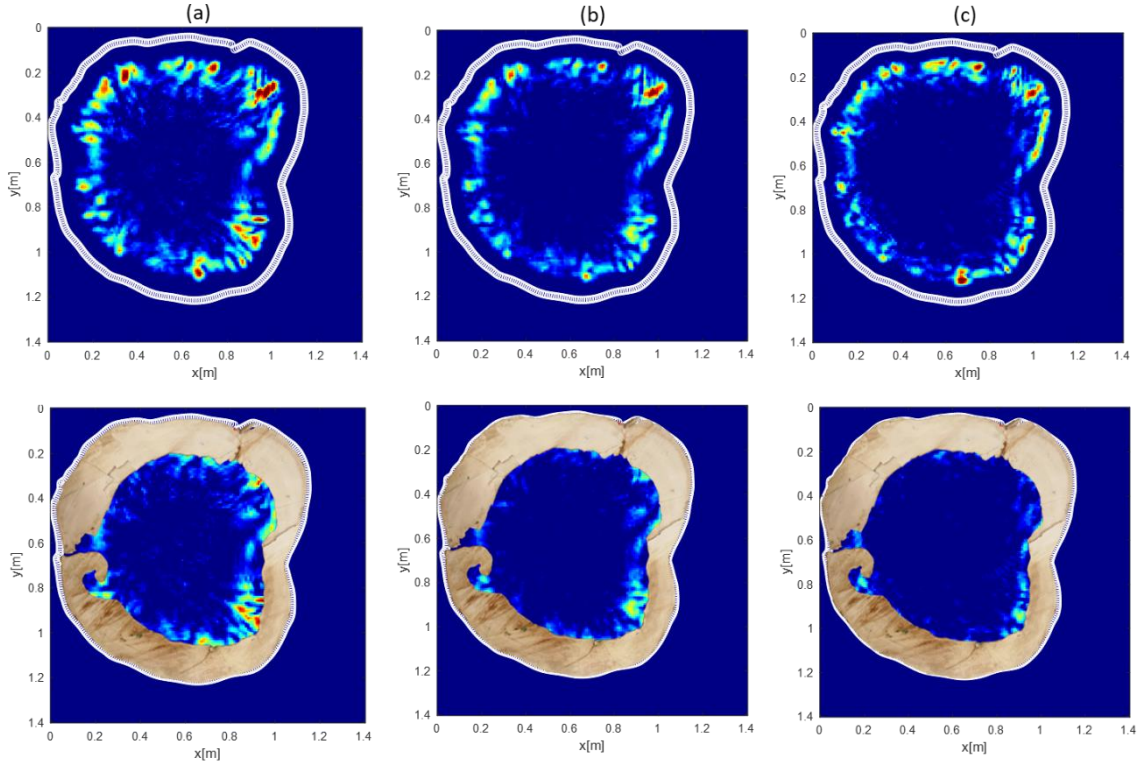

Figure 65: Tomographic images (upper panels) and tomographic images with the actual cross-sections superimposed (lower panels) for the tree section at $h = 0\,m$ and three increasing values (from left to right) of the background relative dielectric permittivity. $\varepsilon_b = 15$ (a). $\varepsilon_b = 20$ (b). $\varepsilon_b = 25$ (c). Colour scale [0.1, 0.8].

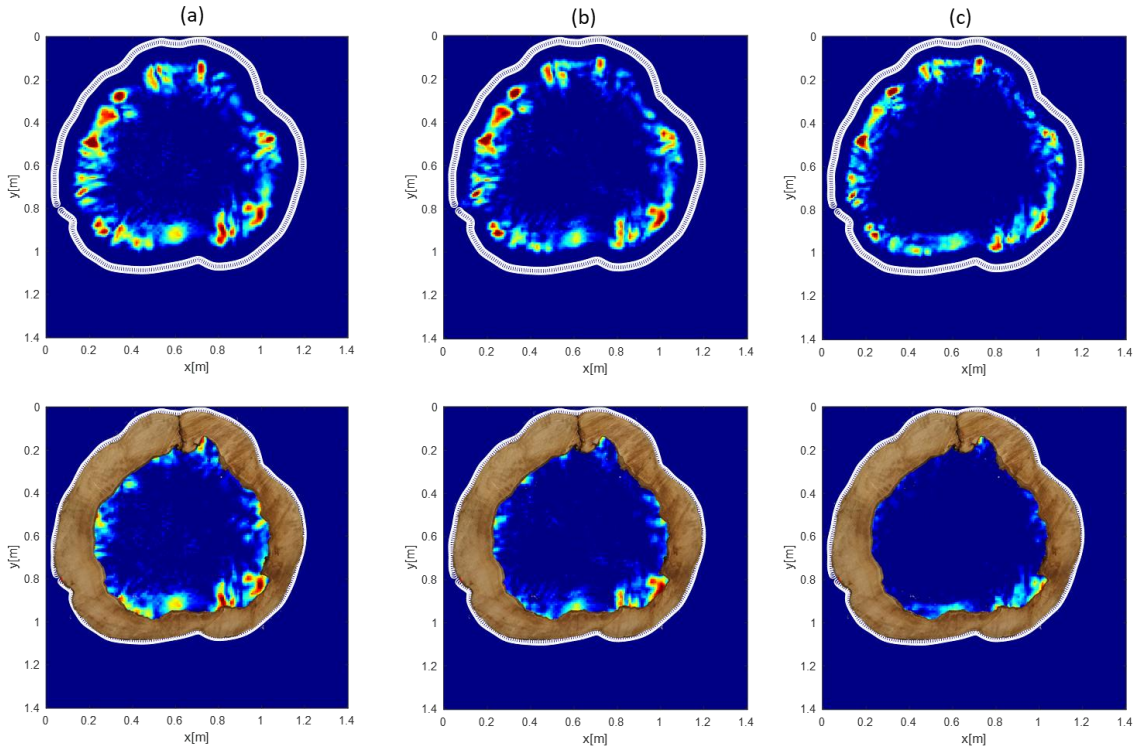

Figure 66: Tomographic images (upper panels) and tomographic images with the actual cross-sections superimposed (lower panels) for the tree section at $h = 0.6\ m$ and three increasing values (from left to right) of the background relative dielectric permittivity. $\varepsilon_b = 15$ (a). $\varepsilon_b = 20$ (b). $\varepsilon_b = 25$ (c). Colour scale [0.1, 0.8].

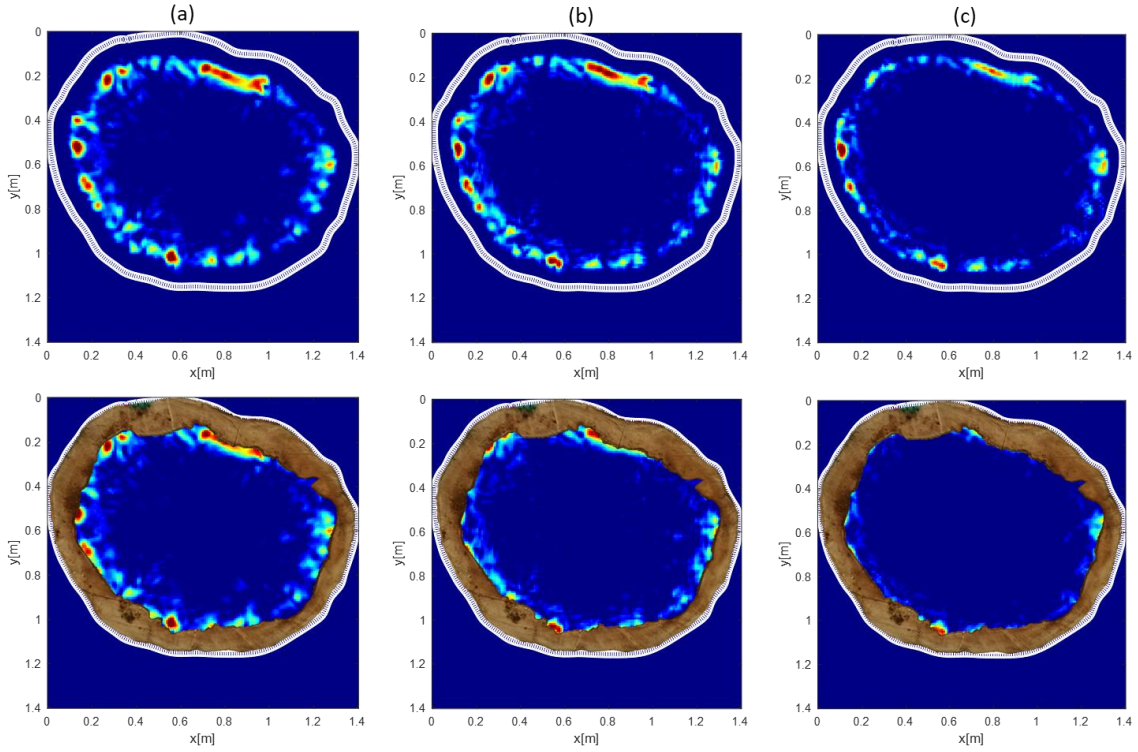

Figure 67: Tomographic images (upper panels) and tomographic images with the actual cross-sections superimposed (lower panels) for the tree section $h = 1.3\ m$ and three increasing values (from left to right) of the background relative dielectric permittivity. $\varepsilon_b = 15$ (a). $\varepsilon_b = 20$ (b). $\varepsilon_b = 25$ (c). Colour scale [0.1, 0.8].

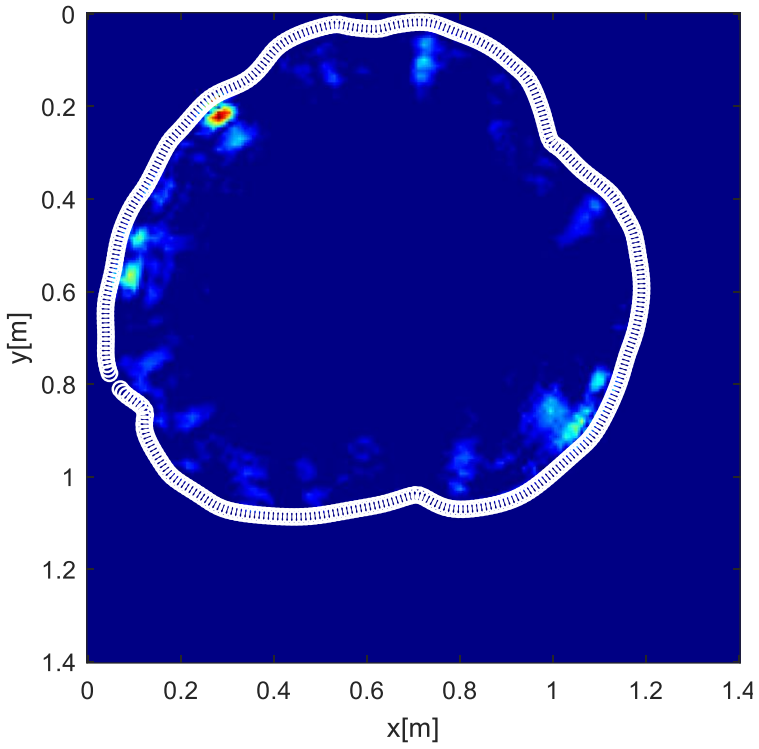

Figure 68: Tomographic image of the tree section at $h = 0.6\ m$ with $\varepsilon_b = 25$. The raw data are filtered by the application of the background removal only.

4.3.6. Conclusions

The potential of GPR and the use of a tomographic inversion approach in detecting decay and cavities in tree trunks have been demonstrated. To this effect, a set of FDTD simulations of different complexity was used and after the method was validated on a real trunk with several decays.

The radar signals demonstrate that the method can identify signs of inner reflections at the location point of the anomaly in a tree. Concerning the outputs of the numerical simulations, detection becomes more accurate in round-shaped trunks if more severe time-gating is applied to the signal in the time domain. This is particularly relevant for identifying cavities and decay located towards the inner section of a trunk. In the case of more complex-shaped trunks, the results of the simulations show that an effective detection of the target can be achieved as well.

The application of the tomographic inversion approach to a real trunk with several areas of decay was proven effective in identifying all the targets. It was observed that the reflections from targets closer to the bark are stronger than the reflections from targets located more internally in the cross-section.

This research line addresses the following objective of the present Thesis (see Section 3.1):

- *to develop enhanced data processing algorithms and interpretation techniques for tree assessment:* this research presents a novel approach for detection of decays and cavities in tree trunks, in order to improve detection of decays, their shape and dimension. Results were positive, both in the numerical simulations and in the real case study, showing the potential of the proposed methodology. Therefore, the set objective is considered achieved.

5. Use of GPR for the Reconstruction of Tree Root Systems' Architecture

Based on the considerations expressed in Section 2.2, it is clear that knowing the exact location of tree roots is crucial in several different applications, ranging from botany to civil engineering. In fact, this could allow to prevent the spread of infectious diseases among trees, to predict possible damages to buildings and infrastructures and to plan the most appropriate maintenance work.

Regarding the aforementioned investigating methods (Section 2.3), it is undeniable that destructive techniques are not only laborious and time-consuming, but they can destroy root systems if not done appropriately, making long-term repeated measurements inaccurate or impossible. Moreover, most of these techniques are impossible to apply in an urban environment, as trees are growing in a soil difficult to manipulate. Therefore, non-destructive techniques are the most suitable for this kind of applications. Furthermore, with reference to Section 2.4.7, GPR has shown potential and undeniable advantages over other NDT methods.

The main aim of this Section is, therefore, the development of a novel data processing framework to numerically analyse and to interpret GPR signal.

5.1. Data Processing Framework

5.1.1. Preliminary Signal Processing Stage

The primary purpose of this stage is to reduce noise-related information from the GPR data, as well as to achieve quantitative information and easily interpretable images for

The paragraphs of this Chapter have been published as part of journal papers in Remote Sensing (Lantini, et al., 2020) and Adv. in Tr. St. (Lantini, et al., 2019), and as part of a conference paper (Lantini, et al., 2020). Note that minor changes have been introduced to make the text consistent with the other Chapters of this Thesis.

the data analysis and interpretation stage. A signal processing methodology was implemented, based on a combination of standard and more advanced techniques (see Section 2.4.5), which can be applied to any GPR root system's investigation. The raw data were therefore processed based on the following sequence of processing steps:

- Zero-offset removal
- Time-zero correction
- Time-varying gain
- SVD filter
- F-K migration

5.1.2. Analysis of Discontinuity Elements

The presence of elements of discontinuity (e.g., manmade subsurface features such as pipes, conduits or the multi-layered structure of a road pavement) in a dataset including a tree root system architecture are regarded as a potential disruptive factor for the correct execution of the presented data processing methodologies. In fact, the presence of a transversal element in the investigated area interrupts the continuity of the data and creates the conditions for the generation of false alarms in the mapping process of the roots. The potential presence of these disturbing elements must therefore be identified before the application of the main tree root-tracking algorithm. For this purpose, a processing algorithm based on the methodology proposed in Lantini, et al. (2020) is introduced in the main data processing framework. An analysis of the data reflectivity is carried out in order to identify the presence of features not related to roots clearly. To this end, each B-scan in the dataset is tested to evaluate potential changes in the signal reflectivity. If present, these inhomogeneities are

subsequently reprocessed with dedicated signal processing techniques (e.g., in the case of a road pavement structures (Lantini, et al., 2020)), or their reflections are simply removed from the GPR data (e.g., in the case of pipes or other similar manmade buried features (Lantini, et al., 2020)).

5.1.3. Tree Root-Tracking Algorithm

This stage of the methodology is composed of two main parts. First, the initial hypotheses (the data acquisition method and the dielectric properties of the medium), and the data input settings (the outcomes of the pre-processing algorithm, the matrix dimensions and the GPR data acquisition settings) were outlined.

Following this, an iterative procedure was executed in order to analyse the output of the pre-processing stage. The methodology was based on the comparison of the amplitude values, in a random position of the 3D domain, with a given threshold. The following steps were then performed:

- Preliminary hypotheses: The proposed model is based on two main hypotheses regarding:
    - The data acquisition method (longitudinal or circular transects), and
    - The dielectric properties of the investigated medium.

  The acquisition method was performed by rotating the GPR antenna around the tree with a constant radial distance. As already stated, this was due to the radial distribution of roots around a tree trunk, and the necessity to achieve a quasi-perpendicular scan of the targets (Figure 69). The algorithm has therefore been developed with reference to a three-dimensional system of cylindrical coordinates, in which the vertical axis is identified by the axis of the tree trunk and the origin is positioned at its intersection with the plane matching the

ground level. The coordinates of the system are the depth z, the angular coordinate θ and the radial coordinate ρ (Figure 70).

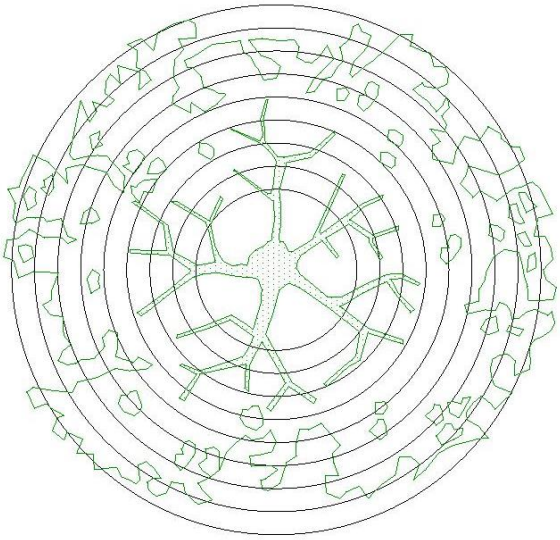

Figure 69: Circular transects scheme.

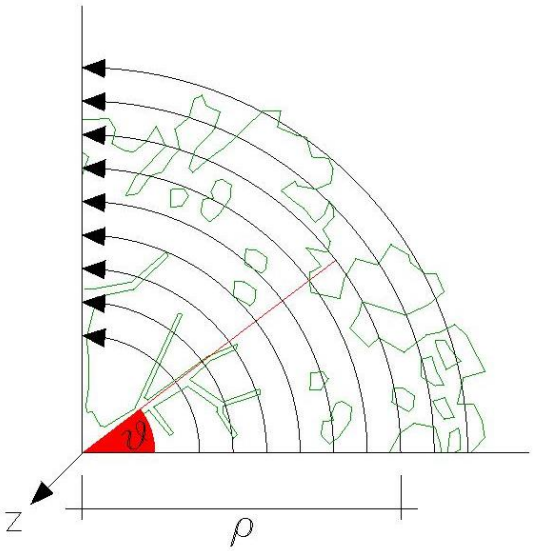

Figure 70: Cylindrical coordinates.

In regard to the relative permittivity of the medium ε_r, this was calculated using a hyperbolic velocity analysis method. This compares the observed reflection hyperbolas with the velocity-specific hyperbolic functions in order to find the function that best fits the data (Jol, 2009). For the purpose of this application,

the wave propagation velocity v in the medium was taken as the average value of velocities, estimated by the application of the hyperbola fitting method to several roots' reflections evenly picked up across the entire survey area.

- Data input: The algorithm expands upon GPR data from the pre-processing phase, in the form of a three-dimensional matrix of real numbers $\boldsymbol{A}(I,J,K)$, composed by the signal amplitude values in a random point of coordinates (i,j,k). The index i indicates the number of GPR scans, limited to I, the index j corresponds to the scan direction, limited to J, and k is the vertical coordinate going into the ground, limited to K. According to a reference polar coordinate system, the coordinates of a random point (i,j,k) can be expressed as follows:

$$x = \rho(i) \cdot cos\vartheta(j) \tag{5.1}$$

$$y = \rho(i) \cdot sin\vartheta(j) \tag{5.2}$$

$$z = z(k) \tag{5.3}$$

- Iterative procedure: The aforementioned assumptions and input information are essential to developing an iterative procedure for the tracking of a root system. Figure 71 shows a flowchart of the methodology followed in this stage.
    - Target identification: The algorithm evaluates the amplitude values in a random position of the 3D domain. In order to filter out the amplitude values that did not likely relate to tree roots, a threshold was set. This threshold value is established a priori based on a preliminary analysis of the data collected, in an effort to isolate as many hyperbolas as possible. Hence, the algorithm is set to analyse the domain until a signal amplitude

value greater than the threshold is found. This step is necessary to identify the apices of the reflection hyperbolae (i.e., the apices of the roots) and filter out amplitude values unrelated to candidate root targets.

- Correlation analysis: This step is focused on the investigation of further vertices in the closest vicinity of those identified at the target identification stage. This is performed to pinpoint other potential amplitude values greater than the threshold. This analysis has been improved in the present study compared to the original version presented in Alani et al. (2018), as the area in which the correlation is sought has been extended to four further points within the 3D domain, i.e., $a(i+1, j-1, k-1)$, $a(i+1, j+1, k-1)$, $a(i+1, j-1, k+1)$, $a(i+1, j+1, k+1)$ (see Figure 71). This improvement is used to smooth the correlation analysis process, including all the points of the 3D domain that could ideally belong to the development of a root.
- Tracking of the root: The algorithm isolates correlated points, creating a vector for the mapping of individual roots.
- Reconstruction of the root system architecture in a 3D domain: Vectors identified in the previous step are positioned in a 3D environment in order to represent the geometry of the tree root system.

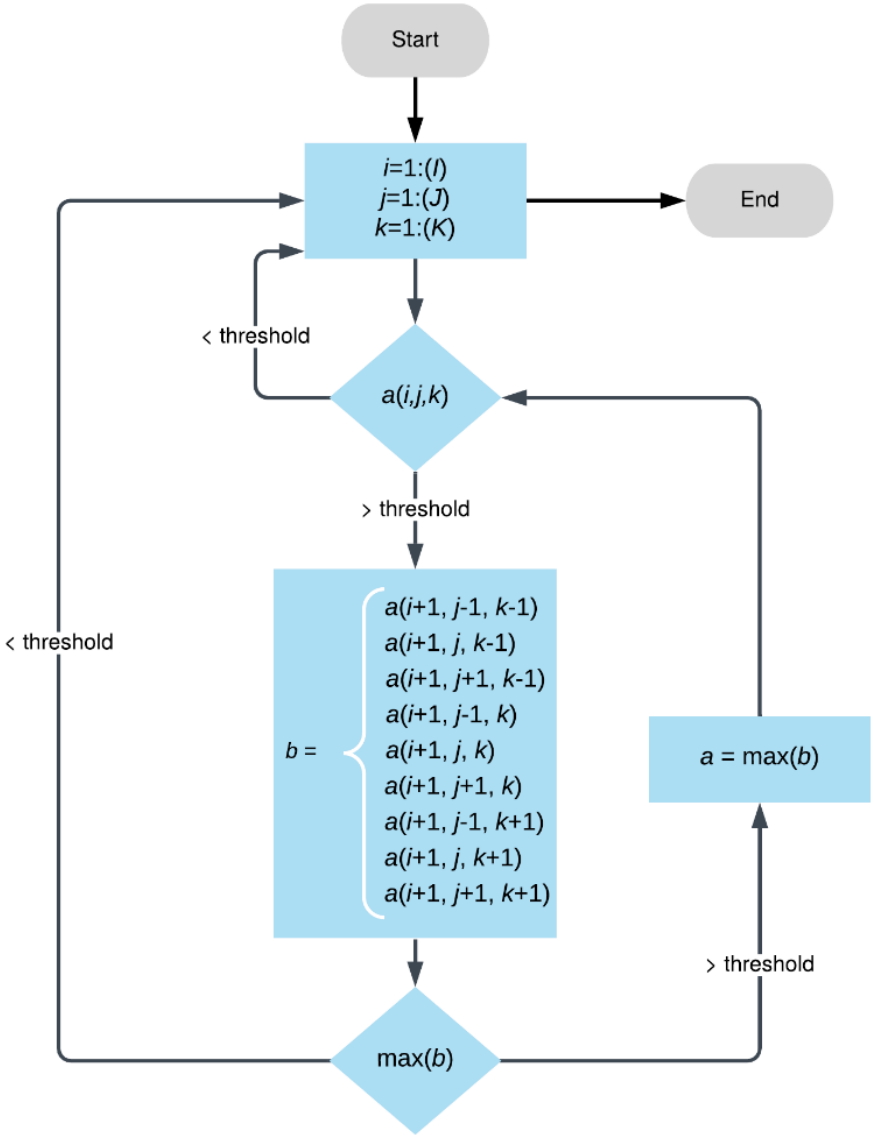

Figure 71: Flowchart of the tree root-tracking algorithm's iterative procedure

It is important to point out that in order to avoid the inclusion in the map of roots not belonging to the investigated tree, the root mapping algorithm is designed to perform a spatial correlation that follows the most likely directions of roots (i.e., from the trunk—source point—outwards). Therefore, the resulting renderings are only related to the examined tree and do not include any potential root belonging to adjacent trees (Figure 72). If present, these will result as uncorrelated with the mapping process and, hence, will be excluded by the algorithm.

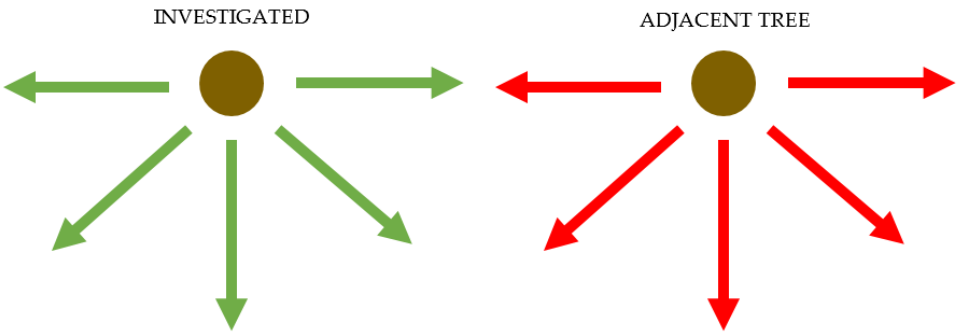

Figure 72: Layout of the roots' main directions in the case of two adjacent trees. Directions of roots of a reference tree (e.g., the tree under investigation in this study) (in green) are not compatible with the roots' directions of a nearby adjacent tree (in red).

5.1.4. Root Mass Density Estimation.

At present, the quantification of the tree roots mass density is considered a controversial task. In this regard, it should be specified that most of the studies deal with the quantification of tree root's biomass, which is an indirect output of GPR data (Guo, et al., 2013). Several studies have been carried out on this topic, both in field conditions (Butnor, et al., 2003) and in a controlled environment (Cui, et al., 2011), achieving reasonably good results. However, the accuracy of current methodologies still is limited. At present, the limiting factor for a correct root density estimate is the root water content that, if too low, can lead to a sub-estimation of root biomass. It should be concluded that existing evaluation methods are currently unable to provide reliable estimates. In this context, the novelty of the presented methodology lies in a new root density index evaluation, based on root location and length as obtained from the root mapping algorithm modelling process. The following stage of the presented methodology is therefore developed to provide a representation of the density of roots in the investigated area, with the main aim of identifying local changes of density.

First, best-fitting functions were used to better approximate root paths in the 3D domain, as well as to identify the length of each root in a continuous domain. Before evaluating the length of the roots in a specified domain, it is necessary to express

these in an analytical form. Each root is a 3D curve with a radial expansion that starts from the centre of the tree trunk. The only way to express 3D curves is through parametric equations or positional vectors (Kreyszig, 2006). As an example, a 3D curve can be expressed either as:

$$x = f(t) \tag{5.4}$$

$$y = g(t) \tag{5.5}$$

$$z = q(t) \tag{5.6}$$

or as:

$$\vec{F} = \langle f(t), g(t), q(t) \rangle \tag{5.7}$$

where $\{t \in R | 0 \leq t \leq 1$ is the parametric variable between zero and one that is chosen arbitrarily. To fit a parametric curve on a given set of 3D points, a polynomial function of nth order is used to approximate each of the parametric functions (Kreyszig, 2006)

$$x = \sum_{i=0}^{n} a_i t^i \tag{5.8}$$

$$y = \sum_{i=0}^{n} b_i t^i \tag{5.9}$$

$$z = \sum_{i=0}^{n} c_i t^i \tag{5.10}$$

The coefficients a_i, b_i, c_i are evaluated using least squares (Hansen, et al., 2013):

$$\boldsymbol{A} = (W^T W)^{-1} W^T \boldsymbol{X} \tag{5.11}$$

$$\boldsymbol{B} = (W^T W)^{-1} W^T \boldsymbol{Y} \tag{5.12}$$

$$\boldsymbol{C} = (W^T W)^{-1} W^T \boldsymbol{Z} \tag{5.13}$$

where $\boldsymbol{A}$, $\boldsymbol{B}$ and $\boldsymbol{C}$ are vectors $\{\mathrm{A}, \mathrm{B}, \mathrm{C} \in R^n\}$ that contain the coefficients a_i, b_i, c_i. The matrices $\boldsymbol{X}$, $\boldsymbol{Y}$ and $\boldsymbol{Z}$ are column vectors $\{\mathrm{X}, \mathrm{Y}, \mathrm{Z} \in R^s\}$ that contain the predicted x, y, z coordinates using the root-detection algorithm. The number of measurements is denoted with the letter s. Notably, when $n > s$, the system becomes underdetermined and no solution without constraints can be obtained. Thus, the number of measurements must always be greater than or equal to the order of the chosen polynomial. Lastly the matrix $\boldsymbol{W}$ $\{\mathrm{W} \in R^{n \times s}\}$ is:

$$\boldsymbol{W} = \begin{bmatrix} t_1^n & \cdots & t_1^0 \\ \vdots & \ddots & \vdots \\ t_s^n & \cdots & t_s^0 \end{bmatrix} \tag{5.14}$$

where $t_1, t_2 \ldots . t_s$, $\{t \in R | t_{i+1} - t_i = \frac{1}{s}\}$ are a set of equidistant points defined in the closed interval [0,1].

Knowing the analytical expression of the vector $\vec{F}$ makes it possible to evaluate its length for a given sample. The length of vector $\vec{F}$ with respect to t equals to (Kreyszig, 2006):

$$L(t) = \int_0^t \left\| \frac{d\vec{F}}{dt} \right\| dt \tag{5.15}$$

The derivative of the vector $\vec{F}$ with respect to t, equals to the derivative of its components:

$$\frac{dx}{dt} = \sum_{i=1}^{n} i a_i t^{i-1} \tag{5.16}$$

$$\frac{dy}{dt} = \sum_{i=1}^{n} i b_i t^{i-1} \tag{5.17}$$

$$\frac{dz}{dt} = \sum_{i=1}^{n} i c_i t^{i-1} \tag{5.18}$$

Therefore, the integral in Equation (5.15) can be rewritten as (Kreyszig, 2006):

$$L(t) = \int_0^t \sqrt{\left(\sum_{i=1}^{n} i a_i t^{i-1}\right)^2 + \left(\sum_{i=1}^{n} i b_i t^{i-1}\right)^2 + \left(\sum_{i=1}^{n} i c_i t^{i-1}\right)^2}\, dt \tag{5.19}$$

The integral above is evaluated using numerical methods (Simpson's rule, Gaussian quadrature) (Fausett, 1999). The length L is related to t, thus it can be calculated for a given segment, allowing to map the length of the roots in a specified domain. The degree of the polynomial n should be chosen with caution since large values can give rise to over-fitting, resulting in poor generalisation capabilities of the fitted polynomial, whereas small values can decrease the overall resolution. As a rule of thumb, the order of the polynomial should be less than half the number of measurements $n < s/2$.

Once the length of the root was known, the domain was partitioned into reference volume units, the dimensions of which depend on the circular scan spacing and the depth resolution required for the density investigation. The length of roots contained in the reference volume was then evaluated as follows:

$$d = \frac{\sum_{i=1}^{n} L_i}{V} \tag{5.20}$$

where

- d is the density $[m/m^3]$
- n is the number of roots contained in a reference unit of volume V $[m^3]$
- L_i is the length of the root $[m]$

5.2. Case Studies

5.2.1. Assessment of Tree Root Systems

5.2.1.1. Methodology

5.2.1.1.1. The Test Site

The survey was carried out in Gunnersbury Park, Ealing, London (United Kingdom) (Figure 73). The tree under investigation, a sycamore (*Acer Pseudoplatanus*), was identified for this study by the London Borough of Ealing's Tree Service. This tree is located along a tree-lined avenue inside the park, at a distance of ~10 m from the adjacent trees (see Section 4.3.4 for further details on the investigated tree).

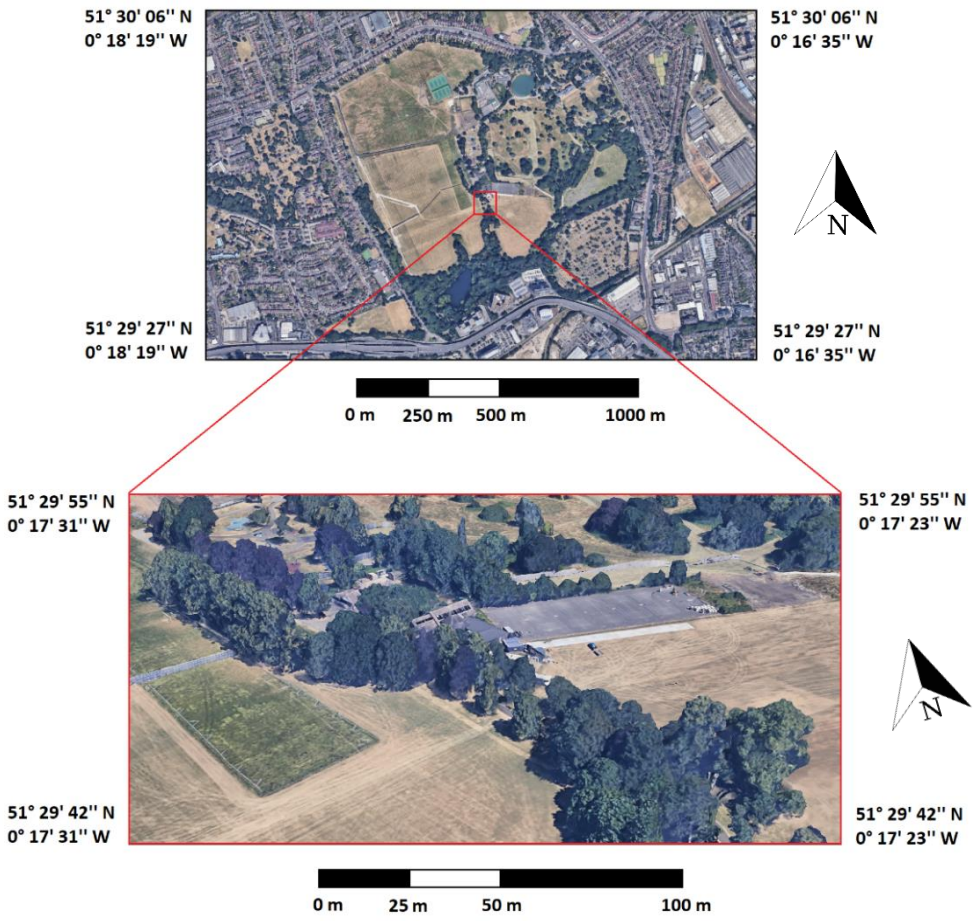

Figure 73: Study site for the GPR investigation (map data: Google, Landsat/Copernicus).

On the survey day, the weather was sunny, with temperatures between 19 and 21 °C and a humidity of 39%. Furthermore, it is important to note that the last episode of light rain occurred ten days before the survey (Time and Date AS, 2019).

5.2.1.1.2. The GPR Survey Technique

The survey technique followed a circular GPR acquisition method, as described in Section 5.1.3. As already stated, this survey methodology was chosen due to the particular configuration of a typical root system, which expands radially from the trunk of the tree outwards (Fayle, 1968; Drexhage, et al., 1999). In fact, GPR surveys carried out around the trunk with constant radial distance have proven capable of providing a quasi-perpendicular scan of the root systems (Alani & Lantini, 2019; Lantini, et al., 2020).

Further, the investigation was carried out on the portion of the tree root system developing below the natural soil, excluding the area covered by an adjacent asphalt pavement (i.e., performing the scans along semi-circular transects) (Figure 74).

Figure 74: Detail of the survey setup.

A set of 36 semi-circular scans were performed around the investigated tree. The first survey transect was positioned 0.50 m from the bark in order to allow enough space for the GPR equipment to manoeuvre around the tree trunk. Subsequently, the spacing between the lines of the scan was set to 0.30 m. Consequently, an overall area of 218.04 m^2 was surveyed around the tree, with an outer radius of 11.86 m and an inner radius of 1.36 m. Figure 75 shows a rendering of the GPR survey setup's main characteristics.

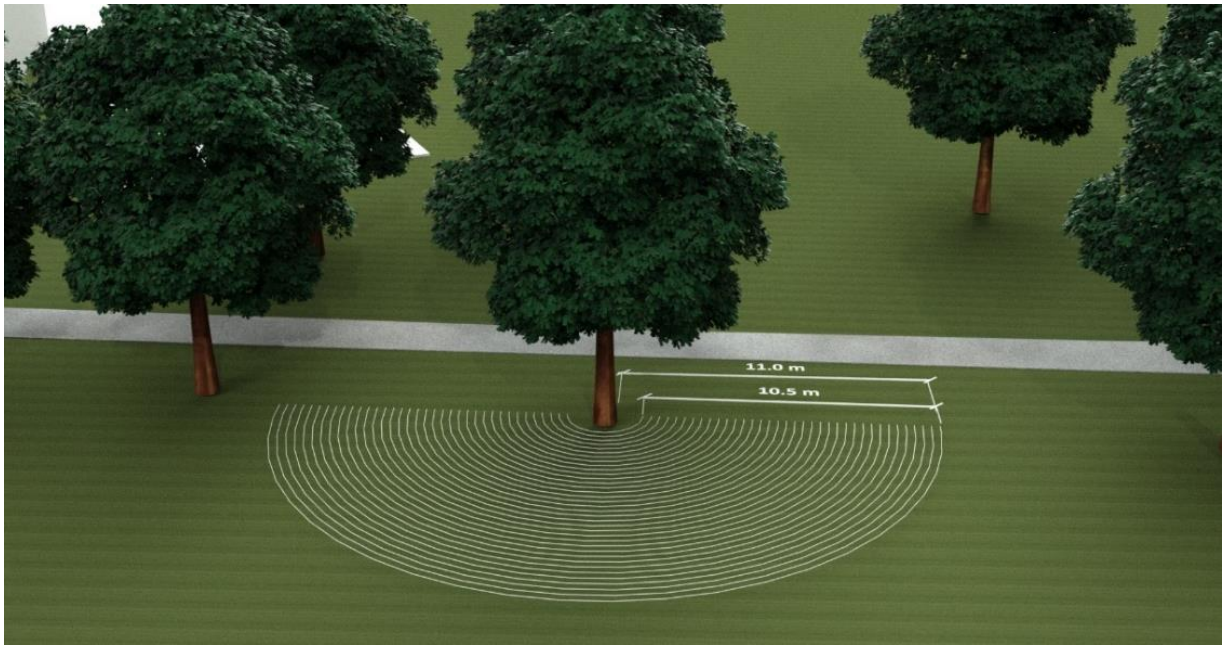

Figure 75: Rendering of the GPR survey setup.

5.2.1.1.3. The GPR Equipment

The Opera Duo ground-coupled GPR system, manufactured by IDS GeoRadar (part of Hexagon) was employed for testing purposes. The system includes two monostatic antennas of 700 and 250 MHz central frequency. Data were collected using a time window of 80 ns, discretised across 512 samples. The horizontal resolution was set to 3.06×10^{-2} m. For the purposes of this study, only data collected using the 700 MHz antenna were analysed in order to provide the highest effective resolution of the deepest layers of the root system (Benedetto, et al., 2011; Benedetto, et al., 2013).

5.2.1.1.4. The Excavation for Validation Purposes

In order to validate the results obtained through the processing of the GPR data, an excavation was carried out near the investigated tree. The exact location of the excavation area was determined a posteriori based on the results obtained, in order to dig a defined area where the preliminary data analysis had highlighted the presence of potential targets.

The excavation took place approximately three months after the GPR survey. In the meantime, the tree was felled as planned, and it was necessary to wait for the technical time of the trunk removal from the investigation area. The whole activity, including finding the area coordinates, excavation, roots' measurements and excavation coverage, was completed in three days.

An area of 4 m per side was accurately identified (Figure 76), based on the coordinates of the GPR survey (see Section 5.2.1.2.5). The excavation was then carried out by removing layers of ~0.10 m of soil at a time.

Figure 76: Verification of the accuracy of the excavation area's coordinates. Note that the tree was felled before the excavation stage (the trunk base is visible on the left-hand side of the picture).

5.2.1.2. Results

5.2.1.2.1. Preliminary Signal Processing Stage

The use of a pre-processing phase on the GPR data enabled achieving a more effective detection of targets with a significant reduction in noise-related features. To elaborate, the application of the SVD filter reduced the effect of reflections from the horizontal layers as well as the multiple reflection patterns caused by ringing noise. Figure 77 shows the result of the application of the discussed signal processing steps. Figure 77a,b clearly show the application of the standard processing techniques and the SVD filter. In particular, the latter has proven effective in significantly removing noise-related features.

Moreover, the application of the F–K migration filter enabled obtaining a more focused representation of the hyperbolic targets, including the roots, hence contributing to improving the effectiveness of the proposed algorithm in the next phase. It is, in fact, fair to comment that, without the application of this particular filter, false alarms were frequent, i.e., points belonging to the tail of the hyperbolas (therefore not representing the actual position of the target) with amplitude values satisfying the threshold value conditions. These points were not discarded by the algorithm and generated false positives. Thus, the application of the migration process has proven to increase the reliability of the algorithm for the detection and tracking of roots in the subsequent steps. Figure 77c shows the result of the F-K migration to the pre-processed data. It is possible to notice how the tails of the hyperbolas have retracted towards the apexes (i.e., the real position of the targets), forming unique focused points. In addition, it is important to observe that the migration provided an estimation for the value of the permittivity equal to 12, which corresponds to a velocity of the EM wave equal to 4.33 $\times 10^7$ m/s.

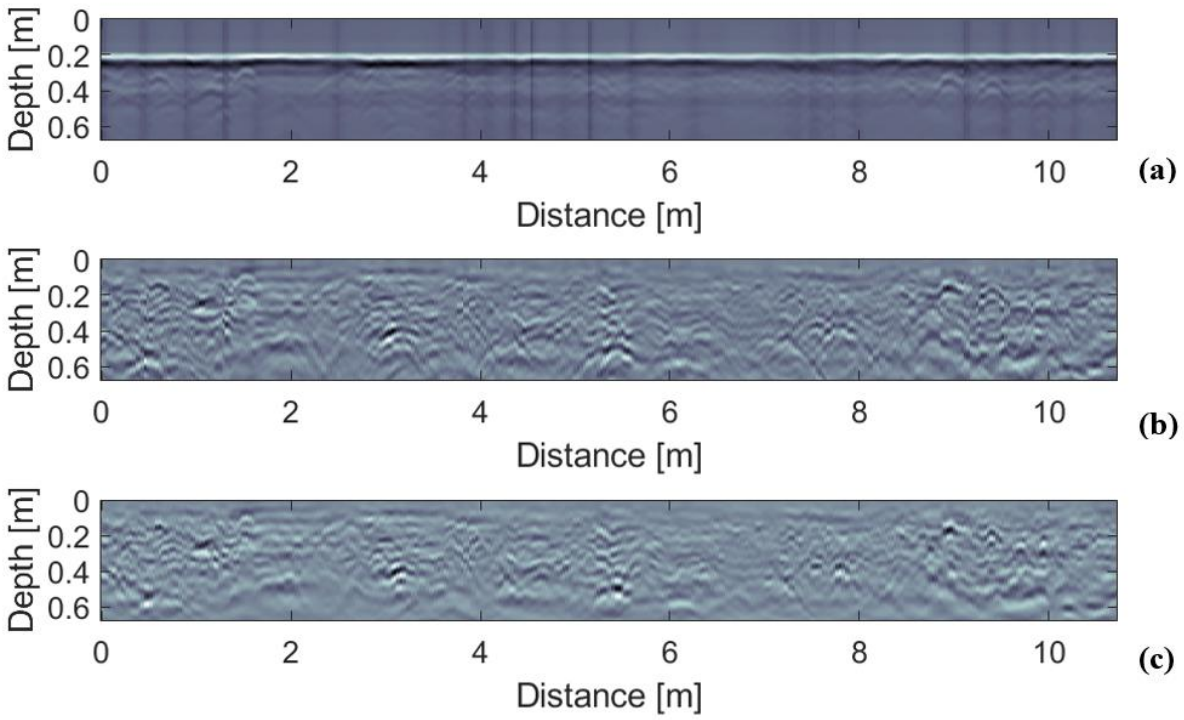

Figure 77: B-scan (a) before the application of the preliminary signal processing stage, (b) after the application of standard signal processing and SVD filter, and (c) after the application of the F–K migration.

5.2.1.2.2. Analysis of Discontinuity Elements: the Detection of a Buried Structure

An in-depth analysis of potential elements of discontinuity across the collected set of B-scans—as per the requirements discussed in Section 5.1.2—revealed the presence of a buried structure, recurring from scan 17 onwards (Figure 78). In order to better understand the nature of such a feature, a tomographic approach was followed to allow for a more comprehensive analysis of the investigated area. For this purposes, C-scans (Daniels, 2004) were created at different depths, which highlighted the presence of a subsurface linear structure, approximately 2 m wide and 5 m distant from the tree, crossing the investigation area (Figure 79). The analysis of both B-scans and C-scans suggests the presence of a reinforced concrete structure, as hyperbolic and evenly spaced reflections, potentially attributable to reinforcement bars, can be observed. Considering the layout of the site and the characteristics of the feature (i.e.,

estimated dimensions and construction materials), the latter was interpreted to be a conduit, serving an artificial lake located in the vicinity of the survey area.

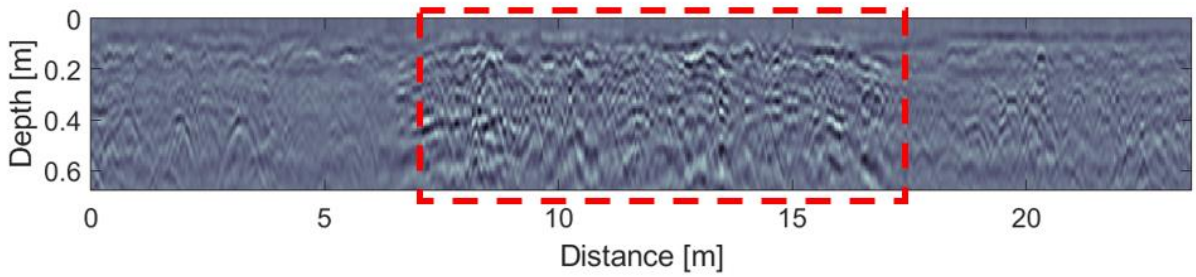

Figure 78: A B-scan showing the presence of a buried structure (highlighted by the red dashed square).

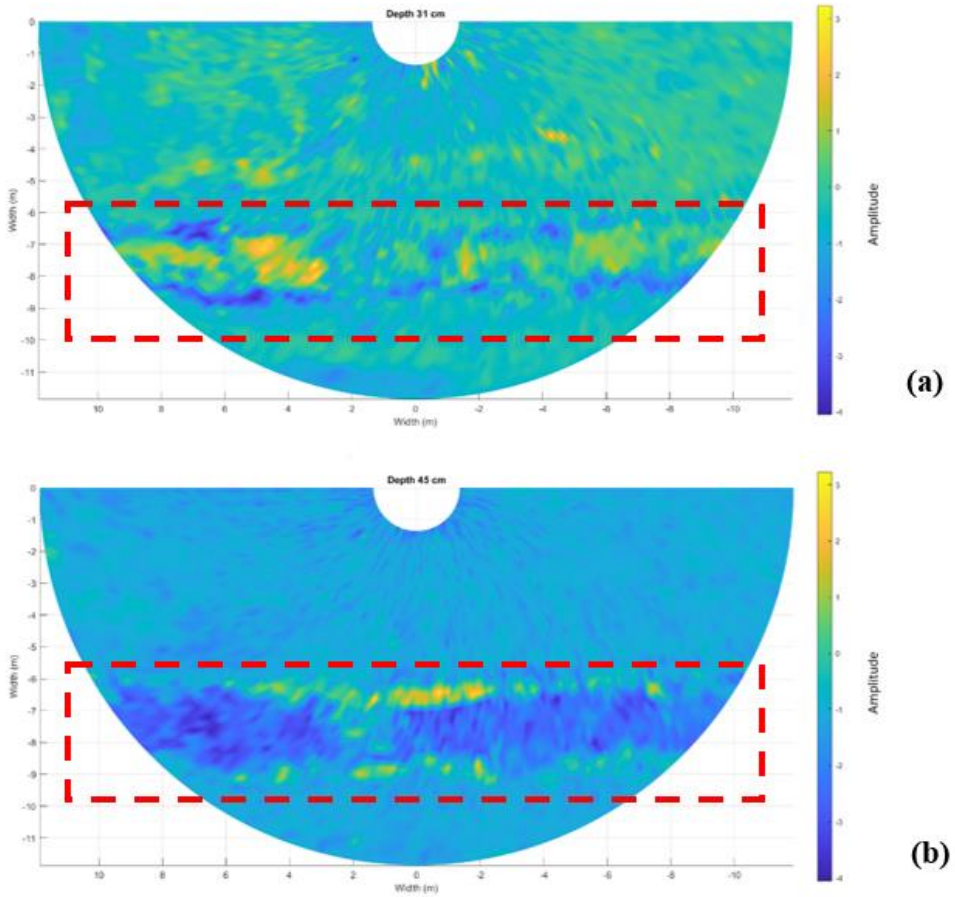

Figure 79: C-scans of the investigated area at (a) 0.31 m of depth and (b) 0.45 m of depth. The red dashed areas clearly show the presence of a buried structure.

In addition to the above, it is important to note that a difference in the appearance of the ground was noticed, based on a visual inspection carried out on the study area. This feature was observed exactly at the location coordinates of the identified structure

(Figure 80). It is therefore reasonable to assume that a conduit was introduced in relatively recent times, and that the required excavation and groundwork have interfered with the existing root system, cutting off roots and undermining the already decayed conditions of the tree.

Figure 80: Aerial view of the investigated area. The red dashed area highlights a difference in the ground appearance matching the identified location of the discontinuity feature.

In terms of the data processing, the presence of this particular feature interferes with the application of the tree root-tracking algorithm in the following stages. In addition, it implies that no roots are present within the volume occupied by the identified underground structure. For the purposes of this study, it was therefore decided to remove the reflections related to this particular type of discontinuity feature. A processing framework based on the methodology introduced in Lantini, et al. (2020) was hence followed. The analysis of the data reflectivity was carried out to quantitatively locate the buried structure and eliminate the related reflections from the B-scans. Figure 81 shows the application of this processing scheme, proving that analysing the signal reflectivity is a valid tool to achieve an accurate detection of major elements of discontinuity.

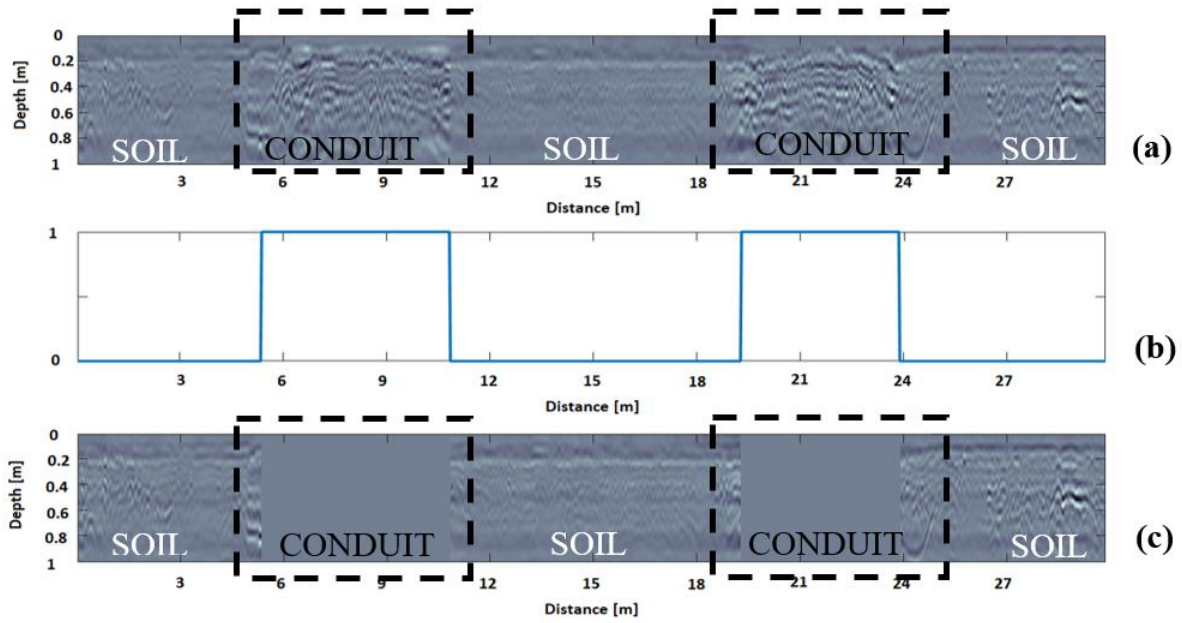

Figure 81: An example of the GPR reflectivity analysis. (a) B-scan after the preliminary signal processing stage, (b) analysis of the signal reflectivity, showing a maximum value at the section coordinates of the identified buried feature, and (c) B-scan after a targeted trace removal.

5.2.1.2.3. Tree Root-Tracking Algorithm

Following the application of the preliminary signal processing stage and the analysis of the signal discontinuity, the tree root-tracking algorithm was applied for the reconstruction of the root system architecture in a three-dimensional environment. Figure 82 shows the outcome of this procedure, which is a 2D planar view (a) and a 3D view (b and c) of the reconstructed root system architecture. To aid with the interpretation of results, shallow-buried roots (i.e., within the first 0.25 m of soil) and deeper roots (i.e., below the first 0.25 m of soil) have been represented with different colours.

The analysis of the results showed that reflections were located within the first 0.70 m of soil. This is apparently not in line with the expectation for the root system of sycamore trees, as their roots can reach a depth of approximately 1.40–1.50 m (Köstler, et al., 1968; Crow, 2005). Nevertheless, Crow (2005) reports that 90% to 99% of tree roots are usually found within the first metre of soil. The absence of reflections

from deeper roots could be linked to the presence of death roots, having a value of dielectric permittivity close to that of the soil. Similarly, as shown in Figure 82, a discontinuity of the root system is visible in certain areas, mainly in the central region of the investigated soil. This could likely be an effect of the conduit installation, which may have interfered with the original structure of the root system and caused irreversible damage.

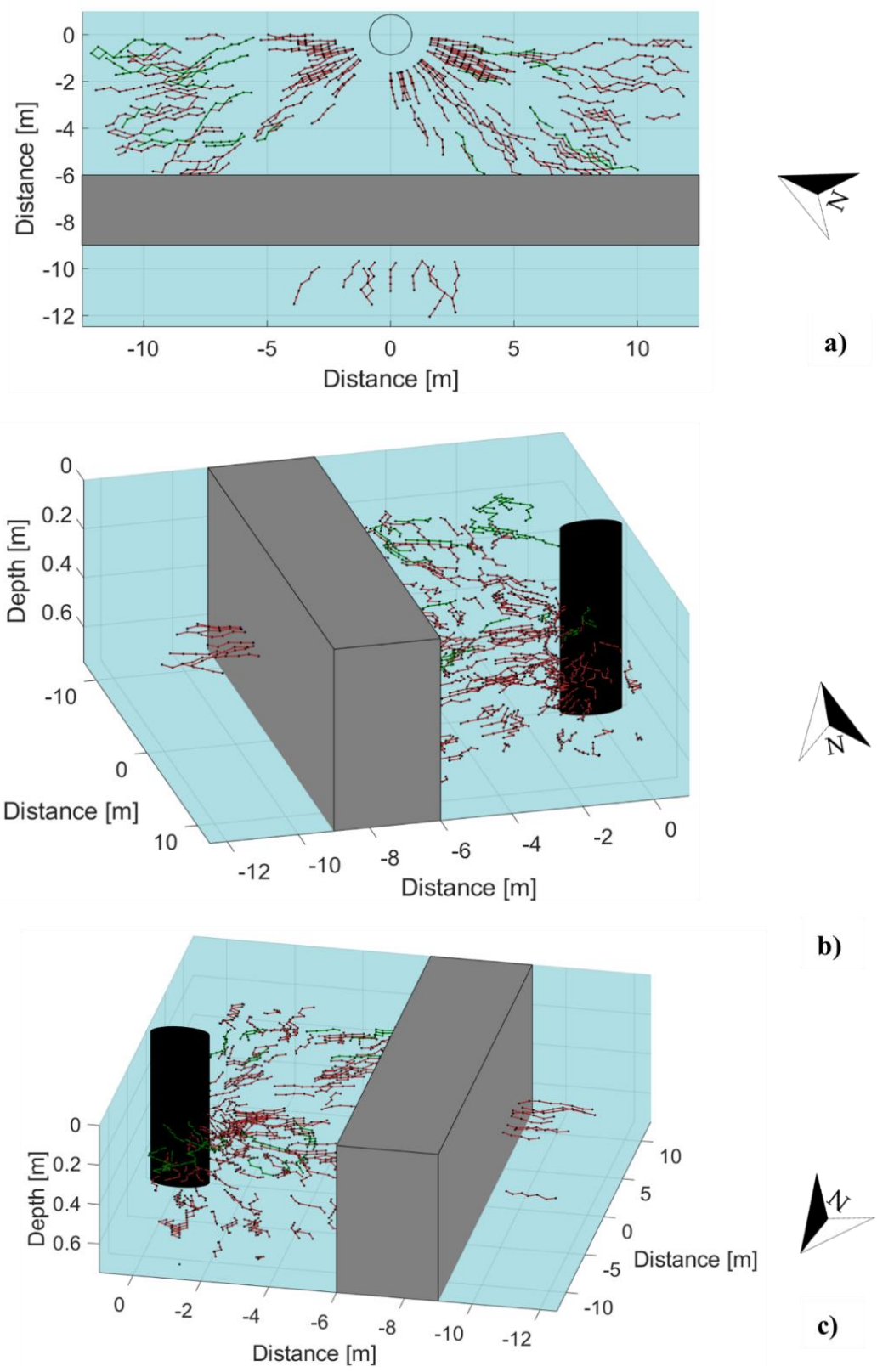

Figure 82: Reconstructed map of the tree root system architecture: (a) 2D planar view, (b) 3D view from South-West, and (c) in a 3D view from North-West. The grey block represents the volume occupied by the buried feature.

Finally, it is worth noting that the algorithm is designed to discard shorter segments, which might relate to non-root targets (e.g., boulders). The results achieved at this stage of the data processing are consistent with this particular algorithm feature.

5.2.1.2.4. The Root Mass Density Maps

The architecture of the root system was then further investigated through the evaluation of the root density at different depths (Equation (5.20)). The investigated domain was divided into reference volumes of 0.30 m × 0.30 m × 0.10 m, where the dimension 0.30 m was chosen for consistency with the spacing between the scans, and the depth dimension 0.10 m was selected for consistency with the excavation steps performed at the validation stage. Hence, the domain was analysed to determine the total root length per reference unit.

Figure 83, Figure 84 and Figure 85 show the outcomes of this processing stage, where several areas with a high density of roots can be identified. In order to further analyse the density variations, the maps were divided into homogeneous zones, as shown in Table 6. The minimum and maximum density values, the average density and standard deviation were calculated at every identified area.

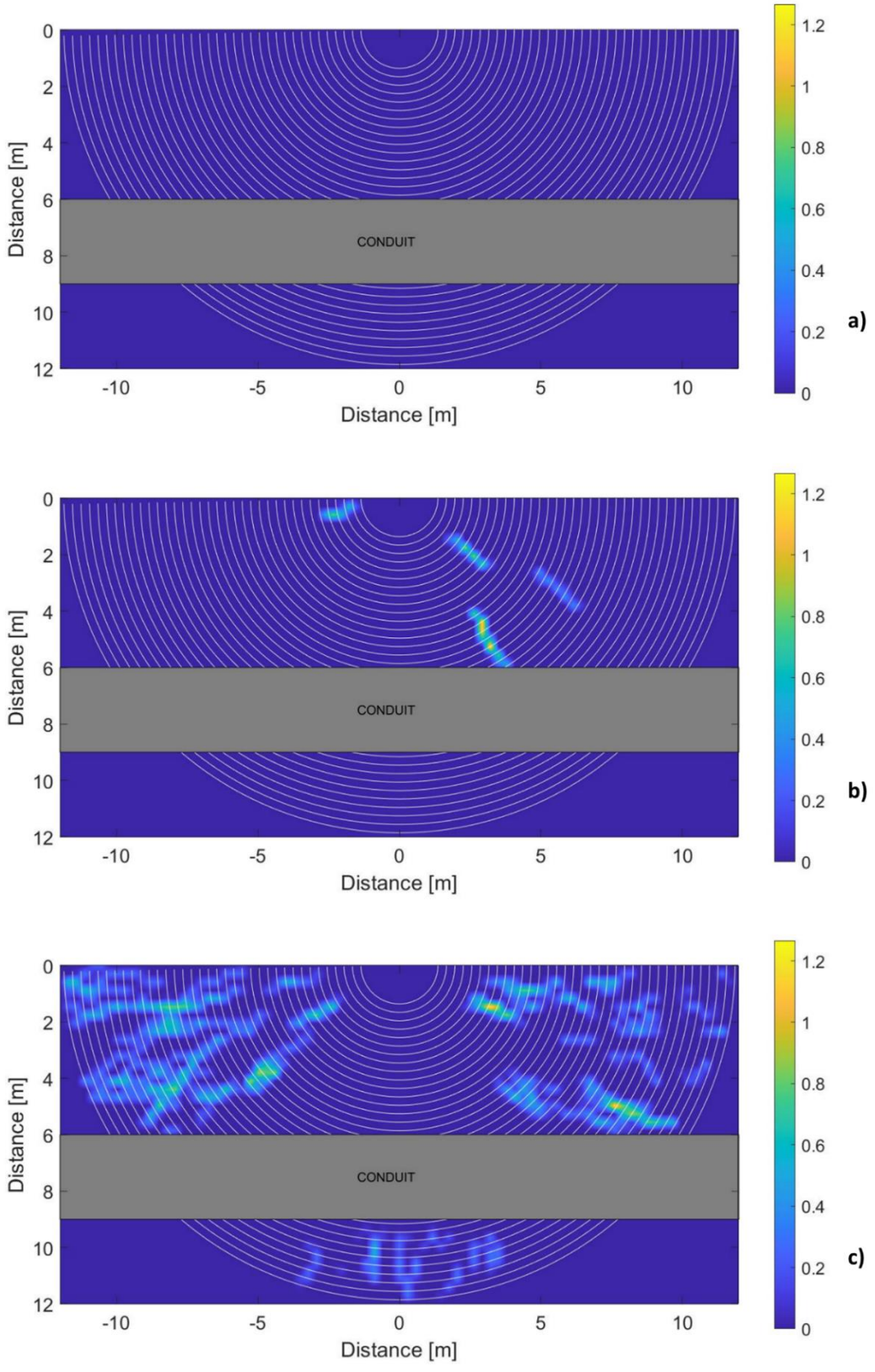

Figure 83: Root mass density maps at different depths: (a) from 0 m to 0.10 m, (b) from 0.10 m to 0.20 m, and (c) from 0.20 m to 0.30 m

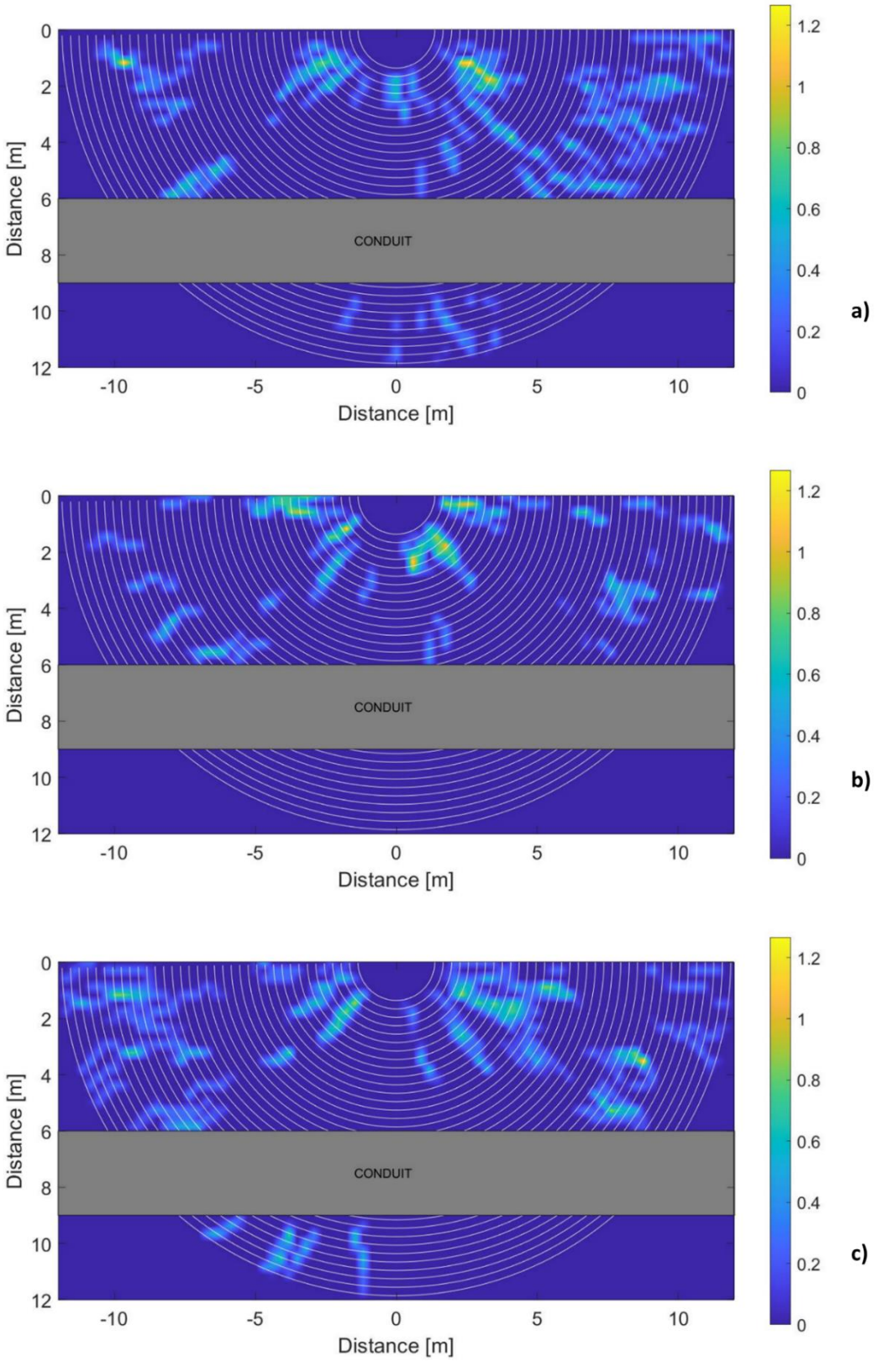

Figure 84: Root mass density maps at different depths: (a) from 0.30 m to 0.40 m, (b) from 0.40 m to 0.50 m, and (c) from 0.50 m to 0.60 m.

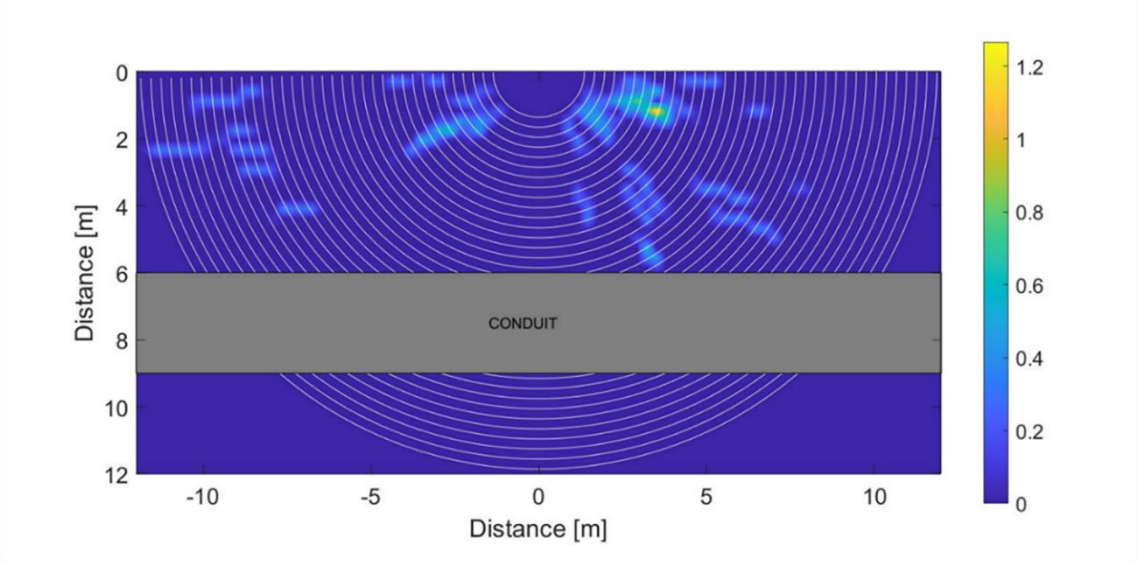

Figure 85: Root mass density map from 0.60 m to 0.70 m.

Table 6: Root mass density zoning for the investigated tree.

Root Mass Density Zoning								
Depth [m]	**x**		**y**		**Minimum Value [m/m³]**	**Maximum Value [m/m³]**	**Average Value [m/m³]**	**Standard Deviation [m/m³]**
	From [m]	To [m]	From [m]	To [m]				
0.10–0.20	−12.60	−8.40	0.00	4.20	0.00	0.00	0.00	0.00
	−8.40	−4.20	0.00	4.20	0.00	0.00	0.00	0.00
	−4.20	0.00	0.00	4.20	0.00	0.67	0.01	0.08
	0.00	4.20	0.00	4.20	0.00	0.76	0.02	0.10
	4.20	8.40	0.00	4.20	0.00	0.35	0.01	0.05
	8.40	12.60	0.00	4.20	0.00	0.00	0.00	0.00
	−12.60	−8.40	4.20	8.40	0.00	0.00	0.00	0.00
	−8.40	−4.20	4.20	8.40	0.00	0.00	0.00	0.00
	−4.20	0.00	4.20	8.40	0.00	0.00	0.00	0.00
	0.00	4.20	4.20	8.40	0.00	1.05	0.03	0.15

	4.20	8.40	4.20	8.40	0.00	0.00	0.00	0.00
	8.40	12.60	4.20	8.40	0.00	0.00	0.00	0.00
	−12.60	−8.40	8.40	12.60	0.00	0.00	0.00	0.00
	−8.40	−4.20	8.40	12.60	0.00	0.00	0.00	0.00
	−4.20	0.00	8.40	12.60	0.00	0.00	0.00	0.00
	0.00	4.20	8.40	12.60	0.00	0.00	0.00	0.00
	4.20	8.40	8.40	12.60	0.00	0.00	0.00	0.00
	8.40	12.60	8.40	12.60	0.00	0.00	0.00	0.00
0.20–0.30	−12.60	−8.40	0.00	4.20	0.00	0.91	0.15	0.21
	−8.40	−4.20	0.00	4.20	0.00	1.05	0.15	0.23
	−4.20	0.00	0.00	4.20	0.00	0.88	0.04	0.13
	0.00	4.20	0.00	4.20	0.00	1.44	0.06	0.19
	4.20	8.40	0.00	4.20	0.00	0.91	0.09	0.18
	8.40	12.60	0.00	4.20	0.00	0.58	0.05	0.12
	−12.60	−8.40	4.20	8.40	0.00	0.91	0.07	0.17
	−8.40	−4.20	4.20	8.40	0.00	1.07	0.06	0.17
	−4.20	0.00	4.20	8.40	0.00	0.00	0.00	0.00
	0.00	4.20	4.20	8.40	0.00	0.75	0.01	0.07
	4.20	8.40	4.20	8.40	0.00	1.41	0.10	0.21
	8.40	12.60	4.20	8.40	0.00	0.92	0.03	0.14
	−12.60	−8.40	8.40	12.60	0.00	0.00	0.00	0.00
	−8.40	−4.20	8.40	12.60	0.00	0.00	0.00	0.00

	−4.20	0.00	8.40	12.60	0.00	0.65	0.04	0.10
	0.00	4.20	8.40	12.60	0.00	0.36	0.04	0.09
	4.20	8.40	8.40	12.60	0.00	0.00	0.00	0.00
	8.40	12.60	8.40	12.60	0.00	0.00	0.00	0.00
0.30–0.40	−12.60	−8.40	0.00	4.20	0.00	1.27	0.05	0.15
	−8.40	−4.20	0.00	4.20	0.00	0.57	0.03	0.09
	−4.20	0.00	0.00	4.20	0.00	0.86	0.10	0.20
	0.00	4.20	0.00	4.20	0.00	1.27	0.14	0.24
	4.20	8.40	0.00	4.20	0.00	0.68	0.06	0.13
	8.40	12.60	0.00	4.20	0.00	0.73	0.10	0.17
	−12.60	−8.40	4.20	8.40	0.00	0.43	0.00	0.03
	−8.40	−4.20	4.20	8.40	0.00	0.74	0.04	0.13
	−4.20	0.00	4.20	8.40	0.00	0.00	0.00	0.00
	0.00	4.20	4.20	8.40	0.00	0.55	0.02	0.08
	4.20	8.40	4.20	8.40	0.00	0.76	0.08	0.17
	8.40	12.60	4.20	8.40	0.00	0.31	0.01	0.05
	−12.60	−8.40	8.40	12.60	0.00	0.00	0.00	0.00
	−8.40	−4.20	8.40	12.60	0.00	0.00	0.00	0.00
	−4.20	0.00	8.40	12.60	0.00	0.34	0.01	0.05
	0.00	4.20	8.40	12.60	0.00	0.50	0.03	0.09
	4.20	8.40	8.40	12.60	0.00	0.00	0.00	0.00
	8.40	12.60	8.40	12.60	0.00	0.00	0.00	0.00

0.40–0.50	−12.60	−8.40	0.00	4.20	0.00	0.35	0.02	0.07
	−8.40	−4.20	0.00	4.20	0.00	0.63	0.04	0.12
	−4.20	0.00	0.00	4.20	0.00	1.09	0.10	0.21
	0.00	4.20	0.00	4.20	0.00	1.06	0.12	0.23
	4.20	8.40	0.00	4.20	0.00	0.67	0.04	0.12
	8.40	12.60	0.00	4.20	0.00	0.65	0.04	0.12
	−12.60	−8.40	4.20	8.40	0.00	0.49	0.01	0.05
	−8.40	−4.20	4.20	8.40	0.00	0.62	0.03	0.11
	−4.20	0.00	4.20	8.40	0.00	0.00	0.00	0.00
	0.00	4.20	4.20	8.40	0.00	0.31	0.01	0.06
	4.20	8.40	4.20	8.40	0.00	0.39	0.01	0.05
	8.40	12.60	4.20	8.40	0.00	0.32	0.00	0.03
	−12.60	−8.40	8.40	12.60	0.00	0.00	0.00	0.00
	−8.40	−4.20	8.40	12.60	0.00	0.00	0.00	0.00
	−4.20	0.00	8.40	12.60	0.00	0.00	0.00	0.00
	0.00	4.20	8.40	12.60	0.00	0.00	0.00	0.00
	4.20	8.40	8.40	12.60	0.00	0.00	0.00	0.00
	8.40	12.60	8.40	12.60	0.00	0.00	0.00	0.00
0.50–0.60	−12.60	−8.40	0.00	4.20	0.00	1.01	0.12	0.19
	−8.40	−4.20	0.00	4.20	0.00	0.62	0.05	0.13
	−4.20	0.00	0.00	4.20	0.00	1.11	0.10	0.22
	0.00	4.20	0.00	4.20	0.00	1.02	0.16	0.24

	4.20	8.40	0.00	4.20	0.00	1.00	0.10	0.19
	8.40	12.60	0.00	4.20	0.00	1.41	0.07	0.17
	−12.60	−8.40	4.20	8.40	0.00	0.45	0.02	0.08
	−8.40	−4.20	4.20	8.40	0.00	0.60	0.04	0.11
	−4.20	0.00	4.20	8.40	0.00	0.00	0.00	0.00
	0.00	4.20	4.20	8.40	0.00	0.29	0.00	0.03
	4.20	8.40	4.20	8.40	0.00	1.00	0.05	0.14
	8.40	12.60	4.20	8.40	0.00	0.64	0.01	0.07
	−12.60	−8.40	8.40	12.60	0.00	0.00	0.00	0.00
	−8.40	−4.20	8.40	12.60	0.00	0.81	0.03	0.12
	−4.20	0.00	8.40	12.60	0.00	0.86	0.05	0.15
	0.00	4.20	8.40	12.60	0.00	0.00	0.00	0.00
	4.20	8.40	8.40	12.60	0.00	0.00	0.00	0.00
	8.40	12.60	8.40	12.60	0.00	0.00	0.00	0.00
0.60–0.70	−12.60	−8.40	0.00	4.20	0.00	0.34	0.04	0.09
	−8.40	−4.20	0.00	4.20	0.00	0.30	0.00	0.03
	−4.20	0.00	0.00	4.20	0.00	0.66	0.04	0.11
	0.00	4.20	0.00	4.20	0.00	1.24	0.10	0.18
	4.20	8.40	0.00	4.20	0.00	0.36	0.02	0.08
	8.40	12.60	0.00	4.20	0.00	0.00	0.00	0.00
	−12.60	−8.40	4.20	8.40	0.00	0.00	0.00	0.00
	−8.40	−4.20	4.20	8.40	0.00	0.35	0.01	0.04

	−4.20	0.00	4.20	8.40	0.00	0.00	0.00	0.00
	0.00	4.20	4.20	8.40	0.00	0.56	0.02	0.08
	4.20	8.40	4.20	8.40	0.00	0.33	0.01	0.06
	8.40	12.60	4.20	8.40	0.00	0.00	0.00	0.00
	−12.60	−8.40	8.40	12.60	0.00	0.00	0.00	0.00
	−8.40	−4.20	8.40	12.60	0.00	0.00	0.00	0.00
	−4.20	0.00	8.40	12.60	0.00	0.00	0.00	0.00
	0.00	4.20	8.40	12.60	0.00	0.00	0.00	0.00
	4.20	8.40	8.40	12.60	0.00	0.00	0.00	0.00
	8.40	12.60	8.40	12.60	0.00	0.00	0.00	0.00

From the analysis of the density maps, the domain portion with a greater root mass density is from a depth of 0.20 m to a depth of 0.60 m (Figure 83c and Figure 84). This is also supported by the analysis of the maximum values reported in Table 6 for these depths. More specifically, the left quadrant of the investigated domain presents a greater density of roots between 0.20 m and 0.30 m of depth, with maximum values ranging from 0.88 m/m^3 to 1.05 m/m^3 (Table 6 −x coordinates −12.60 m to 0.00 m, y coordinates 0.00 m to 4.20 m) (Figure 83c), and between 0.50 m and 0.60 m of depth, with maximum values between 1.00 m/m^3 and 1.11 m/m^3 (Table 6 −x coordinates −12.60 m to 0.00 m, y coordinates 0.00 m to 4.20 m) (Figure 84c). On the other hand, the right quadrant presents higher values of root density between 0.20 m and 0.40 m, with peaks up to 1.44 m/m^3 (Table 6 −x coordinates 0.00 m to 4.20 m, y coordinates 0.00 m to 4.20 m, depth 0.20–0.30 m) (Figure 83c and Figure 84a). A higher root density on the left and the right quadrants can be interpreted as an indirect consequence of the root system's interconnection with two adjacent trees, located

respectively on the North-West and the South-East directions from the investigated one. In fact, it is reasonable to assume that the root density of a specific tree could be higher at root interconnection areas, as roots of individual trees tend to have a closer arrangement between themselves, due to their own interaction with the root systems of adjacent trees. Finally, it should be emphasised that, although the aforementioned high root density concentrations are present, the average density values are still low across the overall investigation area. This confirms that, for each homogeneous area identified, an important amount of areas with very low or zero density can be found.

5.2.1.2.5. Results Validation through Excavation

A representative excavation section was identified after the application of the data processing framework in order to limit the validation stage to a useful portion of the overall investigated area (i.e., 218.04 m^2).

A square area of 4 × 4 m was therefore selected on the South-West side of the investigated tree (Figure 86). The selection was made based on the root mass density distribution in the area and their expected depth. The excavation was performed by removing layers of ~0.10 m of soil up to ~0.50 m. It is worth noting that the soil was significantly dry and compact in the whole excavation area. Its removal therefore presented considerable difficulties, as the excavation had to be carried out with reduced size tools in order to ensure accurate operations and avoid accidental damage of the roots.

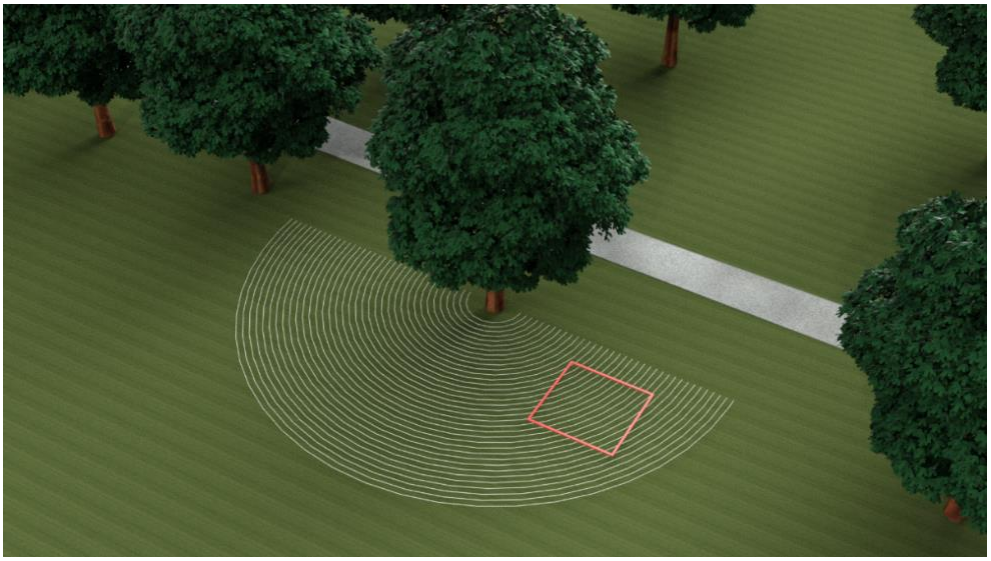

Figure 86: Rendering of the surveyed area, showing the position of the excavated site.

Several roots were found as a result of the validation survey, as shown in Figure 87. A root with an average diameter of 0.06 m crosses the bottom-right part of the excavation for a length of approximately 2.53 m, at a depth varying between 0.26 m and 0.50 m. However, a local increase in density was not found in the concerning density maps (i.e., depth ranges between 0.20 m and 0.30 m, between 0.30 m and 0.40 m, and between 0.40 m and 0.50 m). This is due to the particular orientation of the root that crosses the investigated area along the South-East—North-West direction, transversely to an imaginary radial line traced from the trunk of the tree investigated (Figure 88).

Figure 87: The excavated site.

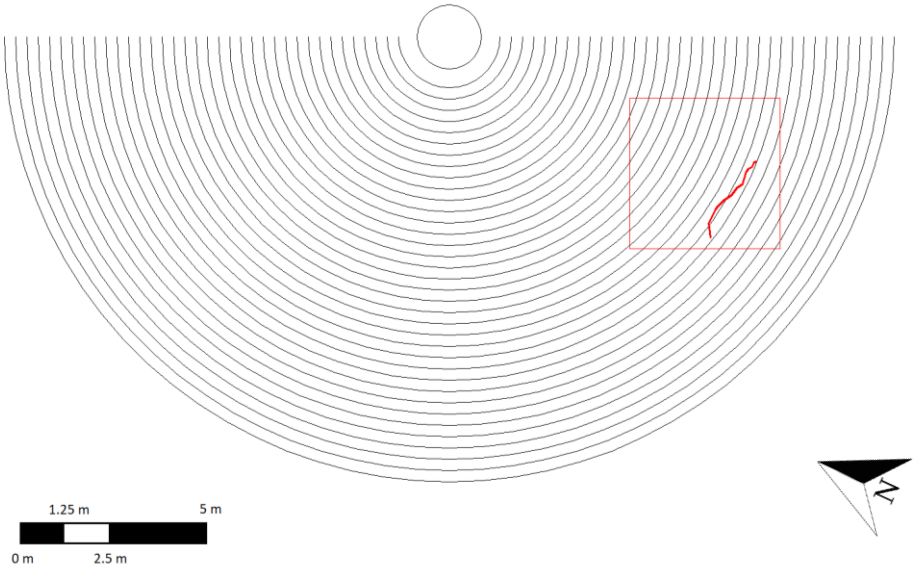

Figure 88: An outline of the survey, showing the orientation of the excavated coarse root (in red) within the test pit area.

Given a typical configuration of a root system, where roots expand radially from the centre of the tree outwards, it is unlikely that the identified coarse root belongs to the tree under consideration. On the contrary, this root likely belongs to the tree located in the vicinity of the investigated one, as its direction matches with that conceivable for

the nearby root system (see Figure 72). This result proves the validity of the proposed methodology in automatically excluding targets not belonging to the investigated tree.

A cluster of roots was also found at the top of the excavation area at a depth between approximately 0.20 m and 0.25 m. Its position matches with the outcomes of the map in the depth range 0.20 ÷ 0.30 m (Figure 89). Similarly, a root with an average diameter of 0.04 m was excavated at the top-right corner, and an evidence was again found in the 0.20–0.30 m density map.

Finally, the left-hand side of the excavation area was dug to validate the local density increase, as highlighted by Figure 90c and Figure 91c. Two roots with an average diameter of 0.04 m and a depth varying from 0.05 m (top-left corner) to 0.20 m (bottom-left corner) were excavated. Considering their position and the diameter similarity, it is reasonable to state that these sections belong to the same root that develops deeper than the performed excavation depth for a short stretch. As shown in Figure 90 and Figure 91, the development of the excavated roots resembles the outputs of the density maps. Lastly, roots of smaller dimensions, grouped together to form a single cluster, were found at a short distance from the two aforementioned roots (Figure 91a).

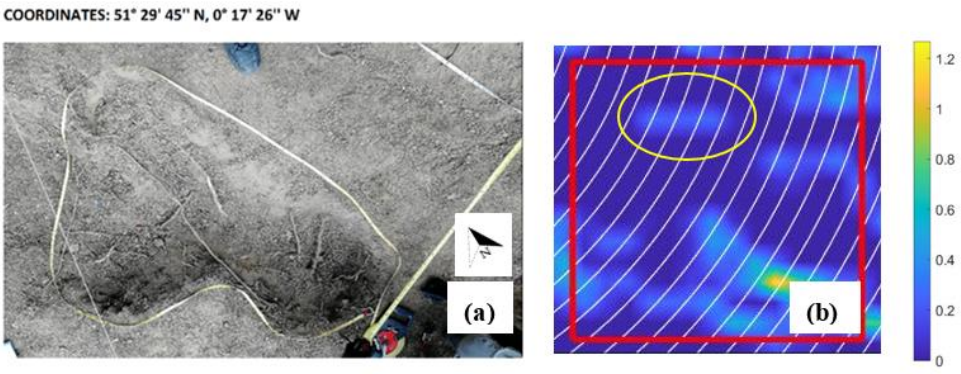

Figure 89: (a) The excavated root cluster, and (b) a close-up view of the 0.20–0.30 m density map. The yellow circle highlights an area with increased density, corresponding to the cluster of roots.

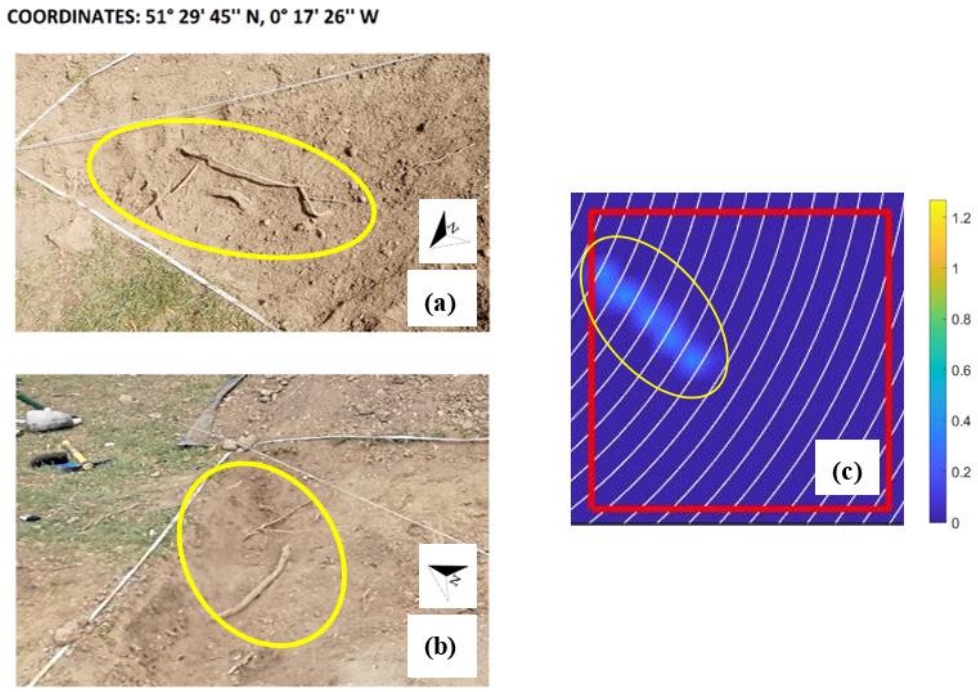

Figure 90: The excavated root at the top-left corner of the excavated area, (a) detail of the excavation, (b) development of the root, and (c) a close-up view of the 0.10–0.20 m density map. The yellow circle highlights an area with an increased density, corresponding to the excavated root.

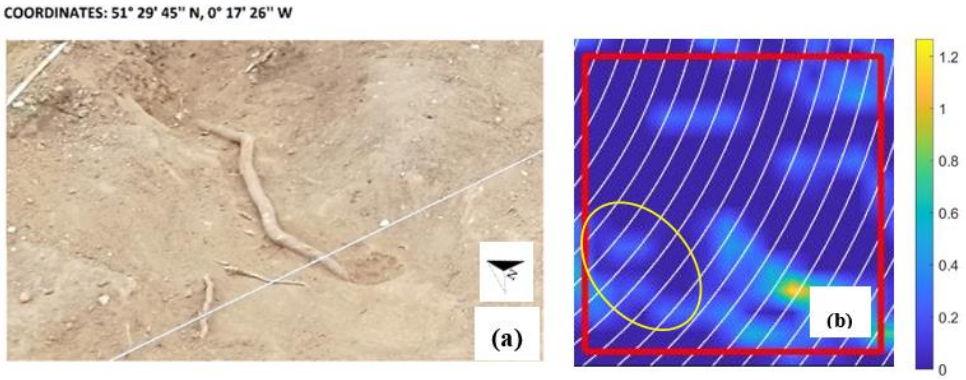

Figure 91: The excavated root at the bottom-left corner of the excavated area, (a) development of the root, and (b) a close-up view of the 0.20–0.30 m density map. The yellow circle highlights an area with an increased density, corresponding to the excavated root.

In addition, the presence of numerous boulders was detected (Figure 92), the main size of which exceeded 0.15 m in some cases. Some of the boulders were found along the top edge of the excavation area, whereas other boulders were found along the left edge.

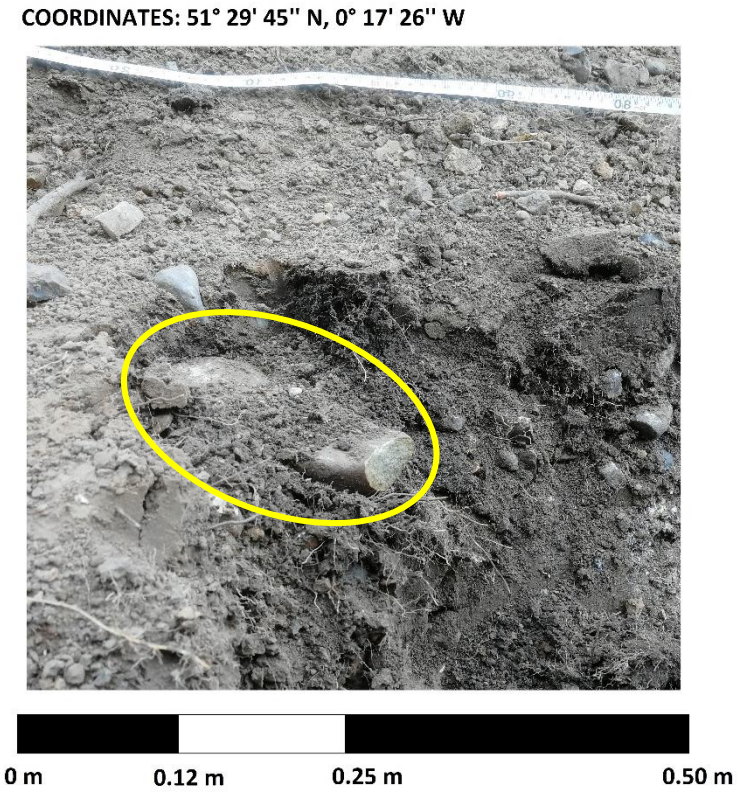

Figure 92: Boulders found along the top edge of the excavation area. The boulder in the foreground has a main axial dimension of approximately 0.15 m.

However, no evidence of their presence was found in the root mass density maps. This confirms the validity of the proposed algorithm, as this is designed not to consider short segments, not correlated with root targets.

5.2.1.3. Conclusions

The present study clearly demonstrated that the use of NDT methods for the investigation of tree root systems is the new frontier of forestry practices and the conservation of the naturalistic heritage. Due to its ease of use, non-intrusiveness and cost-effectiveness, the viability of the GPR technique was proven for root inspection purposes, with a special focus on root detection and the three-dimensional mapping of the root system architecture.

It is believed that this research has contributed and added value to the existing knowledge within the context of understanding the conditions of tree roots in complex

urban environments, supporting the premise that GPR is a powerful NDT method for large-scale forestry applications.

This research line addresses the following objective of the present Thesis (see Section 3.1):

- *to develop novel survey methodologies for three-dimensional root mapping:* in this research, a novel circular survey methodology is employed for GPR data collection, in order to ensure a quasi-perpendicular scanning of the root systems. The cylindrical coordinates system employed has allowed for a comprehensive investigation of the surveyed root systems. Moreover, it has been proven that the selected GPR antenna frequency is suitable for tree root investigation. The set objective is therefore considered achieved.
- *to develop enhanced data processing algorithms and interpretation techniques for tree assessment:* a novel data processing algorithm is developed for the reconstruction of tree root systems. Explanation is given of the assumptions made and the data processing techniques used. Results have shown potential of the proposed technique. The set objective is therefore considered achieved.
- *to estimate tree roots mass density:* a novel index for the estimation of tree root mass density is proposed, in an attempt to overcome the difficulties achieved by the existing evaluation methods. The proposed methodology has proven potential in achieving the result, therefore the set objective is achieved.

5.2.2. Evaluation of Tree Root System Interconnections

5.2.2.1. Methodology

5.2.2.1.1. The Test Site

The survey was carried out in Ealing, London (United Kingdom). The investigated area is part of the University of West London (UWL) premises, and was chosen due to the favourable condition of proximity between the investigated trees (Figure 93). To this extent, the soil between a maple tree (trunk circumference 1.91 m, average radius 0.30 m), and an ash tree (trunk circumference 0.98 m, average radius 0.156 m), was surveyed. The trees were 6.70 m apart from each other.

Figure 93: An overview of the investigated area during the GPR survey.

5.2.2.1.2. The GPR Survey Technique

The experimental design refers to the methodology descripted in Section 5.1.3 and the description given in Section 5.2.2.1.2. A set of 20 semi-circular scans were performed around the maple tree trunk. The first survey transect was positioned 0.50 m from the bark, and the spacing between the lines of the scan was 0.30 m. Likewise, 5 circular scans, starting 0.80 m from the bark and distributed at 0.30 m intervals, were carried out around the trunk of the ash tree. To this effect, an overall area of 65.43 m^2 was surveyed around the maple tree, with an outer radius of 6.50 m and an inner radius of 0.80 m. In regard to the ash tree, an overall area of 11.73 m^2 with an outer radius of 2.16 m and an inner radius of 0.96 m was covered. The purpose of this setup was to create a 5.37 m^2 area of survey, within which potential interconnections between the two root systems could be investigated (Figure 94).

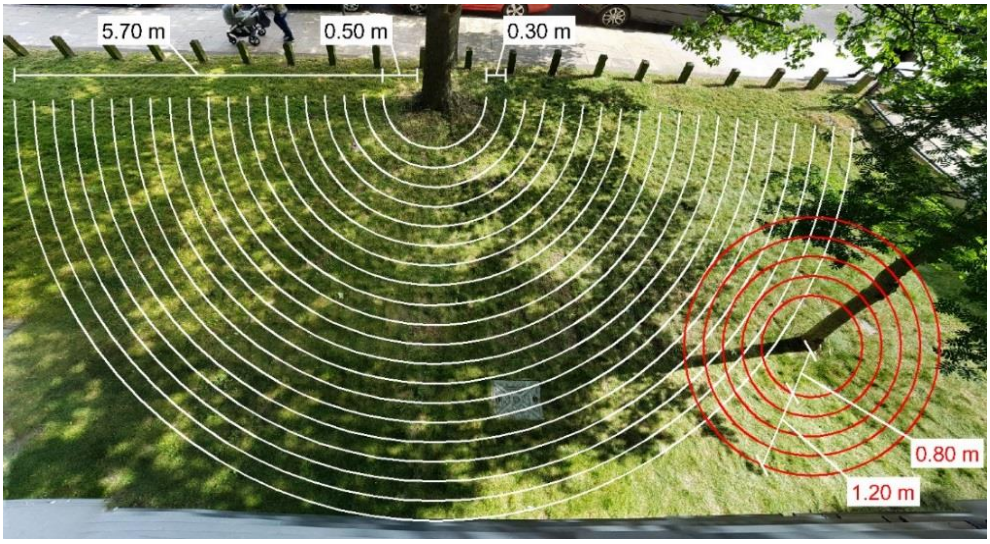

Figure 94: The survey scheme.

5.2.2.1.3. The GPR Equipment

The Opera Duo ground-coupled GPR system, manufactured by IDS Georadar (part of Hexagon) was used for testing purposes (Figure 95). The system is equipped with 700 MHz and 250 MHz central frequency antennas. Data were collected using a time

window of 80 ns and 512 samples. The horizontal resolution was set to 3.2×10^{-2} m. In order to be able to achieve the highest resolution as well as an effective depth of detection, only data collected using the 700 MHz antenna were analysed (Benedetto, et al., 2011; Benedetto, et al., 2013).

Figure 95: Opera Duo GPR system by IDS Georadar (Part of Hexagon) deployed in the survey of the ash tree.

5.2.2.2. Results

The pre-processing algorithm was first applied to the raw data in order to achieve a better visualisation of the targets (hyperbolae) and understanding of details. As an example, Figure 96 reports a longitudinal B-scan obtained along the fourth scan from the bark (the one with radius equal to 1.70 m), before (Figure 96a) and after (Figure 96b) the application of the pre-processing algorithm. It can be observed that the visualisation of the deeper targets has been enhanced by the application of the time-varying gain technique. This permitted the attenuated hyperbolae to be observed and,

as a consequence, increased the likelihood that the algorithm could reconstruct the root system in its entirety with more accuracy.

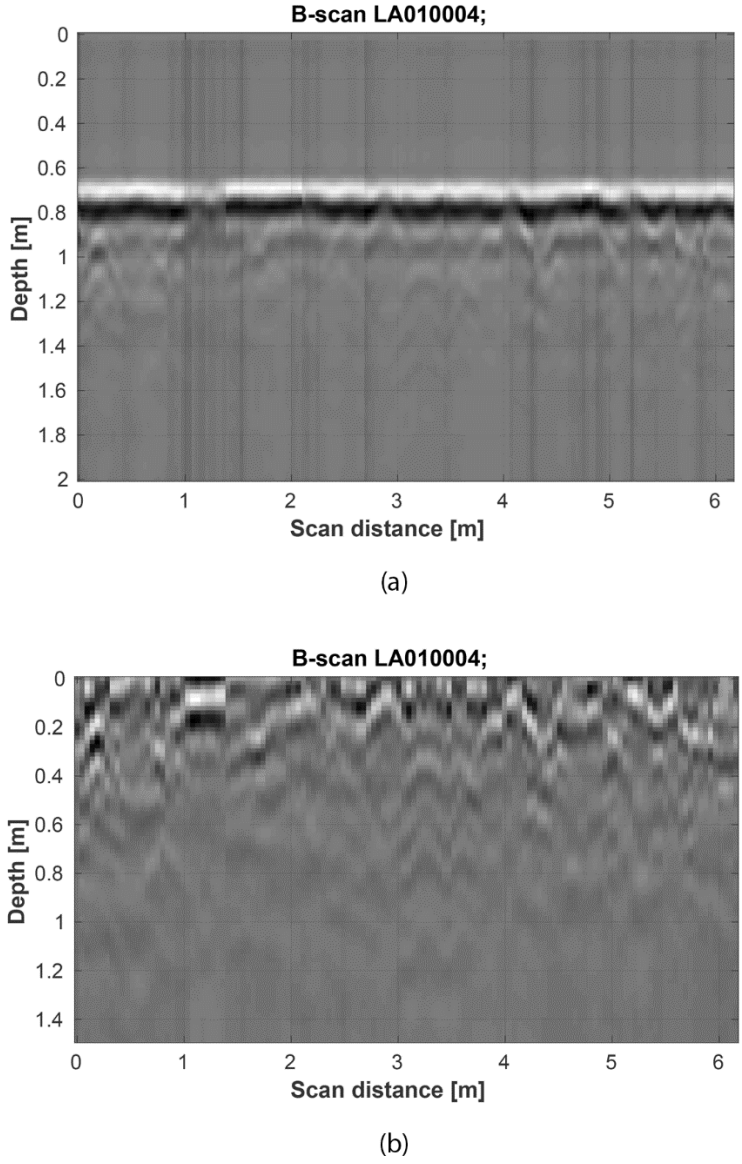

Figure 96: An example of B-scan before (a) and after (b) the application of the pre-processing algorithm.

Following this, the multi-stage algorithm for tracking the tree roots was applied to the processed data. This allowed for the reconstruction of a three-dimensional model of the tree root system architecture of the two investigated trees. Figure 97 shows the results of the application of this methodology to the root system of the maple tree, both in a 2D planar view (Figure 97a) and using a 3D model (Figure 97b). To make

interpreting the results easier, roots located within shallow soil (the first 0.25 m of soil) and deep soil (below 0.25 m of soil) are represented in different colours.

From the analysis of the outputs, the algorithm demonstrated potential in finding paths compatible with root trends. For the sake of consistency, the coordinates of the points were double-checked with the positions of the hyperbola apices detected in the collected B-scans. From the analysis of the B-scans, the hyperbolas turned out to be concentrated within the first 0.60 m of subsoil. On the other hand, the amplitude values for the deeper roots were not detected and considered by the algorithm, given the defined threshold. This occurrence was observed although the presence of deeper reflections, which became visible after the application of the time-varying gain function. However, this result is in line with expectations as maple trees generally possess superficial root systems (Crow, 2005). It is known that the roots of this tree usually develop within the first meter of soil and do not reach larger depths.

As shown in Figure 97, some areas where root tracking is not continuous can be seen. A possible explanation for this can be the presence of subsoil areas characterised by higher moisture content or heavily consolidated clay. Another possible explanation for this result could be the presence of roots that have short horizontal development before going deeper in a quasi-vertical direction. Furthermore, in order to avoid the inclusion of non-root targets within the soil, such as cables or utilities, the algorithm is arranged to eliminate shorter roots.

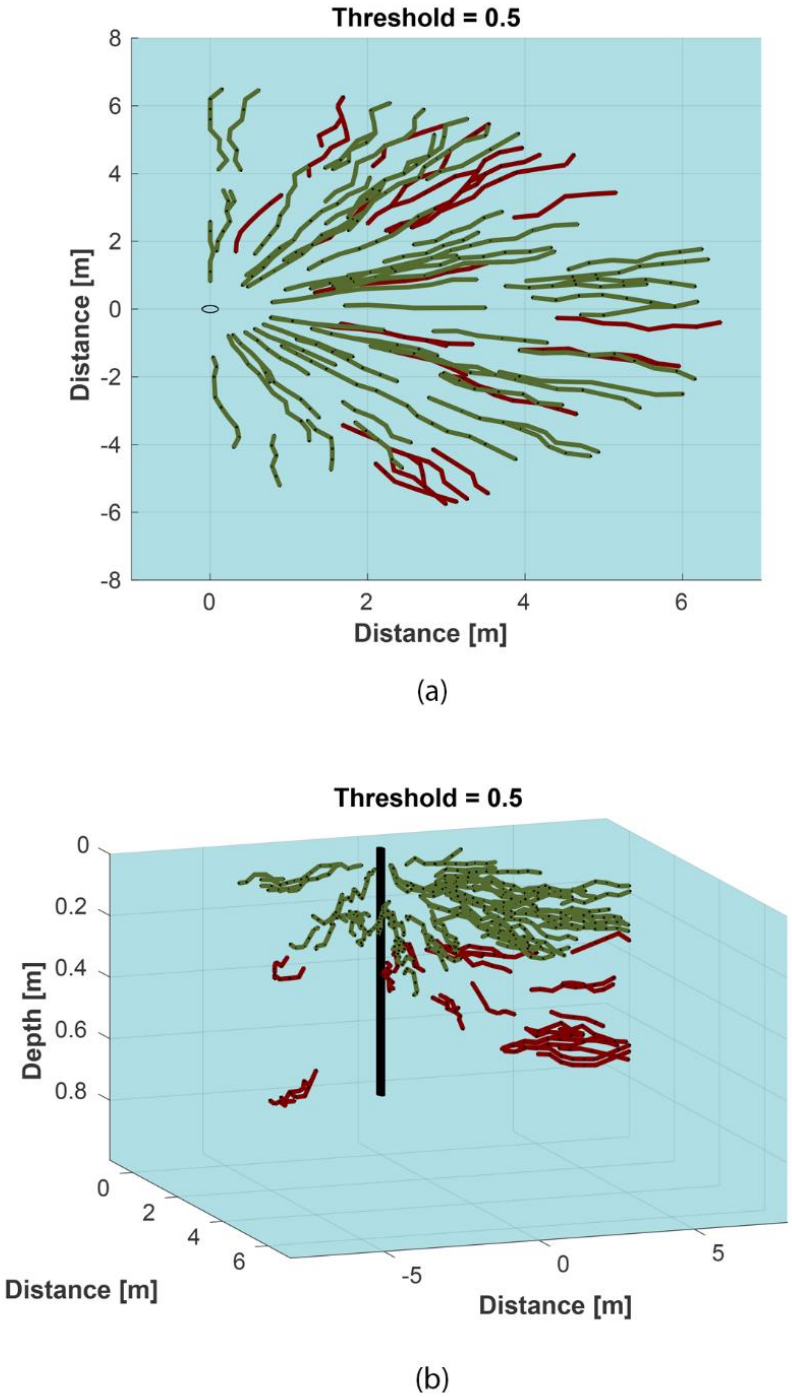

Figure 97: Result of the application of the multi-stage data processing algorithm to the investigated maple tree in a 2-D plan view (a) and using a 3-D rendering (b). Shallow roots (i.e. up to 0.25 m of depth) are highlighted in green, while deeper roots (i.e. deeper roots (i.e. deeper than 0.25 m) are shown in brown.

The application of this methodology to both the investigated tree root systems (maple and ash trees) allowed for a more comprehensive interpretation of the interaction between the two root systems. In addition, the algorithm aided the understanding of the spread of the roots, and the soil use between the two investigated trees. Figure 98a and Figure 98b show a rendering of the surveyed root systems and detail of the investigation area, where an interaction between the root systems is clearly visible.

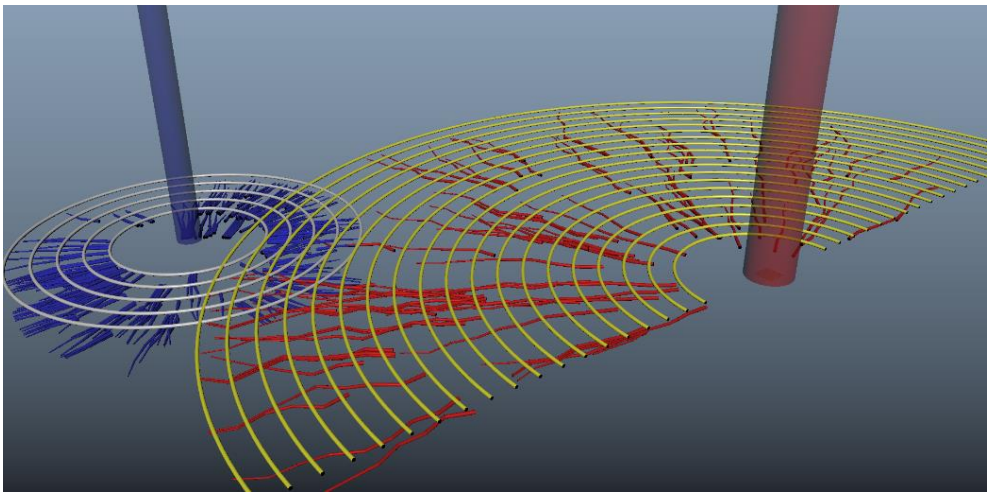

(a)

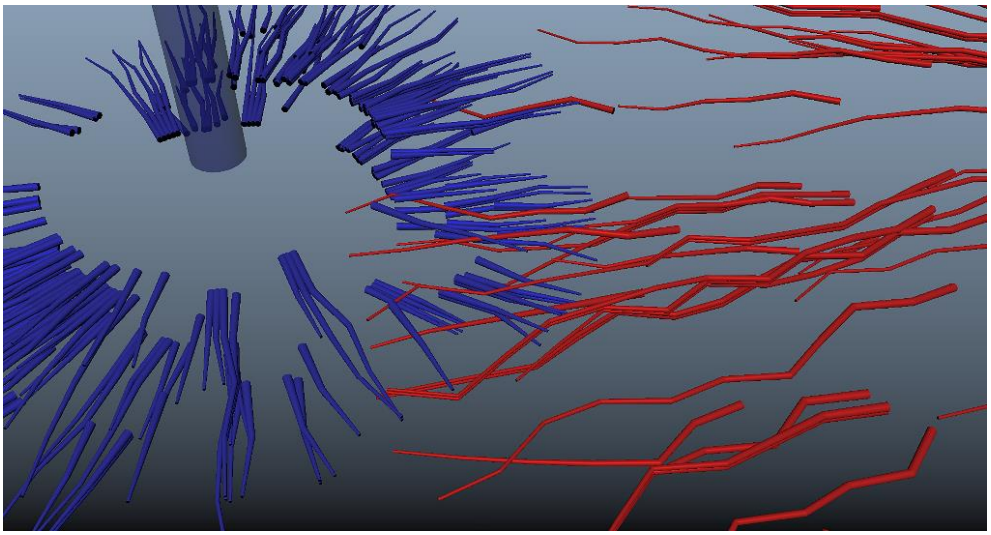

(b)

Figure 98: Overview of the investigated tree root systems (a) and detail of the interaction area (b) (red roots: maple tree; blue roots: ash tree).

The architecture of both root systems and their development in soil was further investigated using a density index and the creation of density maps. The domain was divided into reference units in the form of cuboids, with surfaces 0.30 m x 0.30 m and depths 0.10 m. Therefore, 6 levels of depth were created, in which the total root length per reference unit was estimated. Figure 99 shows the output of this data processing stage in the form of density maps. In this regard, it is worth mentioning that the density values have been normalised.

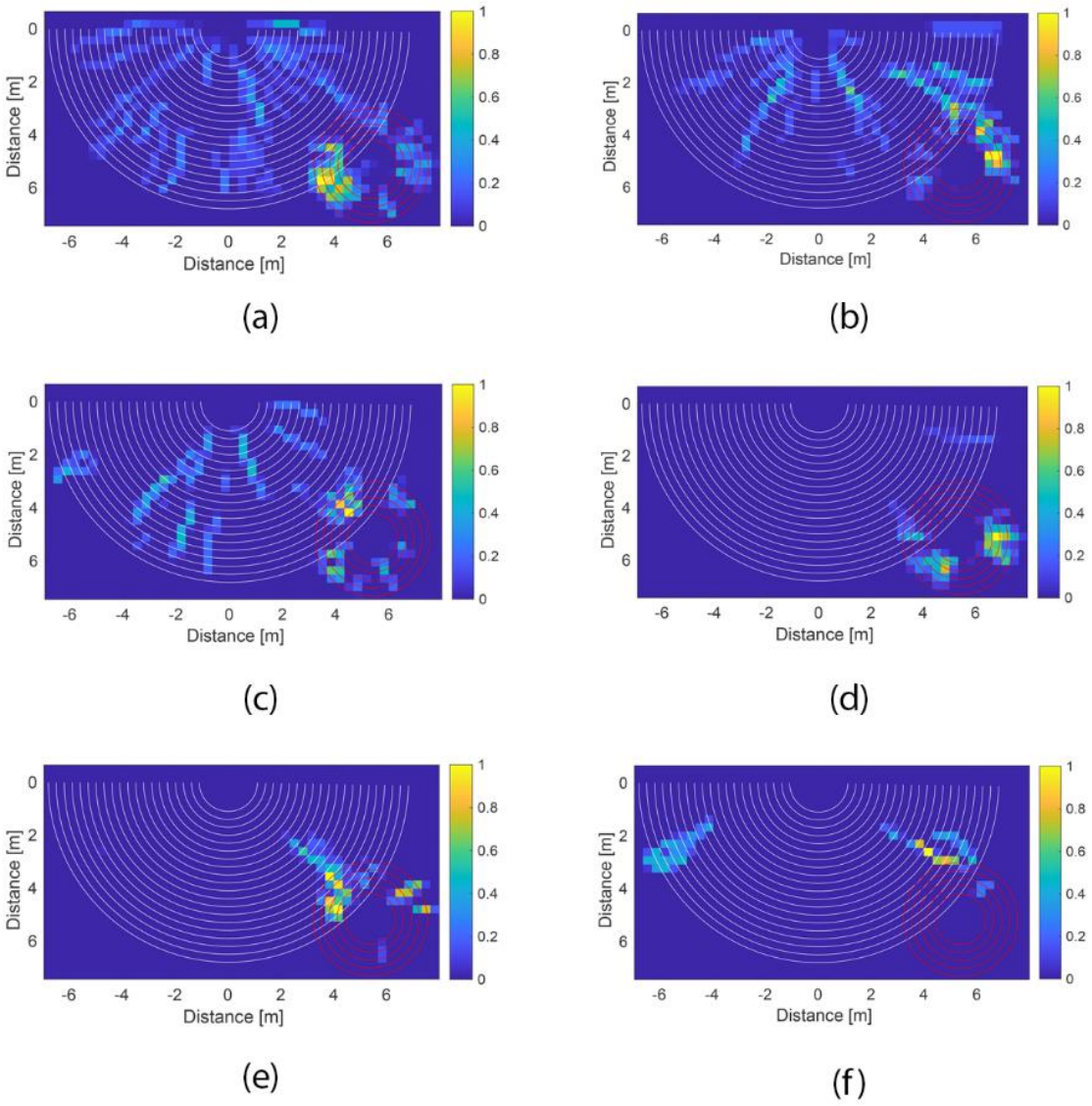

Figure 99: GPR-derived root density maps, related to the following depths: a) from 0 m to 0.10 m; b) from 0.10 m to 0.20 m; c) from 0.20 m to 0.30 m; d) from 0.30 m to 0.40 m; e) from 0.40 m to 0.50 m f) from 0.50 m to 0.60 m.

Regarding the maple tree, it can be observed that its roots were distributed within the first 0.30 m of depth from the surface. The density index was generally low, with average values ranging from 0.03 m/m^3 in the first 0.10 m of soil, 0.03 m/m^3 between 0.10 m and 0.20 m and 0.02 m/m^3 between 0.20 m and 0.30 m deep. Standard deviations for these depth ranges are 0.07, 0.08 and 0.07, respectively.

In regard to the ash tree, the average density value was 0.07 m/m^3 within the first 0.10 m of soil, 0.09 m/m^3 from 0.10 m to 0.20 m, 0.05 m/m^3 from 0.20 to 0.30 m, 0.09 m/m^3 from 0.30 m to 0.40 m, 0.03 m/m^3 from 0.40 m to 0.50 m. It is also observed that the average tends to zero in the last layer (i.e. from 0.50 m to 0.60 m of depth). Standard deviations for these values are 0.13, 0.20, 0.11, 0.19, 0.13 and 0.03.

Table 7 and Table 8 list the areas in which the root length density reached significant values, for the maple and the ash tree respectively.

An interesting observation is that the root density tends to decrease as the distance from the bark increases. However, root density increases locally in the interaction area between the two trees. Table 9 reports the zones of increased density within the common investigation area.

This result shows the potential interaction between the root systems of the investigated maple and ash trees, especially in the first 0.30 m of soil and within a depth of 0.40 m to 0.60 m.

Table 7: Zones of increased density for the maple tree.

MAPLE TREE							
x		**y**		**z**		**Maximum values [m/m³]**	**Description**
from [m]	**to [m]**	**from [m]**	**to [m]**	**from [m]**	**to [m]**		
0.9	1.5	2.7	3.6	0.0	0.1	0.39	Local spots of increased density - low values
1.8	2.7	0.0	0.3			0.46	Local spots of increased density - medium values
3.0	3.3	5.4	6.0			0.39	Local spots of increased density - low values Boundary with the interconnection area
-0.9	-1.5	2.1	3.0	0.1	0.2	0.52	Local spots of increased density - medium values
0.9	1.8	1.8	3.0			0.62	Elongated increase in density - low to medium values
2.7	6.0	1.5	3.0			0.57	Local increases in density along the same direction - low to medium values Boundary with the interconnection area
-0.9	-1.5	4.2	5.4	0.2	0.3	0.47	Elongated increase in density - low to medium values
-1.8	-2.7	3.0	4.2			0.54	Elongated increase in density - low to medium values
0.6	1.2	1.8	3.0			0.50	Elongated increase in density - low to medium values
2.7	3.3	3.0	3.6	0.4	0.5	0.54	Local spots of increased density - medium values Boundary with the interconnection area
-4.2	-5.7	2.4	3.6	0.5	0.6	0.45	Elongated increase in density - low to medium values
2.7	3.0	2.1	2.4			0.39	Local spots of increased density - low values
3.6	3.9	2.4	2.7			0.76	Local spots of increased density - high values Boundary with the interconnection area
4.5	4.8	2.1	2.4			0.39	Local spots of increased density - low values

Table 8: Zones of increased density for the ash tree.

ASH TREE							
x		**y**		**z**		**Maximum values [m/m³]**	**Description**
from [m]	**to [m]**	**from [m]**	**to [m]**	**from [m]**	**to [m]**		
3.6	4.5	6.3	6.6	0.0	0.1	0.68	Elongated increase in density - medium values Boundary with the interconnection area
6.0	6.3	4.5	5.7			0.42	Local increases in density - medium values
5.7	6.9	3.6	5.4	0.1	0.2	1.00	Elongated increase in density - medium to high values Boundary with the interconnection area
3.6	4.2	6.3	6.6	0.2	0.3	0.62	Local spots of increased density - medium values Boundary with the interconnection area
5.4	5.7	6.3	6.6			0.48	Local increases in density - medium values
6.3	6.6	0.9	1.2			0.42	Local increases in density - medium values
4.2	4.8	6.3	6.6	0.3	0.4	0.76	Local spots of increased density - medium to high values Boundary with the interconnection area
6.0	7.2	4.8	6.3			1.00	Elongated increase in density - medium to high values
6.0	7.2	4.2	5.4	0.4	0.5	0.76	Elongated increase in density - medium to high values

Table 9: Zones of increased density within the interconnection area.

INTERCONNECTION AREA							
x		y		z		Maximum values [m/m³]	Description
from [m]	to [m]	from [m]	to [m]	from [m]	to [m]		
3.3	4.5	1.5	6.3	0.0	0.1	1.00	Extended spot of increased density - low to high values
4.5	5.7	3.0	3.6	0.1	0.2	0.71	Elongated increase in density - medium to high values
3.6	4.8	3.3	4.5	0.2	0.3	0.86	Elongated increase in density - medium to high values
3.6	4.2	5.7	6.0			0.62	Local spots of increased density - medium values
3.6	3.9	5.1	5.4	0.3	0.4	0.46	Local spots of increased density - medium values
3.9	5.1	6.0	6.3			0.61	Elongated increase in density - medium values
3.3	4.5	3.3	5.7	0.4	0.5	0.92	Extended spot of increased density - low to high values
4.2	5.7	3.0	3.3	0.5	0.6	0.79	Elongated increase in density - medium to high values

5.2.2.3. Conclusions

The results of the presented case study clearly demonstrate the effectiveness of GPR for root detection and the reconstruction of tree root system architecture. A rendering of the root system was successfully recreated, based on real GPR data, through the development and application of a novel multi-phase signal processing method. Furthermore, the interconnectivity between the two root systems was investigated by the means of a state-of-the-art method, based on the evaluation of a root density index and the subsequent production of root density maps at different depths.

In terms of the appropriateness of the survey methodology, it is essential to emphasise that a novel experimental approach was put into practice in order to compile the data. In practice, the GPR survey was performed using circular transects with pre-defined spacing around the investigated tree targets. A comprehensive collection of

information from the root system was therefore ensured. Moreover, results have proven the effectiveness of a 700 MHz central frequency GPR antenna used in this investigation, as this allowed for information on deeper roots to be obtained, while ensuring an adequate data resolution. The high capability of this antenna frequency system made it possible to detect both superficial (within the first 0.25 m from the soil surface) and deeper (lower than 0.25 m from the soil surface) targets, which has allowed for a comprehensive reconstruction of the tree root system.

As far as the adopted data processing methodology is concerned, the visualisation of the reflection hyperbolas relating to the tree roots was successfully improved by the application of a pre-processing algorithm. This step finds its importance in the removal of the main signal noise and the amplification of reflections from the deepest roots. No doubt, this was instrumental for the interpretation of the processed data at later stages. It could be concluded that the application of the root tracking algorithm (newly developed in-house) was, therefore, less prone to errors and false detection of roots due to the misinterpretation of data.

In terms of the assessment of the root mass density, it is imperative to stress that the existing evaluation methods have failed to provide accurate estimations. Within this context, a novel emerging approach was presented in this study which is based on the evaluation of an innovative root density index. This approach allows for the detection and the assessment of the areas of potential root interconnectivity. It was observed that root density increases locally in the interaction areas between the root systems of different trees. Not least, the importance of evaluating tree root density is essential for several purposes, ranging from the stability and the overall health of the tree to the safety of the surrounding environment.

This research line addresses the following objective of the present Thesis (see Section 3.1):

- *to develop novel survey methodologies for three-dimensional root mapping:* in this research, a novel circular survey methodology is employed for GPR data collection, in order to ensure a quasi-perpendicular scanning of the root systems. The cylindrical coordinates system employed has allowed for a comprehensive investigation of the surveyed root systems. Moreover, it has been proven that the selected GPR antenna frequency is suitable for tree root investigation. The set objective is therefore considered achieved.
- *to develop enhanced data processing algorithms and interpretation techniques for tree assessment:* a novel data processing algorithm is developed for the reconstruction of tree root systems. Explanation is given of the assumptions made and the data processing techniques used. Results have shown potential of the proposed technique, although some uncertainties still remain on the interpretation of results. The set objective is therefore partially achieved, as the methodology needs to be refined.
- *to estimate tree roots mass density:* a novel index for the estimation of tree root mass density is proposed, in an attempt to overcome the difficulties achieved by the existing evaluation methods. The proposed methodology has proven potential in achieving the result, therefore the set objective is achieved.
- *to assess mutual interaction between root systems of different tree species:* the proposed methodology was tested in an area of potential root interconnection between trees belonging to different species. The use of the proposed root mass density index has helped in the identification of zones of increased root

density, proving the presence of interconnected root systems in the identified area. The set objective is therefore considered achieved.

5.2.3. Assessment of Tree Root Systems for Street Trees

The importance of street trees in the urban environment is widely recognised. Nevertheless, the absence of proper urban planning, combined with lack of resources and methodologies for road maintenance, have made the interaction between trees and the urban environment as a priority task to pursue. The uncontrolled development of tree roots can cause extensive damage, such as the cracking and uplifting of pavement and curbs, that could seriously endanger safety of pedestrians, cyclists and drivers. Within this framework, GPR has already proven its effectiveness for the non-destructive evaluation and monitoring of road pavements. The following case study aims to demonstrate the potential of GPR in mapping the root system architecture of street trees.

5.2.3.1. Methodology

5.2.3.1.1. The Test Site

The survey was carried out in Gunnersbury Park, Ealing, London (United Kingdom). The tree under investigation was selected as it was located in the proximity of a sidewalk (Figure 100).

Figure 100: The surveyed area. The yellow tapes indicate one out of the twenty-one semi-circular survey scans around the investigated tree. Notice that the survey line includes measurements both on top of the soil and on top of the road pavement surface.

5.2.3.1.2. The GPR Survey Technique

As per the previous case studies, the experimental design refers to the methodology descripted in Section 5.1.3. A set of 21 semi-circular scans were performed around the investigated tree. The first survey transect was positioned 0.50 m from the bark, and the spacing between the lines of the scan was 0.30 m. Consequently, an overall area of 175.67 m^2 was surveyed around the tree, with an outer radius of 7.66 m and an inner radius of 1.66 m. Setup was planned in order to include a road section with a flexible pavement structure within the surveyed area (see Figure 100). To this effect, the dataset includes information collected above a natural soil and an asphalt-covered road surface.

5.2.3.1.3. The GPR Equipment

As per the above mentioned case studies in this Chapter, the Opera Duo ground-coupled GPR system, manufactured by IDS GeoRadar (part of Hexagon) was used

for testing purposes. The system is equipped with 700 MHz and 250 MHz central frequency antennas. Data were collected using a time window of 80 ns, which was discretised across 512 samples. The horizontal resolution was set to 3.06×10^{-2} m. In order to balance between resolution and penetration depth, only data collected using the 700 MHz antenna were analysed.

5.2.3.2. Results

The proposed acquisition method allowed for a comprehensive identification and localisation of the roots. The pre-processing algorithm was applied to the collected data in order to achieve an enhanced visualisation of the targets. As an example, Figure 101 reports a longitudinal B-scan collected along the 7^{th} scanline.

Figure 101a shows the B-scan before the application of the processing, whereas Fig. Figure 101b shows the B-scan after the application of the main data processing techniques. The presence of road layers is clearly visible on the left side of the B-scans. In this regard, the analysis of the signal reflectivity, as described in Section 5.1.2, has shown effectiveness in automatically detecting the presence of a road structure (Figure 101c), thus allowing for a targeted application of the SVD filter (Figure 101d).

In addition, a C-scan image of the the investigated area at a depth of 0.19 m is provided (Figure 102). Notice that the presence of a road pavement is evident in the upper part of the image.

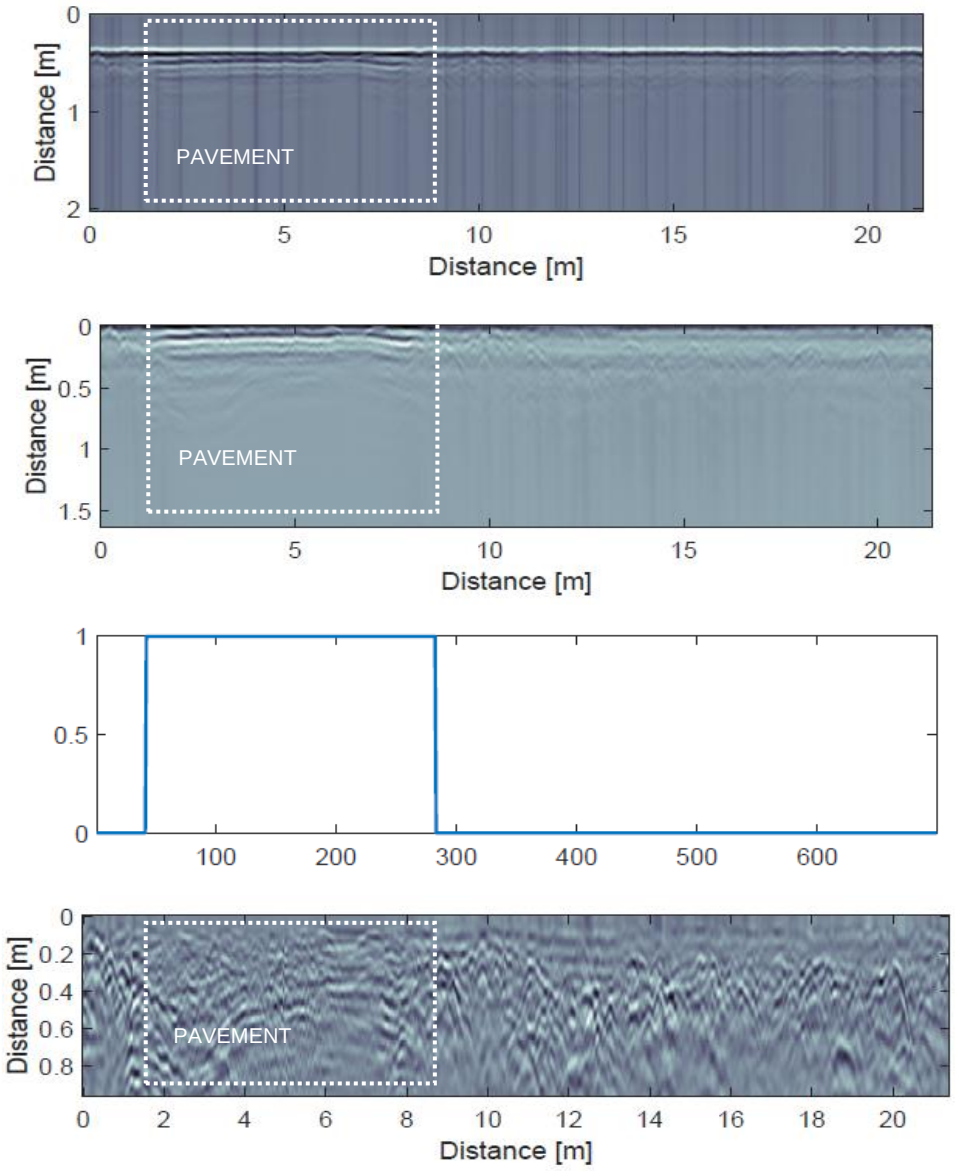

Figure 101: An example of GPR data pre-processing. a) Unprocessed B-scan, b) B-scan after main processing techniques, c) analysis of the signal reflectivity, showing a maximum value at the road pavement section, and d) B-scan after a targeted application of SVD filter

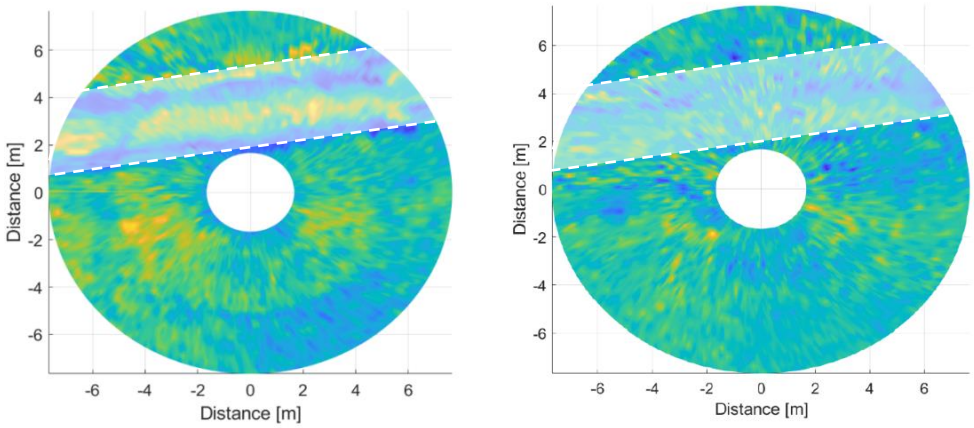

Figure 102: C-scan of the investigated area at a depth of 0.19 m, a) after the application of basic processing techniques and b) after the targeted application of the SVD filter, following the analysis of the signal reflectivity. The dashed area indicates the location of the road pavement in the proximity of the tree.

Subsequently, the algorithm for the analysis of the spatial correlation and the automatic tracking of the roots in three-dimensional space was applied to the processed data. Figure 103 shows the result of this procedure in a 2D planar view (a) and in a 3D environment (b). To simplify the interpretation of the results, the shallow-buried roots (i.e. within the first 0.25 m of soil) have been represented in green, while the deeper roots (i.e., beyond a depth of 0.25 m from the soil surface) have been highlighted in brown. Results clearly show the potential of the algorithm to reconstruct a comprehensive rendering of the root system. For the sake of consistency, the point coordinates were double-checked against the positions of the focused targets, through the analysis of the single B-scans.

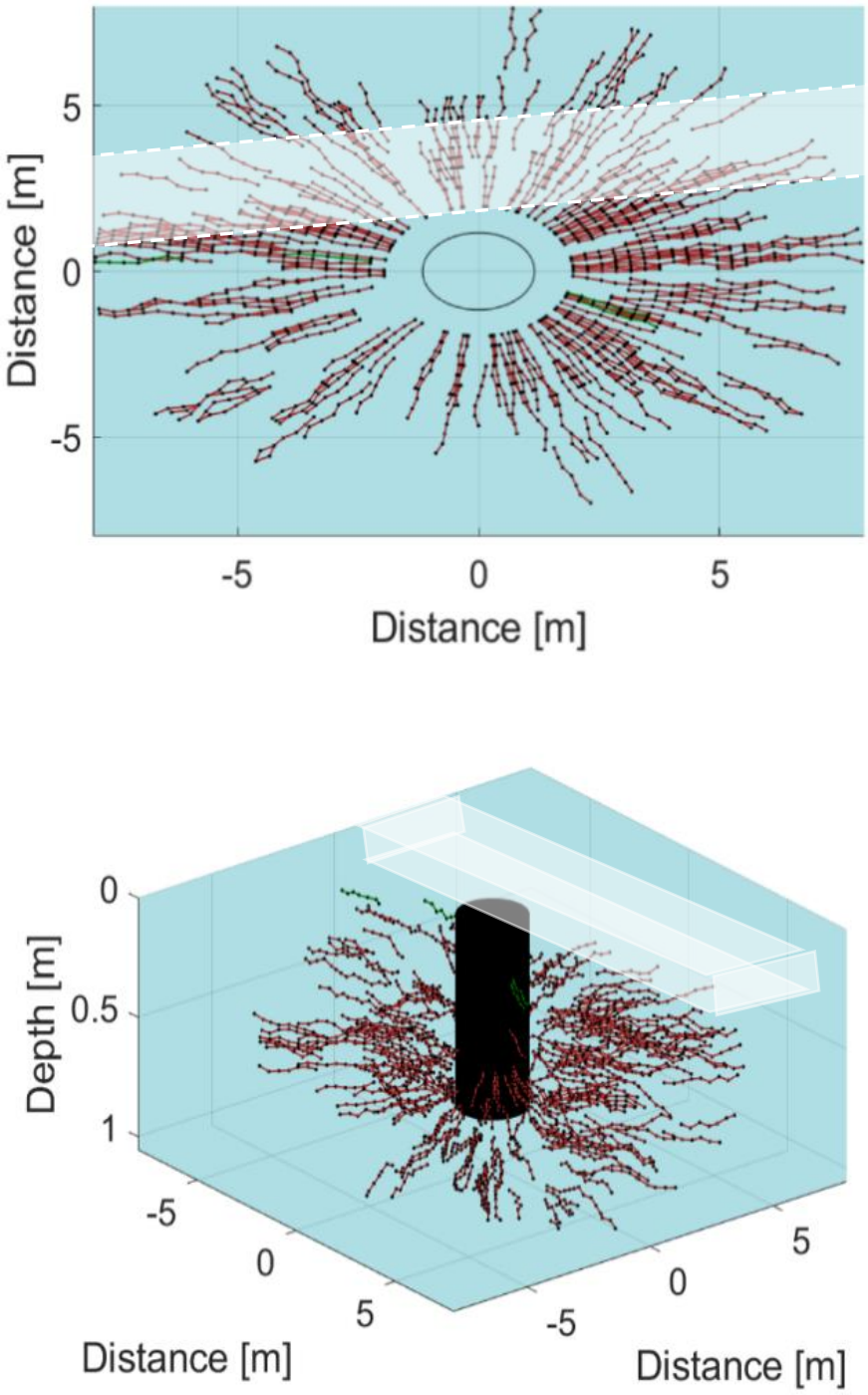

Figure 103: Reconstruction of the root system architecture for the investigated tree: a) 2D planar view and b) 3D reconstruction of the investigated root system. The dashed area (a) and the parallelepiped (b) indicate the location of the road pavement.

From the analysis of the B-scans, the hyperbolas turned out to be concentrated within the first meter of subsoil. This result is in line with the expectations for root systems of the investigated tree type (Crow, 2005). It also worth mentioning that almost no roots

were found in the first 0.25 m of subsoil. This finding is also supported by the analysis of the B-scans and suggests potential decay in the tree.

It is also important to note that Figure 103 shows areas where tracking of roots is not continuous. A possible explanation for this can be related to the presence of sections of the subsoil with a higher moisture content or heavily consolidated clay. Another possible explanation for this could be the presence of roots with a short horizontal development before going deeper in a quasi-vertical direction. Furthermore, it worth reminding that the implementation of the algorithm does not consider short segments in order to avoid false alarms and misinterpretations.

The root system architecture is further investigated by means of density maps at different depths. The domain was divided into reference units in the form of cuboids, with surfaces 0.30 m × 0.30 m and depths 0.10 m. Therefore, nine depth levels were created, from a depth of 0.10 m to a depth of 1.00 m (as the first 0.10 m of the subsoil do not contain any root), in which the total root length per reference unit was estimated. Figure 104 shows the output of this data processing stage in the form of density maps. It is interesting to note that the root density tends to decrease as the distance from the bark increases, as expected. Moreover, the volume of soil with the highest density of roots is located from a depth of 0.30 m to a depth of 0.90 m.

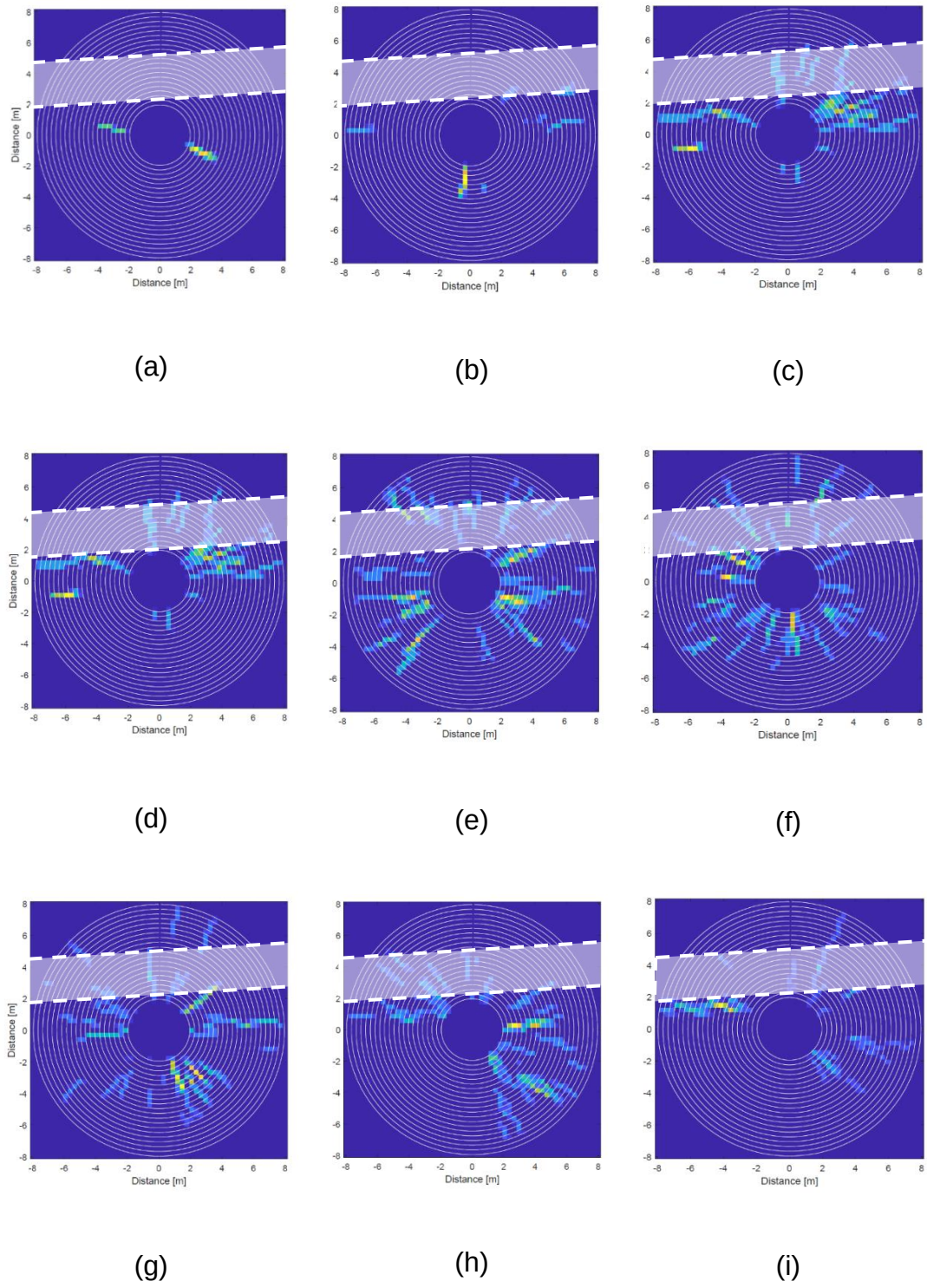

Figure 104: Root density maps. From top left: a) 0.10 m to 0.20 m; b) 0.20 m to 0.30 m; c) 0.30 m to 0.40 m; d) 0.40 m to 0.50 m; e) 0.50 m to 0.60 m; f) 0.60 m to 0.70 m; g) 0.70 m to 0.80 m; h) 0.80 m to 0.90 m; i) 0.90 m to 1.00 m. The dashed area indicates the location of the road pavement.

5.2.3.3. Conclusions

This case study demonstrates the viability of GPR for detection of tree roots, reconstruction of the root system architecture and the estimation of root mass density under road pavement structures. A rendering of a root system was successfully recreated through the application of a novel multi-phase signal processing method for GPR. Furthermore, the density of roots in the investigated volume was evaluated and root density maps were produced at different depths.

It was observed that the most important advantages were provided by i) the removal of the main signal noise, ii) the amplification of reflections from the deepest roots, and iii) the removal of reflections from the layered structure of the road pavement. This step was instrumental for the interpretation of the processed data at later stages. It could be concluded that the application of the root tracking algorithm was, therefore, less prone to errors and false detections of roots due to the misinterpretation of data.

This research line addresses the following objective of the present Thesis (see Section 3.1):

- *to develop enhanced data processing algorithms and interpretation techniques for tree assessment:* a novel data processing technique is developed for the reconstruction of street trees' root systems. Explanation is given of the assumptions made and the data processing techniques used. Results have shown potential of the proposed technique. The set objective is therefore considered achieved.

5.3. Novel Perspectives in the GPR-based Assessment of Tree Root Systems: A Frequency Spectrum-Based Processing Framework

The present study reports the preliminary results of an experimental campaign, conducted with the main aim of investigating the feasibility of a novel tree root assessment approach based on the analysis of GPR data both in time and frequency domain. The suggested processing system may be implemented for expeditious analyses or on trees difficult to reach, such as in some urban environments, where more comprehensive survey methods are not applicable. The specific objectives of this research can be outlined as follows:

- understanding the influence of different features (i.e. roots, layers, etc.) on the time-frequency analysis of GPR data
- identifying recurring patterns in the data analysis, in order to establish a repeatable data processing methodology

To this end, data were processed using a STFT (see Section 2.4.5.8). This approach allows data to be analysed in both time and frequency domain, by evaluating how the frequency spectrum changes with time.

5.3.1. Methodology

5.3.1.1. The Test Site

The survey was carried out in Walpole Park, Ealing, London (United Kingdom). The tree under investigation (Figure 105)

Figure 105: The investigated area.

5.3.1.2. The GPR Survey Technique

As per the previous case studies described in this Chapter, the experimental design refers to the methodology descripted in Section 5.1.3. A number of 24 circular scans were performed around the investigated tree, starting 0.50 m from the bark and spaced 0.30 m from one another, therefore surveying an overall area of 175.67 m^2 around the tree. Among the scans mentioned above, the one located at 2.60 m from the outer surface of the trunk was selected for analysis purposes.

5.3.1.3. The GPR Equipment

As per the above mentioned case studies in this Chapter, The survey was carried out using the Opera Duo ground-coupled GPR system, manufactured by IDS GeoRadar (Part of Hexagon). The system is equipped with 700 MHz and 250 MHz central frequency antennas. Data were collected using a time window of 80 ns, discretised

across 512 samples. The horizontal resolution was set to 3.06 × 10-2 m. In order to achieve the optimal effective resolution, only data collected using the 700 MHz antenna were analysed.

5.3.2. Results

5.3.2.1. Target Identification and Application Windows

Figure 106 shows the radargram of the selected scan after the application of the signal processing techniques. Inside, a smaller area was chosen on which to apply the STFT function. Such area was chosen as it includes two relatively isolated hyperbolas of comparable shape, positioned one above the other at a distance of approximately 5 ns from each other. The two hyperbolas are likely due to the top and bottom reflections of a structural root, with a diameter of about 0.15 m. The root interjects a semi-horizontal layer (presumably a geosynthetic layer), which is visible on both sides of the top hyperbola.

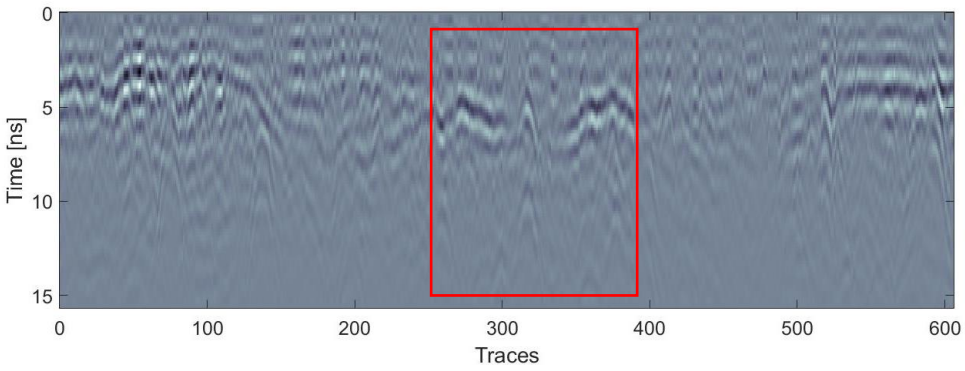

Figure 106: Radargram of the analysed scan. The red square identifies the selected application area.

The selected area was then divided into 5 application windows, as shown in Figure 107. Such windows, tailored to be as wide as the reference hyperbolas, consist of 19 tracks (i.e. A-scan) each, with a width of about 0.55 m per window, for a total width of 2.75 m.

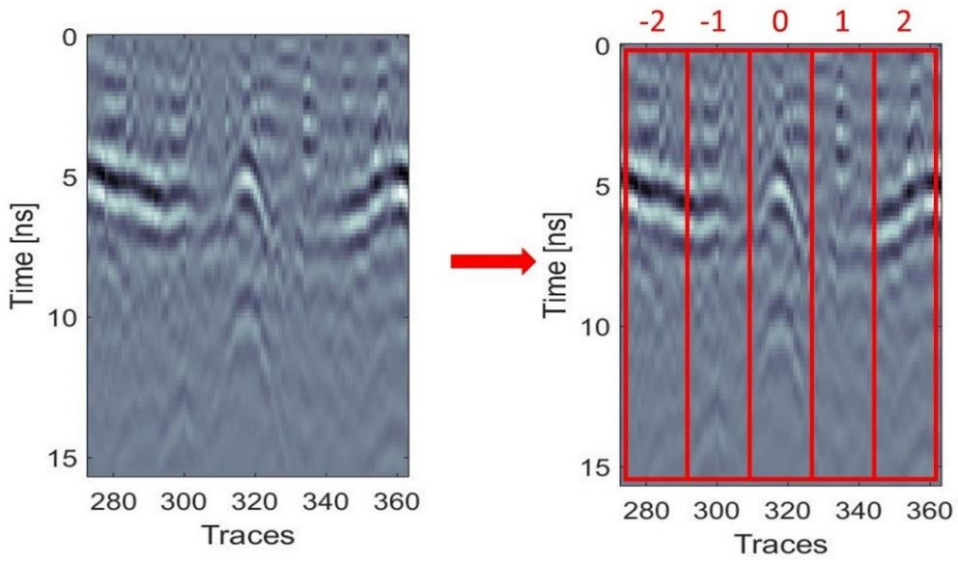

Figure 107: Subdivision of the selected area into application windows.

5.3.2.2. Application of the STFT Function

Within each of the above-identified windows, the average value of the signal was calculated, which was subsequently used for the application of the STFT function. Figure 108 shows the time-frequency analysis carried out using the STFT approach.

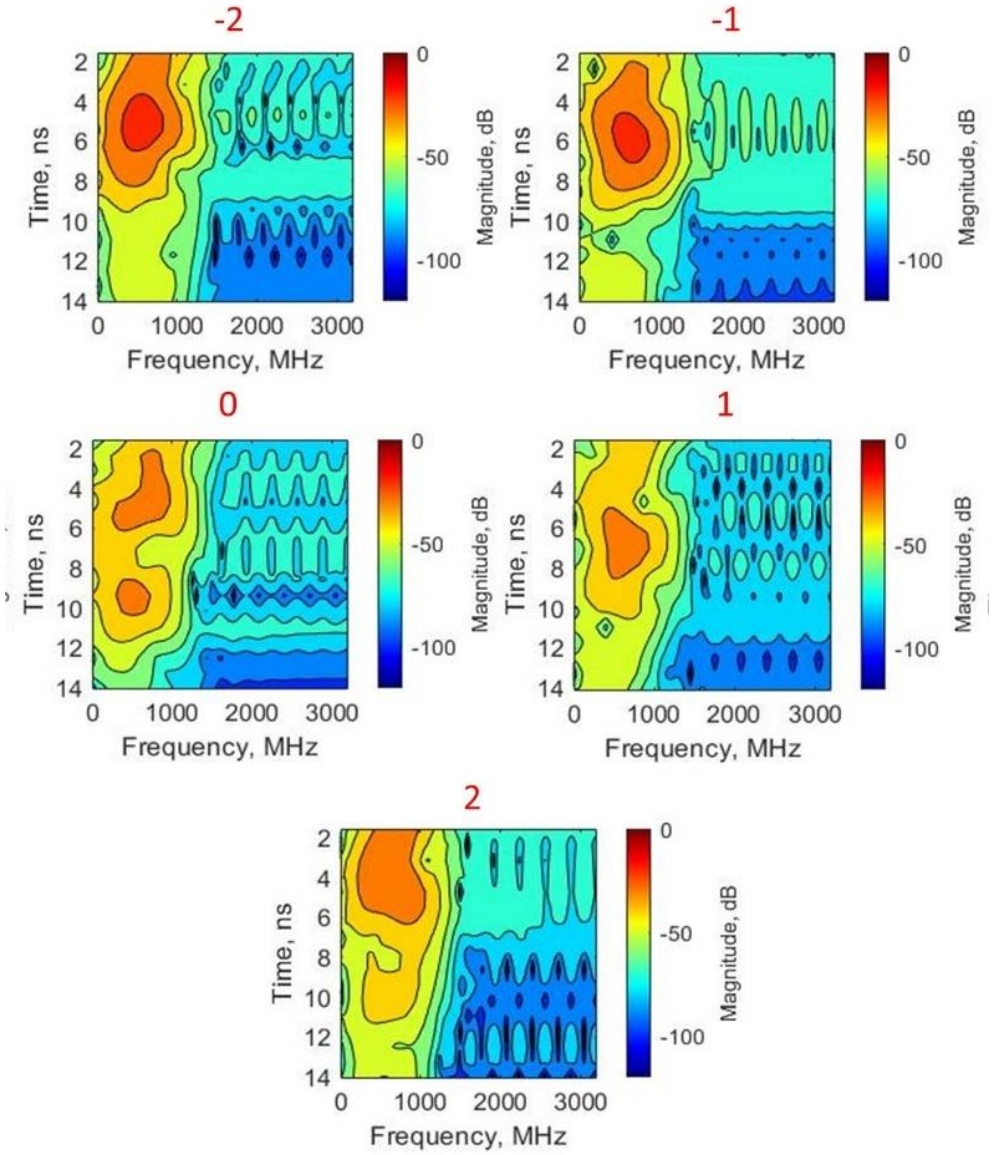

Figure 108: STFT spectra for the selected application windows.

From the analysis of the STFT spectrum of the window 0, it can be seen how the energy is concentrated in two peaks, the first centred at an arrival time of about 5 ns and the second at an arrival time of about 10 ns. This is then followed by an energy drop between 11 and 14 ns. It is worth noting that the centroids of both areas are found in a frequency range between 500 and 700 MHz. Conversely, in the other windows, the energy is concentrated in a single peak, of greater intensity in windows -2 and -1 than in windows 1 and 2. Consistently with the semi-horizontal trend of the layer, as

highlighted in the B-scan, the centroids of the areas of greatest energy are located respectively at 5 ns for the -2 window, at 6 ns for the -1 window, at 7 ns for window 1 and 4 ns for window 2. For all cases, the areas mentioned above are centred in a frequency range between 600 and 700 MHz. Unlike window 0, in all other cases, the energy is attenuated less rapidly.

5.3.2.3. Error Maps

To analyse in more detail the differences in the behaviour of the STFT spectra between the two cases (i.e. root or horizontal layer), error maps have been created, given by the difference between the elements in the examined map and those of the reference map. Figure 109 shows the error maps created for the selected application windows, with reference to the window 0 STFT spectra.

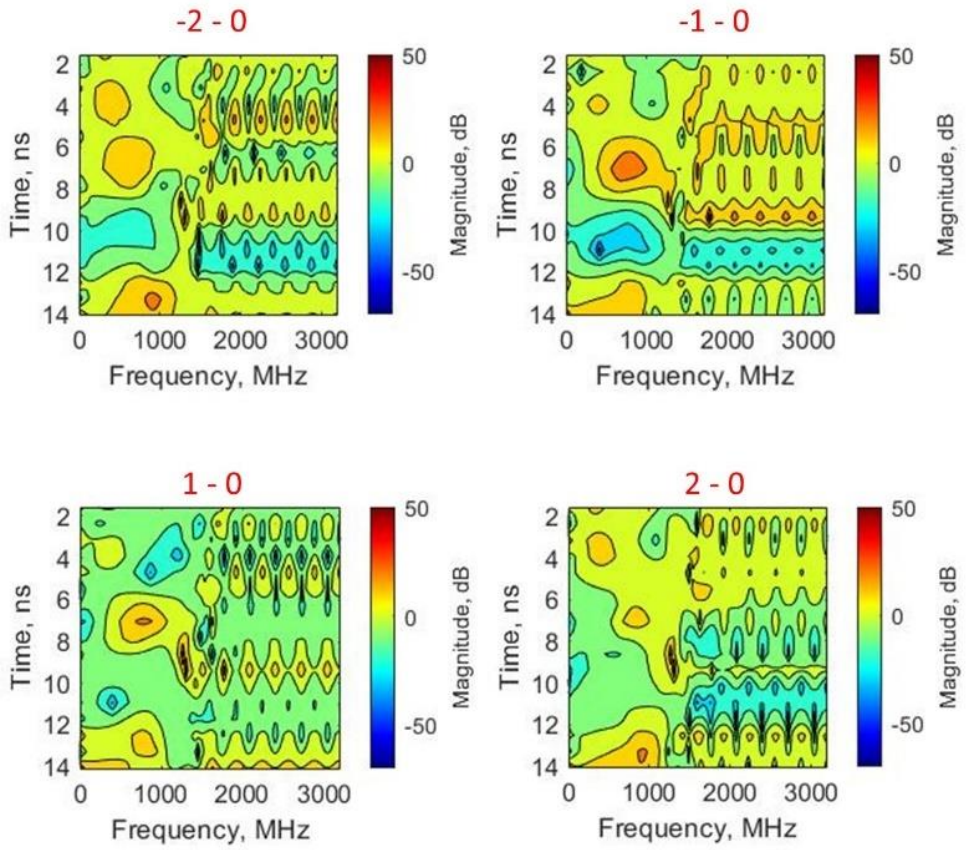

Figure 109: Error maps for the STFT spectra, with reference to the window 0 STFT spectra.

It can be noted how some characteristics occur in all the error maps. For example, the presence of an area of positive energy is recurrent, centred around the 1000 MHz frequency, at an arrival time between 6 and 8 ns. In the same way, it is possible to notice in all the error maps a negative peak, also centred around the 1000 MHz frequency, at an arrival time between 4 and 5 ns. In order to observe the trend of these characteristics, compared with the response of the time-frequency analysis in the presence of a root, the spectra of the energy in the error maps were evaluated. To this extent, a time window was selected, of width and depth equal to those of the reference hyperbola (i.e. between 4.5 ns and 5.5 ns), as shown in Figure 110. The average spectra trend of the error maps within the selected time window is shown in Figure 111. It is worth noting that the error maps' average spectra all have the same trend, with an energy peak around 250 MHz and a negative peak between 600 and 800 MHz.

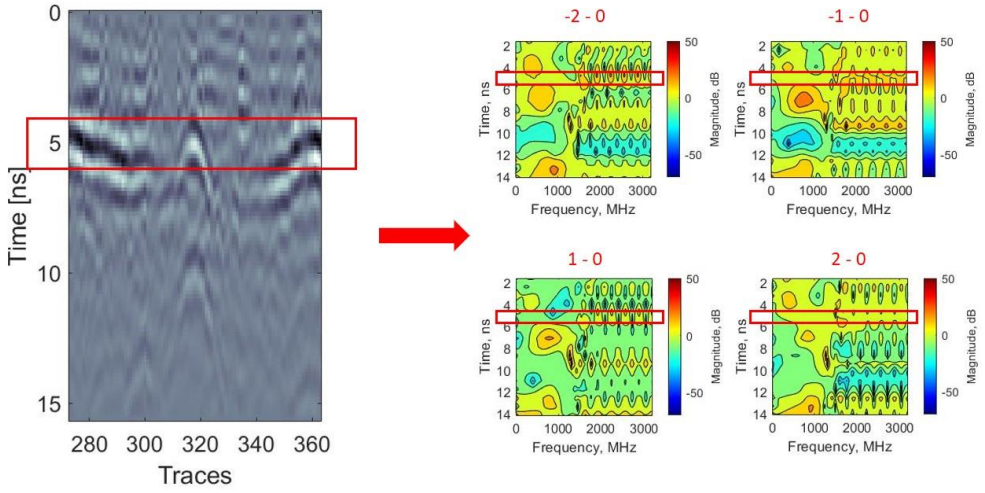

Figure 110: Selection of the time window for the analysis of the error maps' spectra trend.

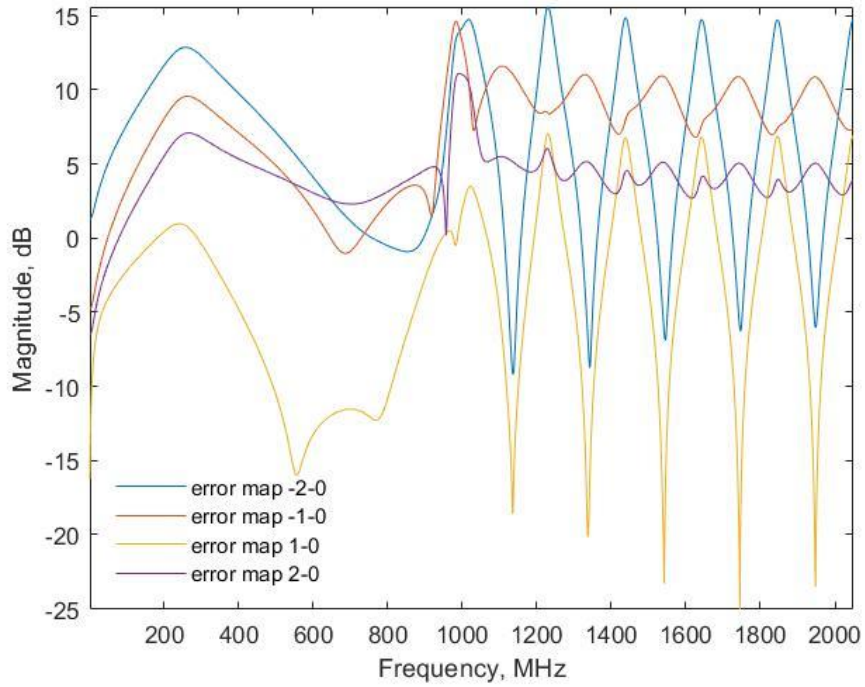

Figure 111: Error maps' average spectra trend between 4.5 and 5.5 ns

5.3.3. Conclusions

This study presents the preliminary outputs of novel research within the context of the applications of GPR in detecting and assessing tree roots systems. Results' interpretation has shown the viability of the presented approach in recognising the influence of different features (i.e. roots, layers, etc.) on the combined time-frequency analysis of GPR data. Besides, the latter allowed the detection of recurring patterns in the data analysis, proving this method to be worthy for further development and implementation in tree root systems' assessment.

The preliminary results have shown the potential of this methodology which, if further investigated and automated, could be successfully used in urban areas, where some trees are difficult to access and to be thoroughly investigated. The presented methodology would allow for the development of an accurate, albeit expeditious,

technology which would allow the protection of the urban natural heritage and the safeguarding of the built environment.

6. Conclusions

This Thesis embodies the methodology and findings of the research project conducted throughout the last three years. The theoretical, numerical and experimental findings discussed in the previous chapters are summarised here. This Chapter concludes the Thesis and provides suggestions for practical applications and use in the area of interest.

6.1. Research Findings

This Thesis addressed the research questions set out in Section 3.2, tackling the major issues related with the early identification of tree decay and tree disease using ground penetrating radar (GPR). Research objectives were addressed on the possibility to achieve a better understanding of the internal configuration of tree trunks and the interaction between the root system and the surrounding environment. In more detail, an outline of the research findings against the set objectives is reported below.

- *to develop novel survey methodologies for tree trunk assessment and three-dimensional root mapping*

In regard to the assessment of tree trunks, the concerning objective is discussed in Chapter 4. In more detail, the effectiveness of examining tree trunks using circular scans is investigated in all the presented case studies (Sections 4.1, 4.2 and 4.3), as the internal structure of the surveyed trees was reconstructed and tree decays were effectively localised.

Regarding the root systems' survey methodology, the objective was addressed in Chapter 5. A circular GPR acquisition method was followed in the GPR data processing framework, as explained in Sections 5.1.3. This method was adopted due to the typical configuration of a root system (i.e., expanding radially from the trunk of

the tree outwards), with the advantage to be more inclusive and accurate compared to a typical longitudinal acquisition method. In fact, circular transects enable the scanning of roots in a quasi-perpendicular setup, i.e., an optimal condition in GPR data collection. Furthermore, this methodology is used to collect information related to the examined tree only, excluding the detection of root targets from neighbouring trees. This feature is essential for the evaluation of the root system of individual trees, in case more detailed analyses are required.

- *to develop enhanced data processing algorithms and interpretation techniques for tree assessment*

The objective of developing data processing algorithms and interpretation techniques for the assessment of tree trunks was addressed in Chapter 4. The main limitation when investigating tree trunks using GPR is in the difficulty to adapt the common signal processing techniques to an irregularly-shaped surface (i.e., the tree bark). To this end, a novel processing framework based on the arc parameterisation was developed (see Section 4.1.1.1), which allowed the processing of GPR data collected on trunks of any shape. Also, the reconstruction of the internal structure of tree trunks and the identification of internal decays was further improved by means of a processing framework based on a modified Kirchhoff migration and the Reverse-Time (RT) migration. The two techniques were successfully applied and results are discussed in Section 4.2. It is also worth noting that the proposed framework can be implemented in a straightforward manner using any commercial GPR device with minimum computational and operational requirements. This makes this method applicable in forestry investigations and represents a step forward in the use of GPR as a diagnostic tool for tree pests and diseases. Finally, a data processing technique based on the

microwave tomography was been successfully applied for the reconstruction of tree trunks' internal decays and hollows (see Section 4.3).

Regarding the tree roots, the case studies reported in Section 5.2 demonstrate the validity of the novel methodology proposed for the assessment of tree root systems. The data processing framework explained in Section 5.1 requires the input of a minimum amount of information related to the specific GPR survey, such as the number of scans carried out and the relative permittivity of the medium, making the data analysis relatively fast. Furthermore, the combination of the presented signal processing techniques allows for a broad applicability of the proposed methodology. A selection of standard techniques was performed to minimise the risk of data overprocessing. As for the more advanced techniques, such as the Singular Value Decomposition (SVD) filter and the Frequency-Wavenumber (F–K) migration, their application has been calibrated to overcome fundamental issues, such as the presence of ringing noise and the accurate localisation of targets, without affecting the original data. The combination of the above-discussed parameters and processing steps can be regarded as a step forward for the development of a fully automated root system assessment methodology, for use of practitioners. At present, the selection of the threshold value for use in the tree root-tracking algorithm is the only step involving the operator's intervention, as explained in Section 5.1.3. Future research could task itself towards the automation of this particular step, using iterative estimations (Kelley, 1999) or machine-learning methods, such as the backpropagation (Hecht-Nielsen, 1992).

- *to develop numerical simulations and modelling of root systems and trunk decays*

Numerical simulations of tree trunks' internal structure and decays were carried out in all the case studies presented in Chapter 4. In this regard, it is well known that outcomes of a real-life survey are likely to be affected by approximations. Moreover, relying solely on field and laboratory tests might involve logistic issues, as it is required to identify trees affected by different types of decays and pathogens. The use of numerical simulations (see Sections 4.1.2, 4.2.2 and 4.3.2), therefore, contributed to examine the fundamental parameters involved in the investigation process (i.e. the dielectric permittivity, the shape of the decay, etc.) and therefore it was instrumental to refine the data processing framework before its application in real-life investigations. It was also essential to analyse multiple experimental scenarios, representing a variety of possible internal defects in terms of shape and formation, as well as to validate results from real tests.

As far as the modelling is concerned, novel algorithms for the 2D and 3D reconstruction of the structure of trees have been developed (see Sections 4.2 and 4.3). Their feasibility has been tested by means of case studies, the positive outcomes of which confirm the potential of the proposed methodologies. Similarly, in regard of tree root systems, the proposed tree root-tracking algorithm (see Section 5.1.3) allowed for a completely non-invasive modelling of the root systems' architecture.

- *to assess mutual interaction between root systems of different tree species*

The application of the data processing methodology to GPR data collected in an area of interconnection between the root systems belonging to two different trees allowed for a more comprehensive interpretation of the interaction between the systems (see

Section 5.2.2). In addition, the algorithm aided a better understanding of the spread of the roots, and the soil.

- *to estimate tree roots' mass density*

A novel technique for the evaluation of tree roots' mass density was proposed in Section 5.1.4. and it has proven to be an effective tool in assessing the root system conditions and its interaction with manmade constructions. To this extent, the provision of routine inspections could be of valuable support to evaluate the health conditions of root systems, as density variations over time can be used as an effective quantitative indicator of any potential diseases or fungal attacks. An early-stage identification of the problem can foster immediate remedial actions, it can contribute to save the tree and prevent the spread of the infection. It is also worth noting the impact of the proposed methodology in large-scale forestry applications, especially in areas with a high density of trees. Implementation of routine inspections could help to identify mass density-related issues for individual trees (e.g., trees requiring special care) much more accurately, as the outcomes of the methodology are independent from the root system of nearby trees.

6.2. Challenges and Limitations

The findings of this study have to be seen in light of some challenges and limitations, which were identified and addressed as follows:

- One of the biggest challenges of this research was to identify real life case studies for data collection and models' validation. In more detail, it was necessary to acquire tree trunk samples to be examined in the laboratory in order to create accurate numerical models. Furthermore, it was necessary to identify case studies concerning diseased trees, on which to carry out GPR

investigations of the trunk and the root zone. These trees then had to be felled in order to verify the validity of the predictions from the developed models. The trees' root zone, likewise, had to be excavated to validate the reconstruction algorithms. The above was possible thanks to the support of industrial and research partners of The Faringdon Centre such as Whitelands Woods (Hampshire, UK), which provided the Research Centre with samples. Furthermore, many of the case studies cited in this Thesis were reported to the Research Centre by the Ealing Council Tree Service, which also provided the necessary permits and support during the investigation.

- While carrying out the studies, it was observed that wood samples, when brought to the laboratory for investigations, tend to lose most of their water content rapidly, drying out and forming cracks that did not exist at the time of cutting. This obviously affects the results of the investigations, especially as regards the estimation of the permittivity value, which must therefore be estimated on the basis of literature data for numerical modelling purposes. To overcome this problem, a survey protocol has been established, according to which the GPR data must be collected preferably on site, at the time of cutting the samples, or within 24 hours following their arrival in the laboratory, to minimise the variation of the sample's water content with respect to the on-field conditions.
- A limitation has been identified in the use of the 2000 MHz antenna system on trees with a small trunk circumference. In such cases, the dimensions of the GPR, however compact, do not allow adequate contact of the encoder wheel with the surface. This implies that no signal is sent from the encoder wheel to the control unit to inform that the GPR is moving forward. This limitation

indicates that a GPR system specifically designed for use on tree trunks and other cylindrical objects is required in this area of endevour (see Chapter 6.3).

- The use of traditional GPR systems (i.e. designed for use in linear acquisition modes) for the investigation of tree roots' architecture based on circular scanning modes, is currently difficult to implement. This is emphasised in case of acquisitions performed in the vicinity of the trunk, where manouvering the radar may be a challenging task. In this Thesis it was demonstrated that use of circular scan is highly effective in mapping root systems (see Chapters 5.1 and 5.2). Nevertheless, their implementation is time-demanding and laborious compared to linear acquisitions. To address this challenge, expeditious and reliable investigation methods based on linear scanning modes are being studied (see Chapter 5.3). However, it is fair to comment that the development of a dedicated GPR system for circular investigations would allow for an in-depth and rapid assessment of root systems.

6.3. Recommendations

As extensively shown in the previous Chapters, GPR has shown effectiveness in characterising the subsurface, demonstrating a great potential in different non-destructive applications. In regard to its use in the assessment of trees, GPR is increasingly regarded as a reliable and efficient technology, as opposed to traditional destructive testing methods and also other non-destructive techniques.

The aim of this Thesis is therefore to give an effective contribution to the field, by exploring the GPR capabilities in assessing the internal structure of tree trunks and reconstructing the architecture of tree root systems. All the efforts have been focused on the possibility to implement effective and efficient methodologies to fulfil this aim.

Therefore, this Section aims at providing effective support for the application and practical use of the tools described. To this end, the following recommendations are given:

- The use of high-frequency antennas (1500 – 2000 MHz) is suggested for the assessment of tree trunks' internal structure and the identification of internal decays or hollows. Such frequencies were proven effective both in numerical simulations and in real-life case studies, which were carried out on laboratory samples ($\varepsilon \approx 3$) and on standing living trees ($\varepsilon \approx 30$ or higher). Nevertheless, it must be acknowledged that high-frequency hand-held GPR system, when used for tomographic approaches for the assessment of hollow trees, generate a considerable amount of clutter. The latter requires a heavy processing to estimate the boundary between the hole and the sapwood.
- A circular acquisition method is envisaged for tree trunks' assessment, as this was found appropriate for this type of investigations. For the detection of early decays in tree trunks, the spacing between scan lines should not be great (i.e. not exceeding 0.05 m), as the detection of small decays could be prevented.
- The design of a novel and dedicated GPR antenna system with innovation in design configurations and functions is strongly envisaged for the assessment of tree trunks, to overcome limitations as explained in Chapter 6.2. To this extent, The Faringdon Centre for Non-Destructive Testing has already started to design new systems based on innovative data processing approaches.
- As regards the detection of tree roots, a medium frequency GPR system (i.e. 600 MHz) is strongly recommended for the reconstruction of the tree root systems' architecture. In fact, this was found to be a appropriate middle ground

between the desired depth of investigation (based on the reported average depth of tree root systems (Crow, 2005)) and the highest effective resolution.

- The use of a survey methodology based on circular acquisition lines is recommended for the reconstruction of the tree root systems' architecture. In fact, such acquisition method has proven effective in the reconstruction of the overall architecture of tree root systems. The use of linear acquisition lines could be employed in surveys with limited access for manoeuvring around the tree (i.e. urban environments). The effectiveness of such methodology is still under investigation, but promising results have been achieved on a novel processing method which could be employed on linear scan lines for expeditious root detections. Also on the survey methodology, a distance of 0.30 m between lines of scan is considered effective, as a larger spacing could introduce errors in the reconstruction and affect the reliability of the results.
- The proposed root density index and the resulting root density maps are valuable tools for a long-term assessment of the tree root system's health. In this regard, it is suggested to carry out the investigation of a tree root system repeatedly over time (e.g. every 3 to 6 months), and to produce root density maps based on every collected dataset. When the tree is healthy and the root growth proceeds as normal, this will be shown by the maps over time. Conversely, a decrease in the density detected between different surveys can indicate the onset of a disease or a fungal attack, with consequent decay and death of the roots. This information, if promptly transmitted to decision-makers, can lead to measures to save the examined tree or prevent neighbouring trees from becoming infected. To this extent, an early-warning monitoring system,

approach based on the analysis of the root density maps, is here proposed, as a tool to limit the rapid spread of Emerging Infectious Diseases (EIDs).

References

911HVAC (2019) *Tree root damage*. Available at: https://www.911hvac.com/plumbing-and-hvac-blog/tree-root-damage (Accessed: Dec 2020).

Abbott, A. (2018) 'Italy's olive crisis intensifies as deadly tree disease spreads', *Nature (London)*, 563(7731), pp. 306-307. doi: 10.1038/d41586-018-07389-8.

Ahmad, N., Wistuba, M. and Lorenzl, H. (Jun 2012) *GPR as a crack detection tool for asphalt pavements: Possibilities and limitations.* 2012 14th International Conference on Ground Penetrating Radar (GPR). IEEE, pp. 551.

al Hagrey, S.A. (2006) 'Electrical resistivity imaging of tree trunks', *Near Surface Geophysics*, 4(3), pp. 179-187. doi: 10.3997/1873-0604.2005043.

Alani, A.M., et al (2018) *Mapping the root system of matured trees using ground penetrating radar*. 2018 17th International Conference on Ground Penetrating Radar (GPR). Rapperswil, Switzerland, June 18-21, 2018. IEEE, pp. 1.

Alani, A.M., Aboutalebi, M. and Kilic, G. (2013) 'Applications of ground penetrating radar (GPR) in bridge deck monitoring and assessment', *Journal of applied geophysics*, 97, pp. 45-54. doi: 10.1016/j.jappgeo.2013.04.009.

Alani, A.M., et al (2020) 'Reverse-time migration for evaluating the internal structure of tree-trunks using ground-penetrating radar', *NDT & E international*, 115, pp. 102294. doi: 10.1016/j.ndteint.2020.102294.

Alani, A.M. and Lantini, L. (2020) 'Recent advances in tree root mapping and assessment using non-destructive testing methods: a focus on ground penetrating

radar', *Surveys in Geophysics*, 41(3), pp. 605-646. doi: 10.1007/s10712-019-09548-6.

Alani, A.M., et al (2019) 'The Use of Ground Penetrating Radar and Microwave Tomography for the Detection of Decay and Cavities in Tree Trunks', *Remote sensing (Basel, Switzerland)*, 11(18), pp. 2073. doi: 10.3390/rs11182073.

Alani, A.M. and Tosti, F. (2018) 'GPR applications in structural detailing of a major tunnel using different frequency antenna systems', *Construction & building materials*, 158, pp. 1111-1122. doi: 10.1016/j.conbuildmat.2017.09.100.

Alani, A.M., et al (2017) *Health monitoring of a matured tree using ground penetrating radar – investigation of the tree root system and soil interaction*. IMEKO International Conference on Metrology for Archaeology and Cultural Heritage. Lecce, Italy, October 23-25, 2017.

Ali, J., et al (2017) 'Ultra-Wideband Antenna Design for GPR Applications: A Review', *International journal of advanced computer science & applications*, 8(7). doi: 10.14569/IJACSA.2017.080753.

Al-Qadi, I.L., Xie, W. and Roberts, R. (2008) 'Time-Frequency Approach for Ground Penetrating Radar Data Analysis to Assess Railroad Ballast Condition', *Research in nondestructive evaluation*, 19(4), pp. 219-237. doi: 10.1080/09349840802015107.

Amato, M., et al (2008) 'In situ detection of tree root distribution and biomass by multi-electrode resistivity imaging', *Tree physiology*, 28(10), pp. 1441-1448. doi: 10.1093/treephys/28.10.1441.

Amato, M., et al (2009) 'Multi-electrode 3D resistivity imaging of alfalfa root zone', *European journal of agronomy*, 31(4), pp. 213-222. doi: 10.1016/j.eja.2009.08.005.

Amato, M. and Ritchie, J.T. (2002) 'Spatial Distribution of Roots and Water Uptake of Maize (Zea mays L.) as Affected by Soil Structure', *Crop science*, 42(3), pp. 773-780. doi: 10.2135/cropsci2002.7730.

Anagnostakis, S.L. (1987) 'Chestnut Blight: The Classical Problem of an Introduced Pathogen', *Mycologia*, 79(1), pp. 23-37. doi: 10.1080/00275514.1987.12025367.

Annan, A.P. and Davis, J.L. (1976) 'Impulse radar sounding in permafrost', *Radio science*, 11(4), pp. 383-394. doi: 10.1029/RS011i004p00383.

Antonsson, K., et al (2005) 'Osmoderma eremita (Coleoptera, Scarabaeidae, Cetoniinae) in Europe', *Animal Biodiversity and Conservation*, 28(1), pp. 1-44.

Aukema, J.E., et al (2011) 'Economic Impacts of Non-Native Forest Insects in the Continental United States', *PloS one*, 6(9), pp. e24587. doi: 10.1371/journal.pone.0024587.

Aulen, M. and Shipley, B. (2012) 'Non-destructive estimation of root mass using electrical capacitance on ten herbaceous species', *Plant and soil*, 355(1/2), pp. 41-49. doi: 10.1007/s11104-011-1077-3.

Balanis, C.A. (1989) *Advanced engineering electromagnetics*. New York u.a: Wiley.

Barker, P.A. (1983) *Some urban trees of California: manteinance problems and genetic improvement possibilities*. United States, Forest Service.

Barton, C.V.M. and Montagu, K.D. (2004) 'Detection of tree roots and determination of root diameters by ground penetrating radar under optimal conditions', *Tree physiology*, 24(12), pp. 1323-1331. doi: 10.1093/treephys/24.12.1323.

Basham, J.T., Good, H.M. and Kadzielawa, S.D. (1968) 'Respiratory activity of fungal associations in zones of heart rot and stain in sugar maple', *Canadian Journal of Botany*, 46(1), pp. 27-36. doi: 10.1139/b68-006.

Basso, B., et al (2010) 'Two-Dimensional Spatial and Temporal Variation of Soil Physical Properties in Tillage Systems Using Electrical Resistivity Tomography', *Agronomy Journal*, 102(2), pp. 440-449. doi: 10.2134/agronj2009.0298.

Bassuk, N., Grabosky, J., Mucciardi, A. and Raffel, G. (2011) 'Ground-penetrating Radar Accurately Locates Tree Roots in Two Soil Media Under Pavement', *Arboriculture & Urban Forestry*, 37, pp. 160-166.

Benedetto, A. (2013) 'A three dimensional approach for tracking cracks in bridges using GPR', *Journal of applied geophysics*, 97, pp. 37-44. doi: 10.1016/j.jappgeo.2012.12.010.

Benedetto, A., Tosti, F., Schettini, G. and Twizere, C. (2011) *Evaluation of geotechnical stability of road using GPR.* 2011 6th International Workshop on Advanced Ground Penetrating Radar (IWAGPR) IEEE, pp. 1.

Benedetto, A., et al (2017) 'Railway ballast condition assessment using ground-penetrating radar – An experimental, numerical simulation and modelling development', *Construction and Building Materials*, 140, pp. 508-520. doi: 10.1016/j.conbuildmat.2017.02.110.

Benedetto, A., Tosti, F., Bianchini Ciampoli, L. and D'Amico, F. (2017) 'An overview of ground-penetrating radar signal processing techniques for road inspections', *Signal Processing*, 132, pp. 201-209. doi: 10.1016/j.sigpro.2016.05.016.

Benedetto, A., et al (2015) 'Mapping the spatial variation of soil moisture at the large scale using GPR for pavement applications', *Near Surface Geophysics*, 13(3), pp. 269-278. doi: 10.3997/1873-0604.2015006.

Benedetto, A., et al (2013) *Soil moisture mapping using GPR for pavement applications.* 2013 7th International Workshop on Advanced Ground Penetrating Radar. Nantes, July 2-5, 2013. IEEE, pp. 1.

Bennett, A.F., Lumsden, L.F. and Nicholls, A.O. (1994) 'Tree hollows as a resource for wildlife in remnant woodlands: spatial and temporal patterns across the northern plains of Victoria, Australia', *Pacific conservation biology*, 1(3), pp. 222. doi: 10.1071/PC940222.

Bertero, M. and Boccacci, P. (1998) *Introduction to inverse problems in imaging*. Bristol [u.a.]: Inst. of Physics Publ.

Besson, A., et al (2004) 'Structural heterogeneity of the soil tilled layer as characterized by 2D electrical resistivity surveying', *Soil & tillage research*, 79(2), pp. 239-249. doi: 10.1016/j.still.2004.07.012.

Bianchini Ciampoli, L., Tosti, F., Economou, N. and Benedetto, F. (2019) 'Signal Processing of GPR Data for Road Surveys', *Geosciences (Basel)*, 9(2), pp. 96. doi: 10.3390/geosciences9020096.

Biddle, G. (2001) 'Tree Root Damage to Buildings', in Vipulanandan, C., Addison, M.B. and Hasen, M. (eds.) *Expansive Clay Soils and Vegetative Influence on Shallow Foundations*, pp. 1-23.

Birchak, J.R., Gardner, C.G., Hipp, J.E. and Victor, J.M. (1974) 'High dielectric constant microwave probes for sensing soil moisture', *Proceedings of the IEEE*, 62(1), pp. 93-98. doi: 10.1109/PROC.1974.9388.

Birouste, M., et al (2014) 'Measurement of fine root tissue density: a comparison of three methods reveals the potential of root dry matter content', *Plant and Soil*, 374(1-2), pp. 299-313.

Blunt, S.M. (2008) 'Trees and pavements - are they compatible?', *Arboricultural journal*, 31(2), pp. 73-80. doi: 10.1080/03071375.2008.9747522.

Böhm, W. (2012) *Methods of studying root systems*. Berlin: Springer Science & Business Media.

Bonan, G.B. (1992) 'Soil temperature as an ecological factor in boreal forests', in Shugart, H.H., Leemans, R. and Bonan, G.B. (eds.) *A Systems Analysis of the Global Boreal Forest.* Cambridge University Press, pp. 126-143.

Bonomo, N., Bullo, D., Villela, A. and Osella, A. (2015) 'Ground-penetrating radar investigation of the cylindrical pedestal of a monument', *Journal of applied geophysics*, 113, pp. 1-13. doi: 10.1016/j.jappgeo.2014.12.009.

Borden, K.A., et al (2014) 'Estimating coarse root biomass with ground penetrating radar in a tree-based intercropping system', *Agroforestry systems*, 88(4), pp. 657-669. doi: 10.1007/s10457-014-9722-5.

Bosso, L., et al (2016) 'Potential distribution of Xylella fastidiosa in Italy: a maximum entropy model', *Phytopathologia mediterranea*, 55(1), pp. 62-72. doi: 10.14601/Phytopathol_Mediterr-16429.

Boyer, J.S. (1995) 'Roots and root systems', in *Water relations of plants and soils* Academic Press, Inc.

Brazee, N.J., Marra, R.E., Gocke, L. and Van Wassenaer, P. (2010) 'Non-destructive assessment of internal decay in three hardwood species of northeastern North America using sonic and electrical impedance tomography', *Forestry (London)*, 84(1), pp. 33-39. doi: 10.1093/forestry/cpq040.

Brennan, G., Patch, D. and Stevens, F.R.W. (1997) *Tree Roots and Underground Pipes - Arboriculture Research Note*. Arboricultural Advisory & Information Service.

Bristow, C.S. and Jol, H.M. (2003) *Ground penetrating radar in sediments*. London: Geological Society of London.

Broadhurst, M.G. (1970) *Complex Dielectric Constant and Dissipation Factor of Foliage*. Available at: http://www.dtic.mil/docs/citations/AD0715792.

Broome, A., Ray, D., Mitchell, R. and Harmer, R. (2019) 'Responding to ash dieback (Hymenoscyphus fraxineus) in the UK: woodland composition and replacement tree species', *Forestry: An International Journal of Forest Research*, 92(1), pp. 108-119. doi: 10.1093/forestry/cpy040.

Brown, G.S. and Curry, W.J. (1982) 'A theory and model for wave propagation through foliage', *Radio science*, 17(5), pp. 1027-1036. doi: 10.1029/RS017i005p01027.

Brudi, E. and Wassenaer, P. (2002) *Trees and Statics: Non-Destructive Failure Analysis*. Champaign, Illinois: International Society of Arboriculture.

Brunet, J., et al (2014) 'Pathogen induced disturbance and succession in temperate forests: Evidence from a 100-year data set in southern Sweden', *Basic and applied ecology*, 15(2), pp. 114-121. doi: 10.1016/j.baae.2014.02.002.

Brunzell, H. (1999) 'Detection of shallowly buried objects using impulse radar', *IEEE Transactions on Geoscience and Remote Sensing*, 37(2), pp. 875-886. doi: 10.1109/36.752207.

Bucur, V. (2006) *Acoustics of Wood*. Springer Science & Business Media.

Butnor, J.R., et al (2001) 'Use of ground-penetrating radar to study tree roots in the southeastern United States', *Tree physiology*, 21(17), pp. 1269-1278. doi: 10.1093/treephys/21.17.1269.

Butnor, J. R., et al. (2008) 'Using Ground-Penetrating Radar to Estimate Tree Root Mass: Comparing Results from Two Florida Surveys', in Daniels, J.J., Ehsani, M.R. and Allred, B. (eds.) *Handbook of Agricultural Geophysics* CRC Press, pp. 397-404.

Butnor, J.R., et al (2009) 'Detecting defects in conifers with ground penetrating radar: applications and challenges', *Forest Pathology*, 39(5), pp. 309-322. doi: 10.1111/j.1439-0329.2009.00590.x.

Butnor, J.R., et al (2003) 'Utility of ground-penetrating radar as a root biomass survey tool in forest systems', *Soil Science Society of America Journal*, 67(5), pp. 1607-1615. doi: 10.2136/sssaj2003.1607.

Buza, ÁK. and Divós, F. (2016) 'Root Stability Evaluation with Non-Destructive Techniques', *Acta silvatica & lignaria Hungarica*, 12(2), pp. 125-134. doi: 10.1515/aslh-2016-0011.

Buza, A.K. and Goncz, B. (2015) 'Comparison of trees and NDT methods', *Wood research*, 60, pp. 45-58.

Canadian Forest Service (2015) *Trees, insects and diseases of Canada's forests - Natural Resources* Canada. Available at: https://tidcf.nrcan.gc.ca/en/diseases/factsheet/16 (Accessed: 10/01/2019).

Caneva, G., Ceschin, S. and De Marco, G. (2006) 'Mapping the risk of damage from tree roots for the conservation of archaeological sites: the case of the Domus Aurea, Rome', *Conservation and management of archaeological sites*, 7(3), pp. 163-170. doi: 10.1179/135050306793137403.

Caneva, G., Galotta, G., Cancellieri, L. and Savo, V. (2009) 'Tree roots and damages in the Jewish catacombs of Villa Torlonia (Roma)', *Journal of cultural heritage*, 10(1), pp. 53-62. doi: 10.1016/j.culher.2008.04.005.

Cassidy, N.J. (2009) 'Ground Penetrating Radar Data Processing, Modelling and Analysis', in Jol, H.M. (ed.) *Ground Penetrating Radar Theory and Applications* Elsevier, pp. 141-176.

Catapano, I., et al (1999) 'Ground-Penetrating Radar: Operation Principle and Data Processing', in *Wiley Encyclopedia of Electrical and Electronics Engineering*. Hoboken, NJ, USA: John Wiley & Sons, Inc, pp. 1-23.

Cella, E., et al (2018) 'Two different Xylella fastidiosa strains circulating in Italy: phylogenetic and evolutionary analyses', *Journal of plant interactions*, 13(1), pp. 428-432. doi: 10.1080/17429145.2018.1475022.

Čermák, J., Hruška, J., Martinková, M. and Prax, A. (2000) 'Urban tree root systems and their survival near houses analyzed using ground penetrating radar and sap flow techniques', *Plant and soil*, 219(1/2), pp. 103-116. doi: 10.1023/A:1004736310417.

Chan, Y.K. and Koo, V.C. (2008) 'An introduction to synthetic aperture radar (SAR)', *Progress in electromagnetics research*. Research B, 2, pp. 27-60. doi: 10.2528/PIERB07110101.

Chauvière, M., Colin, F., Nielsen, C.N. and Drexhage, M. (1999) 'Development of structural root architecture and allometry of Quercus petraea', *Canadian Journal of Forest Research*, 29(5), pp. 600-608. doi: 10.1139/x99-027.

Chave, J. (2005) *Measuring wood density for tropical forest trees*. Touluse, France: .

Clark, D.B. and Clark, D.A. (2000) 'Landscape-scale variation in forest structure and biomass in a tropical rain forest', *Forest ecology and management*, 137(1-3), pp. 185-198. doi: 10.1016/s0378-1127(99)00327-8.

CNT Foundations (2020) Trees and tree roots. Available at: https://www.yourfoundationexperts.com/foundation-repair/what-causes-foundation-problems/trees-and-tree-roots/ (Accessed: Dec 2020).

Cockle, K.L., Martin, K. and Robledo, G. (2012) 'Linking fungi, trees, and hole-using birds in a Neotropical tree-cavity network: Pathways of cavity production and implications for conservation', *Forest Ecology and Management*, 264, pp. 210-219. doi: 10.1016/j.foreco.2011.10.015.

Colla, C., Das, P.C., McCann, D. and Forde, M.C. (1997) 'Sonic, electromagnetic and impulse radar investigation of stone masonry bridges', *NDT & E international*, 30(4), pp. 249-254. doi: 10.1016/S0963-8695(96)00067-9.

Conyers, L.B. (2002) 'Ground penetrating radar', in Hornak, J.P. (ed.) *Encyclopedia of Imaging Science and Technology*.

Costello, L.R. and Jones, K.S. (2003) *Reducing infrastructure damage by tree roots: a compendium of strategies*. Western Chapter of the International Society of Arboriculture (WCISA).

Côté, W.A. (1968) 'The Structure of Wood and the Wood Cell Wall', in *Principles of Wood Science and Technology*. Berlin, Heidelberg: Springer, pp. 1-54.

Coutts, M.P. (1983) 'Root architecture and tree stability', *Plant and Soil*, 71(1/3), pp. 171-188. doi: 10.1007/BF02182653.

Crow, P. (2005) *The influence of soils and species on tree root depth*. Edinburgh: Forestry Commission. Available at: https://www.urbanforestrysouth.org/resources/library/ttresources/the-influence-of-soils-and-species-on-tree-root-depth/at_download/file.

Cui, X.H., et al (2011) 'Modeling tree root diameter and biomass by ground-penetrating radar', *Science China. Earth sciences*, 54(5), pp. 711-719. doi: 10.1007/s11430-010-4103-z.

Cutler, D.F. and Richardson, I.B. (1981) *Tree roots and buildings*. 2nd edn. Singapore: Longman.

Daniels, D.J. (2004) *Ground Penetrating Radar*. 2nd edn. London: The Institution of Electrical Engineers.

Daniels, D.J. (1996) 'Surface-penetrating radar', *Electronics & Communication Engineering Journal*, 8(4), pp. 165-182. doi: 10.1049/ecej:19960402.

Day, R.W. (1991) 'Damage of Structures due to Tree Roots', *Journal of performance of constructed facilities*, 5(3), pp. 200-207. doi: 10.1061/(ASCE)0887-3828(1991)5:3(200).

Denman, S., et al (2014) 'A description of the symptoms of Acute Oak Decline in Britain and a comparative review on causes of similar disorders on oak in Europe', *Forestry (London)*, 87(4), pp. 535-551. doi: 10.1093/forestry/cpu010.

Divos, F., Bejo, L. and Toth, A. (2009) *Instrument supported tree evaluation in Hungary*. Beijing: Beijing Forestry University.

Driscoll, R. (1983) 'The influence of vegetation on the swelling and shrinking of clay soils in Britain', *Géotechnique*, 33(2), pp. 93-105. doi: 10.1680/geot.1983.33.2.93.

Eberhart, R. and Kennedy, J. (1995) *Particle swarm optimization*. Proceedings of ICNN'95-International Conference on Neural Networks. IEEE, pp. 1942.

Edworthy, A.B. and Martin, K. (2014) 'Long-term dynamics of the characteristics of tree cavities used for nesting by vertebrates', *Forest Ecology and Management*, 334, pp. 122-128. doi: 10.1016/j.foreco.2014.09.001.

Ellison, A.M., et al (2005) 'Loss of Foundation Species: Consequences for the Structure and Dynamics of Forested Ecosystems', *Frontiers in Ecology and the Environment*, 3(9), pp. 479-486. doi: 10.2307/3868635.

Eshel, A. and Beeckman, T. (2013) *Plant Roots: The Hidden Half*. 4th edn. New York: CRC Press.

Fang, G.Y. and Sato, M. (2005) 'Stepped-frequency ground penetrating radar and its application for landmine detection', *Dianzi Xuebao (Acta Electronica Sinica)*, 33(3), pp. 436-439.

Fausett, L.V. (1999) *Applied numerical analysis using MATLAB*. 2nd edn. Upper Saddle River: Prentice Hall.

Fay, N. (2014) *Appraisal of Trees at Walpole Park*. London: Ealing Council.

Fayle, D.C.F. (1968) *Radial Growth in Tree Roots: Distribution, Timing, Anatomy.* Toronto, Canada: University of Toronto, Faculty of Forestry.

Feynman, R.P., Leighton, R.B. and Sands, M.L. (1963) *The Feynman lectures on physics*. 3rd edn. Reading, Mass.: Addison-Wesley.

Fioranelli, F., Salous, S. and Raimundo, X. (2014) 'Frequency-Modulated Interrupted Continuous Wave as Wall Removal Technique in Through-the-Wall Imaging', *IEEE transactions on geoscience and remote sensing*, 52(10), pp. 6272-6283. doi: 10.1109/TGRS.2013.2295835.

Fisher, E., McMechan, G.A. and Annan, P.A. (1992) 'Acquisition and processing of wide-aperture ground-penetrating radar data', *Geophysics*, 57(3), pp. 495-504. doi: 10.1190/1.1443265.

Fisher, M.C., et al (2012) 'Emerging fungal threats to animal, plant and ecosystem health', *Nature (London)*, 484(7393), pp. 186-194. doi: 10.1038/nature10947.

Francis, J.K., Parresol, B.R. and de Patino, J.M. (1996) 'Probability of Damage to Sidewalks and Curbs by Street Trees in the Tropics', *Journal of Arboriculture*, 22.

Friends of Gunnersbury Park and Museum (2010) *Gunnersbury Park Trees*. Available at: https://gunnersburyfriends.org/gunnersbury-park-trees/ (Accessed: Jul 15, 2020).

Fromm, J.H., et al (2001) 'Xylem Water Content and Wood Density in Spruce and Oak Trees Detected by High-Resolution Computed Tomography', *Plant Physiology*, 127(2), pp. 416-425. doi: 10.1104/pp.010194.

Fu, L., Liu, S. and Liu, L. (Jun 2014) *Internal structure characterization of living tree trunk cross-section using GPR: Numerical examples and field data analysis*. Proceedings of the 15th International Conference on Ground Penetrating RadarIEEE, pp. 155.

Gaikwad, A.N., Singh, D. and Nigam, M.J. (2011) 'Application of clutter reduction techniques for detection of metallic and low dielectric target behind the brick wall by stepped frequency continuous wave radar in ultra-wideband range', *IET radar, sonar & navigation*, 5(4), pp. 416-425. doi: 10.1049/iet-rsn.2010.0059.

Giannakis, I. (2016) *Realistic numerical modelling of ground penetrating radar for landmine detection*. The University of Edinburgh. Available at: http://hdl.handle.net/1842/20449.

Giannakis, I. and Giannopoulos, A. (2014a) 'A Novel Piecewise Linear Recursive Convolution Approach for Dispersive Media Using the Finite-Difference Time-Domain Method', *IEEE transactions on antennas and propagation*, 62(5), pp. 2669-2678. doi: 10.1109/TAP.2014.2308549.

Giannakis, I. and Giannopoulos, A. (2014b) 'Time-Synchronized Convolutional Perfectly Matched Layer for Improved Absorbing Performance in FDTD', *IEEE*

antennas and wireless propagation letters, 14, pp. 690-693. doi: 10.1109/LAWP.2014.2376981.

Giannakis, I., Giannopoulos, A. and Warren, C. (2018) 'Realistic FDTD GPR Antenna Models Optimized Using a Novel Linear/Nonlinear Full-Waveform Inversion', *IEEE transactions on geoscience and remote sensing*, 57(3), pp. 1768-1778. doi: 10.1109/TGRS.2018.2869027.

Giannakis, I., Giannopoulos, A., Warren, C. and Davidson, N. (Jul 2015) *Numerical modelling and neural networks for landmine detection using ground penetrating radar*. 2015 8th International Workshop on Advanced Ground Penetrating Radar (IWAGPR) IEEE, pp. 1.

Giannakis, I., et al (Jul 2016) *Signal processing for landmine detection using ground penetrating radar*. 2016 IEEE International Geoscience and Remote Sensing Symposium (IGARSS) IEEE, pp. 7442.

Giannakis, I., Tosti, F., Lantini, L. and Alani, A.M. (2019a) 'Diagnosing Emerging Infectious Diseases of Trees Using Ground Penetrating Radar', *IEEE transactions on geoscience and remote sensing*, 58(2), pp. 1146-1155. doi: 10.1109/tgrs.2019.2944070.

Giannakis, I., Tosti, F., Lantini, L. and Alani, A.M. (2019b) 'Health Monitoring of Tree Trunks Using Ground Penetrating Radar', *IEEE transactions on geoscience and remote sensing*, 57(10), pp. 8317-8326. doi: 10.1109/tgrs.2019.2920224.

Gibbons, P. and Lindenmayer, D. (2002) *Tree Hollows and Wildlife Conservation in Australia*. Victoria: CSIRO Publishing.

Goodman, D. (1994) 'Ground-penetrating radar simulation in engineering and archaeology', *Geophysics*, 59(2), pp. 224-232. doi: 10.1190/1.1443584.

Grabianowski, M., Manley, B. and Walker, J.C.F. (2006) 'Acoustic measurements on standing trees, logs and green lumber', *Wood science and technology*, 40(3), pp. 205-216. doi: 10.1007/s00226-005-0038-5.

Grabosky, J., Bassuk, N., Irwin, L. and Van Es, H. (1998) *Pilot field study of structural soil materials in pavement profiles*. The Landscape Below Ground II: Proceedings of an International Workshop on Tree Root Development in Urban Soils. San Francisco, CAInternational Society of Arboriculture, .

Grabosky, J., Haffner, E. and Bassuk, N. (2009) 'Plant available moisture in stone-soil media for use under pavement while allowing urban tree root growth', *Arboriculture & Urban Forestry*, 35(5), pp. 271-278.

Gregory, P.J. (2006) *Plant roots: growth, activity, and interaction with soils*. Wiley-Blackwell.

Gregory, P.J., et al (2003) 'Non-invasive imaging of roots with high resolution X-ray micro-tomography', in Abe, J. (ed.) *Roots: the dynamic interface between plants and the Earth* Dordrecht: Springer, pp. 351-359.

Grissino-Mayer, H.D. (2003) 'A Manual and Tutorial for the Proper Use of an Increment Borer', *Tree-Ring Research*, 59(2), pp. 63-79.

Guba, E.G. (1990) *The Paradigm dialog*. San Francisco, CA: Sage Publications, Inc.

Guenter, B. and Parent, R. (1990) 'Computing the arc length of parametric curves', *IEEE computer graphics and applications*, 10(3), pp. 72-78. doi: 10.1109/38.55155.

Guo, L., et al (2013) 'Application of ground penetrating radar for coarse root detection and quantification: a review', *Plant and Soil*, 362(1-2), pp. 1-23. doi: 10.1007/s11104-012-1455-5.

Guo, Q., Rejmanek, M. and Wen, J. (2012) 'Geographical, socioeconomic, and ecological determinants of exotic plant naturalization in the United States: insights and updates from improved data', *NeoBiota*, 12(12), pp. 41-55. doi: 10.3897/neobiota.12.2419.

Guyot, A., et al (2013) 'Using electrical resistivity tomography to differentiate sapwood from heartwood: application to conifers', *Tree Physiology*, 33(2), pp. 187-194. doi: 10.1093/treephys/tps128.

Habermehl, A. (1982) 'A new non-destructive method for determining internal wood condition and decay in living trees. Part 1. Principles, method and apparatus', *Arboricultural journal*, 6(1), pp. 1-8. doi: 10.1080/03071375.1982.9746543.

Hansen, E.M. and Goheen, E.M. (2000) 'Phellinus Weirii and Other Native Root Pathogens as Determinants of Forest Structure and Process in Western North America', *Annual review of phytopathology*, 38, pp. 515-539. doi: 10.1146/annurev.phyto.38.1.515.

Hansen, P.C., Pereyra, V. and Scherer, G. (2013) *Least Squares Data Fitting with Applications*. Baltimore: Johns Hopkins University Press.

Hargreaves, C., Gregory, P.J. and Bengough, A.G. (2009) 'Measuring root traits in barley (Hordeum vulgare ssp. vulgare and ssp. spontaneum) seedlings using gel chambers, soil sacs and X-ray microtomography', *Plant and soil*, 316(1-2), pp. 285-297. doi: 10.1007/s11104-008-9780-4.

Hecht-Nielsen, R. (1992) 'Theory of the backpropagation neural network', in Wechsler, H. (ed.) *Neural Networks for Perception* Academic Press, Inc., pp. 65-93.

Heeraman, D.A., Hopmans, J.W. and Clausnitzer, V. (1997) 'Three dimensional imaging of plant roots in situ with X-ray Computed Tomography', *Plant and soil*, 189(2), pp. 167-179. doi: 10.1023/B:PLSO.0000009694.64377.6f.

Heeraman, D.A. and Juma, N.G. (1993) 'A comparison of minirhizotron, core and monolith methods for quantifying barley (Hordeum vulgare L.) and fababean (Yicia faba L.) root distribution', *Plant and soil*, 148(1), pp. 29-41. doi: 10.1007/BF02185382.

Henwood, K. (1973) 'A Structural Model of Forces in Buttressed Tropical Rain Forest Trees', *Biotropica*, 5(2), pp. 83-93. doi: 10.2307/2989657.

Hervé, V., et al (2014) 'Density mapping of decaying wood using X-ray computed tomography', *International Biodeterioration & Biodegradation*, 86, pp. 358-363. doi: 10.1016/j.ibiod.2013.10.009.

Hirano, Y., et al (2009) 'Limiting factors in the detection of tree roots using ground-penetrating radar', *Plant and Soil*, 319(1-2), pp. 15-24. doi: 10.1007/s11104-008-9845-4.

Hruska, J., Čermák, J. and Šustek, S. (1999) 'Mapping tree root systems with ground-penetrating radar', *Tree physiology*, 19(2), pp. 125-130.

Huisman, J.A., Hubbard, S.S., Redman, J.D. and Annan, A.P. (2003) 'Measuring Soil Water Content with Ground Penetrating Radar: A Review', *Vadose Zone Journal*, 2(4), pp. 476-491. doi: 10.2113/2.4.476.

Hunt, A.R. (2009) 'Use of a Frequency-Hopping Radar for Imaging and Motion Detection Through Walls', *IEEE transactions on geoscience and remote sensing*, 47(5), pp. 1402-1408. doi: 10.1109/TGRS.2009.2016084.

Ihamouten, A., et al (2018) 'Full-waveform inversion using a stepped-frequency GPR to characterize the tack coat in hot-mix asphalt (HMA) layers of flexible pavements', *NDT & E international*, 95, pp. 17-25. doi: 10.1016/j.ndteint.2017.12.006.

Iizuka, K., et al (1984) 'Step-frequency radar', *Journal of Applied Physics*, 56(9), pp. 2572-2583. doi: 10.1063/1.334286.

Innes, J.L. (1993) *Forest health: its assessment and status*. CAB international.

Iwase, J., et al (2015) 'Non-invasive Acoustic Sensing of Belowground Wooden Tissues: Possible Application to Spatial Mapping of Soil Usage by Tree Roots', *Environment control in biology*, 53(3), pp. 175-179. doi: 10.2525/ecb.53.175.

J. Rishbeth (1972) 'Resistance to Fungal Pathogens of Tree Roots', *Proceedings of the Royal Society of London. Series B. Biological Sciences*, 181(1064), pp. 333-351. doi: 10.1098/rspb.1972.0054.

Jackson, J.D. (1999) *Classical Electrodynamics*. 3rd edn.Wiley.

Jackson, R.B., et al (1996) 'A Global Analysis of Root Distributions for Terrestrial Biomes', *Oecologia*, 108(3), pp. 389-411. doi: 10.1007/BF00333714.

James, W.L. (1975) *Dielectric properties of wood and hardboard: variation with temperature, frequency, moisture content, and grain orientation*, District of Columbia: Dept. of Agriculture, Forest Service, Forest Products Laboratory.

Janse, J.D. and Obradovic, A. (2010) 'Xylella fastidiosa: its biology, diagnosis, control and risks', *Journal of Plant Pathology*, 92, pp. S35-S48. doi: 10.4454/JPP.V92I1SUP.2504.

Ježová, J., Harou, J. and Lambot, S. (2018) 'Reflection waveforms occurring in bistatic radar testing of columns and tree trunks', *Construction & Building Materials*, 174, pp. 388-400. doi: 10.1016/j.conbuildmat.2018.04.128.

Ježová, J., Mertens, L. and Lambot, S. (2016) 'Ground-penetrating radar for observing tree trunks and other cylindrical objects', *Construction & building materials*, 123, pp. 214-225. doi: 10.1016/j.conbuildmat.2016.07.005.

Jol, H.M. (2009) *Ground penetrating radar theory and applications*. 1st edn. Amsterdam: Elsevier.

Jung, T. (2009) 'Beech decline in Central Europe driven by the interaction between Phytophthora infections and climatic extremes', *Forest Pathology*, 39(2), pp. 73-94. doi: 10.1111/j.1439-0329.2008.00566.x.

Kaboub, F. (2001) *Positivist and hermeneutic paradigms: A critical evaluation under the structure of scientific practice*. Kansas City, MO: University of Missouri-Kansas City.

Kaestner, A., Schneebeli, M. and Graf, F. (2006) 'Visualizing three-dimensional root networks using computed tomography', *Geoderma*, 136(1), pp. 459-469. doi: 10.1016/j.geoderma.2006.04.009.

Kantartzis, N.V. and Tsiboukis, T.D. (2005) *Higher order FDTD schemes for waveguide and antenna structures*. 1st edn. San Rafael, Calif.: Morgan & Claypool.

Kearey, P., Brooks, M. and Hill, I. (2013) *An Introduction to Geophysical Exploration*. Hoboken: John Wiley & Sons, Incorporated.

Kehtarnavaz, N. (2008) *Digital signal processing system design*. 2nd edn. Amsterdam: Academic Press.

Kelley, C.T. (1999) *Iterative methods for optimization*. Philadelphia, PA: Society for Industrial and Applied Mathematics.

Kelley, D.F., Destan, T.J. and Luebbers, R.J. (2007) 'Debye Function Expansions of Complex Permittivity Using a Hybrid Particle Swarm-Least Squares Optimization Approach', *IEEE transactions on antennas and propagation*, 55(7), pp. 1999-2005. doi: 10.1109/TAP.2007.900230.

Kim, J., Cho, S. and Yi, M. (2007) 'Removal of ringing noise in GPR data by signal processing', *Geosciences Journal*, 11(1), pp. 75-81. doi: 10.1007/BF02910382.

Kivunja, C. and Kuyini, A.B. (2017) 'Understanding and Applying Research Paradigms in Educational Contexts', *International journal of higher education*, 6(5), pp. 26. doi: 10.5430/ijhe.v6n5p26.

Kjær, E.D., et al (2012) 'Adaptive potential of ash (Fraxinus excelsior) populations against the novel emerging pathogen Hymenoscyphus pseudoalbidus', *Evolutionary applications*, 5(3), pp. 219-228. doi: 10.1111/j.1752-4571.2011.00222.x.

Kopinga, J. (1994) *Aspects of the damage to asphalt road pavings caused by tree roots*. Savoy, IL: International Society of Arboriculture.

Köstler, J., Brückner, E. and Bibelriether, H. (1968) *Die Wurzeln der Waldbäume*. Hamburg: P. Parey.

Koubaa, A., Perré, P., Hutcheon, R.M. and Lessard, J. (2008) 'Complex Dielectric Properties of the Sapwood of Aspen, White Birch, Yellow Birch, and Sugar Maple', *Drying technology*, 26(5), pp. 568-578. doi: 10.1080/07373930801944762.

Krainyukov, A. and Lyaksa, I. (2016) 'Detection of Tree Roots in an Urban Area with the Use of Ground Penetrating Radar', *Transport and telecommunication*, 17(4), pp. 362-370. doi: 10.1515/ttj-2016-0032.

Kreyszig, E. (2006) *Advanced engineering mathematics*. 9th edn. John Wiley & Sons.

Lahouar, S., et al (2002) 'Approach to Determining In Situ Dielectric Constant of Pavements: Development and Implementation at Interstate 81 in Virginia', *Transportation research record*, 1806(1), pp. 81-87. doi: 10.3141/1806-09.

Lambot, S., Javaux, M., Hupet, F. and Vanclooster, M. (2002) 'A global multilevel coordinate search procedure for estimating the unsaturated soil hydraulic properties', *Water resources research*, 38(11), pp. 6-15. doi: 10.1029/2001WR001224.

Lambot, S., et al (2003) *GPR design and modeling for identifying the shallow subsurface dielectric properties*. Proceedings of the 2nd International Workshop on Advanced Ground Penetrating Radar, 2003IEEE, pp. 130.

Lameri, S., et al (Aug 2017) *Landmine detection from GPR data using convolutional neural networks*. 2017 25th European Signal Processing Conference (EUSIPCO). IEEE, pp. 508.

Lantini, L., et al (2019) 'Application of ground penetrating radar for mapping tree root system architecture and mass density of street trees', *Advances in Transportation Studies*, (3), pp. 51-62.

Lantini, L., et al (2020) *A Reflectivity-Based GPR Signal Processing Methodology for Mapping Tree Root Systems of Street Trees*. 2020 43rd International Conference on Telecommunications and Signal Processing (TSP). IEEE, pp. 449.

Lantini, L., Tosti, F., Bianchini Ciampoli, L. and Alani, A.M. (2020) *A frequency spectrum-based processing framework for the assessment of tree root systems*. SPIE Future Sensing Technologies International Society for Optics and Photonics, pp. 115251J.

Lantini, L., et al (2020) 'An Enhanced Data Processing Framework for Mapping Tree Root Systems Using Ground Penetrating Radar', *Remote Sensing*, 12(20), pp. 3417. doi: 10.3390/rs12203417.

Larsson, B., Bengtsson, B. and Gustafsson, M. (2004) 'Nondestructive detection of decay in living trees', *Tree physiology*, 24(7), pp. 853-858. doi: 10.1093/treephys/24.7.853.

Leskovar, D.I., Cantliffe, D.J. and Stoffella, P.J. (1994) 'Transplant Production Systems Influence Growth and Yield of Fresh-market Tomatoes', *Journal of the American Society for Horticultural Science*, 119(4), pp. 662-668. doi: 10.21273/JASHS.119.4.662.

Leucci, G., Masini, N., Persico, R. and Soldovieri, F. (2011) 'GPR and sonic tomography for structural restoration: the case of the cathedral of Tricarico', *Journal of geophysics and engineering*, 8(3), pp. S76-S92. doi: 10.1088/1742-2132/8/3/S08.

Leuschen, C.J. and Plumb, R.G. (2001) 'A matched-filter-based reverse-time migration algorithm for ground-penetrating radar data', *IEEE transactions on geoscience and remote sensing*, 39(5), pp. 929-936. doi: 10.1109/36.921410.

Lindsey, P. and Barlow, L. (1994) *The Design of Structural Soil Mixes for Trees in Urban Areas*. UC Davis, CA: Coorperative Extension Department of Environmental Horti-culture.

Loh, F.C.W., Grabosky, J.C. and Bassuk, N.L. (2003) 'Growth response of Ficus benjamina to limited soil volume and soil dilution in a skeletal soil container study', *Urban forestry & urban greening*, 2(1), pp. 53-62. doi: 10.1078/1618-8667-00023.

Loizos, A. and Plati, C. (2007) 'Accuracy of Ground Penetrating Radar Horn-Antenna Technique for Sensing Pavement Subsurface', *IEEE Sensors Journal*, 7(5), pp. 842-850. doi: 10.1109/JSEN.2007.894152.

Loperte. A., et al. (2006) '2D and 3D high resolution geoelectrical tomography for non - destructive determination of the spatial variability of plant root distribution: laboratory experiments and field measurements', *Geophysical Resource Abstract*, 8.

Lorenzo, H., Pérez-Gracia, V., Novo, A. and Armesto, J. (2010) 'Forestry applications of ground-penetrating radar', *Forest systems*, 19(1), pp. 5. doi: 10.5424/fs/2010191-01163.

Lucke, T., et al (2011) *Using permeable pavements to promote street tree health, to minimize pavement damage and to reduce stormwater flows*. International Conference on Urban Drainage International Water Association.

Lundström, T., Jonsson, M.J. and Kalberer, M. (2007) 'The root–soil system of Norway spruce subjected to turning moment: resistance as a function of rotation', *Plant and soil*, 300(1/2), pp. 35-49. doi: 10.1007/s11104-007-9386-2.

MacLeod, R.D. and Cram, J.W. (1996) *Forces exerted by tree roots*. UK: Arboriculture Research and Information Note Department of the Environment.

Mahesh, M. (2002) 'The AAPM/RSNA physics tutorial for residents: search for isotropic resolution in CT from conventional through multiple-row detector', *Radiographics*, 22(4), pp. 949-962. doi: 10.1148/radiographics.22.4.g02jl14949.

Majdi, H. (1996) 'Root sampling methods - applications and limitations of the minirhizotron technique', *Plant and soil*, 185(2), pp. 255-258. doi: 10.1007/BF02257530.

Majdi, H., et al (2005) 'Measuring fine root turnover in forest ecosystems', *Plant and soil*, 276(1/2), pp. 1-8. doi: 10.1007/s11104-005-3104-8.

Marchi, L., et al (2018) 'State of the Art on the Use of Trees as Supports and Anchors in Forest Operations', *Forests*, 9(8), pp. 467. doi: 10.3390/f9080467.

Martínez, J. L. F. et al. (2010) 'PSO: A powerful algorithm to solve geophysical inverse problems Application to a 1 D-DC resistivity case', *Journal of Applied Geophysics*, 71(1), pp. 13-25.

Mattheck, C., Bethge, K. and West, P.W. (1994) 'Breakage of hollow tree stems', *Trees (Berlin, West)*, 9(1). doi: 10.1007/BF00197869.

McPherson, E.G. and Peper, P. (2000) *Costs due to conflicts between street tree root growth and hardscape*. Cohasset, CA: Western Chapter (International Society of Arboriculture).

Mertens, L., Persico, R., Matera, L. and Lambot, S. (2015) 'Automated Detection of Reflection Hyperbolas in Complex GPR Images With No A Priori Knowledge on the Medium', *IEEE transactions on geoscience and remote sensing*, 54(1), pp. 580-596. doi: 10.1109/TGRS.2015.2462727.

Miao, Z. and Kosmas, P. (2017) 'Multiple-Frequency DBIM-TwIST Algorithm for Microwave Breast Imaging', *IEEE Transactions on Antennas and Propagation*, 65(5), pp. 2507-2516. doi: 10.1109/TAP.2017.2679067.

Monte, L.L., Erricolo, D., Soldovieri, F. and Wicks, M.C. (2010) 'Radio Frequency Tomography for Tunnel Detection', *IEEE Transactions on Geoscience and Remote Sensing*, 48(3), pp. 1128-1137. doi: 10.1109/TGRS.2009.2029341.

Mooney, S.J., Pridmore, T.P., Helliwell, J. and Bennett, M.J. (2012) 'Developing X-ray Computed Tomography to non-invasively image 3-D root systems architecture in soil', *Plant and soil*, 352(1), pp. 1-22. doi: 10.1007/s11104-011-1039-9.

Moran, M., Arcone, S.A., Delaney, A.J. and Greenfield, R. (1998) *3-D Migration/array processing using GPR data*. Lawrence, KS.

Morey, R. (1974) *Geophysical surveying system employing electromagnetic impulses. Authoring organisation*. U.S. Patent No. 3,806,795.

Mullaney, J., Lucke, T. and Trueman, S.J. (2015) 'A review of benefits and challenges in growing street trees in paved urban environments', *Landscape and urban planning*, 134, pp. 157-166. doi: 10.1016/j.landurbplan.2014.10.013.

Negishi, T., et al (2020) 'Radio Frequency Tomography for Nondestructive Testing of Pillars', *IEEE transactions on geoscience and remote sensing*, 58(6), pp. 3916-3926. doi: 10.1109/TGRS.2019.2959589.

Neumann, G., George, T.S. and Plassard, C. (2009) 'Strategies and methods for studying the rhizosphere—the plant science toolbox', *Plant and soil*, 321(1/2), pp. 431-456. doi: 10.1007/s11104-009-9953-9.

Nicolaescu, I. and van Genderen, P. (2012) 'Performances of a stepped-frequency continuous-wave ground penetrating radar', *Journal of applied geophysics*, 82, pp. 59-67. doi: 10.1016/j.jappgeo.2012.04.001.

Nicoll, B.C. and Armstrong, A. (1998) 'Development of Prunus root systems in a city street: Pavement damage and root architecture', *Arboricultural journal*, 22(3), pp. 259-270. doi: 10.1080/03071375.1998.9747209.

Ningal, T., Mills, G. and Smithwick, P. (2010) 'An inventory of trees in Dublin city centre', *Irish geography*, 43(2), pp. 161-176. doi: 10.1080/00750778.2010.500525.

Nixon, M. and Aguado, A. (2008) *Feature Extraction & Image Processing*. 2nd edn. Oxford, UK: Academic Press.

Nobel, P.S. (1988) *Environmental biology of agaves and cacti*. 1st edn. Cambridge u.a: Cambridge Univ. Pr.

Olhoeft, G.R. (1998) Electrical, magnetic and geometric properties that determine ground penetrating radar performance. *Proceedings of GPR,* pp. 177.

Olhoeft, G.R. (2000) 'Maximizing the information return from ground penetrating radar', *Journal of applied geophysics*, 43(2), pp. 175-187. doi: 10.1016/S0926-9851(99)00057-9.

Ow, L.F. and Sim, E.K. (2012) 'Detection of urban tree roots with the ground penetrating radar', *Plant biosystems*, 146(sup1), pp. 288-297. doi: 10.1080/11263504.2012.731018.

Paglis, C.M. (2013) 'Application of electrical resistivity tomography for detecting root biomass in coffee trees', *International Journal of Geophysics*, 2013, pp. 6. doi: 10.1155/2013/383261.

Pallardy, S.G. (2008) *Physiology of woody plants*. 3rd edn. Academic Press.

Panissod, C., Michot, D., Benderitter, Y. and Tabbagh, A. (2001) 'On the effectiveness of 2D electrical inversion results: an agricultural case study', *Geophysical Prospecting*, 49(5), pp. 570-576. doi: 10.1046/j.1365-2478.2001.00277.x.

Pastorino, M. (2010) *Microwave Imaging*. Hoboken, NJ, USA: John Wiley & Sons, Inc.

Peplinski, N.R., Ulaby, F.T. and Dobson, M.C. (1995) 'Dielectric properties of soils in the 0.3-1.3-GHz range', *IEEE transactions on geoscience and remote sensing*, 33(3), pp. 803-807. doi: 10.1109/36.387598.

Perez-Gracia, V., et al (2014) *Study of wood beams in buildings with ground penetrating radar*. Proceedings of the 15th International Conference on Ground Penetrating Radar. IEEE, pp. 31.

Perret, J.S., Al-Belushi, M.E. and Deadman, M. (2007) 'Non-destructive visualization and quantification of roots using computed tomography', *Soil biology & biochemistry*, 39(2), pp. 391-399. doi: 10.1016/j.soilbio.2006.07.018.

Persico, R., Bernini, R. and Soldovieri, F. (2005) 'The role of the measurement configuration in inverse scattering from buried objects under the Born approximation', *IEEE transactions on antennas and propagation*, 53(6), pp. 1875-1887. doi: 10.1109/TAP.2005.848468.

Persico, R. (2014) *Introduction to ground penetrating radar: inverse scattering and data processing*. John Wiley & Sons, Inc.

Pipan, M., Finetti, I. and Ferigo, F. (1996) 'Multi-fold GPR techniques with applications to high-resolution studies: two case histories', *European Journal of Environmental and Engineering Geophysics*, 1, pp. 83-103.

Pokorny, K. (2003) *Urban tree risk management: a community guide to program design and implementation*. Minnesota: USDA Forest Service, Northeastern Area, State and Private Forestry.

Potin, D., Duflos, E. and Vanheeghe, P. (2006) 'Landmines Ground-Penetrating Radar Signal Enhancement by Digital Filtering', *IEEE Transactions on Geoscience and Remote Sensing*, 44(9), pp. 2393-2406. doi: 10.1109/TGRS.2006.875356.

Powers, M.H. (1997) 'Modeling frequency-dependent GPR', *Leading edge*, 16(11), pp. 1657-1662. doi: 10.1190/1.1437549.

Radzevicius, S.J. and Daniels, J.J. (2000) 'Ground penetrating radar polarization and scattering from cylinders', *Journal of applied geophysics*, 45(2), pp. 111-125. doi: 10.1016/S0926-9851(00)00023-9.

Randrup, T.B., McPherson, E.G. and Costello, L.R. (2001) 'A review of tree root conflicts with sidewalks, curbs, and roads', *Urban ecosystems*, 5(3), pp. 209-225. doi: 10.1023/A:1024046004731.

Randrup, T.B., McPherson, E.G. and Costello, L.R. (2001) 'Tree Root Intrusion in Sewer Systems: Review of Extent and Costs', *Journal of infrastructure systems*, 7(1), pp. 26-31. doi: 10.1061/(ASCE)1076-0342(2001)7:1(26).

Ranius, T. and Hedin, J. (2001) 'The dispersal rate of a beetle, Osmoderma eremita, living in tree hollows', *Oecologia*, 126(3), pp. 363-370. doi: 10.1007/s004420000529.

Richardson, D.M., et al (2001) 'Naturalization and invasion of alien plants: concepts and definitions', *Diversity & distributions*, 6(2), pp. 93-107. doi: 10.1046/j.1472-4642.2000.00083.x.

Roberts, J., Jackson, N. and Smith, M. (2006) *Tree roots in the built environment*. London: The Stationary Office Books.

Robinson, J. and Rahmat-Samii, Y. (2004) 'Particle swarm optimization in electromagnetics', *IEEE transactions on antennas and propagation*, 52(2), pp. 397-407. doi: 10.1109/TAP.2004.823969.

Robinson, L.A., Weir, W.B. and Young, L. (1974) 'Location and recognition of discontinuities in dielectric media using synthetic RF pulses', *Proceedings of the IEEE*, 62(1), pp. 36-44. doi: 10.1109/PROC.1974.9383.

Robinson, R.A. (1976) *Plant pathosystems*. Berlin: Springer.

Rodriguez-Abad, I., et al (Jun 2011) *Non-destructive characterization of maritime pine sawn timber dielectric anisotropy by means of GPR*. 2011 6th International Workshop on Advanced Ground Penetrating Radar (IWAGPR)IEEE, pp. 1.

Russell, T. and Cutler, C. (2004) *Trees: an illustrated identifier and encyclopedia*. Hermes House.

S. S. Lee and Yahya, N.S. (1999) 'Fungi Associated With Heart Rot of Acacia Mangium Trees in Peninsular Malaysia and East Kalimantan', *Journal of tropical forest science*, 11(1), pp. 240-254.

Salas, W.A., Ranson, J.K., Rock, B.N. and Smith, K.T. (1994) 'Temporal and spatial variations in dielectric constant and water status of dominant forest species from New England', *Remote sensing of environment*, 47(2), pp. 109-119. doi: 10.1016/0034-4257(94)90148-1.

Samouëlian, A., et al (2005) 'Electrical resistivity survey in soil science: a review', *Soil & tillage research*, 83(2), pp. 173-193. doi: 10.1016/j.still.2004.10.004.

Samuelson, L.J., et al (2008) 'Growth and physiology of loblolly pine in response to long-term resource management: defining growth potential in the southern United States', *Canadian Journal of Forest Research*, 38(4), pp. 721-732. doi: 10.1139/X07-191.

Santini, A., et al (2012) 'Biogeographical patterns and determinants of invasion by forest pathogens in Europe', *The New phytologist*, 197(1), pp. 238-250. doi: 10.1111/j.1469-8137.2012.04364.x.

Satriani, A., Loperte, A., Proto, M. and Bavusi, M. (2010) 'Building damage caused by tree roots: laboratory experiments of GPR and ERT surveys', *Advances in geosciences*, 24(24), pp. 133-137. doi: 10.5194/adgeo-24-133-2010.

Schrock, B.J. (1994) *Existing sewer evaluation and rehabilitation*. ASCE Manual and Report on Engineering Practice.

Schuurman, J.J. and Goedewaagen, M.A.J. (1965) *Methods for the examination of root systems and roots*. Wageningen: Centre for agricultural publications and documentation.

Shainsky, L.J. and Radosevich, S.R. (1992) 'Mechanisms of Competition Between Douglas-Fir and Red Alder Seedlings', *Ecology*, 73(1), pp. 30-45. doi: 10.2307/1938718.

Sharpe, R.J. and Thorne, R.W. (1982) 'Numerical method for extracting an arc length parameterization from parametric curves', *Computer aided design*, 14(2), pp. 79-81. doi: 10.1016/0010-4485(82)90171-3.

Shortle, W.C. and Dudzik, K.R. (2012) *Wood Decay in Living and Dead Trees: A Pictorial Overview*. U.S. Forest Service.

Smit, A.L. (2013) *Root methods: a handbook*. Berlin: Springer Science & Business Media.

Soldovieri, F., Lopera, O. and Lambot, S. (2010) 'Combination of Advanced Inversion Techniques for an Accurate Target Localization via GPR for Demining Applications', *IEEE transactions on geoscience and remote sensing*, 49(1), pp. 451-461. doi: 10.1109/TGRS.2010.2051675.

Soldovieri, F. and Solimene, R. (2010) *Ground Penetrating Radar Subsurface Imaging of Buried Objects*. InTech.

Solimene, R., et al (2014) 'SAR Imaging Algorithms and Some Unconventional Applications: A unified mathematical overview', *IEEE signal processing magazine*, 31(4), pp. 90-98. doi: 10.1109/MSP.2014.2311271.

Solimene, R., et al (2013) 'Ground Clutter Removal in GPR Surveys', *IEEE journal of selected topics in applied earth observations and remote sensing*, 7(3), pp. 792-798. doi: 10.1109/JSTARS.2013.2287016.

Stängle, S.M., et al (2015) 'Potentially increased sawmill yield from hardwoods using X-ray computed tomography for knot detection', *Annals of Forest Science*, 72(1), pp. 57-65. doi: 10.1007/s13595-014-0385-1.

Stein, W.E., et al (2020) 'Mid-Devonian Archaeopteris Roots Signal Revolutionary Change in Earliest Fossil Forests', *Current biology*, 30(3), pp. 421-431.e2. doi: 10.1016/j.cub.2019.11.067.

Stocks, J.J., Buggs, R.J.A. and Lee, S.J. (2017) 'A first assessment of Fraxinus excelsior (common ash) susceptibility to Hymenoscyphus fraxineus (ash dieback) throughout the British Isles', *Scientific reports*, 7(1), pp. 16546-7. doi: 10.1038/s41598-017-16706-6.

Stokes, A. (1994) *Responses of young trees to wind: effects on root architecture and anchorage strength*. University of York.

Stokes, A., et al (2002) 'An evaluation of different methods to investigate root system architecture of urban trees in situ: I. Ground-penetrating radar', *Journal of Arborculture*, pp. 2-10.

Stone, E.L. and Kalisz, P.J. (1991) 'On the maximum extent of tree roots', *Forest ecology and management*, 46(1), pp. 59-102. doi: 10.1016/0378-1127(91)90245-Q.

Stover, D.B., Day, F.P., Butnor, J.R. and Drake, B.G. (2007) 'Effect of elevated CO2 on coarse-root biomass in Florida scrub detected by ground-penetrating radar', *Ecology*, 88(5), pp. 1328-1334.

Strong, W.L. and La Roi, G.H. (1983) 'Root-system morphology of common boreal forest trees in Alberta, Canada', *Canadian journal of forest research*, 13(6), pp. 1164-1173. doi: 10.1139/x83-155.

Sullivan, R.H., Gemmell, R.S., Schafer, L.A. and Hurst, W.D. (1977) *Economic analysis, root control, and backwater flow control as related to infiltration/inflow control*. Cincinnati, Ohio: Municipal Environmental Research Laboratory, Office of Research and Development, U.S. Environmental Protection Agency; available through the National Technical Information Service, 1977.

Sustek, S., Hruska, J., Druckmuller, M. and Michalek, T. 'Root surfaces in the large oak tree estimated by image analysis of the map obtained by the ground penetrating radar', *Journal of Forest Science*, 45, pp. 139-143.

Taflove, A. and Hagness, S.C. (2005) *Computational electrodynamics*. 3rd edn. Boston: Artech House.

Taylor, H.M., Upchurch, D.R., Brown, J.M. and Rogers, H.H. (1991) 'Some Methods of Root Investigations', in *Developments in Agricultural and Managed-Forest Ecology* Elsevier Ltd, pp. 553-564.

Time and Date, A S (2019) *Past Weather in London, England, United Kingdom — April 2019*. Available at: https://www.timeanddate.com/weather/uk/london/historic?month=4&year=2019 (Accessed: Jul 3, 2020).

Tomasanis, D. (1990) *Effective Dielectric Constants of Foliage Media*. Waltham, MA: Arcon Corp. Available at: http://www.dtic.mil/docs/citations/ADA226296.

Tosti, F., et al (2020) 'The Use of GPR and Microwave Tomography for the Assessment of the Internal Structure of Hollow Trees', *IEEE Transactions on Geoscience and Remote Sensing (submitted)*.

Tosti, F., Bianchini Ciampoli, L., Brancadoro, M.G. and Alani, A. (2018) 'GPR applications in mapping the subsurface root system of street trees with road safety-critical implications', *Advances in Transportation Studies*. doi: 10.4399/97888255143468.

Tosti, F., et al (2018) 'An experimental-based model for the assessment of the mechanical properties of road pavements using ground-penetrating radar', *Construction & building materials*, 165, pp. 966-974. doi: 10.1016/j.conbuildmat.2018.01.179.

Tosti, F. and Pajewski, L. (2015) *Applications of radar systems in planetary sciences: an overview*. Springer International Publishing.

Tracy, S.R., Black, C.R., Roberts, J.A. and Mooney, S.J. (2011) 'Soil compaction: a review of past and present techniques for investigating effects on root growth', *Journal of the science of food and agriculture*, 91(9), pp. 1528-1537. doi: 10.1002/jsfa.4424.

Tracy, S.R., et al (2010) 'The X-factor: visualizing undisturbed root architecture in soils using X-ray computed tomography', *Journal of experimental botany*, 61(2), pp. 311-313. doi: 10.1093/jxb/erp386.

Trowbridge, P.J. and Bassuk, N.L. (2004) *Trees in the Urban Landscape: Site Assessment, Design, and Installation*. Hoboken, N.J.: Wiley.

Tubbs, C.H. (1977) *Root-crown relations of young sugar maple and yellow birch*. St. Paul, MN: US Dept. of Agriculture, Forest Service, North Central Forest Experiment Station 225.

van Genderen, P. and Nicolaescu, I. (2003) *System description of a stepped frequency CW radar for humanitarian demining*. Proceedings of the 2nd International Workshop on Advanced Ground Penetrating Radar, 2003IEEE, pp. 9.

van Mantgem, P.J. and Stephenson, N.L. (2004) 'Does coring contribute to tree mortality?', *Canadian Journal of Forest Research*, 34(11), pp. 2394-2398. doi: 10.1139/x04-120.

Wagar, J.A. and Barker, P.A. (1983) 'Tree root damage to sidewalks and curbs', *Journal of Arborculture*, 9(7), pp. 177-181.

Wagar, J.A. and Franklin, A.L. (1994) 'Sidewalk effects on soil moisture and temperature', *Journal of Arborculture*, 20, pp. 237.

Wang, Q., Yang, S., Jiang, M. and Cao, J. (2019) 'Non-destructive detection of density and moisture content of heartwood and sapwood based on X-ray computed tomography (X-CT) technology', *European Journal of Wood and Wood Products*, 77(6), pp. 1053-1062. doi: 10.1007/s00107-019-01459-y.

Wang, X., Allison, R.B., Wang, L. and Ross, R.J. (2007) *Acoustic tomography for decay detection in red oak trees*. Madison, WI: U.S. Dept. of Agriculture, Forest Service, Forest Products Laboratory. Available at: http://purl.access.gpo.gov/GPO/LPS93091.

Wang, Z., et al (2006) 'Fine root architecture, morphology, and biomass of different branch orders of two Chinese temperate tree species', *Plant and soil*, 288(1/2), pp. 155-171. doi: 10.1007/s11104-006-9101-8.

Warren, C. and Giannopoulos, A. (2011) 'Creating finite-difference time-domain models of commercial ground-penetrating radar antennas using Taguchi's optimization method', *Geophysics*, 76(2), pp. G37-G47. doi: 10.1190/1.3548506.

Warren, C., Giannopoulos, A. and Giannakis, I. (2016) 'gprMax: Open source software to simulate electromagnetic wave propagation for Ground Penetrating Radar', *Computer physics communications*, 209, pp. 163-170. doi: 10.1016/j.cpc.2016.08.020.

Warren, C., et al (2019) 'A CUDA-based GPU engine for gprMax: Open source FDTD electromagnetic simulation software', *Computer physics communications*, 237, pp. 208-218. doi: 10.1016/j.cpc.2018.11.007.

Weaver, J.E. and Voigt, J.W. (1950) 'Monolith Method of Root-Sampling in Studies on Succession and Degeneration', *Botanical gazette*, 111(3), pp. 286-299. doi: 10.1086/335595.

Wei, X. and Zhang, Y. (2014) 'Autofocusing Techniques for GPR Data from RC Bridge Decks', *IEEE journal of selected topics in applied earth observations and remote sensing*, 7(12), pp. 4860-4868. doi: 10.1109/JSTARS.2014.2321710.

Wielopolski, L., Hendrey, G., Daniels, J.J. and McGuigan, M. (2000) *Imaging tree root systems in situ*. Proceedings of SPIE, pp. 642.

Wildenschild, D., et al (2002) 'Using X-ray computed tomography in hydrology: systems, resolutions, and limitations', *Journal of hydrology*, 267(3-4), pp. 285-297. doi: 10.1016/S0022-1694(02)00157-9.

Williams, R.E., Shaw, C.G., Wargo, P.M. and Sites, W.H. (1986) *Armillaria root disease*. Washington, D. C.: US Department of Agriculture, Forest Service.

Wilson, B.F. (1964) *Structure and growth of woody roots of Acer rubrum L.* Harvard University, Harvard Forest St. Petersham.

Wu, H.Q., Zhou, Q.Y., Liu, H.L. and Tang, M.J. (2009) 'Application of electrical resistivity tomography in studying water uptake process in tree trunk', *Chin J Ecol*, 28, pp. 350-356.

Wu, R., et al (2001) 'Adaptive ground bounce removal', *Electronics letters*, 37(20), pp. 1.

Yarovoy, A., Ligthart, L., Schukin, A. and Kaploun, I. (2002) 'Polarimetric Video Impulse Radar for Landmine Detection', *Subsurface sensing technologies and applications: an international journal*, 3(4), pp. 271-293. doi: 10.1023/A:1020309213661.

Yee, K. (1966) 'Numerical solution of initial boundary value problems involving maxwell's equations in isotropic media', *IEEE transactions on antennas and propagation*, 14(3), pp. 302-307. doi: 10.1109/TAP.1966.1138693.

Yeung, S.W., Yan, W.M. and Hau, C.H.B. (2016) 'Performance of ground penetrating radar in root detection and its application in root diameter estimation under controlled conditions', *Science China. Earth sciences*, 59(1), pp. 145-155. doi: 10.1007/s11430-015-5156-9.

Zarco-Tejada, P.J., et al (2018) 'Previsual symptoms of Xylella fastidiosa infection revealed in spectral plant-trait alterations', *Nature plants*, 4(7), pp. 432-439. doi: 10.1038/s41477-018-0189-7.

Zenone, T., et al (2008) 'Preliminary use of ground-penetrating radar and electrical resistivity tomography to study tree roots in pine forests and poplar plantations', *Functional Plant Biology*, 35(10), pp. 1047-1058. doi: 10.1071/FP08062.

Zheng, Z., et al (2016) 'Hollows in living trees develop slowly but considerably influence the estimate of forest biomass', *Functional ecology*, 30(5), pp. 830-838. doi: 10.1111/1365-2435.12566.

Acknowledgements

This Thesis completes a long process that began several years ago. Along the way I walked with many people, some were inspirational, others were an example, still others were incredibly supportive. I do not have enough words to express my gratitude to everyone who helped me get where I am and make my dream come true. However, I will try to thank those who played an important role in this journey.

First, my gratitude goes to my principal supervisor, Professor Amir M. Alani. Thank you for believing in me, giving me this great chance and many other opportunities to challenge myself. Above all, thank you for supervising not only my work, but also my present and my future.

I owe more than a thank you to my second supervisor, Dr Fabio Tosti. Before anything else, you were a model, an inspiration. When you were the PhD student, and I was the undergraduate student whose Thesis you were supervising, I thought I wanted to be just like you. In a way, it is your “fault” if I chose this life. You have been a guide, a spur, a support when everything seemed impossible to me and the most enthusiastic about my successes. Fabio, at work and in life, you have been an older brother. Grazie.

A special mention goes to the supervisor of my previous studies, Professor Andrea Benedetto. I owe him many technical, professional and life lessons. Thank you for introducing me to the world of GPR and research. I carry your teachings with me every step of the way.

I would like to thank all the people I have collaborated with over the years. In particular, thanks to Dr Luca Bianchini Ciampoli, from Roma Tre University, for his availability,

patience and friendship. Furthermore, heartfelt thanks go to Dr Francesco Soldovieri, from the Italian National Research Council, and to his great research team.

I would like to thank my external examiner, Professor Andreas Loizos, and my internal examiner, Professor Konstantin Nikolic, for taking the time to assess this work and to evaluate my final viva.

Heartfelt thanks go to the research team of The Faringdon Centre for Non-Destructive Testing, Dr Iraklis Giannakis, Dr Lilong Zou and Mr Daniel Egyir. These years of work together, made of field research, long days in the laboratory, coffees (and chamomiles), students to evaluate and papers to write, have been a precious gift and an unforgettable experience for me. You are real friends, and you have taught me a lot.

To my dear friends at the School of Computing and Engineering, Dr Kevin Munisami, Dr Apostolos Georgakis and Dr Anastasia Sofroniou, a big thank you, you made me feel like family. We shared lunches in the lab, coffees in the corridors while you were rushing to lessons and amazing chats in the empty office on Friday evenings. You are great friends and role models for me.

I would also like to thank all the staff at the School of Computing and Engineering, for welcoming me as one of them. It would be impossible to name you all, but each one of you is important to me.

Thanks to my friends and PhD fellows, Herval Almenoar-Webster and Cat Forward. We are a winning team, we have shared the joys and (many) pains of this journey, and we have supported each other every time. We have always found answers to Herval's questions on our projects' ethical implications, too.

A huge thank you to my dearest friend from the other side of the world, Dr Jinghui Peng. Your always sweet and discreet presence, your getting excited about every little thing, our walks to discover London, our conversations, have been an enormous support over the years. I miss you very much now that you are back in your country, but I am grateful for your happiness and success.

It is difficult for me to explain the gratitude I feel for my parents, Ambra and Andrea, in a few lines. Leaving you to chase this future was perhaps the most difficult choice of my life, but you have supported me in my every choice and thanks to you I am here now. You are the example that guides me in life. This result, like the previous one, is dedicated to you.

To my family in Italy: Perla, Elmar, Engel, Alex, Paolo, Luisa, Luca, Claudia, Marco. Thank you very much. Your love and support are for me like the warmth of our sun (which is rarely seen here).

To my sister, Ilaria. I can never thank you enough for everything. I do not know what I would do without your support, your laughter, our getting each other, and the phone calls you make when you feel that something is wrong even if I have not told you anything. You have been making me a better person for more than ten years now. Grazie.

Reza, PhD fellow, friend, confidant, partner in life, fiancé. You have always believed in me with solid determination, celebrating my victories and minimising any failure as an accident. I could not have done all this without you, your support, your encouragement, your smile. I cannot wait to face everything the future holds for us, together.